Synthesis and Characterization of Oxide Materials

Atul V. Thorat

Department of Chemistry

University College Cork, Ireland.

This thesis is presented for the Degree of Doctor of

Philosophy to the National University of Ireland.

Supervisor: Prof. Michael A. Morris

Co- Supervisor: Prof. Justin D. Holmes

Head of the Department: Prof. Martyn Pemble

April 2014

Declaration

I, Atul V. Thorat, certify that this Thesis is my own work and I have not obtained a degree in this University or elsewhere on the basis of this PhD Thesis.

Atul V. Thorat Date

Abstract

Nanostructured materials are central to the evolution of future electronics and biomedical applications amongst other applications. This thesis is focused on developing novel methods to prepare a number of nanostructured metal oxide particles and films by a number of different routes. Part of the aim was to see how techniques used in nanoparticle science could be applied to thin film methods to develop functional surfaces. Wet-chemical methods were employed to synthesize and modify the metal oxide nanostructures (CeO_2 and SiO_2) and their structural properties were characterized through advanced X-ray diffraction, electron microscopy, photoelectron spectroscopy and other techniques. Whilst particulates have uses in many applications, their attachment to surfaces is of importance and this is frequently challenging. We examined the use of block copolymer methods to form very well defined metal oxide particulate-like structures on the surface of a number of substrates.

Chapter 2 describes a robust method to synthesize various sized silica nanoparticles. As-synthesized silica nanoparticles were further functionalized with IR-820 and FITC dyes. The ability to create size controlled nanoparticles with associated (optical) functionality may have significant importance in bio-medical imaging.

Thesis further describes how non-organic modified fluorescent particles might be prepared using inorganic oxides. A study of the concentrations and distributions of europium dopants within the CeO_2 nanoparticles was undertaken and investigated by different microscopic and spectroscopic techniques. The luminescent properties were enhanced by doping and detailed explanations are reported. Additionally, the

morphological and structural evolution and optical properties were correlated as a function of concentrations of europium doping as well as with further annealing. Further work using positron annihilation spectroscopy allowed the study of vacancy type defects formed due to europium doping in CeO_2 crystallites and this was supported by complimentary UV-Vis spectra and XRD work.

During the last few years the interest in mesoporous silica materials has increased due to their typical characteristics such as potential ultra-low dielectric constant materials, large surface area and pore volume, well-ordered and uniform pores with adjustable pores between 2 and 50 nm. A simple, generic and cost-effective route was used to demonstrate the synthesis of 2D mesoporous silica thin films over wafer scale dimensions in chapter 5. Lithographic resist and *in situ* hard mask block copolymer followed by ICP dry etching were used to fabricate mesoporous silica nanostructures. The width of mesoporous silica channels can be varied by using a variety of commercially available lithographic resists whereas depth of the mesoporous silica channels can be varied by altering the etch time. The crystal structure, morphology, pore arrangement, pore diameters, thickness of films and channels were determined by XRD, SEM, ellipsometry and the results reported.

This project also extended work towards the study of the antimicrobial study of nanopatterned silver nanodot arrays formed using the block copolymer approach defined above. Silver nanodot arrays were successfully tested for antimicrobial activity over *S. aureus* and *P. aeruginosa* biofilms and results shows silver nanodots has good antimicrobial activity for both *S. aureus* and *P. aeruginosa* biofilms. Thus, these silver nanodot arrays shows a potential to be used as a substitute for the resolution of infection complications in many areas.

Acknowledgments

First and foremost I would like to express my sincere gratitude to my supervisor, Prof Michael Morris for giving me the opportunity to do my PhD. His valuable time, constant encouragement, vast experience and knowledge of the field were the key for the achievements of this research. Without his inspiration and the confidence he put in me this thesis would not have been possible.

I would like to convey my sincere thanks to co-supervisor Prof Justin Holmes, for the guidance and help he provided over the course of my PhD. Special thanks to Dr John Wenger and Dr Orla Ni Dhubhghaill for monitoring my progress yearly and valuable discussion during my PhD.

Carrying out my PhD studies would not have been possible without the support of many others that somehow have helped me to achieve the set goals. I would like to address my special thanks to Dr Tandra Ghoshal, for her enthusiasm, valuable time and never-ending encouragement throughout the course of this project as well as her help in my personal life. She has also contributed to the direction of this work by giving insightful advice during my PhD programme.

I also take this opportunity to thank Science Foundation Ireland for support of this project through the Strategic Research Cluster FORME grant and the CSET CRANN grant.

I would like to thank Dr Lan Chen who helped me through my first steps in the lab. Special thanks to P. M. G. Nambissan, Matt Shaw, Sozaraj Rasappa, Patrick Carolan, Ramsankar and Marlies Mooij, for their contribution in this thesis. I put my sincere thanks to Dipu, Parvaneh, Colm McManamon, Cian, Timothy, Atul C, Sibu,

all past and present members of lab 343 for much needed support and many enjoyable days in lab.

I would like to express my sincere thanks Mark, Sven, Kamil, Dave, Subhajit, JV, Gill, Olan, Colm O' Regan, John, Brenda, all past and present members of lab 115. Thanks to Colm O' Dwyer and his group members. Thanks to the ERI members Paul, Joe, John, Eoin and especially Pete Fleming for XPS analysis. I also thanks to Tyndall members Nitin Deepak, Nikolay, Vince, Shelly, Roisin and Anushka for their assistance and support.

Sincere thanks to Dr Tarek Lutz and Dr Clive Downing from AML, CRANN, TCD for the TEM and EELS assistance. I would like to thank my friends in cork Pankaj, Abhay, Sanjay, Rakesh and KK for great support and company. My best friends in India: Nitin, Manish, Jayant, Pramod, Anand and Raju, my immense thanks to you guys for your great encouragement and support.

A special thanks to Dr Matthias Jauch for all the IT assistance over the past few years. I always thankful to the administrative and technical staff of Department of Chemistry, UCC for putting up with me in my PhD: Eileen O'Callaghan, Mary, Colette, Christine, Terry, Chrissie, Tina, Pat, Rose, Agnes and Noel.

I cannot express my feeling about my family, for their continuous support in all my success and failures. In particular, my father (Bapu), who always stands with my decisions during whole life.

Last but not the least, the special thanks to my beloved wife, Shital, for her endless support and understanding at all times. Special thanks to the newest addition to my family, Sarvesh, my son, who gave me ecstatic moments during my writing.

Dedicated to my family

Publications and Presentations

1) Atul V. Thorat, Tandra Ghoshal, Justin D. Holmes, P. M. G. Nambissan and Michael A. Morris, A positron annihilation spectroscopic investigation of europium-doped cerium oxide nanoparticles. *Nanoscale*, 2014, **6,** 608-615
2) Atul V. Thorat, Tandra Ghoshal, Patrick Carolan, Justin D. Holmes and Michael A. Morris, Defect Chemistry and Vacancy Concentration of Luminescent Europium Doped Ceria Nanoparticles by Solvothermal Method, *Journal of Physical Chemistry C*, 2014, **118,** 10700-10710.
3) Atul V. Thorat, Tandra Ghoshal, Michael A. Morris and P. M. G. Nambissan, Eu-doped cerium oxide nanoparticles studied by positron annihilation, P*roceeding of 41st Polish Seminar on Positron Annihilation PSPA-13 (Acta Physica Polonica A), 2014, **125**, 756.*
4) Atul V. Thorat, Tandra Ghoshal, Lan Chen, Justin D. Holmes and Michael A. Morris, Synthesis and characterization of dye-doped silica nanoparticles, *In preparation.*
5) Atul V. Thorat, Tandra Ghoshal, Justin D. Holmes and Michael A. Morris, Fabrication of nanopatterned mesoporous silica channels, *In preparation.*
6) Atul V. Thorat, Tandra Ghoshal, Ramsankar Senthamaraikannan, Sozaraj Rasappa, Justin D. Holmes and Michael A. Morris, 11th International Conference on Materials Chemistry (MC11) 8-11 July 2013, University of Warwick, UK
7) Atul V. Thorat, Tandra Ghoshal, Patrick Carolan, Justin D. Holmes, Michael A. Morris, 65th Irish Universities Chemistry Research Colloquium, 27- 28 June, 2013, Trinity College Dublin, Ireland.
8) Atul V. Thorat, Tandra Ghoshal, Justin D. Holmes, Michael A. Morris, MRS Spring meeting, 1-5 April, 2013, San Francisco, USA.
9) Atul V. Thorat, Tandra Ghoshal, Justin D. Holmes, Michael A. Morris, XI International Conference on Nanostructured Materials (NANO2012), 26-31 August, 2012, Rhodes, Greece

Table of contents

Chapter 1

Introduction

1.1. Nanomaterials

Nanotechnology can be defined as a technology of design, fabrication and the applications of nanostructures and nanomaterials. As a scientific term, 'nano' means 10^{-9} where 1 nanometer is equivalent to one thousandth of a micrometer and one billionth of a meter. A nanostructure implies that the structure has at least one dimension between 1 and 100 nm. Small features permit more functionality in a given space, but nanotechnology is not only a simple continuation of miniaturization from micron scale down to the nanometer scale. It involves the ability to fabricate, characterize and manipulate artificial structures, whose features are controlled at the nanometer scale. Nanotechnology embraces areas of research as diverse as engineering, physics, chemistry, materials science and molecular biology. Research in this area has been triggered by the availability of revolutionary instruments and approaches that allow the investigation of material properties with a resolution close to atomic level. Potential applications are possible in various fields, such as agriculture production, food processing and manufacturing, human health and nutrition, biotechnology, medicine and drug delivery, information technology, energy production etc.

Materials on the nanometer scale have received interest as a result of their often unexpected and interesting properties that provide application performance superior to their bulk counterparts.[1-3] The physical properties of nanomaterials can arise from a variety of reasons such as (i) large fraction of surface atoms, (ii) high surface energy, (iii) spatial confinement and (iv) reduced imperfections. Nanomaterials generally have low melting point (the difference can be as large as 1000 °C) and reduced lattice constants compared to bulk materials, since the number of surface atoms or ions becomes a significant fraction of the total number of atoms or ions and the surface energy plays a significant role in the thermal stability.[4] The mechanical properties of nanomaterials may reach the theoretical strength of the materials, which are one or two orders of magnitude higher than that of single crystals in bulk form.[5] The enhancement in mechanical strength is related to the reduced probability of defects in a small volume. The energy band structure and

charge carrier density in the materials can be modified due to quantum confinement which in turn modifies the optical and electronic properties.[6] For example, the optical absorption peak of semiconductor nanoparticles shifts to a short wavelength, due to an increased band gap.[7] For metal nanoparticles, the smaller the particles, the faster the electrons reach the surface of the particles; the electrons can scatter and lose the coherence more quickly. As a result, the plasmon bandwidth increases with decreasing particle size.[8] Electrical conductivity generally decreases with a reduced dimension due to increased surface scattering.[9] There is an exception to this general rule and there is an enhancement in electrical conductivity for polymer fibers due to the formation of ordered microstructure, when the size is reduced to a nanometer scale.[10] Self-purification is an intrinsic thermodynamic property of nanostructures and nanomaterials. Any heat treatment increases the diffusion of impurities, intrinsic structural defects and dislocations, which easily diffuse to the nearby surface. Increased perfection would have appreciable impact on the materials chemical and physical properties.

Among a number of different types of nanomaterials, metal oxide nanoparticles play a very important role in many areas of chemistry, physics and materials science.[11-15] These can adopt a vast number of structural geometries with an electronic structure that can exhibit metallic, semiconductor, or insulator characteristics. In technological applications, oxides are used in the fabrication of microelectronic circuits, sensors, piezoelectric devices, fuel cells, coatings for the passivation of surfaces against corrosion and as catalysts. Oxide nanoparticles can exhibit unique physical and chemical properties due to their limited size and a high density of corner or edge surface sites.[16] Particle size is also expected to influence the fundamental properties in any material. Firstly, the structural characteristics, namely the lattice symmetry and cell parameters can be altered at very small dimension.[17] Bulk oxides are usually robust and stable systems with well-defined crystallographic structures. However, surface free energy and internal mechanical strain with decreasing particle size must be considered: changes in thermodynamic stability associated with size can induce modification of cell parameters and/or structural transformations[18, 19] and in extreme cases the nanoparticle can become

thermodynamically unstable due to interactions with its surrounding environment and a high surface free energy.[20] In order to display mechanical or structural stability, a nanoparticle must have a low surface free energy. Due to that requirement, phases that have a low stability in bulk materials can become very stable in nanostructures. This structural phenomenon has been detected in TiO_2, VO_x, Al_2O_3, MoO_x CeO_2, ZrO_2, Fe_2O_3 systems.[21-25]

1.2. Outline of thesis

This thesis is focused on the synthesis and characterization of different nanostructured metal oxides (CeO_2, SiO_2) and thin films thereof. Different synthesis routes such as solvothermal and precipitation processes were utilized to fabricate these structures. Crystal structures and phases of the products were determined by X-ray diffraction studies. Several microscopic techniques such as scanning electron microscopy, field emission scanning electron microscopy and transmission electron microscopy were used to determine the morphology, size and crystallinity of the products.

The thesis is divided into the following chapters which are briefly described here:

❖ **Chapter 1** discusses the fundamental properties, applications of various metal oxides. Various synthesis techniques to fabricate different nanostructures have been discussed here. All the characterization techniques used to study the morphology and structures of synthesized nanostructures are introduced.

❖ **Chapter 2** is focused on synthesis and characterization of various sized as well as functionalized silica nanoparticles. Selected commercial available, cheap and aqueous soluble fluorescent dyes (IR-820, FITC) were doped into silica nanoparticles. The stability of the dyes capped in various sizes of silica nanoparticles have been studied using absorption spectra.

❖ **Chapter 3** is focused on the formation of europium doped ceria nanoparticles by a solvothermal process. The site occupancy of europium ions in

ceria host is established by different spectroscopic technique. Electron energy loss spectroscopy (EELS) was performed on doped ceria samples to confirm the presence of europium within ceria nanoparticles.

❖ **Chapter 4** deals with positron annihilation spectroscopic investigation of europium-doped cerium oxide nanoparticles. Positron annihilation spectroscopy is used as a means to study the defects and their evolution on doping.

❖ **Chapter 5** deals with the synthesis of thin films of mesoporous silica with a two-dimensional (2D) hexagonal structure using TEOS and Pluronic difunctional block copolymer surfactants. Mesoporous silica channels with uniform lateral spacing were fabricated by employing a lithographic mask and hard mask technique, followed by etching into silica.

❖ **Chapter 6** is aimed towards the development of new antimicrobial silver nanoparticles coating which may have applications in biomedical implant materials. We will investigate the biocidal efficiency of the surfaces on bacterial strains which are most commonly associated with implant infections.

❖ **Chapter 7** provides an overall summary and conclusions of the work.

1.3. Silica nanoparticles

1.3.1. Properties and applications

Silica (silicon dioxide or SiO_2) is the most abundant chemical species present on Earth. Silica is most commonly found in nature as sand or quartz, as well as in the cell walls of diatoms (frustule). The basic chemical formula of silica is SiO_2. It can have many crystalline structures as well as amorphous forms. In the majority of the silicates, the Si atom shows tetrahedral coordination, with 4 oxygen atoms surrounding a central Si atom. The Si-O bond, which is the most stable of all Si-X bonds, has a length of 0.162 nm, which is shorter than the sum of the radius of the Si and O atoms. This short bond is, thus, a quite stable one.[26]

Silica's hardness and transparency properties have been known since ancient times. Silica is used primarily in the production of glass for windows, drinking glasses, beverage bottles and many other uses. The majority of optical fibers for telecommunications are also made from silica. It is a primary raw material for many ceramics such as earthenware, stoneware and porcelain. Silica has been used in many areas due to its unique properties. Silica is optically transparent in the visible and near-infrared region. Silica is a non-toxic compound which is already used as food additive or as carrier material in tablets.[27] Silica nanoparticles have high hydrophilicity and are insensitive to microbial attack. In addition, they do not show any swelling or porosity changes as pH is altered.[28] It's surface usually bears reactive silanol groups, which can allows chemical functionalization. As silica is widely available in nature, it is an inexpensive raw material. Silica has good thermal and electrical insulating properties combined with proven processing, thermal and mechanical properties.

Monodispersed nanometer-sized silica particles have been shown to have important advantages in the scientific field as well as in many industrial applications, e.g. catalysis, pigments, pharmacy, etc.[29] Silica nanoparticles have biomedical applications such as delivery of anticancer drugs,[30] enzymes[31] and DNA.[32]

1.3.2. Fluorescent silica nanoparticles

A fluorophore is a fluorescent chemical compound that can re-emit light upon light excitation. Of the available flurophores, the most common are organic systems. Much research has been carried out on fluorescent molecule to cover the whole light spectrum from ultraviolet to near infrared region.[33] Organic flurophores generally consist of π-conjugated ring structures such as xanthenes, pyrenes or cyanines and their quantum yield can reach up to 97 %. In spite of their wide availability, they have several drawbacks[34]: firstly, they have relatively large emission spectra. Secondly, they are known for their tendency to photoleach or quench and fluorescence is highly dependent on pH or the solvent used.

To avoid some of these issues, many groups have encapsulated these dyes in a variety of host nanometer to micron sized matrixes. The two well-known matrixes are (i) polymers such as polystyrene[35, 36] and (ii) silica.[34, 37-39] Both have been successfully used as fluorescent multiplexed labels. The fluorescent material has to be chosen carefully in order to avoid exchange phenomena and other degradation processes. Moreover, it has to fulfil many other requirements such as stability in solvent and biocompatibility. It should be optically and chemically stable. It should neither interfere with the assay mechanism, nor obstruct or modify its fluorescent readout. Dye-doped silica nanoparticles were first synthesized by Van Blaaderen and co-workers using the Stöber method with the conjugation of fluorescein isothiocyanate (FITC) with (3-aminopropyl) trimethoxysilane.[40] However, the particles obtained by this method were size polydisperse and had a particle diameter of >400 nm. Santra and co-workers synthesized FITC-doped silica nanoparticles in a reverse microemulsion,[41] which were further modified with the TAT peptide, a cell-penetrating peptide.

Dye doped fluorescent silica nanoparticles (FSNP) possess several advantages such as high florescence intensity, good photostability[42, 43] and good potential for surface modification with various biomolecules.[44, 45] To date, thousands of dye molecules have been doped inside the silica matrix as well as on the surface. As a result, probe sensitivity has been greatly improved. There are several advantages in selecting silica-based fluorescent nanoparticles. Dye doped FSNP synthesis is relatively simple and does not require extreme reaction conditions (such as high/low temperature, pressures and inert reaction environment). The silica matrix provides a protective encapsulation around the fluorescent dyes, which can improve dye photostability. Using conventional silica-based chemistry a variety of biomolecules (e.g. antibodies, proteins, peptides, DNA, etc.) can be covalently attached to the silica surface. The silica surface makes these silica nanoparticles chemically inert and physically stable.[46] This can allow ‘targeting’ of functionality on particular cell types.

1.3.3. Synthesis methods for silica nanoparticles

A great many methods have been reported for the preparation of silica nanoparticles, including plasma synthesis,[47] chemical vapour deposition (CVD),[48] sol–gel processing,[49, 50] chemical precipitation,[51] microemulsion processing,[52] combustion synthesis,[53] continuous microwave hydrothermal technique[54] and pressurized carbonation.[55]

The Stöber route

Many years ago, Stöber *et al.*[56] reported a sol-gel method for preparation of monodisperse spherical silica particles, by hydrolysis of tetraethyl orthosilicate (TEOS), in an ethanolic medium in the presence of ammonia. After this novel work, Stöber silica particles have been used as model colloids in a large number of experimental investigations. Using the Stöber method it is possible to achieve excellent control of size, narrow size distribution and smooth spherical morphology of the resulting silica particles. The silica nanoparticles with a size smaller than 400 nm are attractive because of the possible reflection of visible light when they form a close packed structure. In order to prepare uniform-sized spherical particles with a wide size range, it is essential to separate nucleation and growth processes, which basically correlate with monodispersity of products. However, these two processes usually proceed simultaneously.

Microemulsion synthesis

The reverse micelle or water-in oil (w/o) microemulsion system is composed of a homogeneous mixture of water, oil and a surfactant molecule.[52, 57] The single-phase microemulsion system is both isotropic and thermodynamically stable. Water nanodroplets form in the bulk oil phase, which then act as a confined medium (of nanoreactors) for discrete particle formation. Polar and water-soluble dye molecules can be readily encapsulated into silica nanoparticles by this method because of the electrostatic attraction of dye molecules to the negatively charged silica matrix.[58-60] An advantage of the microemulsion system lies in its typical output of monodisperse and highly uniform nanoparticles.[61] However, fluorophores are physically attached to the silica matrix and may leach out of the particles over time. Furthermore, the use

of surfactants necessitates extensive washing to remove the surfactant molecules before any biological application in order to avoid disruption or lysis of biomembranes by the surfactant molecules.

Pressured carbonation synthesis

In recent years, one of the principal world concerns is the 'greenhouse' effect, especially related to carbon dioxide (CO_2). In the last decade, several papers have reported the utilization of CO_2 gas or supercritical CO_2 to synthesize silica powders. For example, Zhang *et al.*[62] proposed a simple acid gelation route to synthesize silica particles using supercritical CO_2 as a special reactant. By adding supercritical CO_2 into the sodium silicate aqueous solutions, porous silica microflowers were produced.

Other methods

Kortshagen *et al.*[47] has demonstrated a plasma process that is capable of producing relatively monodisperse sized and highly oriented nanoparticles, of diameter 20–80 nm, with a predominantly cubic shape. Ahlberg and Simpson,[63] Mertz,[64] White[65] and Lee *et al.*[66] used a peptization method to prepare colloidal silica through wet gel prepared from a mixture of sodium silicate solution with acid and water. The method involves three steps; gelation, peptization and concentration. Mishra *et al.*[51] found that the silica particles obtained by precipitation method are of ~50 nm in diameter with an almost spherical shape and density of 7.68 nm^{-2}. Ferrari *et al.*[54] used the microwave hydrothermal process to synthesize spherical SiO_2 crystals (average dimension 100 nm) only at the lowest flow rate used (43 ml min^{-1}) and the reaction time is shortened for crystallization, compared to the conventional hydrothermal reaction requiring a prolonged time.

1.4. Cerium oxide

1.4.1. Properties and applications

Nanostructures of rare-earth cerium oxide or ceria (CeO_2) have been widely investigated because of its' unique properties such as high refractive index, optical transparency, high dielectric constant, lattice expansion, stability at high temperature

and mechanical robustness. Not only are physical properties are exploited with nanoscale ceria, but special chemical properties have also been investigated with modern techniques.[67, 68] In most of the applications, the catalytic performance is strongly dependent on the particle size and ceria nanoparticles show high catalytic activity.[69] Grain size-dependent electrical conductivity was also observed in electrical application.[70] Recently, besides the conventional application fields mentioned above, ceria-based nanomaterials have been exploited as nanodevices as well. A typical example is that of single nanowire-based gas sensors.[71]

Ceria nanoparticles are among the most unique and promising nanomaterials mainly due to the diffusion and reactivity of oxygen vacancies in ceria, which contribute to its high oxygen storage capability.[72, 73] A high concentration of anion vacancies is related to a greater conversion of cerium ions from the Ce^{4+} states to Ce^{3+} ones. The initial concentration of anion vacancies has been shown to correlate to the oxygen storage capabilities of ceria and the corresponding conversion of cerium ions between the Ce^{3+} and Ce^{4+} states.[74, 75] Thus, the anion vacancy concentration in ceria can be modified post-growth and the reduction in the fluorescence signal arising from Ce^{3+} and Ce^{4+} states of the nanoparticles can be correlated to this change in vacancy concentration.[76]

Due to this unique property of oxygen storage, ceria has multiple applications in areas such as a catalyst, a UV absorber and a UV filter material, oxygen gas sensors, abrasives for the chemical mechanical polishing of silicon and optical devices. Currently fluorite structured materials, such as ceria-based oxides[77, 78] are widely used as electrolytes for solid oxide fuel cells (SOFC). Ceria nanoparticles have emerged as a fascinating and commercial material in biomedical science due to their unique ability to switch oxidation states between III and IV based on environmental conditions.[79]

1.4.2. Cubic Fluorite Crystal Structure of Ceria

Ceria is white crystalline solid that adopts a yellow tinge even when very slightly impure or non-stoichiometric. A unit cell of ceria consists of a cubic array of

oxygen atoms as a framework for the metal atoms which occupy alternate cubes.[80] This is called the fluorite structure, which is named after the mineral form of calcium fluoride, CaF_2 and is illustrated in Figure 1.1. It is described as a face centred cubic (f.c.c.) unit cell with the space group Fm3m and a lattice constant, $\alpha = 0.541134$ nm. In this structure, each cerium cation occupies the face-centred positions and is coordinated by eight equivalent nearest neighbour oxygen anions. The oxygen anions themselves occupy the tetrahedral positions in the lattice and are coordinated by four cations.[81]

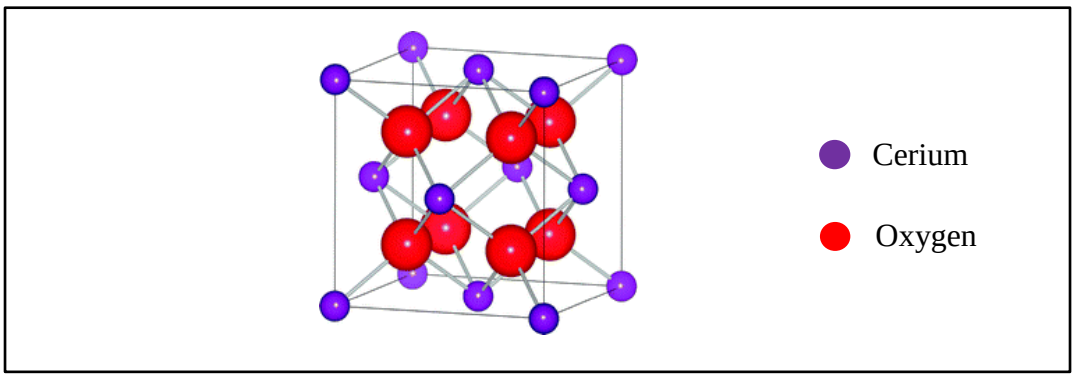

Figure 1.1. The face centred cubic cell of fluorite ceria.

The reductive properties of ceria which readily forms oxygen deficient non-stoichiometric phases is due to its ability to release bulk oxygen and so form a large amount of anion vacancies. The "reduced" structures still retain the fluorite structure, i.e. there is no obvious gross phase transformation to a thermodynamically stable structural entity and can be readily reconverted to ceria by exposure to an oxidising environment.[82-84]

1.4.3. Chemistry of defects in doped ceria

The defect chemistry of ceria is relatively well established. It is generally thought that as trivalent cations are added to the lattice, they are charge compensated by the presence of anion vacancies. These are associated with the dopant cations and randomly distributed on anion sites within the fluorite lattice. In this thesis, we focus on acceptor-doped ceria, in particular on europium doped ceria. During doping, impurity atoms are introduced to form an oxide. Impurity atoms are atoms of a

different element than the atoms of the mixed conductor acting either as donors or acceptors of electrons. Electron donor doping makes the electron concentration increase (this will in turn decrease the resistivity) while acceptor impurity atoms will make the vacancy concentration increase, leading to a net increase of vacancy conductivity. Under reducing conditions, e.g. in H_2 atmospheres, ceria will exchange oxygen anions to the ambient atmosphere (or equivalently lattice oxygen ions are in thermodynamic equilibrium with ambient oxygen molecules). This exchange can also be understood as the creation of oxygen vacancies and a change in the cerium oxidation state from Ce^{4+} to Ce^{3+}.

Defects in doped ceria can be created intrinsically, due to thermochemical conditions of the lattice ceria, or extrinsically, due to addition of dopant to the ceria structure. The defect chemistry of pure cerium oxides has been discussed in detail by various authors,[85, 86] so we will focus on doped ceria. There have been numerous attempts to optimize the physiochemical properties of ceria by inclusion of metallic cation dopants which can control the anion vacancy and Ce^{3+} cation concentrations.[87] Doping can improve the sintering properties of ceria, by stabilizing the ceria surface area and crystallite size.[81] Doping with divalent and trivalent dopants leads to formation of oxygen vacancies and modification of oxygen mobility and ionic conductivity.[88] Unsurprisingly, this is reflected in changing the redox properties and oxygen storage capacity of the ceria. Ceria is a potentially important material in optical and optoelectronic applications but exhibits weak emission characteristics that limit its performance.[89] Doping with lanthanide cations such as europium can enhance the visible emission of ceria nanoparticles through an increase in the concentration of oxygen vacancies.[90-92] Europium is a convenient dopant since the ionic radius of the trivalent europium[93] (0.1066 nm) is between that of Ce^{3+} (0.1143 nm) and Ce^{4+} (0.097 nm) and this allows for extensive solubility in the ceria fluorite structure. The Eu^{3+}/Eu^{2+} redox pair has a potential close about 0.36 V and is expected to create and stabilize the oxygen vacancies for low Eu^{3+}/Ce atomic ratios.[94] This property promotes charge transfer from oxygen ions through the lattice oxide and provides the material with high oxygen ion conductivity.[95] If energy is

transmitted from this charge transfer state to lanthanide ions characteristic emissions are expected to be observed.[96]

1.4.4. Synthesis methods of ceria

The solvent composition, surfactant, pH and the cerium source precursor are of importance in the final product morphology of a chemical synthesis of ceria.[97-99] The reaction temperature, concentration of the cerium precursor and reaction time has significant influence on the yield of ceria. As the morphological properties of ceria, such as the particle size, shape and specific surface area usually determine the performance, various synthetic methods, such as co-precipitation,[100-103] thermal deposition,[104] combustion or flame-synthesis,[105, 106] microemulsion,[86, 107] flow,[108] reverse precipitation,[86] sol–gel processes,[109, 110] sonochemical synthesis,[111] gas condensation,[112] hydrothermal or solvothermal[113, 114] and electrochemical routes,[115] have all been used to prepare ultrafine ceria powder with controlled dimension. Several precipitants and surfactants have also been used to control the particle size and homogeneity such as ammonium hydroxide, urea and ammonium hydrogen carbonate.

Sol-gel Method:

The sol-gel process allows facile fabrication of large-area coatings at a low cost and offers advantages of controlling the composition and microstructure of the film, an asset for eventual technological applications especially to obtain films of desired thickness. A very important factor in obtaining thick films by the sol-gel dip-coating method is to obtain stable, high concentration sols. A few research groups prepared ceria sols by using the commercial 20 wt % ceria aqueous colloidal dispersion[116] or peptizing ceria precipitation by the addition of an equimolar quantity of HNO_3.[117] However, methods for the preparation of high-concentration ceria sols are not well established. The major problem in obtaining high-concentration ceria sols is that the primary particles used in the sol-gel have a high tendency to aggregate.

Precipitation method:

The homogeneous precipitation process based on forced hydrolysis is quite widely applicable and has been used to produce various monodisperse metal oxide precursor particles of various shapes and sizes. Forced hydrolysis is usually accomplished either by increasing the pH of the solution, or by heating the solution to decompose a stable precursor to the base. There are several reports of methods for the preparation of ceria that depend on an increase in pH to cause precipitation. Zhou *et al*.[101] produced ceria particles by co-precipitation method using cerium nitrate and ammonia. Ceria particles were about 4 nm in size from. Chen and Chen[102] prepared ceria particles from cerium nitrate with hexamethylenetetramine, whereas Li *et al*.[103] used ammonia carbonate and diethylamine as the precipitate agents. Yamashita *et al*.[118] produced ceria particles from cerium chloride and sodium hydroxide in the presence of hydrogen peroxide, under pH conditions varying from 6 to 12. Kamruddin *et al*.[104] synthesised ceria with size ranging from 6 to 16 nm were prepared using thermal decomposition in various atmospheres and soft chemical routes under different experimental conditions.

Solvothermal method:

However, through all of the above methods, nanocrystalline ceria is difficult and inconvenient to obtain; calcination is usually necessary for the crystallization of amorphous samples and/or the removal of the surfactants. It is also difficult to synthesize highly uniform and well-dispersed nanocrystalline ceria for following reasons. Firstly, it is not easy to choose the appropriate precursor complexes and the crystallization temperatures for the rare-earth oxides are relatively high. Second, the agglomeration of nanocrystals is very common because the nanocrystals tend to decrease the exposed surface to lower the surface energy.[119] Solvothermal methods[120-122] without involving catalysts, surfactants or templates provides a more promising option for the large scale production of high purity nanoparticles as they are simple, fast and less expensive. Moreover, solvothermal method possesses advantages of single step, low temperature, controlled composition and morphology as well as being less sensitive to particulate aggregation and producing crystalline nanocrystals.

Other methods

Purohit *et al.*[105] used glycine–nitrate combustion for producing the highly sinterable ultrafine ceria powder. Madler *et al.*[106] synthesised ceria with specific surface areas up to 240 $m^2 g^{-1}$ using flame spray pyrolysis. Morris *et al.*[86] synthesised ceria using microemulsion as well as reverse precipitation technique to study the lattice surface defects and size related parameters. Gedanken *et al.*[111] synthesized ceria nanoparticles sonochemically, by using cerium nitrate and azodicarbonamide as starting materials and ethylenediamine or tetraalkylammonium hydroxide as additives. Morris *et al.*[86] used microemulsion technique to synthesis ceria. Microemulsion method is designed to limit aggregation and the size of the ceria nanocrystals as prepared through formation of a reverse micelle structure.

1.5. Mesoporous materials

The porous materials that were investigated in this work are introduced here. According to the International Union of Pure and Applied Chemistry (IUPAC) porous materials can be classified with respect to the diameter of their pores into three categories (Table 1.1):[123]

Table 1.1. IUPAC classification for porous solids

Pore diameter	≤ 2.0 nm	2.0 – 50 nm	≥ 50 nm
Classification	Micropores	Mesopores	Macropores

High surface area, uniform mesopore size and the presence of inherent silanol groups in pore walls have made mesoporous silica materials very attractive in materials-related fields such as chemistry, physics, medicine, electronics, optics and so on.[124-129] Besides these features, mesoporous silica materials also exhibit several kinds of unique and ordered mesostructures such as lamellar,[130, 131] 2D hexagonal,[132-134] 3D hexagonal[135, 136] and 3D cubic[137, 138] structures.

The materials date back to 1992, when scientists of the Mobil company discovered this new class of silica/aluminosilicate mesoporous materials, the so-called M41S materials.[125, 139] In 1998 the portfolio of accessible materials was

enhanced by the emergence of the so-called Santa Barbara Amorphous (SBA) type materials.[140, 141] M41S and SBA type materials are a very versatile class of nanomaterials and ended the long-standing pore-size constraint of zeolites by offering pore sizes ranging from 2 - 30 nm. Besides their pore diameter, surface properties and topologies can be fine-tuned over a large range. This makes them an ideal platform for various applications, since their specifications can be tailor-made according to the individual requirements. Consequently, within the recent years a growing number of applications for mesoporous silica materials has been suggested, such as molecular sieves,[142] catalysis,[143] chromatography,[144] stabilization of conducting nanoscale wires[145, 146] and novel drug-delivery systems.[32, 147, 148]

1.5.1. Thin mesoporous silica films

Mesoporous silica materials can be synthesized in various forms, such as powders or thin films of thicknesses of about 50 nm to several micrometers. Thin films are interesting object since they can act as coatings on diverse substrates for applications either in catalysis or in drug-delivery. Further, thin films can be prepared with large domains of parallely aligned pores. Large domains with good connectivity are a desired feature for many applications. The thin films can be coated on various substrates, e.g. silicon wafers, glass, such that the samples can be studied easily.

Mesoporous silica thin films with highly ordered structures are potentially applicable to devices such as optical devices,[149, 150] gas sensors,[151] low dielectric constant films,[152, 153] etc. Specifically, the idea in device applications is to use the mesopores, 4 - 50 nm, to generate ordered arrays of semiconductor nanocrystals, quantum dots within the pore structure. It is well-known that as semiconducting materials decrease in size, their optical properties drastically change as quantum confinement occurs.[154] The most notable feature is a blue shift in the emission spectrum of the nanocrystals that is tunable with size. In the hopes of utilizing ordered uniform nanometer size mesopores, several groups have developed techniques for depositing semiconductors in the mesoporous materials.

The most promising hi-tech commercial prospect of mesoporous materials is probably low-dielectric constant (low-*k*) materials in chip fabrication.[155] Traditional chips use condensed silicas as dielectrics with *k* values between 3.9 and 4.2 which cannot meet the demands of nanodevices. Low-*k* materials are, thus, required. A possible solution is of mesoporous silicates showing *k* values lower than 2.2.[156] Zhao *et al*.[157] first reported low-*k* mesoporous silica thin films templated by triblock copolymers with values ranging from 1.45 to 2.1. Larger porosities generally give lower *k* values for the same mesostructure.[158] As-made or long-time resting mesoporous thin films have high *k* values by reason of the polarization of surface silanol groups and the adsorption of water molecules.

All porous materials investigated in this work have mesopores and show pore diameters of ~ 6 - 15 nm. The structural framework of the materials consists of silica units and the porosity is created by Evaporation Induced Self-Assembly (EISA) process with the help of a triblock copolymers. Mesoporous silica structures are, thus, a novel class of hybrid nanomaterials.

1.5.2. Synthesis of mesoporous silica thin films

The preparation of silica-based mesoporous thin films via the sol-gel process was reported by Ogawa in 1994.[159] In general, mesoporous silica films have been synthesized using the spontaneous organization of silica-surfactant nanocomposites at solid-liquid interfaces.[159-162] The procedure for this film formation is quite simple and rapid. As in mesoporous powder, the formation of ordered mesoporous materials can take place under alkaline,[163] acidic[164] or neutral conditions[165] via the cooperative interaction of organic surfactants and inorganic species through electrostatic attraction or hydrogen bonding. The fabricated silicate framework film has uniform apertures in the range of 2-30 nm diameter and large surface area of 1000 m^2 g^{-1}.[124, 126] Therefore channel and pore voids provide confined space which is suitable for the accommodation of mesostructured molecules and clusters.[166]

There are basically two methods for the synthesis of mesopores thin films: dip-coating (Figure 1.2a) and spin-coating (Figure 1.2b). Both methods start from a

precursor solution containing silica building blocks, such as tetraethyl orthosilicate (TEOS) and surfactant molecules as templates in an acidic ethanol/water solution. In the dip-coating method (Figure 1.2a), a glass slide or silicon substrate is immersed into the precursor solution and slowly retracted. Through slow retraction of a glass slide or silicon substrate from the precursor solution, a thin film forms on both sides. Solvent evaporation induces the formation of a mesoporous structure. During spin-coating (Figure 1.2b), the precursor solution is placed onto a cover-slip. Rotating the cover slip at about 3000 rotations per minute (rpm) leads to solvent evaporation and the formation of a thin mesoporous film.

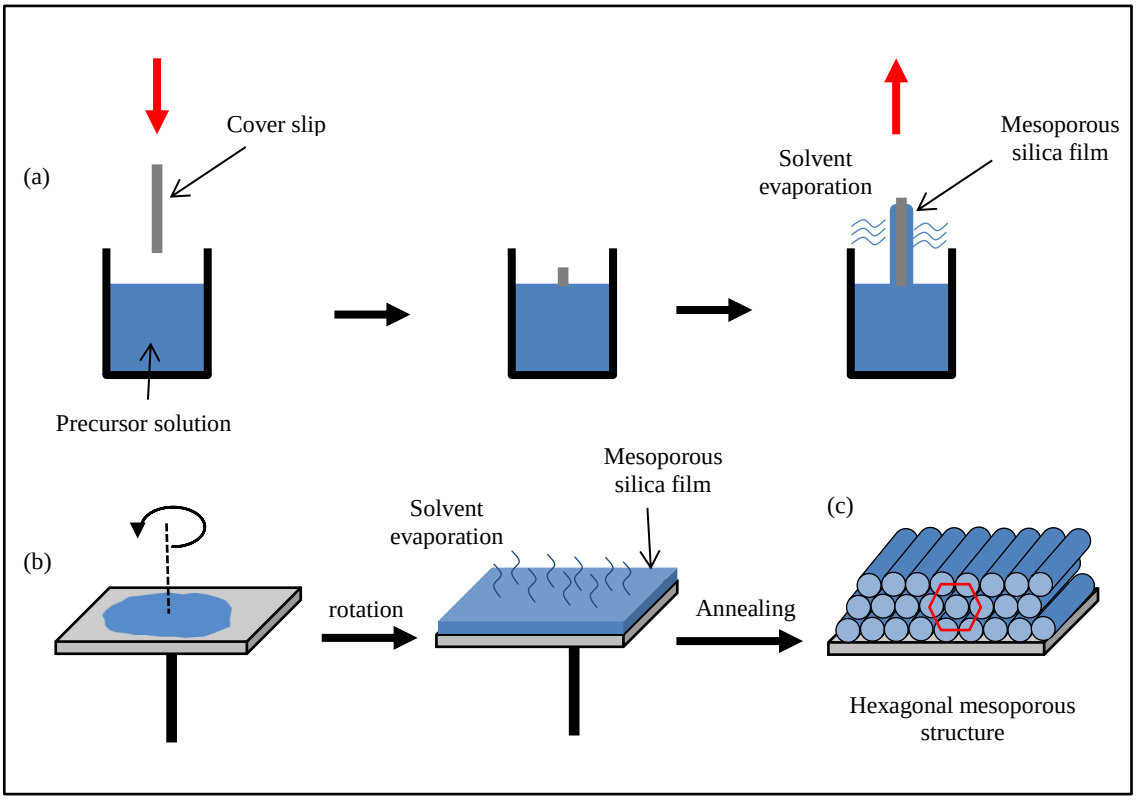

Figure 1.2. Synthesis methods for thin hexagonal mesoporous silica films. (a) Dip-coating. (b) Spin-coating. (c) Schematic view of a hexagonal mesoporous structure.

The evaporation of the solvent during dip- and spin-coating leads to the EISA process which results in the formation of a condensed mesoporous silica structure. There are two synthesis mechanisms that can explain EISA: a two-step mechanism and a cooperative one-step mechanism.[167, 168] In the precursor solution, before EISA occurs, the surfactant concentration is below the critical micelle concentration

(CMC). This means that no surfactant micelles are present. Now, solvent evaporation leads to crossing that CMC. In a two-step mechanism this leads to the formation of a liquid-crystal phase around which the silica can condense subsequently. In contrast, the one-step mechanism postulates a cooperative self-organization of the silica precursor and the surfactant below the CMC. In this case, the inorganic silica induces the formation of an ordered array of surfactant molecules. Recent results favour the one-step mechanism.[127, 169-171] Depending on the silica to surfactant ratio different pore topologies (hexagonal, cubic, lamellar) are accessible.[172-174]

1.5.3. Block copolymers

A copolymer is a polymer derived from two (or more) monomeric species. Copolymers can be classified based on how these units are arranged along the chain. A block copolymer (BCP) is one of the important types of copolymers. BCPs are composed of two or more chemically distinct polymer chains linked together at one or more junction points through covalent or noncovalent bonds.[175-179] BCPs can be made with different architectures. These include linear, branched, star, mikto-arm and graft. BCPs can also be made with varying numbers of blocks: diblock (2), triblock (3), tetrablock (4), etc.[180] Many potential uses of BCPs for different nanotechnologies have been proposed based on their ability to form a large variety of well-ordered microdomain structures of molecular dimension. Although BCPs are capable of forming a variety of highly ordered structures, they often lack long-range alignment (i.e. direction relative to a chosen substrate direction) which is important requirement for many potential applications.

BCPs are usually synthesized by the simultaneous polymerization of different monomer types. The selected blocks are typically incompatible with each other, which cause the synthesized BCPs in solution to self-assemble into micellar structures with the lyophobic block situated in the internal part, surrounded by the lyophilic blocks, forming the outer layer. The relatively simple synthesis allows variation of the block length, which in turn results in interesting self-assembled structures, when dissolved in an appropriate solvent.

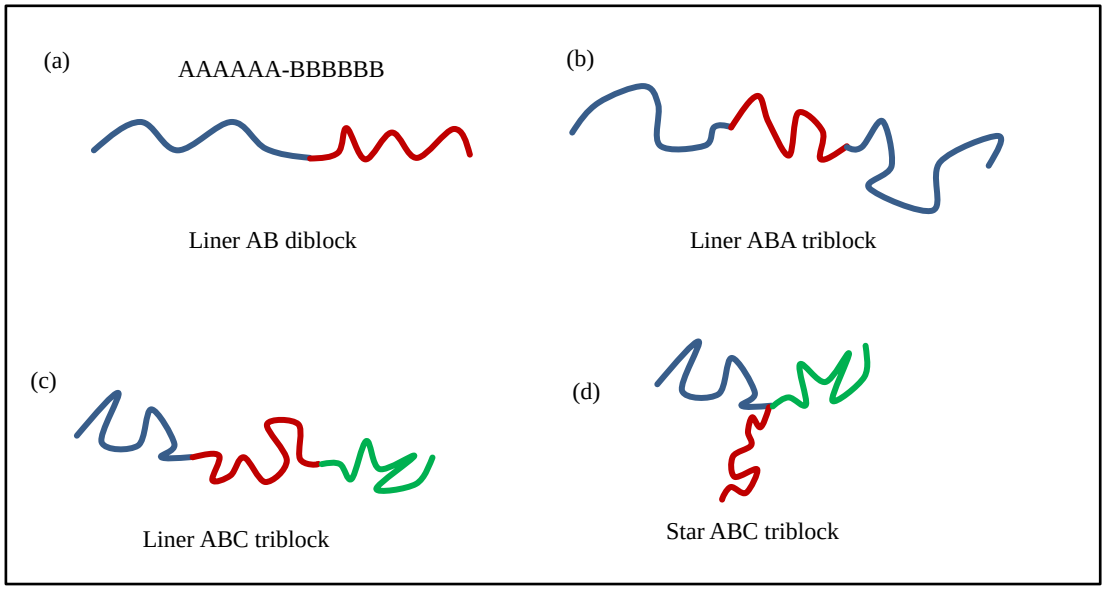

Figure 1.3. Block Copolymer Architectures. (a) Linear AB diblock copolymer. The structure can be represented as chains of monomers (top), lines tracing the backbone of the A (blue) and B (red) blocks or molecular formulae for the A (poly(styrene), PS) and B (poly(ethylene oxide), PEO) blocks. (b) Linear ABA triblock copolymer. (c) Linear ABC triblock copolymer. (d) Star ABC triblock copolymer.

The simplest architecture is the linear AB diblock copolymer shown in Figure 1.3, in which a homopolymer chain of monomers of type 'A' is covalently linked to a homopolymer chain of monomers of type 'B'. A linear AB diblock copolymer is usually prepared via the repeated addition of monomers of 'B' to the end of the previously synthesized chain of poly 'A'. The type of monomer in a block determines many of the properties and modern polymer synthetic techniques provide access to a wide range of components. AB diblock copolymers are frequently described by listing the components in order (e.g. PS-*b*-PEO). PS-*b*-PEO is composed of a chain of styrene monomers covalently bonded at one end to a chain of ethylene oxide monomers. The chemical structure of PS-*b*-PEO is shown in Figure 1.4.

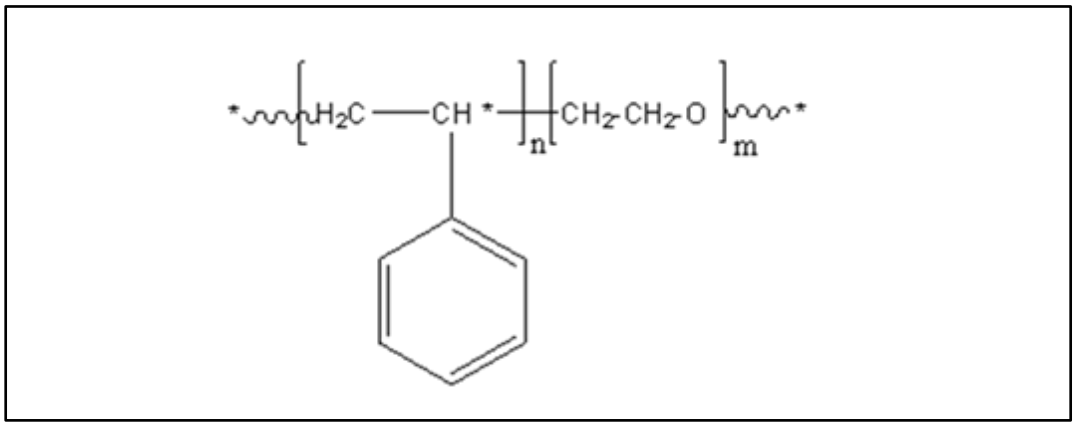

Figure 1.4. Chemical structure of PS-*b*-PEO (polystyrene-*b*-polyethylene oxide) diblock copolymer, where 'n' represents the number of styrene monomer units in each PS chain and 'm' represents the number of ethylene oxide monomer units in each PEO chain.

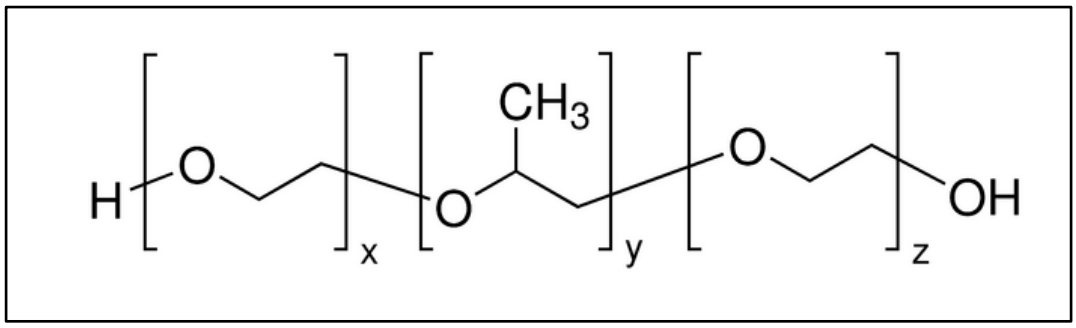

Figure 1.5. Chemical structure of 'Pluronic' triblock copolymer, where 'x' represents the number of ethylene oxide monomer units 'y' represents the number of propylene oxide monomer units and 'z' represents the number of ethylene oxide monomer units.

Besides di-block copolymers, tri-block copolymers have also been thoroughly examined. One of the most frequently studied tri-block copolymer type has ethylene oxide (EO) as end blocks and propylene oxide (PO) as the middle block. These BCPs are known under the brand name 'Pluronics' and have the general formula $(EO)x(PO)_y(EO)_z$, where x and z are the number of EO units and y is the number of PO monomer units per block. The chemical structure of P-123 is shown in Figure 1.5. At low temperatures the aqueous solutions of these polymers consist of unimers,

which self-assemble into micelles as temperature or concentration is increased.[181] The core of the micelles is composed of the polypropylene oxide (PPO) chains, while the polyethylene oxide (PEO) is situated in the corona. At higher temperatures and in the presence of certain salts, or hydrophobic organic compounds, some of the pluronic block copolymers can form worm-like micelles.[182, 183] The morphology of the micelles is strongly dependent on the relative ratio of EO and PO monomers. Tri-block copolymers with a low number of EO units in comparison to PO have a higher tendency to self-assemble into worm-like micelles.[184]

1.5.4. Self-Assembly of BCPs

The term self-assembly should not be confused with self-organisation. Self-assembly generally refers to systems that are driven to equilibrium by physical interactions between entities in order to reach a free energy minimum. Self-assembly requires that equilibrium be achieved in order to obtain ordered structures. For this to takes place, the components either equilibrate between aggregated and non-aggregated states, or adjust their positions relative to one another in an aggregate. Another general requirement for self-assembly processes is that the components must be mobile (i.e. must be able to move with respect to one another), so as to achieve their steady-state position and balance the attractive and repulsive forces.

BCPs are made up of blocks of different polymerized monomers and are useful in creating self-constructing materials, based on their ability to microphase separate in the solid phase. The simplest category of such copolymers can be described as an A-B diblock consisting of a linear chain of type ‘A’ monomers bound on one end to a linear chain of type ‘B’ monomers. Because the blocks are covalently bonded to each other, they cannot mix macroscopically. However, microphase separation does occur, due to chemical incompatibility between the blocks. This is a thermodynamically driven process, whereby chemical dis-affinity between the blocks is counter-balanced by a restorative entropy cost associated with deformation of the random coil structures of the blocks. A minimum free energy is attained through minimisation of repulsive and maximisation of attractive, molecular interactions.[185] Thus, mesoscale regular periodic structures of microphase separated

domains are formed in order to reduce the contact area between dissimilar blocks.[186] From a technological perspective, self-assembly is inexpensive, fast and easily tunable. The underlying physics of BCPs in bulk and thin film has also been well established, with BCP thin films displaying similar mechanical properties to those of conventional polymer photoresists. Applications of these materials are extremely widespread and include use as surfactants, anti-foaming agents, cosmetic materials and surfaces for drug release.[187]

Thermodynamic forces are crucial to understand how the different blocks interact and the self-assembly process can be related to a simple Gibbs free energy equation:

$$\Delta G_{SA} = \Delta H_{SA} - T\Delta S_{SA} \qquad \text{Eq. 1.1}$$

where ΔH_{SA} is the enthalpy change of the process and is highly dependent on the intermolecular forces between the assembling components. ΔS_{SA} is the change in entropy in the process. Self-assembly will occur spontaneously when ΔG_{SA} is negative. Since the organisation process usually brings about an entropy decrease, the enthalpy term must be negative and in excess of the entropy term in order for self-assembly to be spontaneous.

Self-assembly holds a number of advantages over most 'top down' processing techniques. It potentially provides one solution to the fabrication of ordered aggregates from components with sizes from nanometers to micrometers at a lower cost. Since BCP systems with well-defined order-disorder transitions can reach a true equilibrium, the term self-assembly is appropriate here.[186] In the melt, they are driven to segregate into a variety of ordered structures by the repulsion of the immiscible blocks, much as in the case of a blend of immiscible homopolymers. In this far simpler case of a blend of two homopolymers, A and B, the phase behaviour may be controlled by three experimental parameters: the degree of polymerization (N), the composition (f) and the A-B Flory–Huggins interaction parameter (χ).

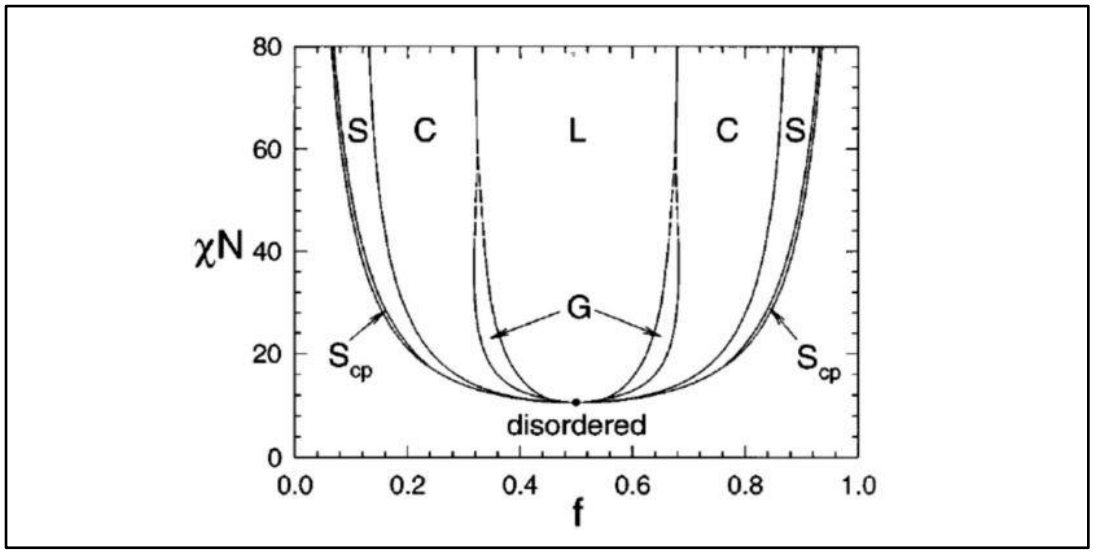

Figure 1.6. Typical phase diagram for a diblock copolymer. f: Volume fraction of one block. χ: Flory-Huggins interaction parameter. N: degree of polymerization. L: lamellae, C: hexagonally packed cylinders, G: gyroid, S: spheres, S_{cp}: closed-packed spheres.[188]

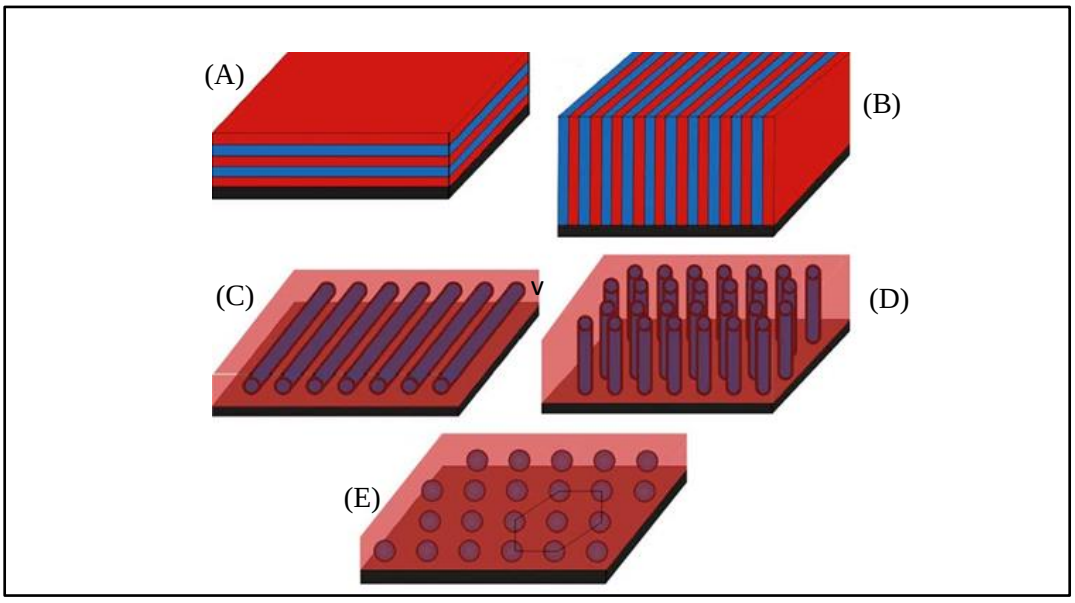

Figure 1.7. (A) Lamellae lying parallel to the substrate, (B) lamellae aligned perpendicular, (C) cylinders lying parallel, (D) cylinders perpendicular and (E) spheres.[189]

The parameter χ_{AB} describes the chemical incompatibility between monomer units and can be estimated by fitting the predictions of thermodynamic theories to X-

ray or neutron scattering data for diblocks or blends.[190] Hence, $\chi_{AB}N$ corresponds to the total dis-affinity over the entire BCP and the likelihood of microphase separation taking place. Microphase separation and/or significant morphology changes of microdomains can be achieved using thermal annealing, in which the temperature is raised to just below the order-disorder temperature (ODT) to improve diffusivity.[191] Below the ODT and when the volume fraction of block A (f_A) is quite small, it forms spheres in a body-centered cubic (BCC) lattice surrounded by a matrix of B. As f_A is increased towards 0.5, the minority nanodomains will form first cylinders in a hexagonal lattice, then a bicontinuous double gyroid structure and finally lamellae as shown in figure 1.6 and figure 1.7.

1.5.5. Pattern transfer process

The pattern transfer process contains two steps: lithographic masking layer patterning and the subsequent etching of the underlying material. Etching refers to a process by which material is selectively removed from the wafer, either from the silicon substrate itself or other material layer on the wafer, which can be applied to both thin film and bulk material. Material is chemically and/or physically attacked and eroded in the unprotected areas during etching. Some materials can be etched spontaneously by a chemical etchant, such as silicon by fluorine, aluminium by chlorine and silicon oxide by hydrofluoric acid. In some cases physical processes such as ion bombardment are needed to assist the etching process. Etching processes are often divided into two classes, wet etching and dry etching. Plasma etching is the most commonly used dry etching method.

Silicon etching has exceptional high rates up to 20 μm min^{-1} in both wet etching ($HF:HNO_3$) and plasma etching [deep reactive ion etching (DRIE) in SF_6].[192] Etching techniques from both classes have been well established for silicon processing. Additionally, masking effects during silicon etching is also a well-studied issue. Masks with high selectivity to the substrate, good adhesion to the surface and patternable high resolution are especially demanded in the fabrication of high aspect ratio structures with controlled sidewall condition.

While top-down UV lithography has traditionally been associated with nanoscale patterning, this is not without many intrinsic limitations. Methods based on electromagnetic radiation, energetic particle beams and scanning probe microscopes suffer from drawbacks including diffraction depth of focus and electrostatic interactions, which compromise the ease and speed of pattern writing.[193] Therefore, the technological applications of BCPs have been increasingly examined in recent years due to their aforementioned tunability of the size, shape and composition. Templating of magnetic materials, thin metal films and nanoparticles have all been achieved. Of particular interest in this study is the use of domains within BCPs as spatially localized synthetic vessels for the growth of nanoparticles. Synthesis of this kind has most commonly been described by loading pre-formed BCP domains with inorganic precursors that are then reduced, although methods of binding the inorganic material to the polymer prior to phase segregation have also been reported.[194] The mechanical, electrical and optical properties of these materials can all be related to molecular architecture.

1.6. Biomineralization at Nanopatterned Surfaces

Biomineralization refers to the processes by which organisms form minerals. The term biomineral refers not only to a mineral produced by organisms, but also to the fact that almost all of these mineralized products are composite materials comprised of both mineral and organic components. Furthermore, having formed under controlled conditions, biomineral phases often have properties such as shape, size, crystallinity, isotopic and trace element compositions quite unlike its inorganically formed counterpart. The term "biomineral" reflects all this complexity.

Nature uses minerals for a wide variety of functions, the most basic of which being skeletal design and mechanical protection. Another fascinating case is the ability of magnetotactic bacteria to synthesize crystalline magnetic nanoparticles for navigation and orientation.[195] Organisms exhibit a level of molecular control over the detailed nano- and microstructure of biomaterials which even the most advanced current materials technologies cannot match. Therefore, understanding the underlying design principles of biomaterials is the key to developing new

approaches to materials fabrication at the nanometer and micrometer scale. Self-assembly is responsible for many fundamental processes in nature, for example, the folding of nucleic acids into their functional forms through specific monomer–monomer interactions.[196] In biomineralization, "matrix" macromolecules can efficiently induce growth of inorganic species at specific locations with controlled orientation. In many cases, these nanomaterials are produced under genetic control, resulting in particular morphologies, sizes and crystallinities of the structures.[197]

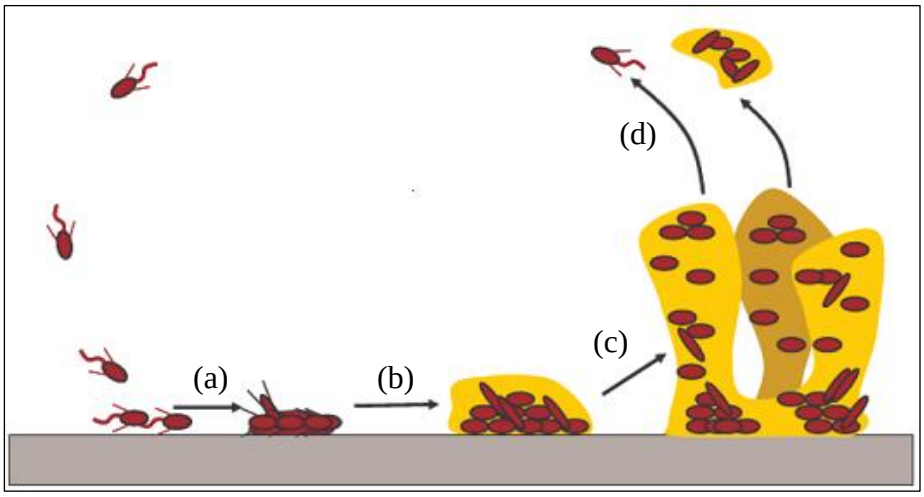

Figure 1.8. Schematic illustration of biofilm formation and development[198] (a) Bacterial colonisation and multiplication. (b) Formation of protective exopolymer saccharides. (c) Growth and maturation of the biofilm. (d) Dispersal of biofilm matrix.

Biomineralization can be problematical. Although an extremely interesting and very often useful, phenomenon as described above, biomineralization is not always desirable. The natural accumulation of deposits on surfaces can have issues for materials and health industries. For instance, such self-assembly processes previously outlined can have detrimental effects through the enhancement of biofilm and plaque formation. A biofilm is a community of bacterial cells which inhabit the surface of a solid substrate and is the most common mode of life for all bacteria, both in vivo and in vitro.[199] This can lead to biofouling of a vast range of surfaces, with relevance in surgical equipment and protective clothing in hospitals, medical implants, food packaging and food storage to name a few.[200] The mechanism of

biofilm formation is outlined in Figure 1.8. Biofilms can also contaminate a variety of infrastructures such as plumbing, oil refineries and water purification systems.[201] Moreover, it is estimated that 80 % or more of all microbial infections in humans are biofilm-related.[202]

1.6.1. Antimicrobial Activity of nanopatterned silver

Million cases of nosocomial infections per year are associated with implant devices such as pacemakers, defibrillators, joint orthopaedic replacements and prosthetic cardiac valves.[203] This usually leads to repeated surgical procedures to remove and replace the contaminated material, the consequences of which can be life-threatening for the patient. The nature of increased antibiotic resistance within bacterial biofilms is usually attributed to the shielding of constituent cells within the film, leading to a lack of accessibility. Clearly there is great need to develop new ways of preventing biofilm formation on biological implants. Typical strategies generally rely either on the local application of biocides or on inhibiting bacterial adhesion. In addition, coatings based on antimicrobial peptides (AMPs), enzymes and photoactive materials are thought to have significant microbicidal potential. However, these biomolecules may lose activity upon incorporation into coatings.[204]

Silver coatings have remained a popular area of research for this reason. One common theory is that silver interacts strongly with thiol groups of essential bacterial enzymes, inactivating them.[205] There is also evidence to suggest that the DNA of target bacteria loses its replication ability after exposure to silver.[206] Silver nanoparticles have recently become much more widely used in medical equipment due to notable slow-release antiseptic activities. Yet there remains a lack of information regarding the biological activities of these nanoparticles on human tissue cells[207] and a number of investigations have reported cytotoxic effects.[208] Furthermore, a uniform dispersion pattern of nanoparticles is extremely difficult to achieve using traditional wet methods of synthesis (generally involving the reduction of a silver salt with a reducing agent in the presence of colloidal stabilizer).[209] Problems in controlling the size and dispersion of particles can lead to agglomeration, which drastically reduces the antimicrobial power of coatings.

An alternative approach is to focus on the fabrication of surfaces which resist bacterial attachment. Research has shown that the adhesion of microbes to surfaces is largely governed by factors such as hydrophobicity, surface roughness, electrostatic interactions and surface compliance.[210] Another method which has been proven to prevent or reduce the adhesion of proteins (and importantly, microorganisms) to materials is to graft PEO chains on the surface. The high mobility of PEO chains and attainment of very large exclusion volumes makes it difficult for incoming particles to approach these surfaces.[211] An investigation by Roosjen *et al*. showed that the application of PEO brushes at surfaces significantly reduced the adhesion of two strains of bacteria under study (S. epidermidis and P. aeruginosa).[212] Although these modified surfaces resist the adsorption of proteins and bacteria, they do not address the issue of deactivating the microbes, which is crucial for preventing microbial contamination.

To date, work carried out by Morris *et al*.[213, 214] in the area of BCP lithography has mainly focussed on applications in electronics and optics. We are now interested in studying the ability of such nanodimensioned templates to resist bacterial adhesion and hence, inhibiting biofilm formation. It is postulated that these nanopatterned surfaces may prevent microbes from adhering due to topographies being far less than typical cell size. As this work is aimed towards the development of new antimicrobial coatings which may have applications in biomedical implant materials, we will investigate the biocidal efficiency of the surfaces on bacterial strains which are most commonly associated with implant infections.

1.7. Structural and Morphological Characterisation Techniques

1.7.1. X-ray diffraction (XRD)

Since the early 1900's, X-ray crystallography has been a valuable tool for obtaining structural parameters of metal oxides.[215] X-ray diffraction powder patterns come from the interference pattern of elastically dispersed X-ray beams by atom cores and in the case of materials with moderate to long-range order, contain information that arises from the atomic structure and the particle characteristics (for example, size, strain). The effect of atomic structure on peak positions and intensities

is described in textbooks[216] and the effect of particle characteristics on peak shape has been recently reviewed.[217] Finally, low angle X-ray diffraction can be used to determine the structure of nanodimensioned thin films.

XRD occurs when the inter-planar distance d in a crystal is of the order of the wavelength λ of the X-ray radiation, usually the Cu Kα emission line with a wavelength of 1.54 Å. Diffraction at an angle θ then occurs when Bragg's law is satisfied. Bragg's law is given in equation 1.2 where n is an integer value.[218]

$$2dsin\theta = n\lambda \qquad \text{Eq. 1.2}$$

A plot of diffraction intensity against angle of reflection (2θ) produces a diffraction pattern from which the crystallographic structure of materials can be determined. The crystallite size was estimated from XRD peak broadening using the Scherrer equation,

$$D = \frac{0.9\lambda}{\beta cos\theta} \qquad \text{Eq. 1.3}$$

where, D is the crystallite size, λ is the wavelength of Cu Kα radiation, β is the full-width at half maximum (FWHM) of the diffraction peak and θ is the diffraction angle. The lattice parameter α of the different samples was estimated as:

$$\alpha = d\sqrt{h^2 + k^2 + l^2} \qquad \text{Eq. 1.4}$$

The interplanar separation d is obtained from the Bragg's equation 1.2. XRD patterns were recorded on a PANalytical MPD instrument using an Xcelerator detector and a Cu Kα radiation source at a working power of 45 kV and 40 mA.

1.7.2. Total reflectance X-ray fluorescence spectroscopy (TXRF)

Total reflectance of X-ray at an optically flat surface for spectrochemical analysis was first mentioned by Y. Toneda and T. Horiyuchi, in 1971.[219] Some years later this promising idea was revelled by Aiginger and Wobrauschek, in 1975.[220] The theory of TXRF is based on the phenomenon that at an incident angle below the critical angle, the narrow collimated primary beam is totally externally reflected from the surface.[221] Thus a beam is reflected from a flat polished surface at the same angle as the incident one and has almost the same intensity as the primary beam

(total intensity is reflected), except for a small portion that is refracted and penetrates the reflecting medium. An evanescent wave loses intensity exponentially as it penetrates deeper into the medium and it is this wave that defines the surface sensitivity of the technique.

The conversion of the measured intensities into concentrations is one of the most important steps in analytical XRF. In the special case of TXRF, the complications are almost completely removed, as the approach for the thin-film sample can be applied (i.e. because the evanescent wave is limited to the surface, matrix absorption effects can be ignored) which leads to a simple and linear relation between the intensity (I) and concentration (C) of the element considered. The addition of an internal standard with known concentration leads to a simple quantification procedure which is described by Wobrauschek *et al.*[222] The concentration of unknown element C_i can be determined by using the relation:

$$C_i = \frac{S^{std}}{S^i} \times \frac{I^i}{I^{std}} \times C^{std} \qquad \text{Eq. 1.5}$$

where S^{std} is sensitivity of internal standard, S^i is sensitivity of unknown element, I^i intensity of unknown element, I^{std} is intensity of internal standard and C^{std} is concentration of internal standard. Software packages such as AXIL and WINQXAS are widely used to deconvolute the spectral lines of the measured spectrum. These background-stripped spectral data allow calculation of the intensities from the number of counts measured in a certain time interval with the spectrometer. Thus, the net counts are available for all measured elements and after the calibration of the spectrometer, the direct calculation of unknown elements using the software can be carried out using the simple quantitative analysis. TXRF was performed on the samples using a Bruker S2 Picofox instrument.

1.7.3. X-ray photoelectron spectroscopy (XPS)

The technique was first known by the acronym ESCA (Electron Spectroscopy for Chemical Analysis). XPS is a quantitative spectroscopic technique that measures the elemental composition, empirical formula, chemical state and electronic state of the elements that exist within a material. XPS also provides

information about the elemental and chemical composition of the uppermost atomic layers. In combination with low energy ion bombardment, which is used for depth profiling, this technique can be used for compositional and chemical analysis at different depths.[223]

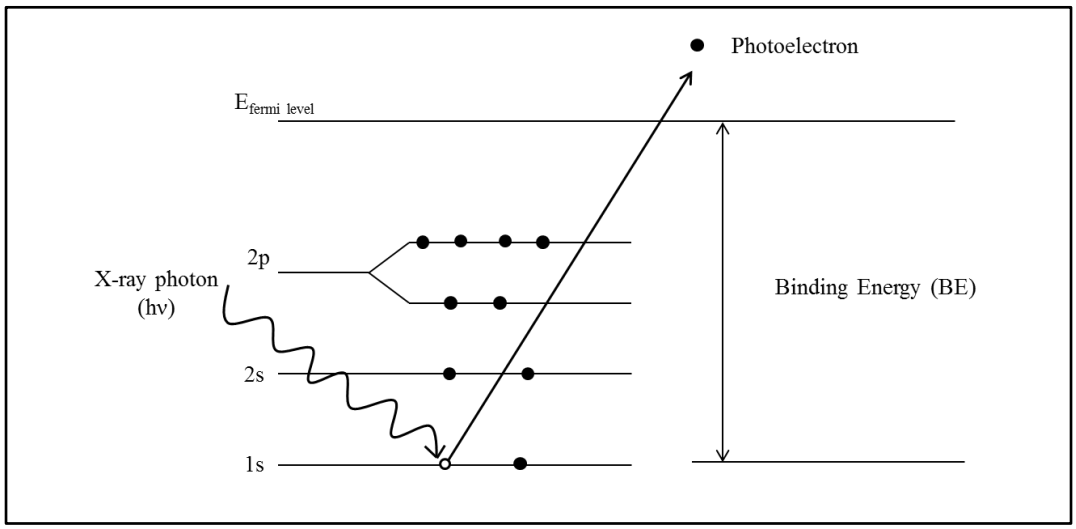

Figure 1.9. Schematic representation of the XPS process.

XPS spectra are obtained by irradiating a material with a beam of X-rays while simultaneously measuring the kinetic energy and number of electrons that escape from the top 1 to 10 nm of the material being analysed. XPS normally requires ultra-high vacuum (UHV) conditions. The XPS is based on the photoelectric effect in which the interaction of an X-ray photon of sufficient energy with a solid resulted in the emission of an electron from surface. The usually applied X-ray radiation (1-15 keV) is capable of photoejecting electrons not only from outer shells but also from core levels of all elements of periodic table. Because the energy of an X-ray with particular wavelength is known, the electron binding energy of each of the emitted electrons can be determined by using an equation:

$$BE = h\nu - KE - \Phi \qquad \text{Eq. 1.6}$$

where, BE is binding energy of the atomic orbital from which the electron originates, hν is characteristic energy of X-ray photon, KE is kinetic energy of ejected photoelectron and Φ is spectrometer work function.[224] Here, XPS work was carried out on a VSW Atomtech system (Al Kα radiation at 50 eV pass energy) instrument.

1.7.4. Transmission Electron Microscopy (TEM)

Transmission Electron Microscopy (TEM) is an imaging technique which is widely used to investigate structures on a nanometer scale. The principle of TEM is based on the imaging of transmitted electrons through a thin sample. The electrons are produced via thermionic emission from a filament and accelerated under high voltage in a vacuum, focused through a number of different lenses to a sample and then finally to an imaging device. A condenser lens focuses the beam of electrons from the electron source on the sample, after the electron beam has passed through the sample the objective and projector lenses image the beam onto the imaging plate or fluorescent screen to produce the magnified image. High resolution TEM (HRTEM) images were acquired using JEOL JEM 2100 HRTEM instrument operating at 200 kV. High-angle annular dark-field (HAADF) scanning TEM images were collected using a JEOL 2010F HRTEM instrument operating at an acceleration voltage of 200 kV. Elemental maps were obtained with a FEI Titan TEM equipped with a magnetic sector electron energy-loss spectrometer and an energy dispersive X ray detector.

1.7.5. Scanning Electron Microscopy (SEM)

Scanning Electron Microscopy (SEM) is a popular imaging technique used to image the topography of a sample. Unlike TEM, SEM irradiates a sample with a scanning electron beam and the resulting emission of electrons from the surface of the sample provides topographical information about the sample. When the scanning beam of electrons hits the sample surface the scanning electrons transfer energy to an electron in an atom at the sample surface, this excited electron (a secondary electron) is subsequently re-emitted. Differences in the topography of the sample will change the amount of secondary electrons emitted and hence provide information about the sample surface. The scanning electrons can also reflect from the sample surface when they collide with surface atoms; atoms with larger atomic numbers back scatter more electrons which provides contrast between different atomic phases. X-rays are also emitted from the irradiation of a sample with the scanning electron beam, these x-rays can be used to determine the chemical composition of the sample and this is known as energy dispersive x-ray spectroscopy. SEM images were collected on a

Zeiss Supra 40 FESEM operating at 10 kV. A JEOL 2000FX TEM operating at an acceleration voltage of 200 kV was used for bright field imaging as well as selective area electron diffraction (SAED). Energy dispersive X-ray (EDX) analysis was performed using an Oxford Instruments INCA energy system fitted to the SEM.

1.7.6. Atomic Force Microscopy (AFM)

Atomic force microscopy (AFM) is based on a very simple principle. An atomically sharp (or as close atomically sharp as possible) tip is scanned over a sample surface at either a constant tip to sample surface distance, or at a constant force experienced between the tip and the sample surface. A piezo-electric motor allows the distance between the tip and the sample surface to be maintained or changed depending on the scanning mode. A laser reflected from the back of the tip cantilever to a photodiode is used to measures the distance between tip and sample surface. A feed-back loop is then employed to keep the distance or force constant. AFM tips are usually made from silicon nitride (Si_3N_4) or silicon to investigate sample topography but an AFM can be used to measure a number of different surface properties depending on the type of tip used, for example a magnetic tip can be used to investigate different areas of magnetic character or a tip can be contacted with the surface to measure conductivity. A DME 2452 Dualscope AFM was used to collect data on samples reported in this thesis. AFM was operated in ac (tapping) mode under ambient conditions using silicon microcantilever probe tips with a force constant of 60 000 N m^{-1} and a scanning force of 0.11 nN. Topographic and phase images were recorded simultaneously.

1.7.7. UV-Visible Spectroscopy (UV-Vis)

Ultraviolet and visible (UV-Vis) absorption spectroscopy is the measurement of light absorption when it is passed through a sample. The principle of UV-Vis spectroscopy is based on the ability of molecule to absorb ultraviolet and visible light. The absorption of light corresponds to the excitation of outer electrons in the molecule. When a molecule absorbs energy and the outer electrons in the molecule excited from the Highest Occupied Molecular Orbital (HOMO) to Lowest Unoccupied Molecule Orbital (LUMO). The occupied molecular orbitals with lowest

energy are known the σ orbitals, at slightly higher energy are called π orbitals and at still higher energy are known non – bonding orbitals (unshared pair electrons). The π* and σ* are called the highest energy state. The figure 1.10 shows the electronic energy levels and transitions.[225]

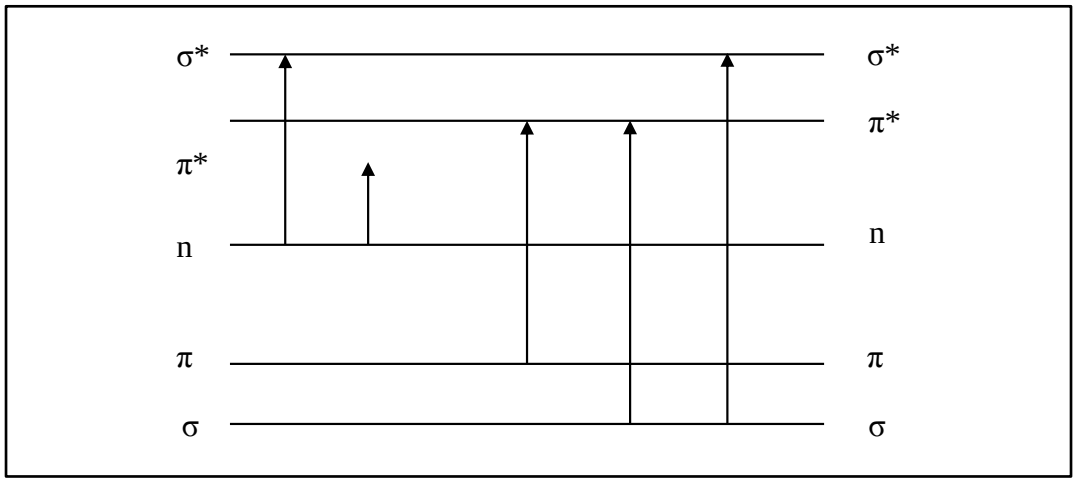

Figure 1.10. Electronic energy level and transition states.

The absorption can be measured at a single wavelength or on spectral extended range. UV-Vis spectroscopy is enough energetic to excite outer electrons to high 14 energy level and it is very useful for quantitative measurement. The Beer – Lambert Law is used to determine the concentration of analyte by measuring the absorbance at various wavelengths.

Beer – Lambert Law is the relationship between absorbance and concentration. It can be written as:

$$A = \varepsilon\, c\, l \qquad \text{Eq. 1.7}$$

where A is the absorbance, ε is the molar absorptivity and expressed in units L mol^{-1} cm^{-1}, *c* is the concentration of the sample (compound) and expressed as mol L^{-1} and *l* is length of cell and expressed in units cm. For absorption measurements, powder samples were dispersed in ethanol using an ultrasonicator and the absorption spectra were recorded with a spectrophotometer Cary 50.

1.7.8. Photoluminescence (PL)

Photoluminescence (PL) is a non-destructive optical technique used for the characterization, investigation and detection of point defects of materials. PL involves the irradiation of the crystal to be characterized with photons of energy greater than the bandgap energy of that material. In the case of a crystal scintillator, the incident photons will create electron hole pairs. When these electrons and holes recombine, this recombination energy will transform partly into non-radiative emission and partly into radiative emission. PL consists of impinging relatively high frequency ($h\nu > E_g$) light onto a material, exciting atomic electrons. Subsequent relaxation may result in the production of photons that are characteristic of the crystal or defect site that emits the light. The luminescent signals detected can result from the band to band recombination, intrinsic crystalline defects (growth defects), dopant impurities (introduced during growth or ion implantation), or other extrinsic defect levels (as a result of radiation or thermal effects). When bombarded with photons of energy greater than the bandgap of the material, an impurity energy level may emit characteristic photons via several different types of radiative recombination events, allowing the resultant PL spectra to be used to determine the specific type of semiconductor defect. This interaction provides a highly sensitive, qualitative measurement of native and extrinsic impurity levels found within the material bandgap. PL measurements were carried out at room temperature using 325 nm as the excitation wavelength with a luminescence spectrometer Perkin Elmer LS 50 B.

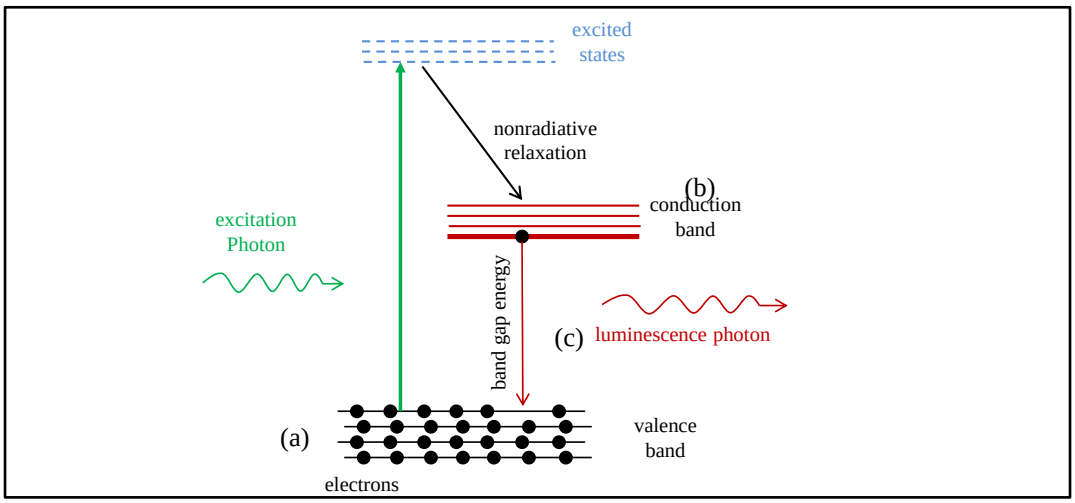

Figure 1.11. Schematic representation of the PL process.

1.7.9. Positron annihilation spectroscopy (PAS)

A positron is the antiparticle of electron and a subatomic particle having the same mass as that of an electron but opposite charge. The annihilation of the positron with an electron in a material results in the emission of gamma rays, which can be detected and analyzed to give information about the electron density and momentum in the material. Hence, this technique is very useful for the studies of structural defects and their evolution in materials. Positron annihilation spectroscopy is also a non-destructive technique for the characterization of defects in materials since the materials are neither chemically nor physically affected by positron bombardment and annihilation. Since the nature and the abundance of the defects control the transport and other physical properties of a system, the utility of this technique has remarkably increased manifold in recent years.

When a positron annihilates with an electron, their rest masses are converted into energy radiation in the form of gamma rays. The single gamma ray emission is possible only from a nuclear field such that the recoiling of the nucleus conserves the gamma ray momentum. In practical application, two-gamma emission is the most probable mode. When a positron enters a sample, its energy is lost in electronic excitation and ionization, besides collision with phonons and plasmons and in the production of electron-hole pairs. Hence, the positron momentum becomes almost zero before the annihilation takes place. In other words, the momentum that contributes to the annihilation gamma rays is that of the electron only. This momentum is conserved only by the emission of the gamma rays with an angular deviation θ and Doppler shift in their energies. Three gamma ray emission and for gamma ray emission are possible but the probabilities are negligibly small.

The positron lifetime is obtained from Dirac's equation[226]:

$$\tau = (\pi\, r_0^2\, c\, \xi\, ne)^{-1} \qquad \text{Eq. 1.8}$$

where r_0 is the classical electron radius, c is the velocity of light and ne is the electron density at the site of annihilation. ξ is an enhancement factor that accounts for the enhancement in the electron density in the region surrounding the positron in the solids due to Coulomb attraction.

The positron annihilation measurement techniques are basically dependent on the three fundamental aspects, viz., positron lifetime, Doppler broadening and angular correlation. These will be discussed in detail in a later chapter but briefly:

Positron lifetime:

The time interval between the event of emission of the positron from a β^+-decaying radioactive isotope and of its subsequent annihilation in a material medium is basically its lifetime, defined as in equation (1.8).

Doppler broadening:

The Doppler broadening of the positron annihilation gamma ray spectrum recorded using a high pure germanium (HPGe) detector gives the momentum distribution of the electrons in the sample. When a positron is emitted from the source, its kinetic energy is lost by ionization, electronic excitation, electron-hole pair creation, phonon interactions etc. Thus, before annihilation, the kinetic energy and linear momentum of the positron are negligible to those of the electron. To conserve the linear momentum of the electron then, the annihilation gamma rays undergo Doppler shift in their energies given by

$$\Delta E = P_x \frac{c}{2} \qquad \text{Eq. 1.9}$$

The value of ΔE corresponds only to the momentum of the annihilating crystal electrons (valence and core). The higher momentum core electrons contribute largest values of ΔE. Hence, Doppler broadened spectra are more sharply peaked for materials containing defects that trap positrons, since there are fewer core electrons at the defect sites. Thus the sharpness (S) of the annihilation gamma ray spectrum is a measure of the overall defect volume in the material. The S parameter is defined as the ratio of counts in channels spreading over 511±0.64 keV to the total area under the spectrum.

Angular correlation:

The conservation of linear momentum also implies that the two gamma rays should deviate by an angle θ in the opposite direction given by

$$\theta = \frac{P_z}{m_0 c} \qquad \text{Eq. 1.10}$$

The number of coincidence gamma rays are recorded for fixed intervals of time at different angles on either side of θ = 0 using NaI(Tl) scintillation detectors. The detectors have to be kept at a few meters apart in order to achieve the desired angular resolution. It is to be mentioned here that the principles of angular correlation measurements have been described here for the sake of completion of discussion only. No such measurements are however reported here in this thesis.

Coincidence Doppler broadening spectroscopy (CDBS):

In Doppler broadening measurements using only one detector, the annihilation gamma ray spectrum grows on the high back ground due to Compton scattering of high-energy gamma rays. The tail region of the spectrum representing the momentum distribution of core electron is submerged in this background. Since the momentum distribution of core electrons helps in the identification of elemental environment around positron annihilation sites, this information is lost in the background. To eliminate this background and to avoid broadening due to detector resolution, a two parameter spectrum is generated from the measured energies of both the annihilation gamma rays and the one dimensional projection on the E_1+E_2 =1022 keV is analyzed.

1.8. References:

1. A. P. Alivisatos, P. F. Barbara, A. W. Castleman, J. Chang, D. A. Dixon, M. L. Klein, G. L. McLendon, J. S. Miller, M. A. Ratner, P. J. Rossky, S. I. Stupp and M. E. Thompson, *Adv Mater*, 1998, **10**, 1297-1336.
2. G. A. Ozin, *Adv Mater*, 1992, **4**, 612-649.
3. A. Thiaville and J. Miltat, *Science*, 1999, **284**, 1939-1940.
4. K. J. Hanszen, *Z Phys*, 1960, **157**, 523-553.
5. G. Cao, in *Nanostructures and Nanomaterials:2nd*, 2011, pp. 433-508.
6. A. M. Smith, A. M. Mohs and S. Nie, *Nat. Nanotechnol.*, 2009, **4**, 56-63.
7. M. Beaudoin, M. Meunier and C. J. Arsenault, *Phys Rev B*, 1993, **47**, 2197-2202.
8. U. Kreibig and C. V. Fragstein, *Z Phys*, 1969, **224**, 307-323.

9. Q. G. Zhang, X. Zhang, B. Y. Cao, M. Fujii, K. Takahashi and T. Ikuta, *Appl. Phys. Lett.*, 2006, **89**, -.
10. Z. H. Cai, J. T. Lei, W. B. Liang, V. Menon and C. R. Martin, *Chem. Mater.*, 1991, **3**, 960-967.
11. C. Noguera, *Physics and Chemistry at Oxide Surfaces*, Cambridge University Press: Cambridge, UK, 1996.
12. H. H. Kung, *Transition Metal Oxides: Surface Chemistry and Catalysis*, Elsevier: Amsterdam, 1989.
13. V. E. Henrich and P. A. Cox, *The Surface Chemistry of Metal Oxides*, Cambridge University Press: Cambridge, UK, 1994.
14. R. J. A. and F.-G. M., *Synthesis, Properties, and Applications of Oxide Nanomaterials*, Wiley: New Jersey, 2007.
15. M. Fernandez-Garcia, A. Martinez-Arias, J. C. Hanson and J. A. Rodriguez, *Chem Rev*, 2004, **104**, 4063-4104.
16. B. R. Stoner and J. T. Glass, *Diamond Relat. Mater.*, 2012, **23**, 130-134.
17. P. Ayyub, V. R. Palkar, S. Chattopadhyay and M. Multani, *Phys Rev B*, 1995, **51**, 6135-6138.
18. N. Millot, D. Aymes, F. Bernard, J. C. Niepce, A. Traverse, F. Bouree, B. L. Cheng and P. Perriat, *J. Phys. Chem. B*, 2003, **107**, 5740-5750.
19. J. M. McHale, A. Auroux, A. J. Perrotta and A. Navrotsky, *Science*, 1997, **277**, 788-791.
20. V. M. Samsonov, N. Y. Sdobnyakov and A. N. Bazulev, *Surf. Sci.*, 2003, **532**, 526-530.
21. H. Zhang and J. F. Banfield, *J. Mater. Chem.*, 1998, **8**, 2073-2076.
22. M. D. Hernandez-Alonso, A. Belen Hungria, A. Martinez-Arias, J. M. Coronado, J. Carlos Conesa, J. Soria and M. Fernandez-Garcia, *Phys. Chem. Chem. Phys.*, 2004, **6**, 3524-3529.
23. P. Ayyub, M. Multani, M. Barma, V. R. Palkar and R. Vijayaraghavan, *J Phys C Solid State*, 1988, **21**, 2229-2245.
24. V. M. Samsonov, N. Y. Sdobnyakov and A. N. Bazulev, *Surf. Sci.*, 2003, **532–535**, 526-530.

25. Z. Song, T. Cai, Z. Chang, G. Liu, J. A. Rodriguez and J. Hrbek, *J. Am. Chem. Soc.*, 2003, **125**, 8059-8066.
26. H. E. Bergna and W. O. Roberts, *Colloidal Silica: Fundamentals and Applications*, CRC Press, 2005.
27. C. Barbé, J. Bartlett, L. Kong, K. Finnie, H. Q. Lin, M. Larkin, S. Calleja, A. Bush and G. Calleja, *Adv Mater*, 2004, **16**, 1959-1966.
28. T. K. Jain, I. Roy, T. K. De and A. Maitra, *J. Am. Chem. Soc.*, 1998, **120**, 11092-11095.
29. G. Herbert, *J. Eur. Ceram. Soc.*, 1994, **14**, 205-214.
30. J. Lu, M. Liong, J. I. Zink and F. Tamanoi, *Small*, 2007, **3**, 1341-1346.
31. I. I. Slowing, B. G. Trewyn and V. S. Y. Lin, *J. Am. Chem. Soc.*, 2007, **129**, 8845-8849.
32. F. Torney, B. G. Trewyn, V. S. Y. Lin and K. Wang, *Nat. Nanotechnol.*, 2007, **2**, 295-300.
33. B. Valeur, *Molecular Fluorescence: Principles and Applications*, New York, Wiley-VCH, 2002.
34. A. Burns, H. Ow and U. Wiesner, *Chem. Soc. Rev.*, 2006, **35**, 1028-1042.
35. R. J. Fulton, R. L. McDade, P. L. Smith, L. J. Kienker and J. R. Kettman, Jr., *Clinical Chemistry*, 1997, **43**, 1749-1756.
36. S. Fournier-Bidoz, T. L. Jennings, J. M. Klostranec, W. Fung, A. Rhee, D. Li and W. C. W. Chan, *Angew. Chem., Int. Ed.*, 2008, **47**, 5577-5581.
37. J. Xu, J. Liang, J. Li and W. Yang, *Langmuir*, 2010, **26**, 15722-15725.
38. X. Zhao, R. P. Bagwe and W. Tan, *Adv Mater*, 2004, **16**, 173-176.
39. A. L. Rogach, D. Nagesha, J. W. Ostrander, M. Giersig and N. A. Kotov, *Chem. Mater.*, 2000, **12**, 2676-2685.
40. A. Vanblaaderen and A. Vrij, *Langmuir*, 1992, **8**, 2921-2931.
41. S. Santra, H. Yang, D. Dutta, J. T. Stanley, P. H. Holloway, W. H. Tan, B. M. Moudgil and R. A. Mericle, *Chem. Commun.*, 2004, 2810-2811.
42. T. Deng, J.-S. Li, J.-H. Jiang, G.-L. Shen and R.-Q. Yu, *Adv. Funct. Mater.*, 2006, **16**, 2147-2155.
43. R. Kumar, T. Y. Ohulchanskyy, I. Roy, S. K. Gupta, C. Borek, M. E. Thompson and P. N. Prasad, *Acs Appl Mater Inter*, 2009, **1**, 1474-1481.

44. W. H. Tan, K. M. Wang, X. X. He, X. J. Zhao, T. Drake, L. Wang and R. P. Bagwe, *Med. Res. Rev.*, 2004, **24**, 621-638.
45. G. Yao, L. Wang, Y. Wu, J. Smith, J. Xu, W. Zhao, E. Lee and W. Tan, *Anal. Bioanal. Chem.*, 2006, **385**, 518-524.
46. J. E. Smith, L. Wang and W. Tan, *Trac-Trends in Analytical Chemistry*, 2006, **25**, 848-855.
47. A. Bapat, C. Anderson, C. R. Perrey, C. B. Carter, S. A. Campbell and U. Kortshagen, *Plasma Phys. Controlled Fusion*, 2004, **46**, B97-B109.
48. N. Awaji, S. Ohkubo, T. Nakanishi, T. Aoyama, Y. Sugita, K. Takasaki and S. Komiya, *Appl. Phys. Lett.*, 1997, **71**, 1954-1956.
49. B. G. Trewyn, I. I. Slowing, S. Giri, H.-T. Chen and V. S. Y. Lin, *Acc. Chem. Res.*, 2007, **40**, 846-853.
50. M. Jafarzadeh, I. A. Rahman and C. S. Sipaut, *J. Sol-Gel Sci. Technol.*, 2009, **50**, 328-336.
51. P. K. Jal, M. Sudarshan, A. Saha, S. Patel and B. K. Mishra, *Colloids and Surfaces A: Physicochemical and Engineering Aspects*, 2004, **240**, 173-178.
52. T. Aubert, F. Grasset, S. Mornet, E. Duguet, O. Cador, S. Cordier, Y. Molard, V. Demange, M. Mortier and H. Haneda, *J. Colloid Interface Sci.*, 2010, **341**, 201-208.
53. M. S. Wooldridge, P. V. Torek, M. T. Donovan, D. L. Hall, T. A. Miller, T. R. Palmer and C. R. Schrock, *Combust. Flame*, 2002, **131**, 98-109.
54. A. B. Corradi, F. Bondioli, A. M. Ferrari, B. Focher and C. Leonelli, *Powder Technol.*, 2006, **167**, 45-48.
55. X. Cai, R. Y. Hong, L. S. Wang, X. Y. Wang, H. Z. Li, Y. Zheng and D. G. Wei, *Chem. Eng. J.*, 2009, **151**, 380-386.
56. W. Stober, A. Fink and E. Bohn, *J. Colloid Interface Sci.*, 1968, **26**, 62-69.
57. K. Osseo-Asare and F. J. Arriagada, *Colloids Surf.*, 1990, **50**, 321-339.
58. S. Santra, R. Tapec, N. Theodoropoulou, J. Dobson, A. Hebard and W. Tan, *Langmuir*, 2001, **17**, 2900-2906.
59. S. Santra, K. Wang, R. Tapec and W. Tan, *J Biomed Opt*, 2001, **6**, 160-166.
60. S. Santra, P. Zhang, K. Wang, R. Tapec and W. Tan, *Anal. Chem.*, 2001, **73**, 4988-4993.

61. J. Schmidt, C. Guesdon and R. Schomäcker, *J Nanopart Res*, 1999, **1**, 267-276.
62. J. Zhang, Z. Liu, B. Han, Y. Wang, Z. Li and G. Yang, *Microporous Mesoporous Mater.*, 2005, **87**, 10-14.
63. J. E. Alberg and E. A. Simpson, US patent 2, 900, 348, 1959.
64. G. Mertz, German Patent 2, 6, 21, 1971.
65. J. F. White, US patent 2, 375, 738, 1945.
66. Y.-K. Lee, Y. Rock Yoon and H.-K. Rhee, *Colloids and Surfaces A: Physicochemical and Engineering Aspects*, 2000, **173**, 109-116.
67. L. Wu, H. J. Wiesmann, A. R. Moodenbaugh, R. F. Klie, Y. Zhu, D. O. Welch and M. Suenaga, *Phys Rev B*, 2004, **69**, 125415.
68. S. Tsunekawa, T. Fukuda and A. Kasuya, *Surf. Sci.*, 2000, **457**, L437-L440.
69. S. Carrettin, P. Concepcion, A. Corma, J. M. L. Nieto and V. F. Puntes, *Angew Chem Int Edit*, 2004, **43**, 2538-2540.
70. A. Tschope, E. Sommer and R. Birringer, *Solid State Ionics*, 2001, **139**, 255-265.
71. L. Liao, H. X. Mai, Q. Yuan, H. B. Lu, J. C. Li, C. Liu, C. H. Yan, Z. X. Shen and T. Yu, *J. Phys. Chem. C*, 2008, **112**, 9061-9065.
72. S. Basu, P. S. Devi and H. S. Maiti, *J. Mater. Res.*, 2004, **19**, 3162-3171.
73. J. L. Lu, H. J. Gao, S. Shaikhutdinov and H. J. Freund, *Surf. Sci.*, 2006, **600**, 5004-5010.
74. E. Mamontov, T. Egami, R. Brezny, M. Koranne and S. Tyagi, *J. Phys. Chem. B*, 2000, **104**, 11110-11116.
75. N. V. Skorodumova, S. I. Simak, B. I. Lundqvist, I. A. Abrikosov and B. Johansson, *Phys. Rev. Lett.*, 2002, **89**.
76. N. Shehata, K. Meehan and D. Leber, 2012, 84630P-84630P.
77. H. Inaba and H. Tagawa, *Solid State Ionics*, 1996, **83**, 1-16.
78. B. C. H. Steele, *Solid State Ionics*, 2000, **129**, 95-110.
79. A. S. Karakoti, S. V. N. T. Kuchibhatla, K. S. Babu and S. Seal, *J. Phys. Chem. C*, 2007, **111**, 17232-17240.
80. P. Li, I. W. Chen, J. E. Pennerhahn and T. Y. Tien, *J. Am. Ceram. Soc.*, 1991, **74**, 958-967.
81. A. Trovarelli, *Catal. Rev.*, 1996, **38**, 439-520.

82. A. Laachir, V. Perrichon, A. Badri, J. Lamotte, E. Catherine, J. C. Lavalley, J. Elfallah, L. Hilaire, F. Lenormand, E. Quemere, G. N. Sauvion and O. Touret, *J Chem Soc Faraday T*, 1991, **87**, 1601-1609.
83. A. Badri, J. Lamotte, J. C. Lavalley, A. Laachir, V. Perrichon, O. Touret, G. N. Sauvion and E. Quemere, *Eur. J. Solid State Inorg. Chem.*, 1991, **28**, 445-448.
84. J. L. Duplan and H. Praliaud, *Appl Catal*, 1991, **67**, 325-335.
85. A. Trovarelli, *Catalysis by Ceria and Related Materials, volume 2 of Catalytic Science Series*, Imperial College Press, London, 2001.
86. L. Chen, P. Fleming, V. Morris, J. D. Holmes and M. A. Morris, *J. Phys. Chem. C*, 2010, **114**, 12909-12919.
87. T. H. Etsell and S. N. Flengas, *Chem Rev*, 1970, **70**, 339-376.
88. H. Inaba and H. Tagawa, *Solid State Ionics*, 1996, **83**, 1-16.
89. G. Mialon, M. Poggi, D. Casanova, T. L. Nguyen, S. Turkcan, A. Alexandrou, T. Gacoin and J. P. Boilot, *J. Lumin.*, 2009, **129**, 1706-1710.
90. D. A. Andersson, S. I. Simak, N. V. Skorodumova, I. A. Abrikosov and B. Johansson, *Proc. Natl. Acad. Sci. U. S. A.*, 2006, **103**, 3518-3521.
91. C. Frayret, A. Villesuzanne, M. Pouchard, F. Mauvy, J. M. Bassat and J. C. Grenier, *J. Phys. Chem. C*, 2010, **114**, 19062-19076.
92. X. Wang, J. C. Hanson, G. Liu, J. A. Rodriguez, A. Iglesias-Juez and M. Fernández-García, *J. Chem. Phys.*, 2004, **121**, 5434-5444.
93. R. Shannon, *Acta Cryst.*, 1976, **32**, 751-767.
94. C. Tiseanu, V. I. Parvulescu, M. Boutonnet, B. Cojocaru, P. A. Primus, C. M. Teodorescu, C. Solans and M. Sanchez-Dominguez, *Phys. Chem. Chem. Phys.*, 2011, **13**, 21652-21653.
95. H. Yokokawa, T. Horita, N. Sakai, K. Yamaji, M. E. Brito, Y. P. Xiong and H. Kishimoto, *Solid State Ionics*, 2006, **177**, 1705-1714.
96. S. Fujihara and M. Oikawa, *J. Appl. Phys.*, 2004, **95**, 8002-8006.
97. S. Chunwen, L. Hong, Z. Huairuo, W. Zhaoxiang and C. Liquan, *Nanotechnology*, 2005, **16**, 1454.
98. C. Ho, J. C. Yu, T. Kwong, A. C. Mak and S. Lai, *Chem. Mater.*, 2005, **17**, 4514-4522.
99. E. Matijević and W. P. Hsu, *J. Colloid Interface Sci.*, 1987, **118**, 506-523.

100. B. Djuričić and S. Pickering, *J. Eur. Ceram. Soc.*, 1999, **19**, 1925-1934.
101. X. D. Zhou, W. Huebner and H. U. Anderson, *Appl. Phys. Lett.*, 2002, **80**, 3814-3816.
102. P.-L. Chen and I. W. Chen, *J. Am. Ceram. Soc.*, 1993, **76**, 1577-1583.
103. J.-G. Li, T. Ikegami, Y. Wang and T. Mori, *J. Am. Ceram. Soc.*, 2002, **85**, 2376-2378.
104. M. Kamruddin, P. K. Ajikumar, R. Nithya, A. K. Tyagi and B. Raj, *Scr. Mater.*, 2004, **50**, 417-422.
105. R. D. Purohit, B. P. Sharma, K. T. Pillai and A. K. Tyagi, *Mater. Res. Bull.*, 2001, **36**, 2711-2721.
106. L. Mädler, W. J. Stark and S. E. Pratsinis, *J. Mater. Res.*, 2002, **17**, 1356-1362.
107. M. Boutonnet, J. Kizling and P. Stenius, *Colloids Surf.*, 1982, **5**, 209-225.
108. F. Bondioli, A. B. Corradi, T. Manfredini, C. Leonelli and R. Bertoncello, *Chem. Mater.*, 1999, **12**, 324-330.
109. B. Ksapabutr, E. Gulari and S. Wongkasemjit, *Mater. Chem. Phys.*, 2006, **99**, 318-324.
110. X. Chu, W.-i. Chung and L. D. Schmidt, *J. Am. Ceram. Soc.*, 1993, **76**, 2115-2118.
111. L. Yin, Y. Wang, G. Pang, Y. Koltypin and A. Gedanken, *J. Colloid Interface Sci.*, 2002, **246**, 78-84.
112. N. Guillou, L. C. Nistor, H. Fuess and H. Hahn, *Nanostructured Materials*, 1997, **8**, 545-557.
113. M. Hirano and E. Kato, *J. Am. Ceram. Soc.*, 1999, **82**, 786-788.
114. C. Sun and L. Chen, *Eur. J. Inorg. Chem.*, 2009, **2009**, 3883-3887.
115. Y. Zhou, R. J. Phillips and J. A. Switzer, *J. Am. Ceram. Soc.*, 1995, **78**, 981-985.
116. F. Czerwinski and J. A. Szpunar, *J. Sol-Gel Sci. Technol.*, 1997, **9**, 103-114.
117. A. Turkovic, P. Dubcek, Z. Crnjak-Orel and S. Bernstorff, *Nanostructured Materials*, 1999, **11**, 909-915.
118. M. Yamashita, K. Kameyama, S. Yabe, S. Yoshida, Y. Fujishiro, T. Kawai and T. Sato, *J. Mater. Sci.*, 2002, **37**, 683-687.
119. Z. Wang, Z. Quan and J. Lin, *Inorg. Chem.*, 2007, **46**, 5237-5242.

120. E. Verdon, M. Devalette and G. Demazeau, *Mater. Lett.*, 1995, **25**, 127-131.
121. W. Chengyun, Q. Yitai, Y. Xie, W. Changsui, L. Yang and Z. Guiwen, *Mater. Sci. Eng., B*, 1996, **39**, 160-162.
122. Z. L. Wang and X. D. Feng, *J. Phys. Chem. B*, 2003, **107**, 13563-13566.
123. D. H. Everett and L. K. Koopal, *Manual of Symbols and Terminology for Physicochemical Quantities and Units - Appendix II: Definitions, Terminology and Symbols in Colloid and Surface Chemistry*, International Union of Pure and Applied Chemistry (IUPAC), 1971.
124. S. Inagaki, Y. Fukushima and K. Kuroda, *J Chem Soc Chem Comm*, 1993, 680-682.
125. C. T. Kresge, M. E. Leonowicz, W. J. Roth, J. C. Vartuli and J. S. Beck, *Nature*, 1992, **359**, 710-712.
126. J. S. Beck, J. C. Vartuli, W. J. Roth, M. E. Leonowicz, C. T. Kresge, K. D. Schmitt, C. T. W. Chu, D. H. Olson, E. W. Sheppard, S. B. Mccullen, J. B. Higgins and J. L. Schlenker, *J. Am. Chem. Soc.*, 1992, **114**, 10834-10843.
127. Q. S. Huo, D. I. Margolese, U. Ciesla, P. Y. Feng, T. E. Gier, P. Sieger, R. Leon, P. M. Petroff, F. Schuth and G. D. Stucky, *Nature*, 1994, **368**, 317-321.
128. H. Yang, A. Kuperman, N. Coombs, S. MamicheAfara and G. A. Ozin, *Nature*, 1996, **379**, 703-705.
129. H. Yang, N. Coombs, I. Sokolov and G. A. Ozin, *Nature*, 1996, **381**, 589-592.
130. T. Kimura, D. Itoh, N. Okazaki, M. Kaneda, Y. Sakamoto, O. Terasaki, Y. Sugahara and K. Kuroda, *Langmuir*, 2000, **16**, 7624-7628.
131. A. Shimojima and K. Kuroda, *Angew Chem Int Edit*, 2003, **42**, 4057-4060.
132. M. Ogawa, *Chem. Commun.*, 1996, 1149-1150.
133. H. Miyata and K. Kuroda, *Chem. Mater.*, 1999, **11**, 1609-1614.
134. C. W. Wu, J. B. Pang and M. Kuwabara, *Chem. Lett.*, 2002, 974-975.
135. H. Miyata, T. Suzuki, A. Fukuoka, T. Sawada, M. Watanabe, T. Noma, K. Takada, T. Mukaide and K. Kuroda, *Nat. Mater.*, 2004, **3**, 651-656.
136. D. Grosso, A. R. Balkenende, P. A. Albouy, M. Lavergne, L. Mazerolles and F. Babonneau, *J. Mater. Chem.*, 2000, **10**, 2085-2089.
137. J. Fan, C. Z. Yu, T. Gao, J. Lei, B. Z. Tian, L. M. Wang, Q. Luo, B. Tu, W. Z. Zhou and D. Y. Zhao, *Angew Chem Int Edit*, 2003, **42**, 3146-3150.

138. Y. Q. Wang, C. M. Yang, B. Zibrowius, B. Spliethoff, M. Linden and F. Schuth, *Chem. Mater.*, 2003, **15**, 5029-5035.
139. J. S. Beck, J. C. Vartuli, W. J. Roth, M. E. Leonowicz, C. T. Kresge, K. D. Schmitt, C. T. W. Chu, D. H. Olson and E. W. Sheppard, *J. Am. Chem. Soc.*, 1992, **114**, 10834-10843.
140. D. Zhao, J. Feng, Q. Huo, N. Melosh, G. H. Fredrickson, B. F. Chmelka and G. D. Stucky, *Science*, 1998, **279**, 548-552.
141. D. Zhao, Q. Huo, J. Feng, B. F. Chmelka and G. D. Stucky, *J. Am. Chem. Soc.*, 1998, **120**, 6024-6036.
142. S. J. Billinge, E. J. McKimmy, M. Shatnawi, H. Kim, V. Petkov, D. Wermeille and T. J. Pinnavaia, *J. Am. Chem. Soc.*, 2005, **127**, 8492-8498.
143. D. E. De Vos, M. Dams, B. F. Sels and P. A. Jacobs, *Chem Rev*, 2002, **102**, 3615-3640.
144. V. Rebbin, R. Schmidt and M. Froba, *Angew Chem Int Ed Engl*, 2006, **45**, 5210-5214.
145. N. Petkov, N. Stock and T. Bein, *J. Phys. Chem. B*, 2005, **109**, 10737-10743.
146. B. Ye, M. L. Trudeau and D. M. Antonelli, *Adv Mater*, 2001, **13**, 561-565.
147. I. Roy, T. Y. Ohulchanskyy, D. J. Bharali, H. E. Pudavar, R. A. Mistretta, N. Kaur and P. N. Prasad, *Proc. Natl. Acad. Sci. U. S. A.*, 2005, **102**, 279-284.
148. S. Giri, B. G. Trewyn and V. S. Lin, *Nanomedicine*, 2007, **2**, 99-111.
149. W. C. Molenkamp, M. Watanabe, H. Miyata and S. H. Tolbert, *J. Am. Chem. Soc.*, 2004, **126**, 4476-4477.
150. B. J. Scott, G. Wirnsberger and G. D. Stucky, *Chem. Mater.*, 2001, **13**, 3140-3150.
151. T. Yamada, H. S. Zhou, H. Uchida, M. Tomita, Y. Ueno, T. Ichino, I. Honma, K. Asai and T. Katsube, *Adv Mater*, 2002, **14**, 812-815.
152. C. M. Yang, A. T. Cho, F. M. Pan, T. G. Tsai and K. J. Chao, *Adv Mater*, 2001, **13**, 1099-1102.
153. B. D. Hatton, K. Landskron, W. Whitnall, D. D. Perovic and G. A. Ozin, *Adv. Funct. Mater.*, 2005, **15**, 823-829.
154. A. P. Alivisatos, *J. Phys. Chem.*, 1996, **100**, 13226-13239.
155. M. E. Davis, *Nature*, 2002, **417**, 813-821.

156. S. Baskaran, J. Liu, K. Domansky, N. Kohler, X. H. Li, C. Coyle, G. E. Fryxell, S. Thevuthasan and R. E. Williford, *Adv Mater*, 2000, **12**, 291-294.
157. D. Zhao, P. Yang, N. Melosh, J. Feng, B. F. Chmelka and G. D. Stucky, *Adv Mater*, 1998, **10**, 1380-+.
158. H. Y. Fan, F. Van Swol, Y. F. Lu and C. J. Brinker, *J. Non-Cryst. Solids*, 2001, **285**, 71-78.
159. M. Ogawa, *J. Am. Chem. Soc.*, 1994, **116**, 7941-7942.
160. Y. F. Lu, R. Ganguli, C. A. Drewien, M. T. Anderson, C. J. Brinker, W. L. Gong, Y. X. Guo, H. Soyez, B. Dunn, M. H. Huang and J. I. Zink, *Nature*, 1997, **389**, 364-368.
161. D. Zhao, P. Yang, D. I. Margolese and G. D. Stucky, *Chem. Commun.*, 1998, 2499-2500.
162. C. Sanchez, C. Boissiere, D. Grosso, C. Laberty and L. Nicole, *Chem. Mater.*, 2008, **20**, 682-737.
163. X. S. Zhao, G. Q. M. Lu and G. J. Millar, *Ind. Eng. Chem. Res.*, 1996, **35**, 2075-2090.
164. A. Sayari, B. H. Han and Y. Yang, *J. Am. Chem. Soc.*, 2004, **126**, 14348-14349.
165. P. T. Tanev and T. J. Pinnavaia, *Chem. Mater.*, 1996, **8**, 2068-2079.
166. K. Moller and T. Bein, *Chem. Mater.*, 1998, **10**, 2950-2963.
167. J. Y. Ying, C. P. Mehnert and M. S. Wong, *Angew. Chem.*, 1999, **111**, 58-82.
168. G. Oye, J. Sjöblom and M. Stöcker, *Adv. Colloid Interface Sci.*, 2001, **89–90**, 439-466.
169. A. Monnier, F. Schüth, Q. Huo, D. Kumar, D. Margolese, R. S. Maxwell, G. D. Stucky, M. Krishnamurty, P. Petroff, A. Firouzi, M. Janicke and B. F. Chmelka, *Science*, 1993, **261**, 1299-1303.
170. A. Firouzi, D. J. Schaefer, S. H. Tolbert, G. D. Stucky and B. F. Chmelka, *J. Am. Chem. Soc.*, 1997, **119**, 9466-9477.
171. Q. Huo, R. Leon, P. M. Petroff and G. D. Stucky, *Science*, 1995, **268**, 1324-1327.
172. P. C. A. Alberius, K. L. Frindell, R. C. Hayward, E. J. Kramer, G. D. Stucky and B. F. Chmelka, *Chem. Mater.*, 2002, **14**, 3284-3294.

173. S. Besson, T. Gacoin, C. Ricolleau, C. Jacquiod and J.-P. Boilot, *J. Mater. Chem.*, 2003, **13**, 404-409.
174. F. Cagnol, D. Grosso, G. J. d. A. A. Soler-Illia, E. L. Crepaldi, F. Babonneau, H. Amenitsch and C. Sanchez, *J. Mater. Chem.*, 2003, **13**, 61-66.
175. V. Abetz and P. F. W. Simon, *Block Copolymers I*, Vol. 189 (Ed.:V. Abetz) Springer, Berlin, 2005, 125-212.
176. N. A. Lynd, A. J. Meuler and M. A. Hillmyer, *Prog. Polym. Sci.*, 2008, **33**, 875-893.
177. I. W. Hamley, *Block Copolymers in Solution: Fundamentals and Applications*, Wiley, Chichester, 2005.
178. H. C. Kim, S. M. Park and W. D. Hinsberg, *Chem Rev*, 2010, **110**, 146-177.
179. M. Lazzari, G. Liu and S. Lecommandoux, *Block Copolymers in Nanoscience*, Wiley-VCH, Weinheim, 2006.
180. F. J. Balta Calleja and Z. Roslaniec, *Block copolymers*, CRC Press, New York, NY, 2000.
181. P. Alexandridis, J. F. Holzwarth and T. A. Hatton, *Macromolecules*, 1994, **27**, 2414-2425.
182. E. B. Jorgensen, S. Hvidt, W. Brown and K. Schillen, *Macromolecules*, 1997, **30**, 2355-2364.
183. L. Guo, R. H. Colby, M. Y. Lin and G. P. Dado, *J Rheol*, 2001, **45**, 1223-1243.
184. V. K. Aswal, A. G. Wagh and M. Kammel, *J Phys-Condens Mat*, 2007, **19**, 116101.
185. G. M. Whitesides and B. Grzybowski, *Science*, 2002, **295**, 2418-2421.
186. R. A. Farrell, T. G. Fitzgerald, D. Borah, J. D. Holmes and M. A. Morris, *Int J Mol Sci*, 2009, **10**, 3671-3712.
187. M. L. Adams, A. Lavasanifar and G. S. Kwon, *J. Pharm. Sci.*, 2003, **92**, 1343-1355.
188. E. W. Cochran, C. J. Garcia-Cervera and G. H. Fredrickson, *Macromolecules*, 2006, **39**, 2449-2451.
189. R. A. Segalman, *Mat Sci Eng R*, 2005, **48**, 191-226.
190. J. R. Fried, *Polymer Science and Technology (2nd Ed.)*, Prentice Hall: NJ, USA, 2003.

191. H. C. Kim and T. P. Russell, *J Polym Sci Pol Phys*, 2001, **39**, 663-668.
192. S. Franssila, *Introduction to Microfabrication*, 2nd ed. Chichester: John Wiley & Sons Ltd., 2010.
193. S. B. Darling, *Prog. Polym. Sci.*, 2007, **32**, 1152-1204.
194. I. W. Hamley, *Nanotechnology*, 2003, **14**, R39-R54.
195. A. Komeili, *Annu. Rev. Biochem.*, 2007, **76**, 351-366.
196. S. Neidle, *Oxford Handbook of Nucleic Acid*, Oxford University Press: Oxford, UK, 1999.
197. W. J. Crookes-Goodson, J. M. Slocik and R. R. Naik, *Chem. Soc. Rev.*, 2008, **37**, 2403-2412.
198. S. E. Abed, S. K. Ibnsouda, L. H. and F. Hamadi, *Scanning Electron Microscopy (SEM) and Environmental SEM: Suitable Tools for Study of Adhesion Stage and Biofilm Formation*, InTech: Morocco, 2012.
199. J. A. Shapiro, *Annu. Rev. Microbiol.*, 1998, **52**, 81-104.
200. X. H. Li, Y. Xing, Y. H. Jiang, Y. L. Ding and W. L. Li, *Int. J. Food Sci. Technol.*, 2009, **44**, 2161-2168.
201. J. S. Vrouwenvelder, J. C. Kruithof and M. C. M. Van Loosdrecht, *Water Sci. Technol.*, 2010, **62**, 2477-2490.
202. R. M. Klevens, J. R. Edwards, C. L. Richards, T. C. Horan, R. P. Gaynes, D. A. Pollock and D. M. Cardo, *Public Health Rep*, 2007, **122**, 160-166.
203. R. O. Darouiche, *N. Engl. J. Med.*, 2004, **350**, 1422-1429.
204. I. Banerjee, R. C. Pangule and R. S. Kane, *Adv Mater*, 2011, **23**, 690-718.
205. Y. Matsumura, K. Yoshikata, S. Kunisaki and T. Tsuchido, *Appl. Environ. Microbiol.*, 2003, **69**, 4278-4281.
206. Q. L. Feng, J. Wu, G. Q. Chen, F. Z. Cui, T. N. Kim and J. O. Kim, *J Biomed Mater Res*, 2000, **52**, 662-668.
207. C. Greulich, S. Kittler, M. Epple, G. Muhr and M. Koller, *Langenbeck Arch Surg*, 2009, **394**, 495-502.
208. N. Miura and Y. Shinohara, *Biochem. Biophys. Res. Commun.*, 2009, **390**, 733-737.
209. J. Siegel, O. Kvitek, P. Ulbrich, Z. Kolska, P. Slepicka and V. Svorcik, *Mater. Lett.*, 2012, **89**, 47-50.

210. S. Bratskaya, D. Marinin, F. Simon, A. Synytska, S. Zschoche, H. J. Busscher, D. Jager and H. C. van der Mei, *Biomacromolecules*, 2007, **8**, 2960-2968.
211. P. Pang and P. Englezos, *Colloid Surface A*, 2002, **204**, 23-30.
212. A. Roosjen, H. C. van der Mei, H. J. Busscher and W. Norde, *Langmuir*, 2004, **20**, 10949-10955.
213. T. Ghoshal, R. Senthamaraikannan, M. T. Shaw, J. D. Holmes and M. A. Morris, *Nanoscale*, 2012, **4**, 7743-7750.
214. T. Ghoshal, T. Maity, J. F. Godsell, S. Roy and M. A. Morris, *Adv Mater*, 2012, **24**, 2390-2397.
215. R. W. G. Wyckoff, *Crystal Structures, 2nd ed.*, Wiley: New York, 1964.
216. G. Stout and L. Jensen, *X-ray Structure Determination: A Practical Guide*, John Wiley & Sons: New York, 1989.
217. R. L. Snyder, J. Fiala and H. J. Bunge, *Defect and Microstructure Analysis by Diffraction*, Oxford University Press: New York, 1999.
218. W. L. Bragg, *Proceedings of the Cambridge Philosophical Society*, 1913, **17**, 43.
219. Y. Yoneda and T. Horiuchi, *Rev. Sci. Instrum.*, 1971, **42**, 1069-1070.
220. P. Wobrauschek and H. Aiginger, *Anal. Chem.*, 1975, **47**, 852-855.
221. L. G. Parratt, *Phys. Rev.*, 1954, **95**, 359-369.
222. P. Wobrauschek, *X-Ray Spectrom.*, 2007, **36**, 289-300.
223. D. Briggs and M. P. Seah, *Practical surface analysis by Auger and X-ray photoelectron spectroscopy*, In: Briggs D, Seah MP (eds) Wiley, Chichester, 1983.
224. J. F. Watts and J. Wolstenholme, *An Introduction to Surface Analysis by XPS and AES*, John Wiley & Sons, Ltd., Chichester, 1st edn., 2003.
225. D. L. Pavia, G. M. Lampman and G. S. Kriz, *Introduction to Spectroscopy*, Saunders Golden Sunburst Series: 2nd edition, 1997.
226. R. W. Siegel, *Annu Rev Mater Sci*, 1980, **10**, 393-425.

Chapter 2

Synthesis and characterization of dye-doped silica nanoparticles

2.1. Abstract

Encapsulation of dye molecules into a silica framework promises to overcome some of the functional limitations of free organic dyes. The incorporation or grafting of fluorescent dyes into nanosized silica particles has been the sponsor of a significant amount of research in recent years due to the excellent properties that the silica nanoparticles have. These include their high chemical/physical solubility, low toxicity and slow degradation with time. In the present work, dye-doped monodisperse silica nanoparticles have been successfully synthesized by a modified Stöber process, where the different ratio between precursors and solvents has been used in order to control the particle size. The UV-Vis absorbance spectra of the dispersed dye-doped silica nanoparticles show varied change of absorption intensity with time for the different dye systems used. A clear zero-sum increase-decrease relation of the absorbance intensity at 366 and 750 nm for IR-820 dye has been observed. The decrease at 750 nm indicates the degradation of the IR-820 dye molecules in aqueous solution while the increase at 366 nm implies the formation of new substances. However, the feature absorbance peak of fluorescein isothiocyanate (FITC) at 490 nm is kept constant for all FITC dye-doped silica nanoparticles indicating the FITC molecules are more stable than the IR-820 dye-doped silica nanoparticles under the same conditions.

2.2. Introduction

NPs have great promise in bioanalysis and biotechnological applications because of their unique optical properties, high surface-to-volume ratio, and other size-dependent qualities. When combined with surface modifications and composition control, these properties provide probes for highly selective and ultrasensitive bioassays. Silica has been used in many areas due to its unique properties. Silica is optically transparent in the visible and near-infrared region. Silica is a non-toxic compound which is already used as food additive or as carrier material in tablets.[1] Silica nanoparticles have high hydrophilicity and are insensitive to microbial attack. In addition, they do not show any swelling or porosity changes as pH is altered.[2] It's surface usually bears reactive silanol groups, which can allows chemical functionalization. As silica is widely available in nature, it is an

inexpensive raw material. Silica has good thermal and electrical insulating properties combined with proven processing, thermal and mechanical properties. Monodispersed nanometer-sized silica particles have been shown to have important advantages in the scientific field as well as in many industrial applications, e.g. catalysis, pigments, pharmacy, etc.[3] Silica nanoparticles have biomedical applications such as delivery of anticancer drugs,[4] enzymes[5] and DNA.[6]

Dye doped fluorescent silica nanoparticles (FSNP) possess several advantages such as high florescence intensity, good photostability[7, 8] and good potential for surface modification with various biomolecules.[9, 10] To date, thousands of dye molecules have been doped inside the silica matrix as well as on the surface. As a result, probe sensitivity has been greatly improved. There are several advantages in selecting silica-based fluorescent nanoparticles. Dye doped FSNP synthesis is relatively simple and does not require extreme reaction conditions (such as high/low temperature, pressures and inert reaction environment). The silica matrix provides a protective encapsulation around the fluorescent dyes, which can improve dye photostability. Using conventional silica-based chemistry a variety of biomolecules (e.g. antibodies, proteins, peptides, DNA, etc.) can be covalently attached to the silica surface. The silica surface makes these silica nanoparticles chemically inert and physically stable.[11] This can allow 'targeting' of functionality on particular cell types.

Herein, we have synthesised various sizes of silica nanoparticles using Stöber method.[12] Two different dyes (IR-820 and FITC) were successfully grafted on silica surfaces and stability of these dye grafted dyes is studied using UV-Vis spectroscopy. Also, a new type of dual dye-doped hybrid silica nanoparticles has been developed. The combination use of TEM, SEM, UV-Vis and confocal microscope shows the synthesis parameters have significant effects on the particle shape and size and the size is tuneable from a few nanometers to a few hundred nanometers. The ability to create size controlled nanoparticles with associated (optical) functionality may have significant importance in bio-medical imaging.

2.3. Experimental:

2.3.1. Materials

IR-820, Fluorescein isothiocyanate (FITC), tetraethyl orthosilicate (TEOS, 99.99%), (3-aminopropyl) trimethoxysilane (APS), tert-butyl methyl ether (TBME), dimethyl formamide (DMF), (3-mercaptopropyl) trimethoxysilane, anhydrous ethanol (≥99.9%), 28% aqueous ammonia and toluene were purchased from Sigma Aldrich and used as received.

2.3.2. Synthesis of silica nanoparticles

Various sizes of the silica nanoparticles were prepared by base hydrolysis and condensation (polymerisation) of TEOS. 0.37 M of TEOS was added into 50 ml of anhydrous ethanol with stirring to form solution 'A'. In another bottle, given volume (weight) of ammonium hydroxide was mixed with 50 ml anhydrous ethanol to form solution 'B'. Then, solution 'A' was poured into 'B' under rigorous stirring. The mixed solution was kept stirring at room temperature for 24 h. The final molar ratio of TEOS:NH_4OH:ethanol was variable following the relationship, 1:(2.22 – 8.86):1.7. Finally, the white precipitates were collected by filtration on a piece of Millipore filter paper (pore size ranges from 0.015 – 0.2 μm) followed by washing with ethanol and acetone. Samples were dried under vacuum at room temperature. In order to investigate the effects of the chemical composition in the starting solution on the particle size, amount of the aqueous ammonium hydroxide was varied. Samples with varying sizes of silica nanoparticles are represented as SiNX, where X= 20, 52, 95, 210 and 410 nm were the determined particle sizes of silica nanoparticles.

2.3.3. Synthesis of IR-820 and FITC dye conjugates

IR-820 (0.6 mM), anhydrous DMF (0.1 M), (3-mercaptopropyl) trimethoxysilane (0.7 mM) and triethyl amine (0.7 mM) were mixed together and stirred for 24 h at room temperature. The conjugated dye was precipitated by TBME. The 'wet' product was collected by filtration and washed three times using TBME. The washed conjugate was dried in vacuum at room temperature. Alternatively, FITC (0.8 mM) dye was added to the APS (10 mM). The excess of APS was added

to FITC to prevent bleaching of the dye. The mixture was stirred for 48 h at room temperature. Then this mixture was precipitated by TBME and sonicated for 20 min. The product was collected by centrifugation at 8000 rpm for 15 min followed by washing with TBME. Then the conjugate was dried under vacuum at room temperature.

2.3.4. Synthesis of dye-doped silica nanoparticles

A simple impregnation method was used to prepare dye-doped silica nanoparticles. As prepared silica nanoparticles (0.1 g) were mixed with toluene and sonicated for 20 min. IR-820 dye conjugate (0.005-0.05 g) was added to the above solution and then refluxed at 120 °C for 12 h. The solution was filtered using filter paper and the solid recovered washed several times with ethanol and water. All samples were dried under vacuum at room temperature. Similarly, FITC dye conjugate (0.025-0.05 g) was added to solution of as-synthesized silica nanoparticles and toluene. This solution was also refluxed at 120 °C for 12 h. The solutions were filtered using filter paper and washed several times with ethanol and water. All samples were dried under vacuum at room temperature.

2.3.5. Synthesis of dual dye-doped silica nanoparticles

0.1 g of silica nanoparticles (SiN95) were mixed with toluene and sonicated for 20 min. IR-820 dye conjugate (0.005 g) was added to the above solution and then refluxed at 120 °C for 12 h. The solution was filtered using filter paper and the solid recovered washed several times with ethanol and water. The sample was dried under vacuum at room temperature. Resultant IR-820 doped silica nanoparticles were again dispersed in toluene and sonicated for 20 min. The FITC dye conjugate (0.01g in 5 ml of toluene) was added to above solution and refluxed at 120 °C for 12 h. The solution was filtered using filter paper and washed several times with ethanol and water. The sample was dried under vacuum at room temperature.

2.4. Results and Discussion

2.4.1. Morphological characterization of silica nanoparticles by SEM and TEM

One of the important aims of our work was to control the size of silica nanoparticles during the synthesis. For potential biomedical applications silica nanoparticles of small sizes are required [Usually, a small physical size of silica is desired for in vivo studies, because smaller particles may cause less perturbation (compared to similar particles of larger size) to the biological systems when inserted[13]]. The most important parameter involved in the production of these particles are the quantities of the reagents i.e. TEOS, ethanol, water and ammonium hydroxide solution. Varying each of these parameters one at a time would be inefficient and time consuming. However, monodispersed spherical silica nanoparticles with a size range of 20 to 52, 95, 210 and 410 nm were successfully prepared by controlled base hydrolysis of TEOS in ethanol and varying the ratio of the base to the silica precursor.

It was found that the particle size gradually increased when the added amount of ammonium hydroxide was increased. This may be seen counter initiative as it would be experienced that the number of nuclei per unit volume in the reaction increases with increasing the amount of ammonium hydroxide. However, ammonium hydroxide is the base catalyst for the hydrolysis as well as for the condensation of TEOS resulting in faster kinetics and consequently larger particle sizes.[14]

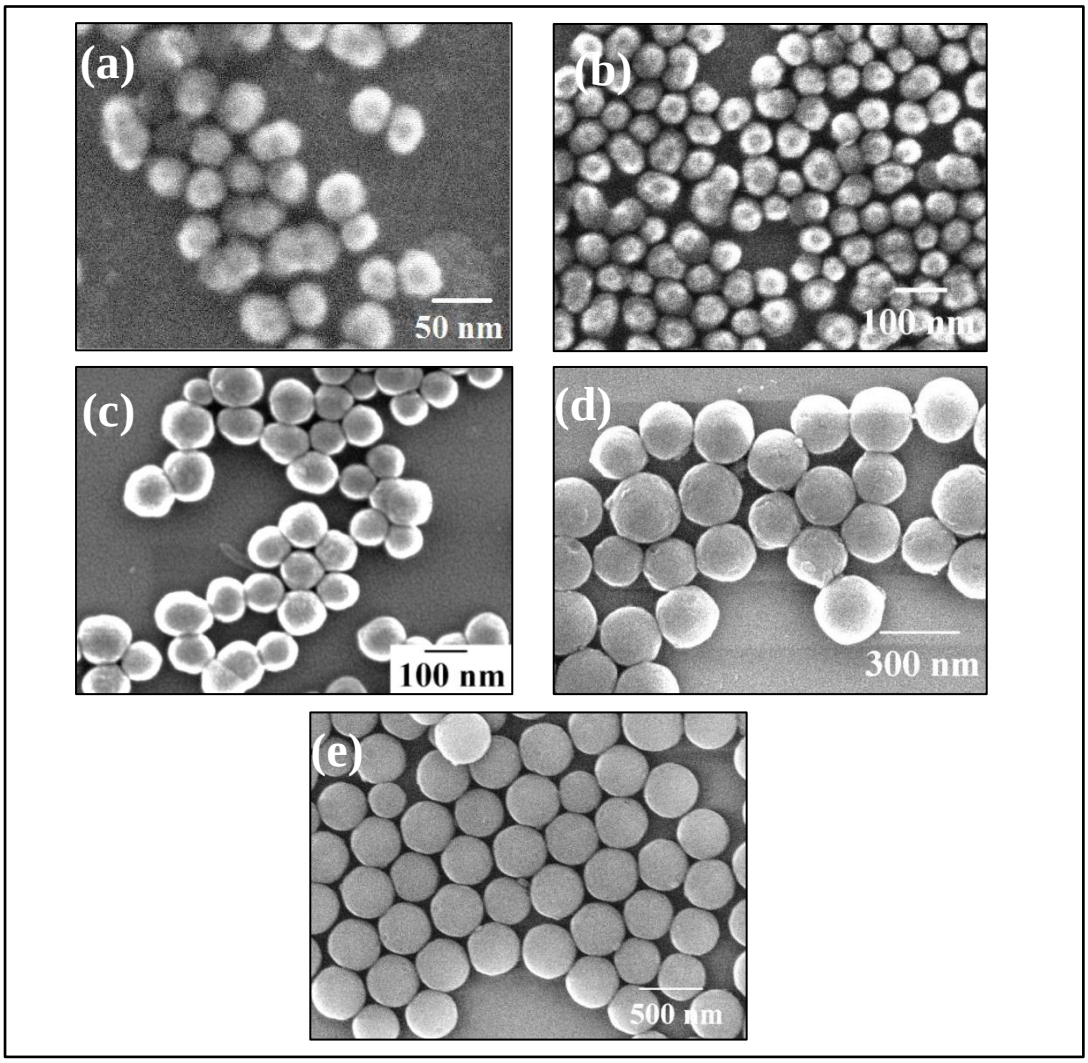

Figure 2.1. SEM images of silica nanoparticles (a) SiN20 (b) SiN52 (c) SiN95 (d) SiN210 and (e) SiN410.

In table 2.1, the experimental variation in ingredients is shown. In figures 2.1 and 2.3 indicative results of SEM and TEM analysis are provided. As stated above, the SEM (Figure 2.1) and TEM (Figure 2.3) observations indicated that the particle size was increased as the ratio of NH_3:TEOS increased from 2.22 to 8.86. Figure 2.4 shows the plot of particle size against the NH_3/TEOS ratio. Particle size distributions obtained from SEM images of the silica nanoparticles are shown in Figure 2.2 and indicate particles of good size monodispersivity. As can be seen in the figures and Table 2.1, the particle diameter of synthesized silica nanoparticles could be controllably varies from 20 nm to 410 nm without significant increase in the particle

size distribution. As shown in TEM micrographs (Figure 2.3), the silica nanoparticles showed a uniform spherical shape especially for the larger particles. This contrasts the SEM results which appeared to indicate almost polyhedral shapes (Figure 2.1) but this might be due to higher TEM resolutions.

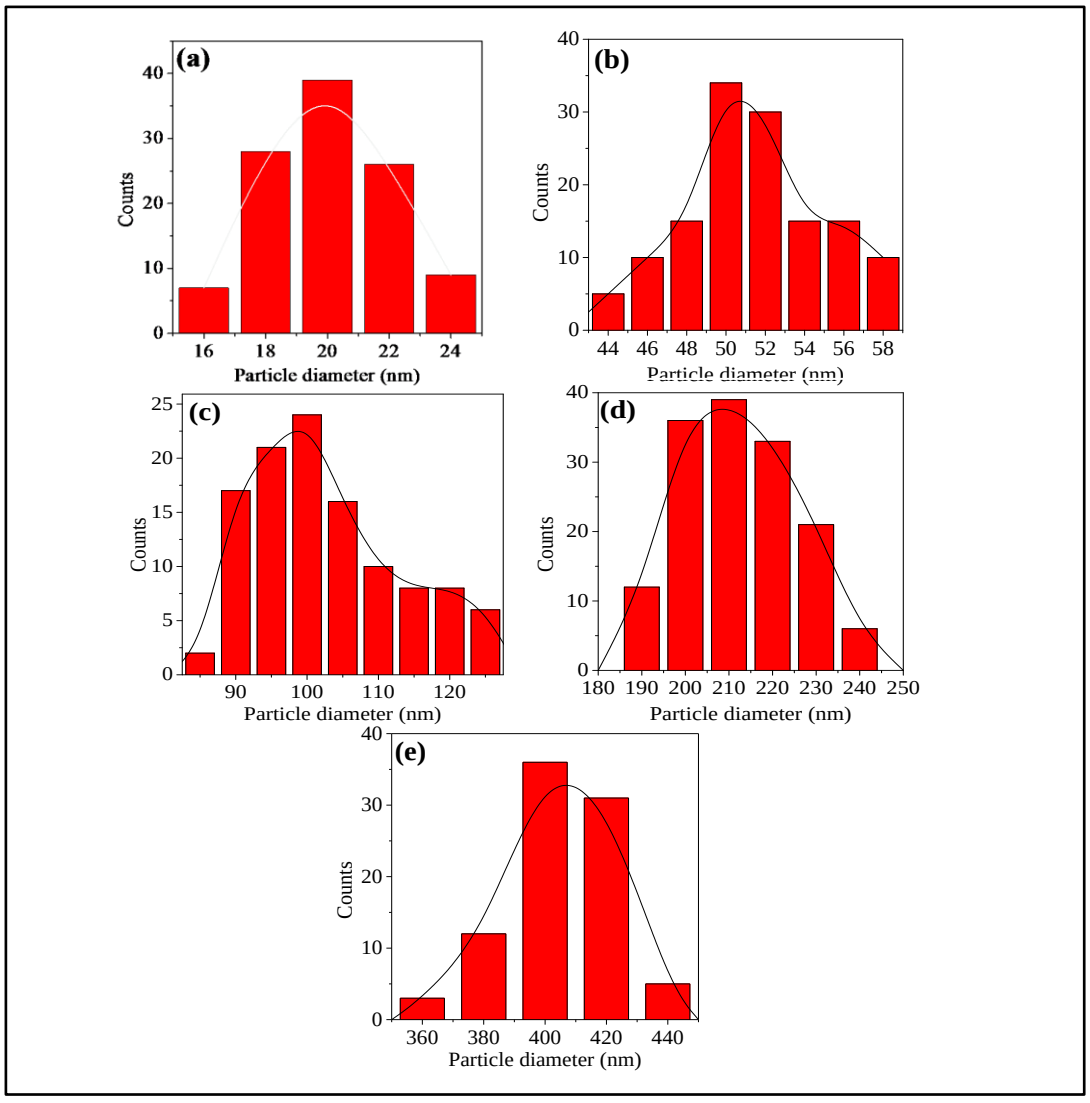

Figure 2.2. Particle size distribution of silica nanoparticles (a) SiN20 (b) SiN52 (c) SiN95 (d) SiN210 and (e) SiN410.

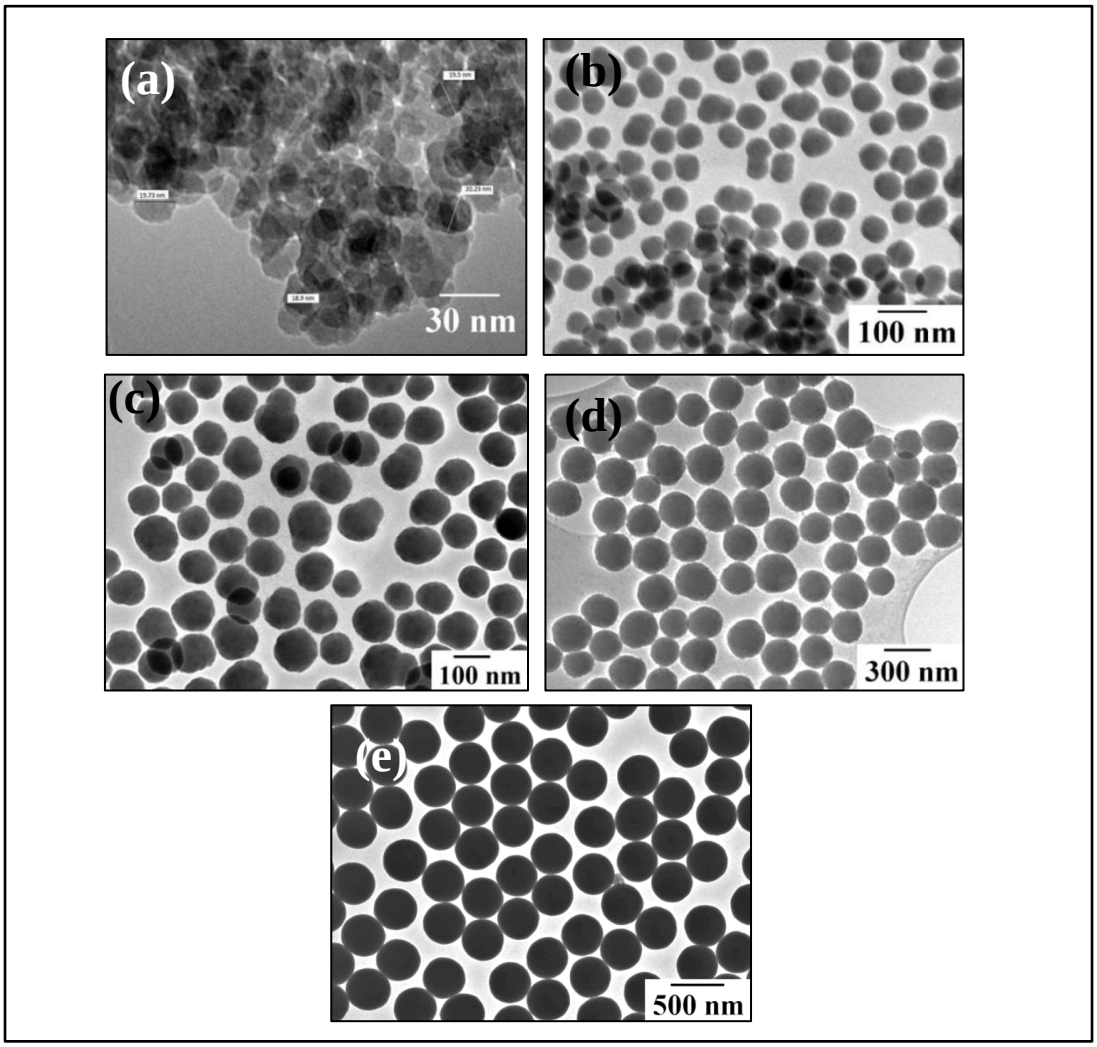

Figure 2.3. TEM images of the silica nanoparticles (a) SiN20 (b) SiN52 (c) SiN95 (d) SiN210 and (e) SiN410

Table 2.1. Different molar ratios of precursors to synthesis the silica nanoparticles

Sample	NH_3/ TEOS	NH_3/EtOH	Particle Size (nm)
SiN20	2.22	0.47	20
SiN52	3.55	0.75	52
SiN95	4.69	0.99	95
SiN210	7.92	1.15	210
SiN410	8.86	1.68	410

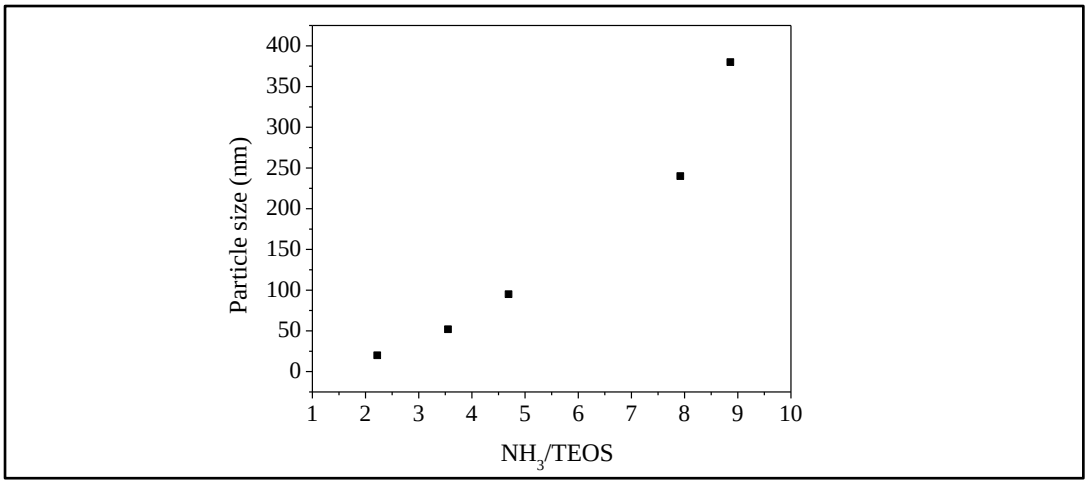

Figure 2.4. Plot of particle size vs the NH_3/TEOS ratio.

The surface area and porosity of the silica nanoparticles were characterized by nitrogen adsorption (Table 2.2). As can be seen in the table, as size increases the surface area and pore size decreases according to BET. The decrease in surface area is as expected from geometrical considerations.

If we assume that the number of particles in 1 g of a powder is:

$$\frac{1}{\frac{4}{3}(\pi r^3 p)} \qquad \text{Eq. 2.1}$$

where, p = density, r = radius of the particles. The surface area of 1 g of particles is given by:

$$4\pi r^2 \times \frac{1}{\frac{4}{3}(\pi r^3 p)} \qquad \text{Eq. 2.2}$$

The surface area can be estimated as:

$$\frac{3}{pr} \times 10^3 \qquad \text{Eq. 2.3}$$

This assumes the particles are dense and have a bulk density of 2.65 g cm^{-2}. The calculated (shown in brackets) and measured surface area of the particles is shown in table 2.2. The data are in good agreement suggesting that the particles are essentially non-porous in nature. This is supported by the SEM and TEM images that give little indication of pores. Since these might be expected to increase the surface area considerably. The calculated surface areas are somewhat higher at smaller

particle sizes but this may related to the slower growth kinetics which might allow some nuclei aggregation and resulting in trapped pore volume. This is indicated by the decrease in pore volume with increasing particle size. The decrease in pore size noted probably reflects only the packing of the particles and is related to the pore structure formed between the particles. As size increases, the particles became more regular in size and pack more efficiently decreasing the effective pore size.

Table 2.2. BET Surface Area, BJH Pore Volume and Pore diameter of each product

Sample	NH_3/ TEOS	BET surface area (m^2 g^{-1})	BJH pore volume (cm^3 g^{-1})	Pore diameter (Å)
SiN20	2.22	101 (114)	0.30	120
SiN52	3.55	64 (43)	0.13	96
SiN95	4.69	31 (24)	0.05	85
SiN210	7.92	8 (10.8)	0.01	77
SiN410	8.86	5 (5.5)	0.003	72

2.4.2. Functionalization of silica nanoparticles with fluorescent dyes

An extensive review of the synthesis procedures and methods for surface modification of fluorescent silica nanoparticles has been presented earlier.[9, 15] A wide variety of organic dye molecules, magnetic nanoparticles and luminescent quantum dots can be incorporated into the silica nanoparticles.[16, 17] The dyes can be added directly during the growth of the nanoparticles so that dyes can be simply physically trapped in the structure. Alternatively, the dyes can be added to previously synthesized silica nanoparticles to enable its binding to the surface of the silica matrix. We have used the second method to overcome dye leakage problem. To prevent dye leakage, we attached FITC molecules covalently to the silica nanoparticles via a stable thiourea linkage. To improve photostability of dye-doped silica nanoparticles, dye molecules should be well protected from oxygenated environment. Otherwise, photodegradation of dye molecules would occur in presence of oxygen molecules.[18] Thus, we prepared the fluorescent silica nanoparticles through a two-step process. In the first step, dyes were covalently attached to the coupling agent and in the second step, these activated fluorescent dye

conjugates were attached to as synthesized silica nanoparticles by impregnation of the dyes on the silica network via the formation of covalent bonds between the dye conjugates and a silane group of silica nanoparticles.[19-21]

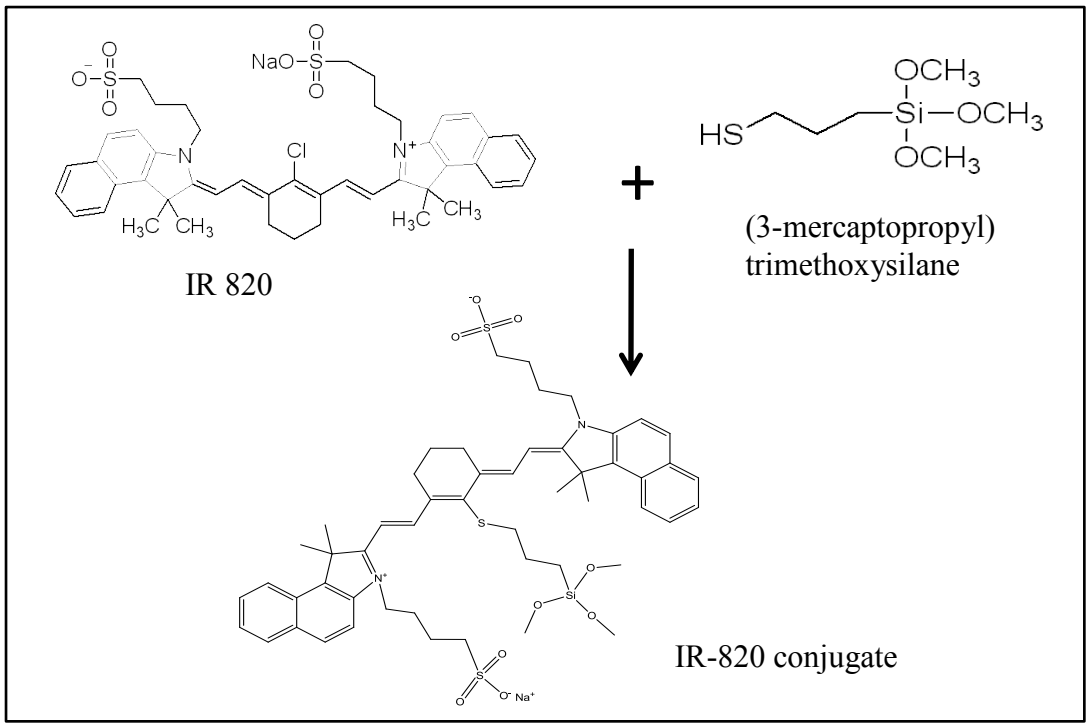

Scheme 2.1. Schematic representation of the nucleophilic reaction of IR-820 and (3-mercaptopropyl) trimethoxysilane.

Firstly, the dye IR-820 was covalently attached to the coupling agent (3-mercaptopropyl) trimethoxy silane in presence of DMF and triethyl amine (Scheme 2.1). Great care was used to exclude any water from the process in order to prevent hydrolysis and condensation of the (3-mercaptopropyl) trimethoxy silane molecules. This activated IR-820 conjugate was attached to as synthesized silica nanoparticles (SiN95) by simple impregnation method (Scheme 2.2). Once the dye molecules were trapped at the surface of the silica matrix, the nanoparticles were washed with acetone and water to remove any weakly attached materials. Samples were centrifuged to separate the dye-doped nanoparticles from the supernate that might contain free dye molecules that leached out from the particles during synthesis.

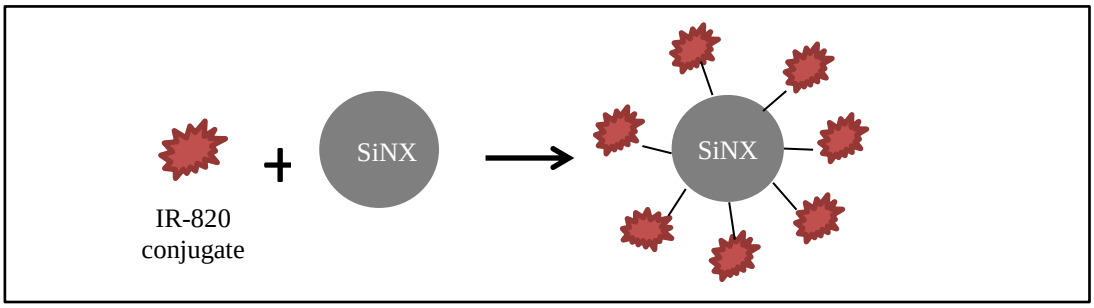

Scheme 2.2. Schematic representation of doping of IR-820 conjugate in silica nanoparticles

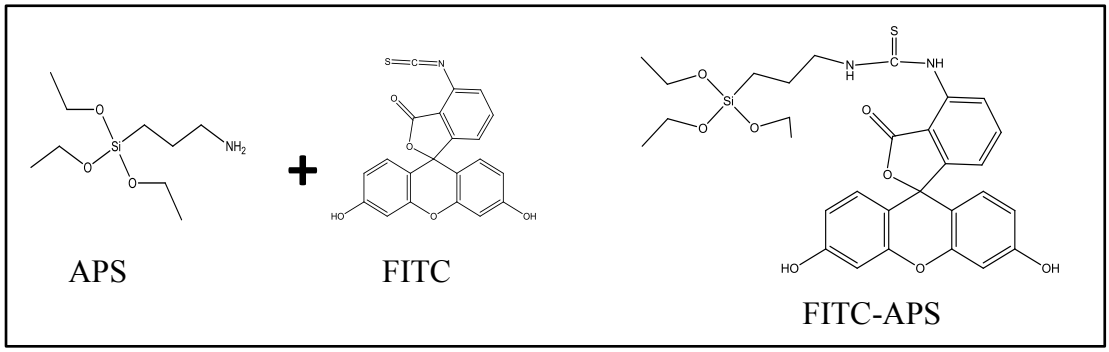

Scheme 2.3. Schematic representation of the nucleophilic reaction of FITC and APS

Scheme 2.3 shows the nucleophilic addition reaction of FITC and APS. The amine group of silane coupling agent (APS) reacts with the isothiocyanate group of FITC[22] to form N-1-(3-triethoxysilylpropyl)-N-fluoresceinyl thiourea. It showed a nucleophilic addition between the FITC and APS. The amino group of APS attacked the thioisocyanate group of FITC, which forms the Schiff base.[23] Water was excluded from this reaction to prevent hydrolysis and condensation of the APS molecules. This activated FITC-APS conjugate was attached to as synthesized silica nanoparticles (SiN95) by the simple impregnation method (Scheme 2.4).

These dye-doped silica nanoparticles also washed with water and acetone and centrifuged to remove the free dye molecules that leached out from particles. Fluorescein has very high molar absorptivity at the wavelength of the argon laser (488 nm) and it has a high quantum yield dye. Because of these attractive features, FITC has been very popular among organic-based dye and has been extensively used as a sensitive fluorescent label for the application of fluorescence and confocal

microscopy.[24-26] FITC has an excitation wavelength of 488 nm and emission wavelength of 525 nm (green). Recent years have seen many studies of fluorescent organic nanoparticles, among which dye-doped silica nanoparticles have potential application as fluorescence probes in various types of biological detection. The dye-doped silica nanoparticle traps a large number of fluorophores in the silica matrix, which produce a strong fluorescence when excited properly.

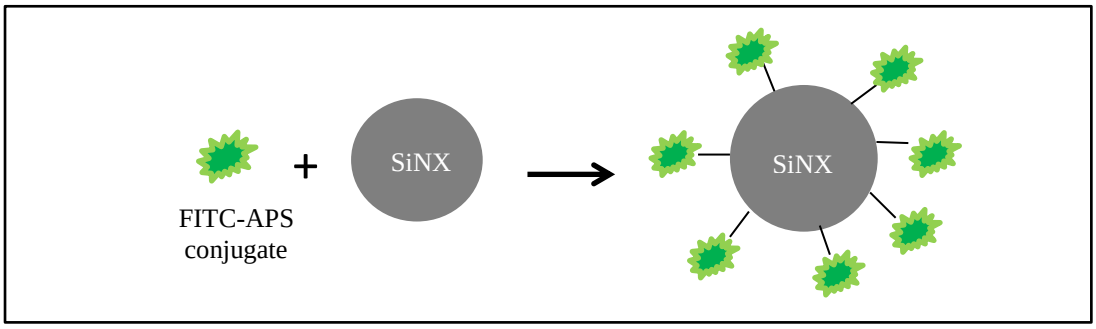

Scheme 2.4. Schematic representation of doping of FITC-APS conjugate in silica nanoparticles.

2.4.3. Stability of dye-doped silica nanoparticles

The samples for elution testing were prepared by taking 0.01 g of dye-doped silica nanoparticles (SiN95) in 10 ml of ethanol. The UV-Vis absorbance spectra of the dispersed dye-doped silica nanoparticles solution showed changes in the absorbed intensity after different aging time viz. 0 min, 4 h, 24 h, 4 days, 8 days and 1 month as shown in Figure 2.5 and Figure 2.6. A clear zero-sum increase-decrease relation of the absorbance intensity at 366 nm and 750 nm for IR-820 dye-doped silica nanoparticles has been observed. The decrease at 750 nm indicates the degradation of the IR-820 dye molecules in aqueous solution while the increase at 366 nm implies the formation of some new absorbers possibly due to intermolecular reactions. At the moment we have been unable to identify these species.

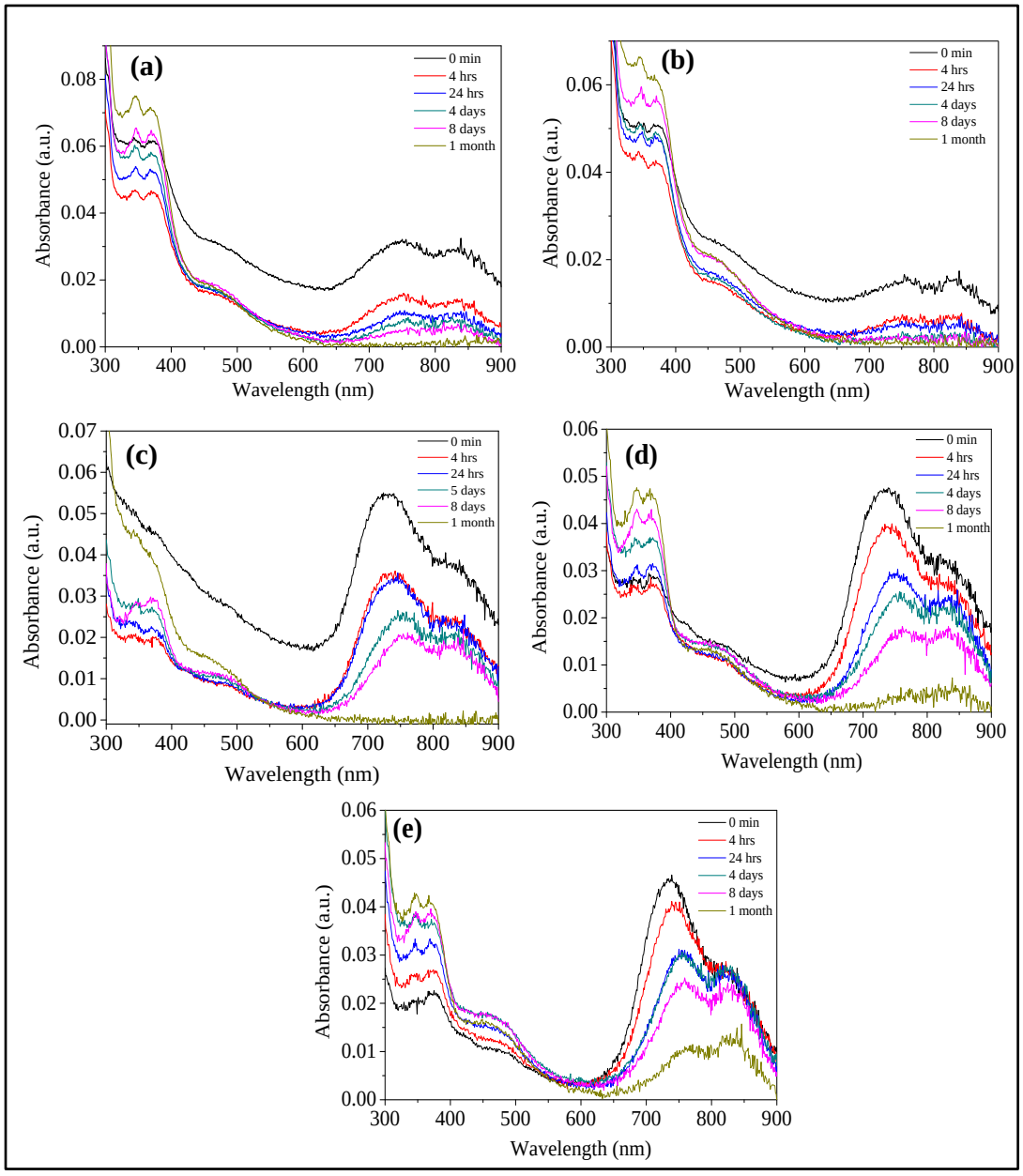

Figure 2.5. UV-Vis absorbance spectra of IR-820 dye-doped silica nanoparticles (a) SiN20 (b) SiN52 (c) SiN95 (d) SiN210 and (e) SiN410 with different aging time.

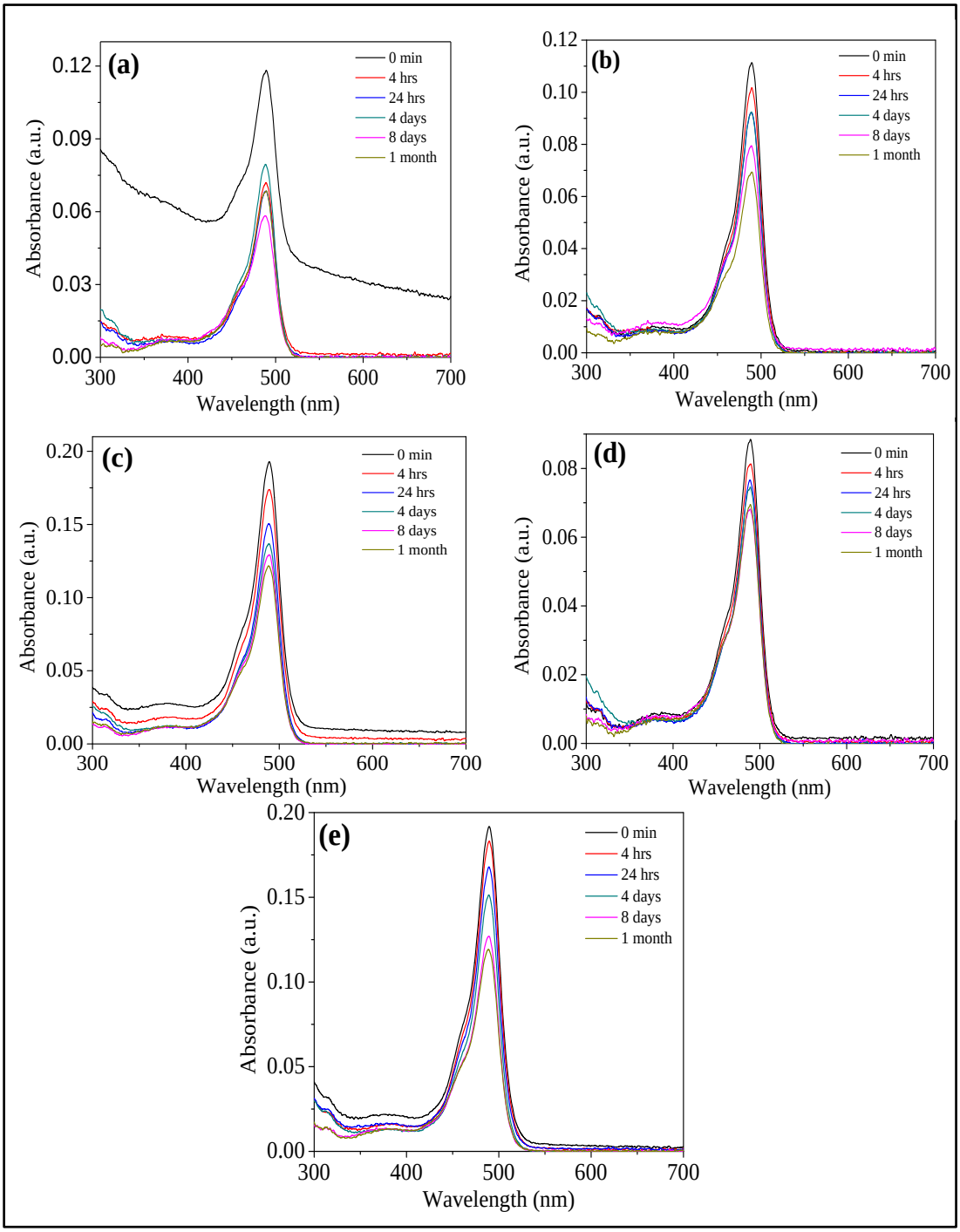

Figure 2.6. UV-Vis absorbance spectra of FITC dye-doped silica nanoparticles (a) SiN20 (b) SiN52 (c) SiN95 (d) SiN210 and (e) SiN410 silica nanoparticles with different aging time.

However, the feature absorbance peak of FITC at 490 nm is constant for all samples (Figure 2.6) indicating the FITC doped silica nanoparticles are more stable

than the IR-820 doped silica nanoparticles under the same conditions. The FITC dye has excitation and emission spectrum peak wavelengths of approximately 495 nm and 521 nm. The excitation spectra of FITC doped silica nanoparticles showed a peak at 492.3 nm and the emission spectra of FITC doped silica nanoparticles showed the peak at 518.6 nm when excited at 450 nm as shown in Figure 2.7. The excitation spectrum generally is identical to the absorption spectrum as the fluorescence intensity is proportional to the absorption.

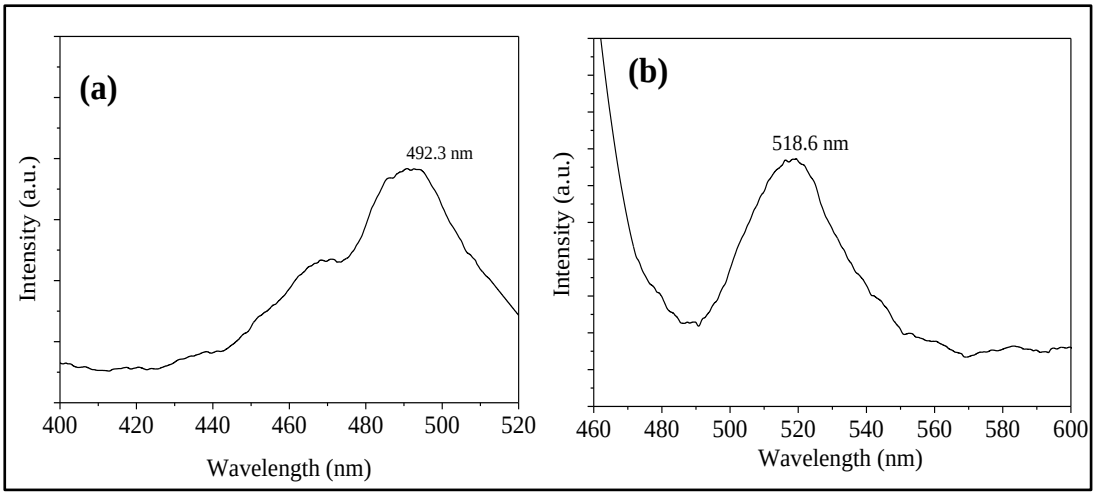

Figure 2.7. (a) Excitation spectra of FITC doped silica nanoparticles (SiN95). Emission wavelength was 520 nm (b) Emission spectra of FITC doped silica nanoparticles (SiN95). The excitation wavelength was 450 nm.

2.4.4. Dual dye-doped silica nanoparticles (FITC- IR820-SiO_2)

The fabrication of the FITC-IR820-SiO_2 nanoparticles was carried out by three steps: the synthesis of bare silica nanoparticles with tuneable size; the modification of dyes by reactive silanes and the graft of the bare nanoparticles by the modified dyes. The schematic representation for doping IR-820 and FITC dyes on silica nanoparticles (SiN95) are shown in Scheme 2.5.

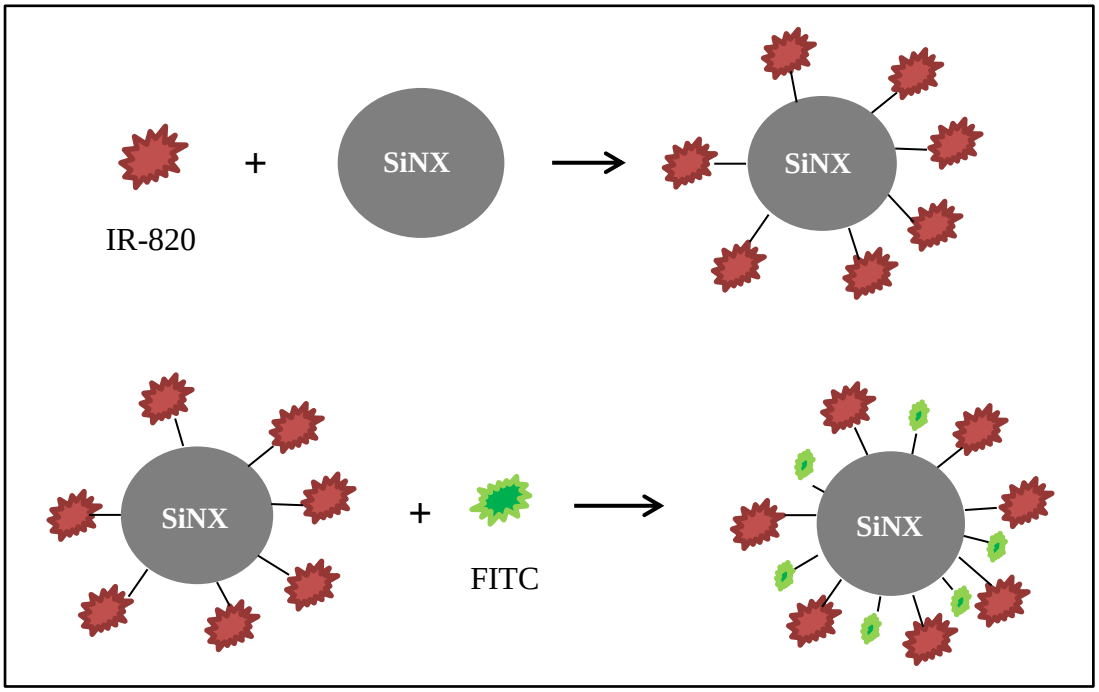

Scheme 2.5. Scheme for the silica nanoparticles (SiN95) grafted with dye combinations.

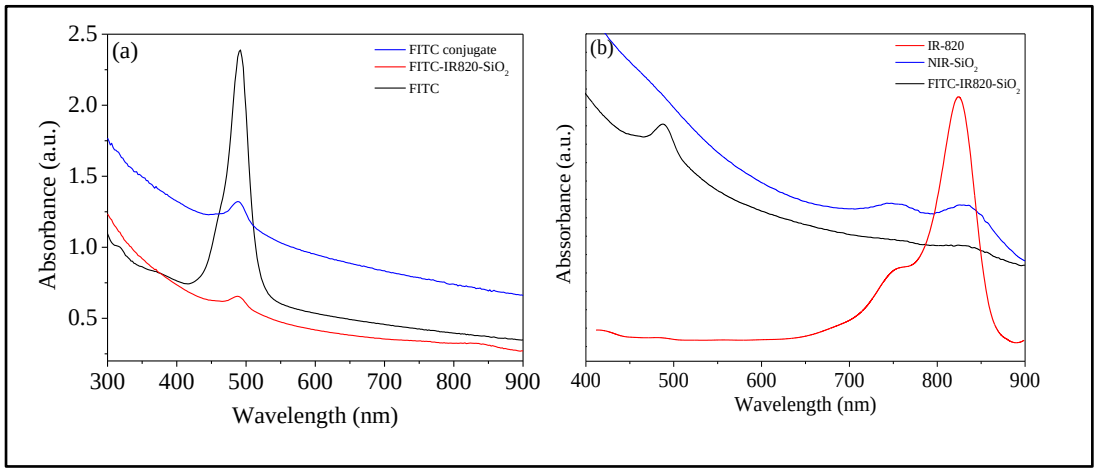

Figure 2.8. UV-Vis absorbance spectra of (a) FITC dye, dye conjugate and dual dye-doped silica nanoparticles (SiN95). (b) IR-820 dye, dye conjugate and dual dye-doped silica nanoparticles (SiN95).

The UV-Vis absorbance spectra (Figure 2.8) show the presence of both IR-820 and FITC dyes in the silica nanoparticles (SiN95). The peak at 495 nm is due to FITC dye and peak at 840 nm is due to IR-820 dye. This confirms that both the dyes are well incorporated at the surface of the silica nanoparticles.

2.4.5. Confocal laser scanning microscopic study of dual dye-doped silica nanoparticles

The novel fluorescent silica nanoparticles not only showed promise for material science but also could lead to a new class of fluorescence probes in biological imaging. The incorporation of dyes in to silica matrix was observed by using confocal laser scanning microscopy. Figure 2.9 shows that confocal laser scanning microscope images of dual dye-doped silica nanoparticles have excellent solubility and stability in water, ethanol and acetonitrile. Figure 2.9 clearly showed that the dye-doped silica had a strong green fluorescence when they excited at 488 nm and strong red fluorescence when they excited at 633 nm laser light. The synthesized fluorescent silica nanoparticles could be easily functionalized with different groups,[27] so it could also be further conjugated with a variety of biospecies.

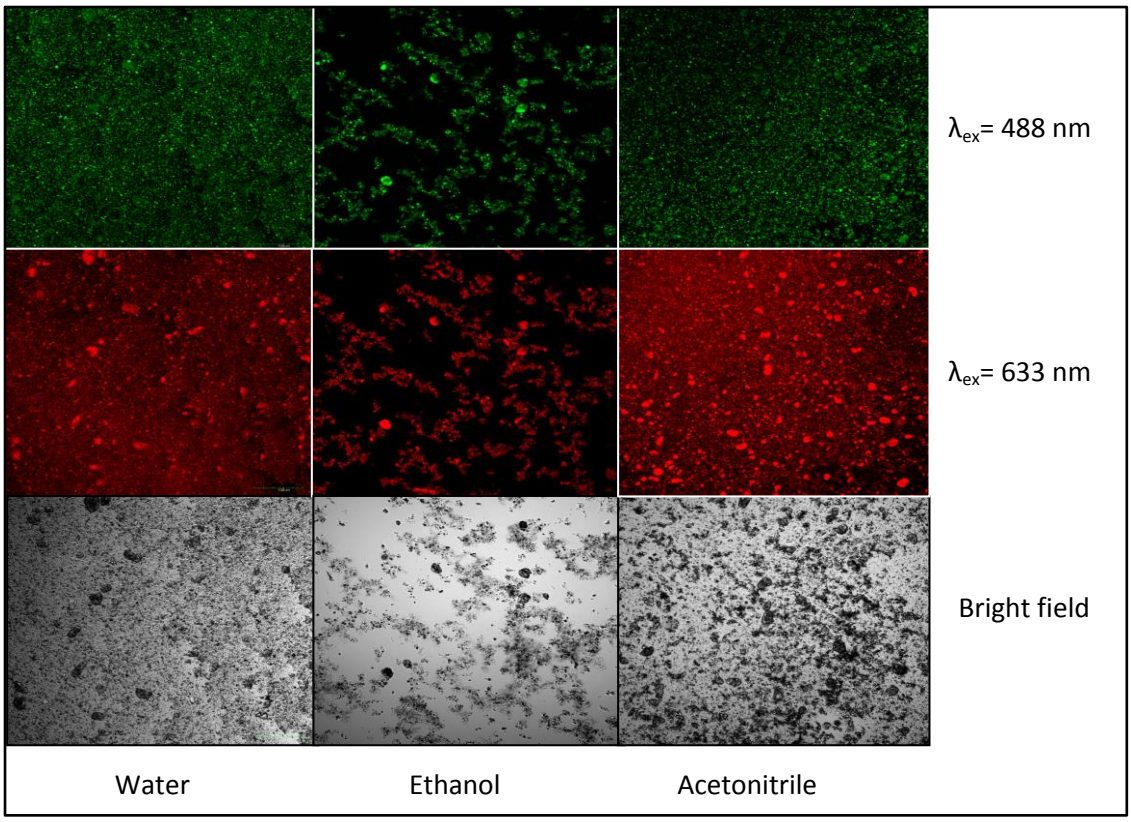

Figure 2.9. Confocal laser scanning microscope images of FITC-IR820-SiO_2 nanoparticles.

In figure 2.10, XY-Lambda scan shows a strong emission with a Stökes shift of 172 (660-488) nm and a weak emission with an unprecedented Stökes shift of 302 (790-488) nm in the dispersed FITC-IR820-SiO_2 nanoparticles in ethanol. However, standard data about the Stökes shift due to dye-doped silica nanoparticles is not known. A lambda scan records a series of individual images within a user-defined wavelength range; each image will be detected at a specific emission wavelength. This can be used to measure the emission spectrum of new fluorochromes or to determine the emission maximum of a fluorescent dye in a specific sample to optimize detection.

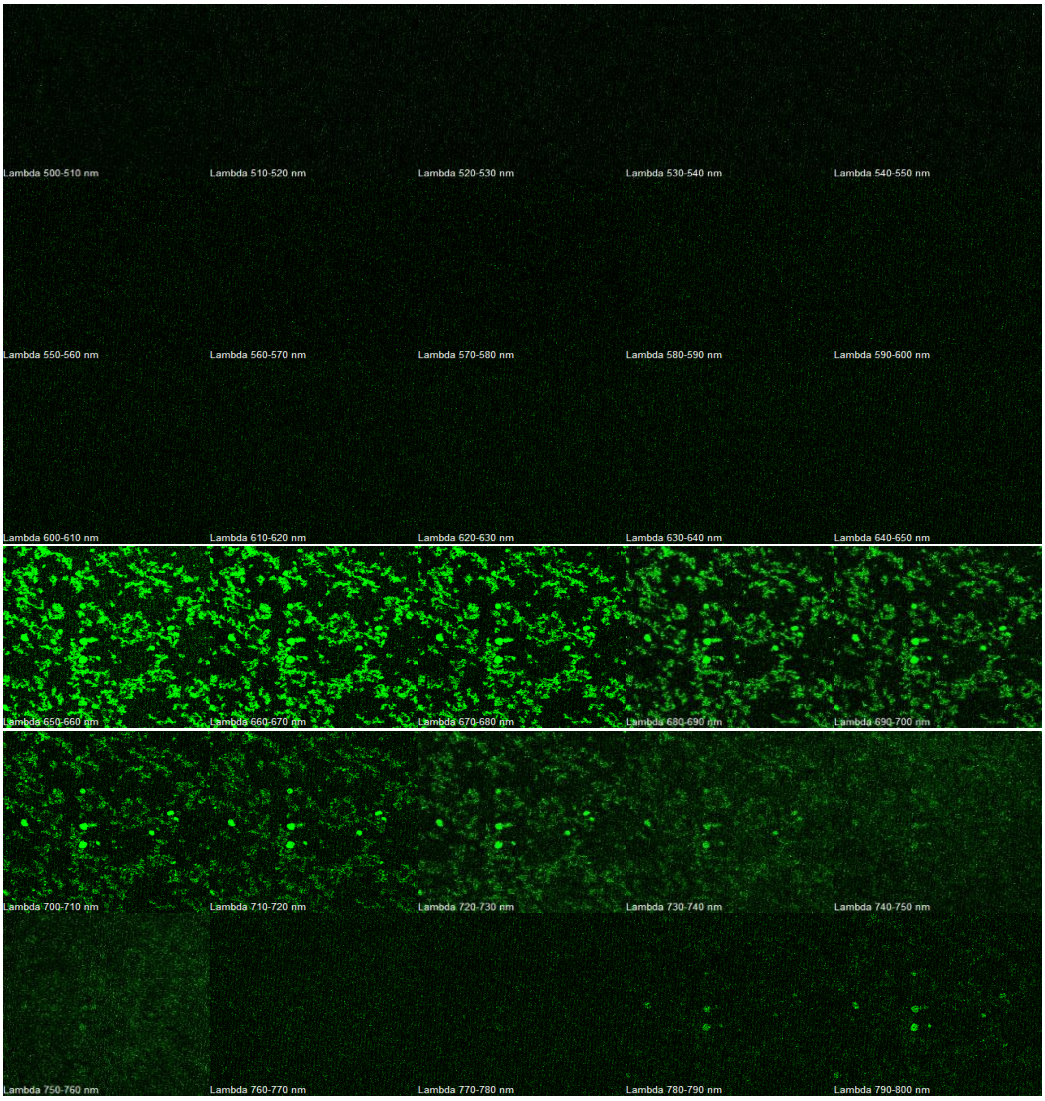

Figure 2.10. XY-Lambda scan emission images of dispersed FITC-IR820-SiO_2 nanoparticles in ethanol collected in different wavelength windows.

2.5. Conclusion

In this study, we have established a stable method to synthesize fluorescent dye-doped silica nanoparticles with different particle sizes. The method is relatively inexpensive. Also, a new type of dual dye-doped hybrid silica nanoparticles has been developed. The combination use of TEM, SEM, UV-Vis and confocal microscope shows the synthesis parameters have significant effects on the particle shape and size and the size is tuneable from a few nanometers to a few hundred nanometers. The ability to create size controlled nanoparticles with associated (optical) functionality may have significant importance in bio-medical imaging.

2.6. References:

1. C. Barbé, J. Bartlett, L. Kong, K. Finnie, H. Q. Lin, M. Larkin, S. Calleja, A. Bush and G. Calleja, *Adv Mater*, 2004, **16**, 1959-1966.
2. T. K. Jain, I. Roy, T. K. De and A. Maitra, *J. Am. Chem. Soc.*, 1998, **120**, 11092-11095.
3. G. Herbert, *J. Eur. Ceram. Soc.*, 1994, **14**, 205-214.
4. J. Lu, M. Liong, J. I. Zink and F. Tamanoi, *Small*, 2007, **3**, 1341-1346.
5. I. I. Slowing, B. G. Trewyn and V. S. Y. Lin, *J. Am. Chem. Soc.*, 2007, **129**, 8845-8849.
6. F. Torney, B. G. Trewyn, V. S. Y. Lin and K. Wang, *Nat. Nanotechnol.*, 2007, **2**, 295-300.
7. T. Deng, J.-S. Li, J.-H. Jiang, G.-L. Shen and R.-Q. Yu, *Adv. Funct. Mater.*, 2006, **16**, 2147-2155.
8. R. Kumar, T. Y. Ohulchanskyy, I. Roy, S. K. Gupta, C. Borek, M. E. Thompson and P. N. Prasad, *Acs Appl Mater Inter*, 2009, **1**, 1474-1481.
9. W. H. Tan, K. M. Wang, X. X. He, X. J. Zhao, T. Drake, L. Wang and R. P. Bagwe, *Med. Res. Rev.*, 2004, **24**, 621-638.
10. G. Yao, L. Wang, Y. Wu, J. Smith, J. Xu, W. Zhao, E. Lee and W. Tan, *Anal. Bioanal. Chem.*, 2006, **385**, 518-524.
11. J. E. Smith, L. Wang and W. Tan, *Trac-Trends in Analytical Chemistry*, 2006, **25**, 848-855.

12. W. Stober, A. Fink and E. Bohn, *J. Colloid Interface Sci.*, 1968, **26**, 62-69.
13. H. Xu, F. Yan, E. E. Monson and R. Kopelman, *J Biomed Mater Res A*, 2003, **66A**, 870-879.
14. T. Matsoukas and E. Gulari, *J. Colloid Interface Sci.*, 1988, **124**, 252-261.
15. L. Wang, W. Zhao and W. Tan, *Nano Research*, 2008, **1**, 99-115.
16. A. Guerrero-Martinez, J. Perez-Juste and L. M. Liz-Marzan, *Adv Mater*, 2010, **22**, 1182-1195.
17. S. Giri, B. G. Trewyn and V. S. Y. Lin, *Nanomedicine*, 2007, **2**, 99-111.
18. S. Santra, B. Liesenfeld, C. Bertolino, D. Dutta, Z. H. Cao, W. H. Tan, B. M. Moudgil and R. A. Mericle, *J. Lumin.*, 2006, **117**, 75-82.
19. L. M. Rossi, L. F. Shi, F. H. Quina and Z. Rosenzweig, *Langmuir*, 2005, **21**, 4277-4280.
20. W. Lian, S. A. Litherland, H. Badrane, W. H. Tan, D. H. Wu, H. V. Baker, P. A. Gulig, D. V. Lim and S. G. Jin, *Anal. Biochem.*, 2004, **334**, 135-144.
21. A. Imhof, M. Megens, J. J. Engelberts, D. T. N. de Lang, R. Sprik and W. L. Vos, *J. Phys. Chem. B*, 1999, **103**, 1408-1415.
22. A. Vanblaaderen and A. Vrij, *Langmuir*, 1992, **8**, 2921-2931.
23. N. Zhang, E. Ding, X. Feng, Y. Xu and H. Cai, *Colloids and Surfaces B-Biointerfaces*, 2012, **89**, 133-138.
24. A. Vanblaaderen, A. Imhof, W. Hage and A. Vrij, *Langmuir*, 1992, **8**, 1514-1517.
25. M. Strathmann, J. Wingender and H. C. Flemming, *J Microbiol Methods*, 2002, **50**, 237-248.
26. S. Bancel and W. S. Hu, *J. Ferment. Bioeng.*, 1996, **81**, 437-444.
27. S. Santra, H. Yang, D. Dutta, J. T. Stanley, P. H. Holloway, W. H. Tan, B. M. Moudgil and R. A. Mericle, *Chem. Commun. (Cambridge, U. K.)*, 2004, 2810-2811.

Chapter 3

Defect chemistry and vacancy concentration of luminescent europium doped ceria nanoparticles by solvothermal method

3.1. Abstract

Pure phase and europium doped ceria nanocrystals have been synthesized by a single step, simple solvothermal process. Different spectroscopic, diffractive and microscopic techniques were used to determine the morphology, size, crystal structure and phase of all the samples. Electron energy loss spectroscopy (EELS) for elemental mapping confirmed that good solid solutions were formed and that the particles had a homogeneous distribution of europium. The defect chemistry was more complex than might be expected with the incorporation of two Eu^{3+} ion resulting in the production of an anion vacancy since the doping results in charge compensating (i.e. for Eu^{3+}) anion vacancies as well as vacancies due to oxygen removal from the crystalline surface. Variations in nanoparticle dimension and lattice parameters were measured as a function of dopant concentrations and their variations explained. The band gap of the samples could be tailored by the doping. The doped samples were found to be luminescent due to the substitution of Ce^{4+} ions in the cubic symmetric lattice by the dopant ions. The thermal stability of the fluorescence properties was also investigated.

3.2. Introduction

Nanostructures of rare-earth cerium oxide (CeO_2) have been widely investigated because of its multiple applications in areas such as catalysis,[1] an electrolyte for solid oxide fuel cells,[2] UV absorbent and UV filter materials,[3] oxygen gas sensors,[4] polishing materials,[5] optical devices[6] and biomedicine.[7] CeO_2 has unique properties such as high refractive index, optical transparency, high dielectric constant, lattice expansion, stability at high temperature and mechanical robustness. Its applications generally take advantage of the excellent redox properties and high oxygen storage capacity (OSC) of CeO_2. This redox chemistry is, in part, related to the similar energy of the 4f and 5d electronic states and a low potential energy barrier to electron exchange between them.[8] In principle, the different electron configurations possible can be determined by core and valence level spectroscopies.[9] The properties of CeO_2 are thought to be controlled by the nature of the oxygen vacancies because oxygen diffusion depends on the type, size and concentration of those vacancies.[10] Therefore, numerous investigations have been conducted to study

the Ce^{3+} and O vacancy defect sites in CeO_2 using techniques including x-ray photoelectron spectroscopy (XPS), x-ray diffraction (XRD), electron paramagnetic resonance (EPR), scanning tunnelling microscopy (STM), Raman spectroscopy and neutron scattering.

There have been numerous attempts to optimize the physiochemical properties of CeO_2 by inclusion of metallic cation dopants which can control the anion vacancy and Ce^{3+} cation concentrations.[11] Doping can improve the sintering properties of CeO_2, by stabilizing the CeO_2 surface area and crystallite size.[12] Doping with divalent and trivalent dopants leads to formation of oxygen vacancies and modification of oxygen mobility and ionic conductivity.[13] Unsurprisingly, this is reflected in changing the redox properties and oxygen storage capacity of the CeO_2. CeO_2 is a potentially important material in optical and optoelectronic applications but exhibits weak emission characteristics that limit its performance.[14] Doping with lanthanide cations such as europium (Eu) can enhance the visible emission of CeO_2 nanoparticles through an increase in the concentration of oxygen vacancies.[15, 16] Europium is a convenient dopant since the ionic radius of the trivalent europium[17] (0.1066 nm) is between that of Ce^{3+} (0.1143 nm) and Ce^{4+} (0.097 nm) and this allows for extensive solubility in the CeO_2 fluorite structure. The Eu^{3+}/Eu^{2+} redox pair has a potential of about 0.36 V and is expected to create and stabilize the oxygen vacancies for low Eu^{3+}/Ce atomic ratios.[18] This property promotes charge transfer from oxygen ions through the lattice oxide and provides the material with high oxygen ion conductivity.[19] If energy is transmitted from this charge transfer state to lanthanide ions characteristic emissions are expected to be observed.[20]

As the morphological properties of CeO_2, such as the particle size, shape and specific surface area, usually determine the performance, various synthetic methods, such as co-precipitation,[21, 22] microemulsion,[23] flow,[24] reverse precipitation,[23] sol–gel processes[25] and electrochemical routes,[26] have all been used to prepare ultrafine CeO_2 powder with controlled dimension. Several precipitants and surfactants have also been used to control the particle size and homogeneity such as ammonium hydroxide, urea and ammonium hydrogen carbonate. However, through all of the

above methods, nanocrystalline CeO_2 is more difficult and inconvenient to obtain; calcination is usually necessary for the crystallization of amorphous samples and/or the removal of the surfactants. It is also difficult to synthesize highly uniform and well-dispersed nanocrystalline CeO_2 on the basis of the following reasons. Firstly, it is not easy to choose the appropriate precursor complexes and the crystalline temperatures for rare-earth oxides are relatively high. Second, the agglomeration of nanocrystals is very common because the nanocrystals tend to decrease the exposed surface to lower the surface energy.[27] Solvothermal methods[28, 29] that do not involve catalysts, surfactants or templates provides a more promising option for the large scale production of high purity nanoparticles as they are simple, fast and less expensive. Moreover, solvothermal method possesses advantages of being single step, low temperature, controlled composition and morphology as well as being less sensitive to particulate aggregation and producing crystalline nanocrystals.

Interestingly, despite the wealth of work, in many cases, the understanding of the defect science in many systems is only poorly understood. The role of anion defects to charge compensate low valency cations in the CeO_2 lattice is accepted but the role of dopants and their effect on neighbouring cerium cations is less clear and this paper reveals an interesting relationship. Here, different concentrations of europium ions were successfully introduced into the cubic phase CeO_2 lattice using solvothermal techniques. In our previous work,[30] a detailed study was carried out to investigate the defect structure and dynamics of Eu doped ceria nanoparticles by using positron annihilation spectroscopy. Here, this work is extended to study the defect chemistry by different spectroscopic techniques and EELS was used to study the concentration and distribution of the dopant ions. Additionally, the morphological and structural evolution and optical properties were correlated as a function of concentrations of europium doping as well as with further annealing.

3.3. Experimental section

3.3.1. Materials

Europium (III) nitrate pentahydrate [$Eu(NO_3)_3.5H_2O$, 99.999%], cerium (III) nitrate hexahydrate [$Ce(NO_3)_3.6H_2O$, 99.999%], anhydrous ethanol (≥99.9%),

absolute ethanol (≥99.8%) and 28% aqueous ammonia were purchased from Sigma-Aldrich and used as received.

3.3.2. Synthesis of Europium doped CeO_2 nanoparticles

For the solvothermal synthesis of the CeO_2 nanoparticles, a closed cylindrical Teflon lined stainless steel chamber with 45 ml capacity was used. 0.1 M (1.52 g) of $Ce(NO_3)_3.6H_2O$ and an appropriate amount of ammonium hydroxide (1-2 g) were dissolved in 35 ml of anhydrous ethanol in a Teflon bottle. This mixture was stirred for 5 min to which was added different concentrations of $Eu(NO_3)_3.5H_2O$ (0.3-50 atom% relative to cerium). The solution was stirred for another 15 min with the formation of milky slurry. Subsequently, the closed Teflon chamber was transferred into a preheated oven and was subjected to solvothermal treatment at 180 °C for 12 h. Yellow precipitates were collected, washed with deionized water and absolute ethanol several times by centrifugation, followed by drying at 50 °C in air overnight. Samples with varying concentrations of europium are represented as CEEUX, where X = 0, 0.2, 0.8, 1.5, 3.9, 7.6, 13.9, 19.2, 24.6 and 29.2 are the determined atom % of Eu.

3.4. Results and Discussion

3.4.1. Dopant ion concentration by TXRF

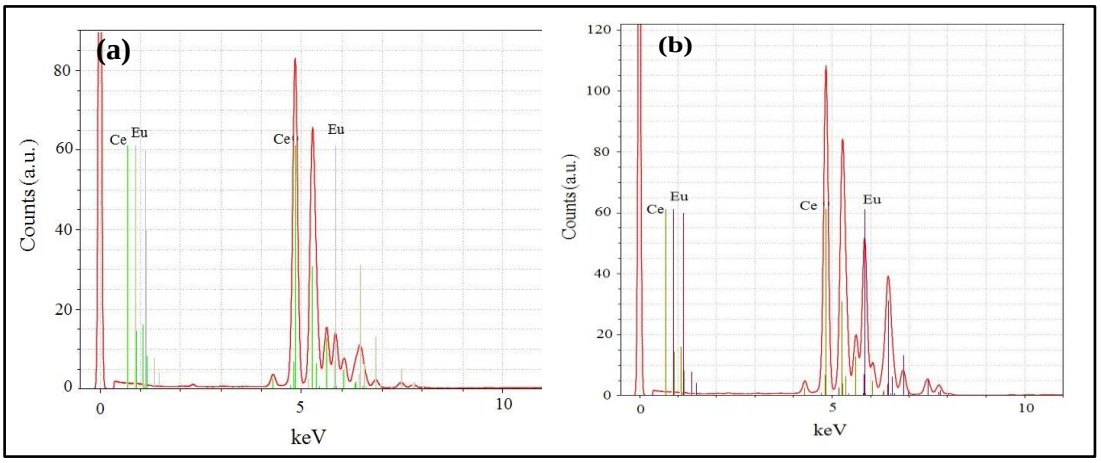

Figure 3.1. Typical TXRF graphs of europium doped ceria nanoparticles showing line positions. (a) CEEU7.6 (b) CEEU19.6

The presence and the actual concentrations of europium ions in the cerium oxide powder was confirmed by TXRF (figure 3.1) and summarized in Table 3.1. In all samples, the actual incorporation of europium concentration was found to be lower than that of added during synthesis. This is normal and is explained by lower solubility of the europium cations in basic conditions.

Table 3.1. Dopant concentration added in solution and actual concentration in solid measured by TXRF

Sample	Europium in solution (atom %)	Europium in solid (atom %)
CEEU0.2	0.3	0.2
CEEU0.8	1	0.8
CEEU1.5	2	1.5
CEEU3.9	5	3.90
CEEU7.6	10	7.62
CEEU13.9	20	13.94
CEEU19.2	30	19.23
CEEU24.6	40	24.58
CEEU29.2	50	29.23

3.4.2. Structural characterization by XRD

Crystal structures of the as-prepared samples were determined from the XRD patterns shown in Figure 3.2 (a). XRD patterns exhibit x-ray diffraction peaks which can be indexed to a cubic fluorite phase (JCPDS no. 04-0593) of ceria. The strongest XRD peak for all the samples was ascribable to the (111) plane of cubic CeO_2. The relative peak intensity of the remaining lattice planes varied with the change in doping concentrations. The existence of higher order features indicates good solid solutions were formed throughout the composition range. The broad nature of the peaks reveals the nanocrystalline nature of the samples. The patterns did not show any extra peaks, indicating that the samples are good solid solutions and there is no secondary phase indicative of the formation of europium oxides.

The crystallite size was estimated from XRD peak broadening using the Scherrer equation,

$$d = \frac{0.9\lambda}{\beta \cos\theta} \qquad \text{Eq. 3.1}$$

where *d* is the crystallite size, λ is the wavelength of Cu Kα radiation, β is the full-width at half maximum (FWHM) of the diffraction peak and θ is the diffraction angle.

Figure 3.2b (i) shows the variation of crystallite size with doping concentrations. A sharp decrease in the crystallite size was observed with increasing the doping concentration up to 7.6 % and becomes almost constant with further doping. The decrease in crystallite size suggests that the dopant introduces significant lattice strain (the ionic radius of Eu^{3+} (0.107 nm) is about 10 % larger than that of Ce^{4+} (0.097 nm)[31]) and this reduces ion transport and sintering as noted previously for doped CeO_2.[32] The measured lattice parameter of undoped CeO_2 was found to be 0.542 nm somewhat higher than that reported for bulk CeO_2 (0.541 nm) but may be due to lattice expansion due to the presence of anion vacancies resulting from the preparation.[23]

Figure 3.2b (ii) shows the variation of lattice parameters with doping concentrations. An initial decrease in the lattice parameter was observed with increase in europium doping up to 1.5 % but increases upon further doping. The expansion of the lattice with increasing dopant concentration is consistent with the substitution of the smaller Ce^{4+} ions by the larger Eu^{3+} ions. A similar trend was reported due to the incorporation of another trivalent dopant Gd^{3+} in ceria as the ionic radius of Gd^{3+} is 0.1053 nm, higher than that of Ce^{4+} ions.[33, 34] The increase in lattice parameter is mirrored by the decrease in crystallite size almost exactly confirming the relationship of these two effects. The relationship of both parameters is not linearly dependent on the dopant concentration but, rather, tends towards a limiting value.

This is not consistent with a random substitution of CeO_2 cations with europium cations and suggests this is at least a locally ordered arrangement. The

small but reproducible decrease in the lattice parameter at low dopant concentrations is consistent with a surface-tension type effect at very small crystallite sizes as discussed by us previously.[23] It is asserted that as the crystallite size decreases very rapidly at low dopant concentration, the lattice contraction due to surface tension exceeds the small expansion due to europium addition. Table 3.2 summarizes the variation of crystallite size, lattice parameters and lattice strains with europium concentrations.

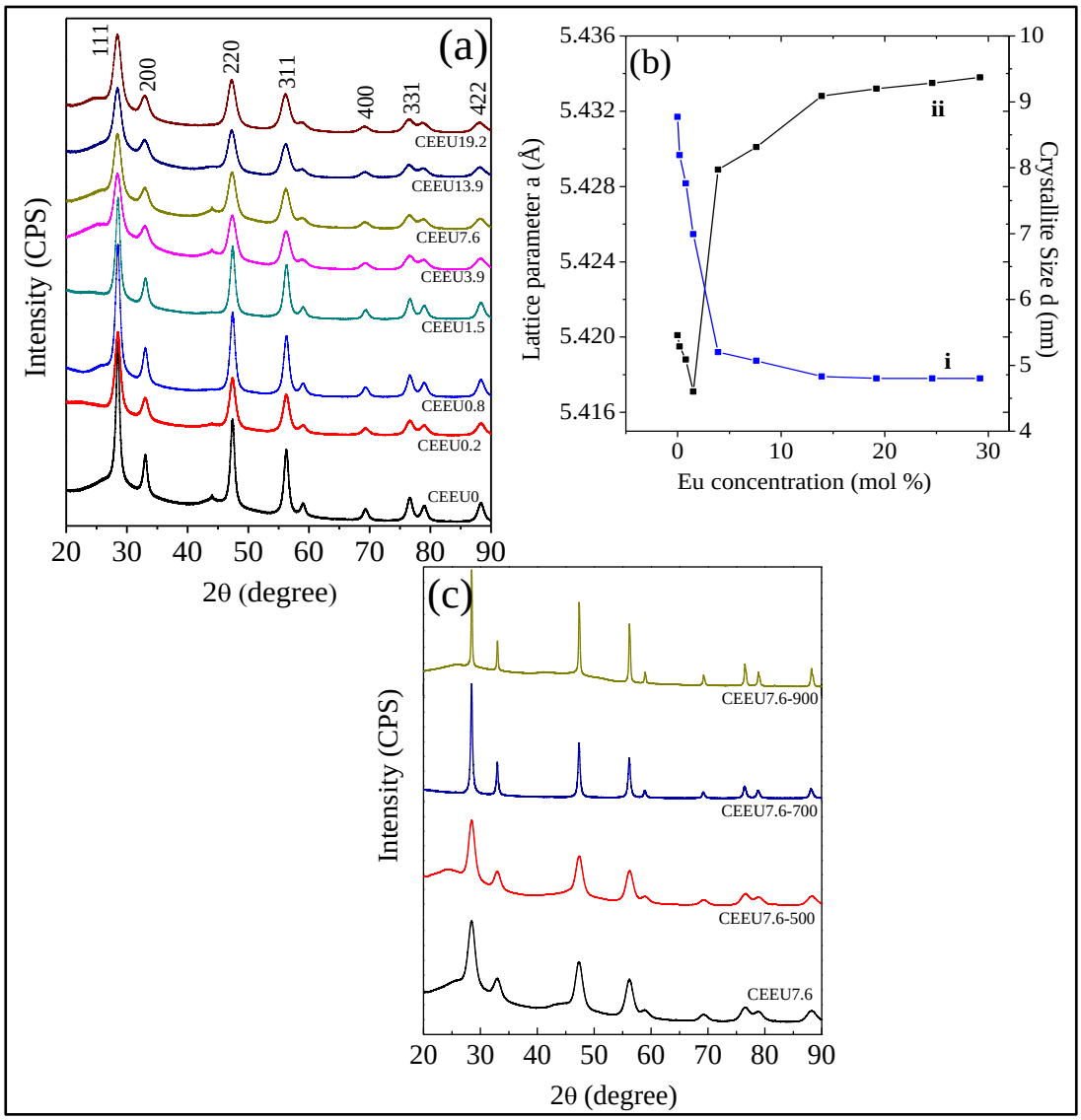

Figure 3.2. (a) XRD spectra of undoped and Europium doped cerium oxide samples (b) Crystallite size [i] and lattice parameter [ii] variation with increase in Europium concentration. (c) XRD spectra of CEEU7.6 sample annealed at different temperatures.

The as-synthesized samples were annealed at different temperatures to study structural evolution. Figure 3.2 (c) shows illustrative XRD patterns of CEEU7.6 annealed at different temperatures. As above, only the fluorite structure was present in all scans suggesting good solid solutions were formed at all temperatures. The existence of small amounts of europium oxide could be dispersed at the surface of CeO_2. The XRD reflections peak widths and the background signal reduce as the calcination temperature is increased consistent with grain coarsening. Table 3.2 summarizes the variation of crystallite size, lattice parameters and lattice strains for sample CEEU7.6 annealed at different temperatures.

Table 3.2. Variation of particle size, band gap, Ce^{3+} ions concentration, lattice parameter and strain measurements with different europium concentrations and annealed ceria nanoparticles

Sample	Eu in solid sample (atom %)	Particle size (nm)	Band gap (eV)	Ce^{3+} (%)	Lattice parameter α (Å)	Strain (10^{-3})
CEEU0	Undoped	8.77	3.34	0	5.4201	1.65
CEEU0.2	0.2	8.19	3.26	-	5.4195	1.68
CEEU0.8	0.8	7.76	3.21	-	5.4188	1.75
CEEU1.5	1.5	6.99	3.17	1	5.4171	1.91
CEEU3.9	3.9	5.2	3.13	4	5.4289	3.26
CEEU7.6	7.6	5.07	3.11	7	5.4301	3.49
CEEU13.9	13.9	4.83	3.07	14	5.4328	3.98
CEEU19.2	19.2	4.8	3.05	19	5.4332	4.06
CEEU24.6	24.6	4.8	3.03	24	5.4335	4.58
CEEU29.2	29.2	4.8	3.02	29	5.4338	5.07
CEEU7.6-500	7.6	5.31	3.12	5	5.4270	2.89
CEEU7.6-700	7.6	9.48	3.17	4	5.4249	2.29
CEEU7.6-900	7.6	27.23	3.30	4	5.4211	1.81

3.4.3. Composition and Oxidation state determination by XPS

XPS was used to study composition and valence states of the undoped and doped samples. Representative survey spectra of the CEEU0 and CEEU7.6 samples reveal the presence of cerium, oxygen and carbon as well as europium for the doped samples (Figure 3.3 a). There is a significant carbon content which is typical of adventitious carbon arising from atmospheric exposure. No other significant contamination was detected. The Ce3d photoelectron spectra of cerium compounds can be used to identify cerium valence states but this is notable as the spectra are complicated because of final state effects on the hybridization of the Ce4f orbitals with O2p orbitals and fractional occupancy of the valence 4f orbitals.[35, 36] Because of these effects, electron transfer from O2p to Ce4f orbitals can occur during photoemission giving rise to the appearance of multiple oxidation states. Thus, the Ce $3d_{5/2}$ photoelectron spectrum has three principle features (for each spin-orbit doublet) in the case of CeO_2 and two for Ce_2O_3.[37]

In this way, a mixed valence sample can contain ten peaks altogether for overlapping Ce $3d_{5/2}$ and Ce $3d_{3/2}$ spin-orbit bands.[38] These peaks are usually described by nomenclature developed by Burroughs *et al*.[39] U, $U^{//}$, $U^{///}$ and V, $V^{//}$, $V^{///}$ (note states labelled U or V refer to $3d_{3/2}$ and $3d_{5/2}$ respectively) are characteristic of Ce(IV)3d final states; while U_0, $U^{/}$ and V_0, $V^{/}$ refer to Ce(III) 3d final states. The high binding energy doublet $V^{///}/U^{///}$ at 898.2 eV and 916.4 eV are assigned to a Ce(IV) final state of $3d^94f^0O2p^6$. Doublets $V^{//}/U^{//}$ at 888.4 eV and 907.6 eV were attributed to the hybridization state of Ce(IV)$3d^94f^1O2p^5$ and doublets V/U at 882.3 eV and 901.1 eV correspond to the state of Ce(IV)$3d^94f^2O2p^4$. Doublets $V^{/}/U^{/}$ and V_0/U_0 are due to a mixture of Ce(III)$3d^94f^2O2p^4$ and Ce(III)$3d^94f^1O2p^5$ configurations at 886 eV, 904.6 eV and 880.3 eV, 899.2 eV respectively.[40] By comparison to previous work it can be concluded that the Ce3d spectrum for the undoped sample indicates it is essentially a stoichiometric CeO_2 structure (Figure 3.3.b). The Ce3d photoelectron spectra for the doped samples exhibits features which can be assigned to the presence of Ce(III) states (Figure 3.3.b).

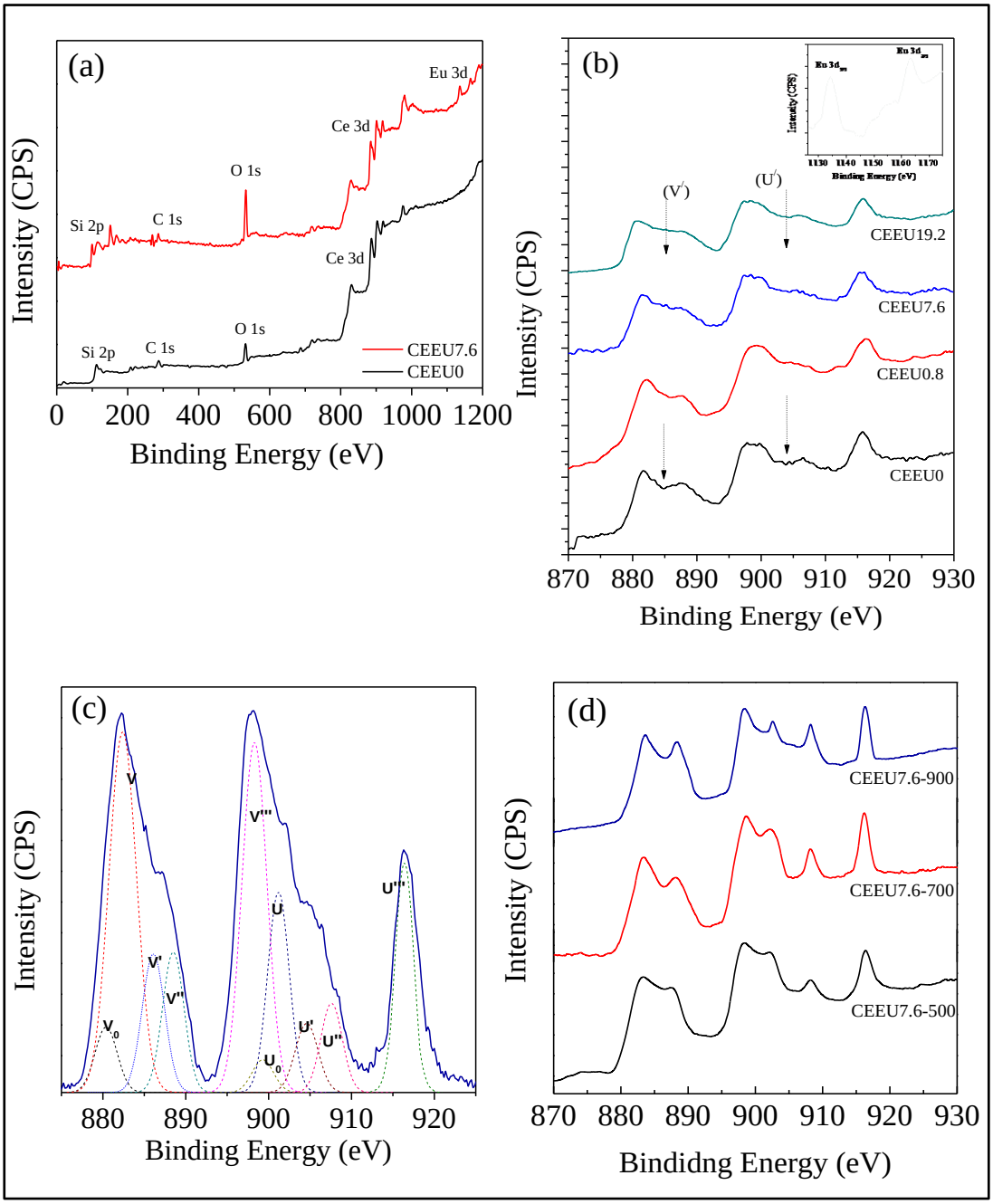

Figure 3.3. (a) XPS survey spectra of CEEU0 and CEEU7.6 samples. (b) Ce 3d spectra of CEEU0, CEEU0.8, CEEU7.6 and CEEU19.2 samples. Inset shows the Eu 3d spectrum of CEEU7.6 (c) Cerium 3d spectra of CEEU7.6 (d) Ce 3d spectra of CEEU7.6 sample annealed at various temperatures.

Most obvious is an increased intensity at around 886 eV and 904 eV (marked with an arrow in Figure 3.3 b) and a reduction in relative peak intensity for the

feature around 918 eV. It is clear that these contributions increase with dopant concentration. Figure 3.3 c is curve-fitted data for the Ce3d spectrum of sample CEEU7.6 and is consistent with a mixed valence CeO_2 material. Other materials gave similar data. Curve-fitting of the spectra from the samples allows quantification of the atomic% of Ce(III)[41, 42] using Equation 3.2 and is summarized in Table 3.2 for all the samples.

$$[Ce^{3+}] = \frac{U_0 + U' + V_0 + V'}{U_0 + U' + V_0 + V' + U + U'' + U''' + V + V'' + V'''} \qquad \text{Eq. 3.2}$$

From the data provided in Table 3.2, it is seen that the concentration of Ce^{3+} increases linearly with europium addition. Indeed, if the actual europium concentration is compared to the measured Ce^{3+} concentration, it can be seen that around one Ce^{3+} cation is created for every Eu^{3+} addition through the formation of oxygen vacancy (V_0). This is somewhat unexpected. Indeed, according to results gathered in Table 2, highest Ce3+ contents are found for highest strain values.

Using Kröger–Vink notation the generally accepted mechanism for dissolution of a trivalent lanthanide oxide such as europium oxide into ceria can be described by the equation[43]:

$$Eu_2O_3 + 2Ce^x{}_{Ce} + O_O^x \rightarrow 2Eu'_{Ce} + V_O^{\bullet\bullet} + 2CeO_2 \qquad \text{Eq. 3.3}$$

where, Eu'_{Ce} signifies a dopant substitution (of a cerium cation) and $V_0^{\bullet\bullet}$ an oxygen vacancy. In this way, each Eu ion dopant replaces host cations (Ce^{4+}) by Eu^{3+}. The substitution also results in the formation of an oxygen vacancy to satisfy charge neutrality. Note that, having an effective charge of opposite signs, oxygen vacancies and trivalent dopants can attract each other. Chemically, this vacancy mechanism can be represented as:

$$CeO_2 + x/2Eu_2O_3 \rightarrow Ce_{1-x}Eu_xO_{2-x/2} \qquad \text{Eq.3.4}$$

where the resultant solid solution has a structure similar to that of fluorite (CeO_2) apart from a distribution of anion vacancies. However, this does not reflect the formation of Ce^{3+} cations observed here and a more reasonable representation is given by:

$$Eu_2O_3 + 2Ce^x{}_{Ce} \rightarrow 2Ce'_{Ce} + 2Eu'_{Ce} + 2V_O^{\bullet\bullet} + 2O_O^x + 1/2O_2 \quad \text{Eq. 3.5}$$

This shows that trivalent europium cation is accompanied by the production of a cerium trivalent cation (plus an additional vacancy for each of these and gas phase oxygen). In simple chemical terms the solid state solution can be written stoichiometrically as $Ce_{1-x}Eu_xO_{2-}x$. This implies that there is additional thermodynamic stability of defect clusters such as Eu^{3+}-V_o-Ce^{3+} compared to Eu^{3+}-V_o-Ce^{4+}. Note that, these are simple representations of what will actually be 3D structural arrangements and are used for brevity here. The existence of this kind of defect clustering was reported for large to small (La or Lu) dopant incorporation into the ceria lattice in order to achieve electrostatic stabilization of the crystal.[44, 45] This kind of vacancy agglomeration was also observed by us before[30] which increases with increasing the dopant concentration. This higher content of vacancies at the surface for highly doped samples might decrease the reducibility of the compounds in order to preserve the equilibrium of reaction. This is evident from Table 2 which depicts the rate of formation of Ce^{3+} decreases with higher doping concentrations as proposed for Gd^{3+} dopant.[33] Recent work by Nolan et al.[46] suggest that O^- species may also be stable in doped CeO_2 fluorite structures although there is no direct evidence for this mechanism here.

Ceria-based nanopowders, are important for their surface redox capabilities and their general catalytic activity.[47] Their surface redox capability possibly incorporates switching between Ce^{4+} and Ce^{3+} oxidation states through an ability to absorb and release oxygen by generating oxygen vacancies in the ceria lattice. The experiment was performed in a closed solvothermal chamber for which it can be considered that the concentration of oxygen in the atmosphere around the sample is orders of magnitude lower than the concentration of oxygen at the surfaces of CeO_2 particles.[48] This gradient of concentration might be the driving force for the oxygen removal from the surface of the particle which reduces Ce^{4+} into Ce^{3+}.

The possibility of oxidizing some of the Ce^{3+} ions to Ce^{4+} at higher temperatures is revealed in Figure 2d which shows the Ce3d spectra of the CEEU7.6 sample

annealed at 500 °C, 700 °C and 900 °C for 2 h. These data are also indicative of mixed Ce(III) and Ce(IV) valence states but at reduced concentration compared to the non-calcined form suggesting that the system has a well-defined redox chemistry. Table 2 describes that the concentrations of Ce^{3+} ions decreases with the increase in annealing temperature. It is suggested that some of the surface oxygen vacancies were oxidized by the high temperature exposure to atmospheric oxygen which transforms Ce^{3+} ions into Ce^{4+} ions. The particle sizes also increases with the increases in annealing temperature through particle agglomeration. Thus, the annealing step results an increase in particle sizes and changes in oxidation state.

The valence state of europium is confirmed by Eu3d XPS spectrum. All samples gave similar spectra and representative Eu3d data are shown in Figure 3.3.b (inset) for sample CEEU7.6. The two characteristic peaks at 1134 ($3d_{5/2}$) and 1163 eV ($3d_{3/2}$) correspond to the Eu^{3+} state. Previous work has shown that the binding energy shift of Eu3d features for Eu^{3+} and Eu^{2+} are around 10 eV[49] and this assignment is rather clear.

3.4.4. Morphological and compositional studies by TEM

TEM images of the undoped and doped CeO_2 samples confirm the nanocrystalline nature of the samples. Figure 3.4 a, b, c and d represent TEM micrographs for the CEEU0, CEEU0.8, CEEU7.6 and CEEU19.2 samples. There was no obvious particulate morphology change and all the samples were composed of small agglomerated crystallites with an irregular pseudo-spherical shape of uniform size distribution and a diameter between 5 to 10 nm, similar to that estimated from XRD analysis. The mean diameters measured confirm a size decrease with increased europium concentration. Clearly visible lattice fringes suggest a high degree of crystallinity of the particles for all the samples. Analysis suggests the facets are (111) planes consistent with other work and known stabilities.[50, 51] The measured interplanar distance is 0.32 nm corresponds to the (111) plane of fluorite cubic structure of CeO_2. The SAED patterns shown in the inset of Figure 3.4 also indicate high degrees of crystallinity and are consistent with (111), (220) and (311) reflections from a fluorite phase.

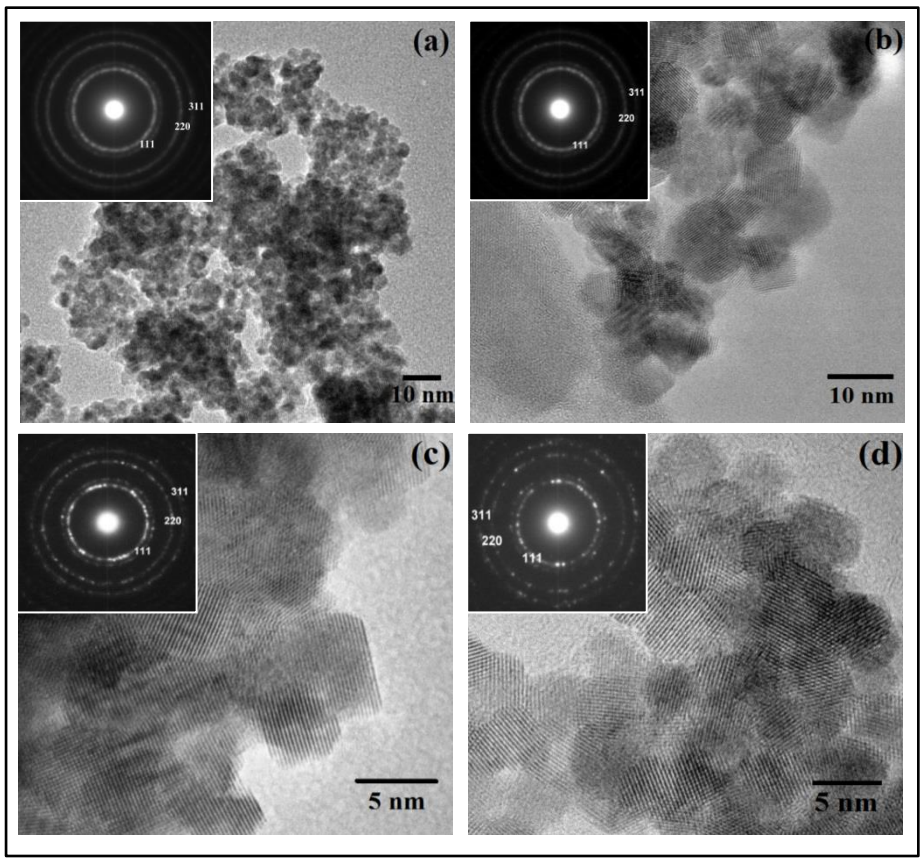

Figure 3.4. TEM images of undoped and europium doped CeO_2 nanoparticles (a) CEEU0 (b) CEEU0.8 (c) CEEU7.6 (d) CEEU19.2. (Inset shows corresponding SAED)

A highlight of this work was the use of high spatial resolution EELS to demonstrate the location of Eu in these materials and confirm solid state solution. Figure 3.5.a and b shows the dark field TEM image and Ce Lα, Eu Lα, O Kα elemental mapping of a nanoparticle of 4.5 nm in diameter for the sample CEEU7.6 and CEEU19.2 respectively. The image (red square box) represents the CeO_2 nanoparticle which provides a reference to locate the area of the elemental map. The mapping was obtained as a pixel-by-pixel mapping of the integrated intensity of the EELS spectrum. The spectrum taken from few of the nanoparticles in different area was essentially the same. The elemental maps confirm the presence of Eu, Ce and O throughout the nanoparticle. This results indicate that the Eu incorporation inside the ceria nanocrystal and not present as a free species within the powdered sample and suggest little surface segregation etc. Corresponding EDX spectrum also confirms an increase in the intensity of the Eu peak with the increment of doping concentrations.

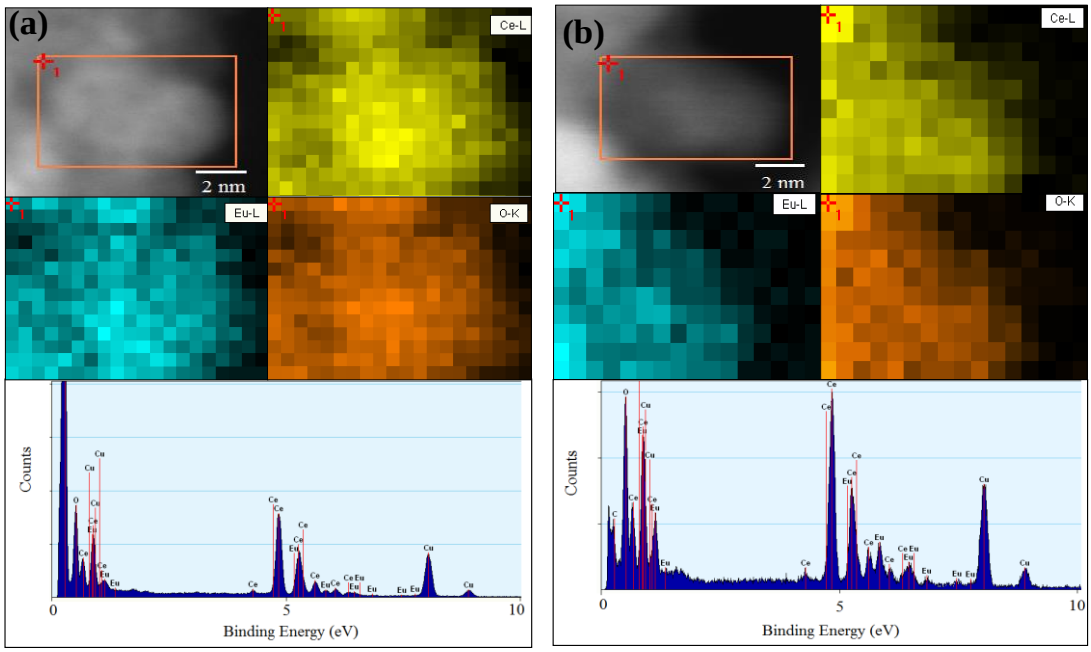

Figure 3.5. Ce-L, Eu-L, O-K mapping of europium doped CeO_2 and respective EDX spectrum recorded on a single nanoparticle in the marked box (a) CEEU7.6 (b) CEEU19.2

3.4.5. Optical properties

Figure 3.6 shows the U Absorption spectra of nanomaterials can provide useful analysis of nanophase oxide materials. V-Visible spectra of undoped and europium doped CeO_2 nanoparticles. It can be seen that the absorbance peaks shifts towards higher wavelength (red-shift) with the increasing europium content characteristic of electron-phonon coupling phenomenon[52] and decreasing nanocrystallite sizes increase electron-phonon-coupling coefficients. These effects derive from changes in the band structure with reduced dimension which modify the effective mass/mobility and lattice scattering of the carriers and result in a red-shift of the emission band.[53] It has also been suggested that the red-shift of the absorption bands observed in nanocrystalline CeO_2 can be explained by the formation of localized states within the band gap owing to oxygen vacancies and an increase of the Ce^{3+} ion concentration.[54, 55] This phenomenon is related to the shift of absorbance band towards longer wavelength. Chowdhury *et al.* and other authors reported the similar red shift in wavelength with the increase in Ce^{3+} concentration.[54, 56] The

band gap of undoped and europium doped CeO_2 samples are calculated from UV-Vis spectra and listed in Table 3.2.

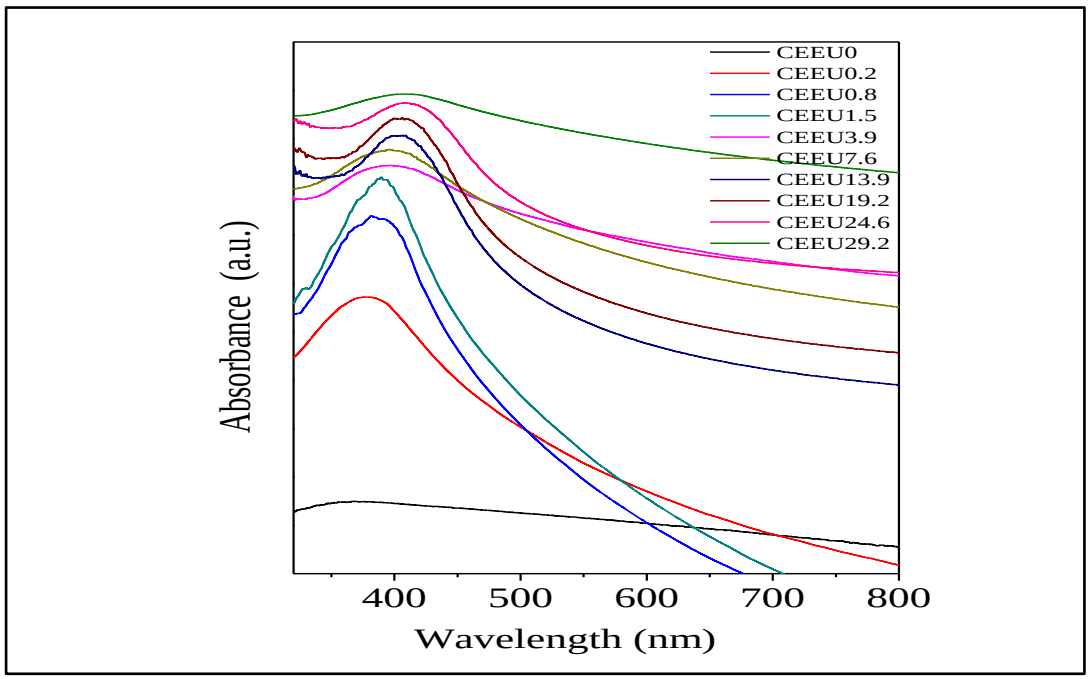

Figure 3.6. UV-Vis absorption spectra of undoped and europium doped CeO_2 nanoparticles.

Photoluminescence (PL) spectroscopy is an effective method to determine the optical properties of materials and the defect chemistry associated with those properties.[31, 57, 58] Figure 3.7 a shows the excitation spectra for emission at 608 nm of undoped and europium doped CeO_2 samples. CEEU0 does not show any emission peak around the excitation energy but well-defined features around 466 nm characteristic of europium 4f-4f transitions[59] were observed in all europium doped samples. Because the O^{2-}-Eu^{3+} charge transfer lies in a much shorter wavelengths and CeO_2 has a band gap around 3.3 eV (~470 nm), the broad peak is related to mainly Ce^{4+}-O^{2-} charge transfer[60] with some overlapping with the intraconfigurational Eu 4f-4f transitions. As evident from Figure 3.7.a, with increasing europium content the intra $4f^6$ transition bands of Eu^{3+} become generally stronger to a maximum of 19.2 % beyond which the intensity decreases due to a concentration quenching effect.[61] Figure 3.7 b describes the excitation spectra of CEEU7.6 with different annealing temperatures. The intensity of the peak at 466 nm

increases with the annealing temperature because Ce^{4+}-O^{2-} charge transfer becomes predominant due to the formation of more Ce^{4+}.

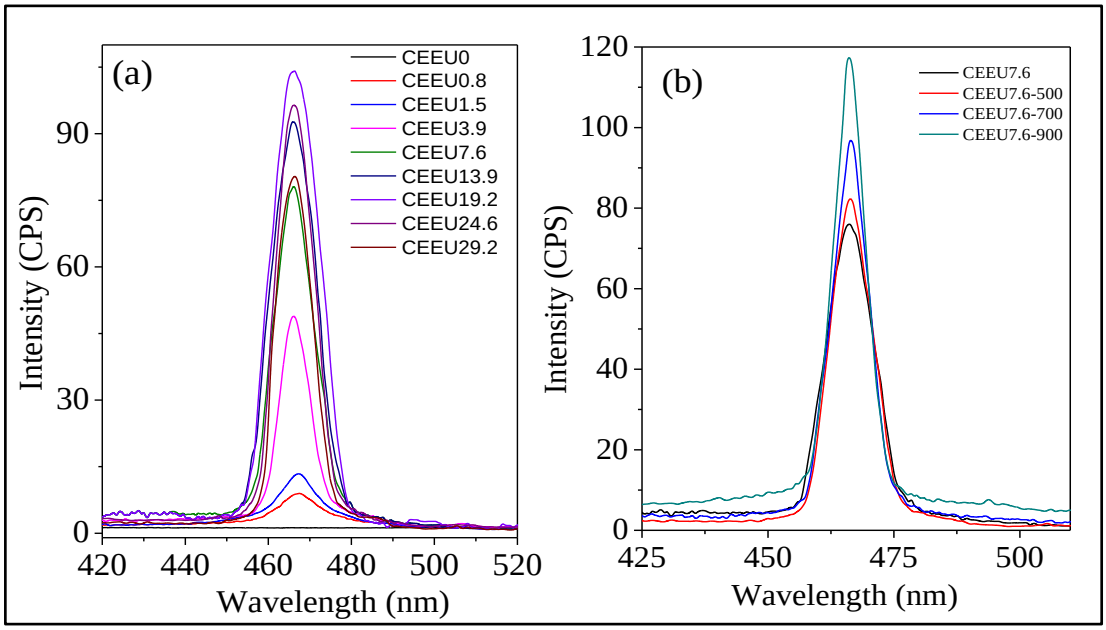

Figure 3.7. Excitation spectra with emission at 608 nm for (a) as prepared samples (b) CEEU7.6 sample annealed at various temperatures.

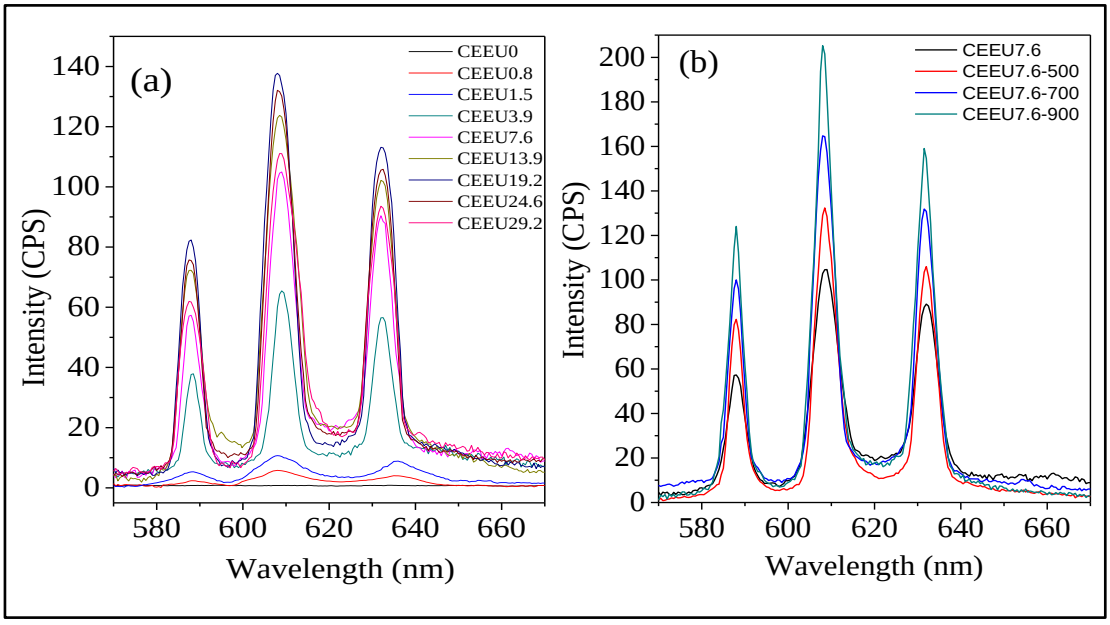

Figure 3.8. Emission spectra with excitation at 466 nm for (a) as-prepared samples (b) CEEU7.6 sample annealed at various temperatures.

Figure 3.8 a and b shows the emission spectra of various europium doped and annealed CeO_2 samples for excitation at 466 nm. As seen in the higher wavelength excitation, with increasing Eu^{3+} concentration, there is an increase in intensity up to 19.2 % a further increase in dopant concentration decreases the Eu^{3+}-Eu^{3+} distance, indicating an effective energy transfer between the neighbouring ions. Hence, the excited state is quenched, scattering the energy non-radiatively and decreasing the emission intensity decreases. The emission spectra reveal a characteristic Eu^{3+} emission and can be assigned to various transitions $^5D_0$-^7F_J (J=0, 1, 2 etc.) that reveal the local environment of the Eu^{3+} ion. The multiple peaks in the spectra are due to the splitting of the Eu^{3+} 4f shell. The Judd-Ofelt (J-O)[62, 63] theory is the most useful method in the analysis of spectroscopic studies of lanthanide ions in different hosts.

As per J-O theory, the emission lines are a cumulative effect of magnetic dipole (MD) transition and electric dipole (ED) transition, depending on the specific environment of Eu^{3+} in any matrix. According to the J-O theory, the ED transition (^5D_o-$^7F_2$) centered at about 611 and 629 nm, is only allowed in the absence of inversion symmetry and is hypersensitive to the local electric field. On the other hand, the MD transition (^5D_o-$^7F_1$) with emission at 591 nm is a magnetic dipole allowed transition, which is insensitive to the crystal environment. CeO_2 has a cubic fluorite structure with every Ce ion surrounded by eight equatorial oxygen ions in O_h symmetry. The emission intensity of Eu^{3+} is very critical to its location in the lattice, that is, the type of environment around Eu^{3+} ions. When Ce^{4+} is replaced with Eu^{3+}, the symmetry can be lowered or increased depending on the site occupied by the dopant. In the present case, the ED transition intensity was found to be higher, indicating that Eu^{3+} mainly occupies the lattice sites. The absence of any forbidden electric or magnetic dipole transitions also indicates a high symmetry Eu site suggesting simple substitution with fluorite Ce^{4+} sites.

The emission intensity was found to increase with the increase in annealing temperature (Figure 3.8 b). The temperature insensitivity of the form of the PL emission peaks confirms that Eu^{3+} ions occupy fluorite structure cation sites substitutionally at all temperatures. The similarity in the data also demonstrates that

the interaction between the europium-dopant and oxygen vacancy resulting from charge compensation Eu^{3+}–Ce^{4+} is neither enhanced nor diminished with the increasing temperature. However, the increase in intensity and narrowing of peaks is due to the more crystalline-like environment obtained at higher calcinations.

3.5. Conclusion

In summary, europium doped CeO_2 nanoparticles have been successfully synthesized by a single step simple solvothermal process. The as-formed nanoparticles are highly crystalline and their sizes varied in the range of 3-9 nm depending on the europium concentrations. An increase in the measured lattice parameter was observed due to inclusion of the larger europium cations but at very small doping concentrations, lattice contraction was observed due to surface tension-type effects. The europium ion site occupancy through the substitution of Ce^{4+} ions in the cubic symmetric lattice was verified and found to be less compared to the dopant ion added during synthesis. The insertion of the rare earth cations in the CeO_2 structure provokes an increase in the oxygen vacancies concentration through the promotion of the non-stoichiometric condition of the cerium oxide, by the reduction of Ce^{4+} to Ce^{3+}. The crystal structure and spectroscopic analysis reveals almost similar concentrations for Ce^{3+} and Eu^{3+} suggest the europium species are mainly located in the lattice sites. The incorporation and homogeneous distribution of europium ions in the ceria nanoparticle is also confirmed. The band gap of the doped CeO_2 nanocrystals were found to decrease with the doping due to the formation of localized states within the band gap owing to the increase in oxygen vacancies and Ce^{3+} concentrations. The PL spectra indicate the high symmetry europium ions substitution with Ce^{4+} which is not affected with the calcinations temperature. The high temperature calcinations reduce the defect density, increasing the crystallite size thereby increasing the degree of crystallization. The ability to tailor the ionization state of cerium and the oxygen vacancy concentration in CeO_2 has applications in a broad range of fields, which include catalysis, biomedicine, electronics and environmental sensing.

3.6. References:

1. P. Bera, A. Gayen, M. S. Hegde, N. P. Lalla, L. Spadaro, F. Frusteri and F. Arena, *J. Phys. Chem. B*, 2003, **107**, 6122-6130.
2. M. Mogensen, N. M. Sammes and G. A. Tompsett, *Solid State Ionics*, 2000, **129**, 63-94.
3. R. Li, S. Yabe, M. Yamashita, S. Momose, S. Yoshida, S. Yin and T. Sato, *Solid State Ionics*, 2002, **151**, 235-241.
4. R. Bene, I. V. Perczel, F. Réti, F. A. Meyer, M. Fleisher and H. Meixner, *Sens. Actuators, B*, 2000, **71**, 36-41.
5. H. Treichel, R. Frausto, S. Srivatsan, B. Whithers, T. Meyer and R. Morishige, *J. Vac. Sci. Technol., A*, 1999, **17**, 1160-1167.
6. F. Goubin, X. Rocquefelte, M.-H. Whangbo, Y. Montardi, R. Brec and S. Jobic, *Chem. Mater.*, 2004, **16**, 662-669.
7. J. P. Chen, S. Patil, S. Seal and J. F. McGinnis, *Nat. Nanotechnol.*, 2006, **1**, 142-150.
8. A. Macedo, S. E. Fernandes, A. Valente, R. A. Ferreira, L. Carlos and J. Rocha, *Molecules*, 2010, **15**, 747-765.
9. S. Hufner, *J Phys F Met Phys*, 1986, **16**, L31-L34.
10. P. Dutta, S. Pal, M. S. Seehra, Y. Shi, E. M. Eyring and R. D. Ernst, *Chem. Mater.*, 2006, **18**, 5144-5146.
11. T. H. Etsell and S. N. Flengas, *Chem Rev*, 1970, **70**, 339-376.
12. A. Trovarelli, *Catal. Rev.*, 1996, **38**, 439-520.
13. H. Inaba and H. Tagawa, *Solid State Ionics*, 1996, **83**, 1-16.
14. G. Mialon, M. Poggi, D. Casanova, T. L. Nguyen, S. Turkcan, A. Alexandrou, T. Gacoin and J. P. Boilot, *J. Lumin.*, 2009, **129**, 1706-1710.
15. X. Wang, J. C. Hanson, G. Liu, J. A. Rodriguez, A. Iglesias-Juez and M. Fernández-García, *J. Chem. Phys.*, 2004, **121**, 5434-5444.
16. H. Borchert, Y. V. Frolova, V. V. Kaichev, I. P. Prosvirin, G. M. Alikina, A. I. Lukashevich, V. I. Zaikovskii, E. M. Moroz, S. N. Trukhan, V. P. Ivanov, E. A. Paukshtis, V. I. Bukhtiyarov and V. A. Sadykov, *J. Phys. Chem. B*, 2005, **109**, 5728-5738.
17. R. Shannon, *Acta Cryst.*, 1976, **32**, 751-767.

18. C. Tiseanu, V. I. Parvulescu, M. Boutonnet, B. Cojocaru, P. A. Primus, C. M. Teodorescu, C. Solans and M. Sanchez Dominguez, *Phys. Chem. Chem. Phys.*, 2011, **13**, 17135-17145.
19. H. Yokokawa, T. Horita, N. Sakai, K. Yamaji, M. E. Brito, Y. P. Xiong and H. Kishimoto, *Solid State Ionics*, 2006, **177**, 1705-1714.
20. S. Fujihara and M. Oikawa, *J. Appl. Phys.*, 2004, **95**, 8002-8006.
21. B. Djuričić and S. Pickering, *J. Eur. Ceram. Soc.*, 1999, **19**, 1925-1934.
22. C. Sun, H. Li and L. Chen, *Energy Environ. Sci.*, 2012, **5**, 8475-8505.
23. L. Chen, P. Fleming, V. Morris, J. D. Holmes and M. A. Morris, *J. Phys. Chem. C*, 2010, **114**, 12909-12919.
24. F. Bondioli, A. B. Corradi, T. Manfredini, C. Leonelli and R. Bertoncello, *Chem. Mater.*, 1999, **12**, 324-330.
25. B. Ksapabutr, E. Gulari and S. Wongkasemjit, *Mater. Chem. Phys.*, 2006, **99**, 318-324.
26. Y. Zhou, R. J. Phillips and J. A. Switzer, *J. Am. Ceram. Soc.*, 1995, **78**, 981-985.
27. Z. Wang, Z. Quan and J. Lin, *Inorg. Chem.*, 2007, **46**, 5237-5242.
28. W. Chengyun, Q. Yitai, Y. Xie, W. Changsui, L. Yang and Z. Guiwen, *Mater. Sci. Eng., B*, 1996, **39**, 160-162.
29. Z. L. Wang and X. D. Feng, *J. Phys. Chem. B*, 2003, **107**, 13563-13566.
30. A. V. Thorat, T. Ghoshal, J. D. Holmes, P. M. Nambissan and M. A. Morris, *Nanoscale*, 2013, **6**, 608-615.
31. A. Kumar, S. Babu, A. S. Karakoti, A. Schulte and S. Seal, *Langmuir*, 2009, **25**, 10998-11007.
32. K. M. Ryan, J. P. McGrath, R. A. Farrell, W. M. O'Neill, C. J. Barnes and M. A. Morris, *J Phys-Condens Mat*, 2003, **15**, L49-L58.
33. B. Suresh, T. Ranjith, I. Talgat, D. Richard, E. M. Artëm, S. Alfons and S. Sudipta, *Nanotechnology*, 2009, **20**, 085713.
34. A. Le Gal and S. Abanades, *J. Phys. Chem. C*, 2012, **116**, 13516-13523.
35. G. S. Herman, Y. J. Kim, S. A. Chambers and C. H. F. Peden, *Langmuir*, 1999, **15**, 3993-3997.

36. G. Liu, J. A. Rodriguez, J. Hrbek, J. Dvorak and C. H. F. Peden, *J. Phys. Chem. B*, 2001, **105**, 7762-7770.
37. P. W. Park and J. S. Ledford, *Langmuir*, 1996, **12**, 1794-1799.
38. M. Romeo, K. Bak, J. El Fallah, F. Le Normand and L. Hilaire, *Surf. Interface Anal.*, 1993, **20**, 508-512.
39. P. Burroughs, A. Hamnett, A. F. Orchard and G. Thornton, *J. Chem. Soc., Dalton Trans.*, 1976, 1686-1698.
40. T. Ghoshal, P. G. Fleming, J. D. Holmes and M. A. Morris, *J. Mater. Chem.*, 2012, **22**, 22949-22957.
41. S. Deshpande, S. Patil, S. V. N. T. Kuchibhatla and S. Seal, *Appl Phys Lett*, 2005, **87**, 133113-133113.
42. S. Tsunekawa, T. Fukuda and A. Kasuya, *Surf. Sci.*, 2000, **457**, L437-L440.
43. B. C. Morris, W. R. Flavell, W. C. Mackrodt and M. A. Morris, *J. Mater. Chem.*, 1993, **3**, 1007.
44. D. A. Andersson, S. I. Simak, N. V. Skorodumova, I. A. Abrikosov and B. Johansson, *Proc. Natl. Acad. Sci. U. S. A.*, 2006, **103**, 3518-3521.
45. C. Frayret, A. Villesuzanne, M. Pouchard, F. Mauvy, J. M. Bassat and J. C. Grenier, *J. Phys. Chem. C*, 2010, **114**, 19062-19076.
46. I. Yeriskin and M. Nolan, *J Phys Condens Matter*, 2010, **22**, 135004.
47. M. Y. Chen, X. T. Zu, X. Xiang and H. L. Zhang, *Physica B*, 2007, **389**, 263-268.
48. M. Stan, Y. T. Zhu, H. Jiang and D. P. Butt, *J. Appl. Phys.*, 2004, **95**, 3358-3361.
49. E. J. Cho and S. J. Oh, *Phys Rev B*, 1999, **59**, R15613-R15616.
50. T. X. T. Sayle, S. C. Parker and C. R. A. Catlow, *Surf. Sci.*, 1994, **316**, 329-336.
51. A. S. Barnard and A. I. Kirkland, *Chem. Mater.*, 2008, **20**, 5460-5463.
52. Y. Zhang, T. Cheng, Q. Hu, Z. Fang and K. Han, *J. Mater. Res.*, 2007, **22**, 1472-1478.
53. B. Zhou, L. Xiao, T. J. Li, J. Zhao, Z. Lai and S. Gu, *Appl. Phys. Lett.*, 1991, **59**, 1826-1828.
54. X. Lu, X. Li, F. Chen, C. Ni and Z. Chen, *J. Alloys Compd.*, 2009, **476**, 958-962.

55. C. P. Charitidis, P.; Logothetidis, S., *J. Phys. Conf. Ser.*, 2005, **10**, 226-229.
56. K. S. Lin and S. Chowdhury, *Int J Mol Sci*, 2010, **11**, 3226-3251.
57. C. Tiseanu and V. A. Lorenz-Fonfria, *J. Nanosci. Nanotechnol.*, 2010, **10**, 2803-2810.
58. C. Tiseanu, V. I. Parvulescu, M. Boutonnet, B. Cojocaru, P. A. Primus, C. M. Teodorescu, C. Solans and M. Sanchez-Dominguez, *Phys. Chem. Chem. Phys.*, 2011, **13**, 21652-21653.
59. I. Hemmilä, V.-M. Mukkala and H. Takalo, *J. Alloys Compd.*, 1997, **249**, 158-162.
60. L. Li, S. Zhou and S. Zhang, *Chem. Phys. Lett.*, 2008, **453**, 283-289.
61. J. Li and M. Kuwabara, *Key Eng Mat*, 2003, **248**, 129-132.
62. B. R. Judd, *Phys. Rev.*, 1962, **127**, 750-761.
63. G. S. Ofelt, *J. Chem. Phys.*, 1962, **37**, 511-520.

Chapter 4

A positron annihilation spectroscopic investigation of europium doped cerium oxide nanoparticles

4.1. Abstract

Doping in ceria (CeO_2) nanoparticles with europium (Eu) of varying concentrations (0, 0.1, 0.5, …, 50 atom%) are studied using complementary experimental techniques and novel observations were made during the investigation. The immediate observable effect was a distinct reduction in particle sizes with increasing europium concentration attributed to the relaxation of strain introduced due to the replacement of Ce^{4+} ions by Eu^{3+} ions of larger radius. However, this general trend was reversed in the doping concentration range of 0.1 - 1 atom % due to the reduction of Ce^{4+} to Ce^{3+} and the formation of anion vacancies. Quantum confinement effects became evident with the increase of band gap energy when the particle sizes reduced below 7-8 nm. Positron annihilation studies indicated the presence of vacancy type defects in the form of vacancy clusters within the nanoparticles. Some positron annihilation was also seen on the surface of crystallites as a result of diffusion of thermalized positrons before annihilation. Coincidence Doppler broadening measurements indicated the annihilation of positrons with electrons of the different species of atoms and the characteristic *S* - *W* plot showed a kink-like feature at the particle sizes where quantum confinement effects began.

4.2. Introduction

Ceria is an oxide with a wide range of uses including polishing material, catalysis, fuel cells, advanced ceramics and sensors amongst others.[1-4] Many of its applications rely on the ability of ceria to transport and act as a labile source of oxygen.[5, 6] To this effect, it is often 'doped' with lower valence ions particularly trivalent lanthanide cations.[7-9] These ions are introduced into the lattice to substitute for Ce^{4+} ions and it is generally believed that anion vacancies are created as a means of charge compensation[10] although other defect mechanisms have been proposed by Yeriskin et al.[11] The study of the defect chemistry of cerium oxide nanoparticles doped by europium (Eu) ions has become of significant interest because of the modification of the optical and luminescent properties of the material on doping.[12] Numerous studies have recently appeared in the literature emphasizing the roles of vacancy type defects and their evolution during the changes in crystallite sizes[13] and doping concentrations.[14] However, a comprehensive study of defect structure and

dynamics has yet to be carried out for this system. In this work, we will address this issue with a systematic study of the defects generated by europium doping. We shall also study the interaction of the defects with the dopant ions when Eu is doped in discrete and varying concentrations. Positron annihilation spectroscopy is used as an effective method to study the defects and their evolution on doping. It is thought this is extremely pertinent since, discussed by us earlier, techniques such as x-ray photoelectron spectroscopy (XPS) and x-ray diffraction (XRD) have limitations in the study of these systems because of complex spectral peak shapes and the sensitivity of ceria to x-ray irradiation.[12] Positron annihilation is a technique that can be used to study defects in material systems very reliably and it can be sensitive to even very low defect concentrations.[15, 16]

4.3. Experimental

4.3.1.Synthesis of ceria nanoparticles

Synthesis of the ceria nanoparticles is explained in section 3.3.2. Samples with varying concentrations of europium are represented as CEX, where X = 0, 0.1, 0.3, 0.5, 1, 5, 10, 20, 30, 40 and 50 are the doped atom % of Eu.

4.3.2. Positron annihilation studies

Positron annihilation experiments were performed by placing sufficient sample in a glass tube of approximately 10 mm diameter so as to embed a positron emitting ^{22}Na radioactive isotope at its geometric centre. The source, about 400 kBq in strength, was made in the form of a small deposition of $^{22}NaHCO_3$ on part of a thin (~ 2 mg cm^{-2}) Ni foil with remaining foil used to cover and protect the source. The glass tube containing the source-sample assembly was continuously evacuated to maintain a clean and dry atmosphere in it. The gamma rays resulting from positron emission and subsequent annihilation were recorded using nuclear radiation detectors and the signals were processed using the associated electronics.

Two types of experiments were carried out, the first of which recorded the positron lifetime spectrum using a gamma-gamma slow-fast coincidence spectrometer and the other recording the Doppler broadening of the positron

annihilation gamma ray spectrum in coincidence mode using two high pure germanium (HPGe) detectors.[17] In the former, about 1-1.5 million counts were collected in each spectrum and the spectra were analyzed using the program PALSfit.[18] In the coincidence Doppler broadening spectra (CDBS), about 8 million events were generated from the counts accumulated. Briefly, gamma ray events at energies E_1 and E_2 were recorded from two high sensitive HPGe detectors and a two-parameter spectrum was generated from their time corrections with $E_1 + E_2$ and $E_1 - E_2$ as two coplanar axes and counts distributed accordingly.[19, 20] The projected one-dimensional spectrum parallel to the energy-difference axis within the energy-sum segment $(1022 - 2.4)$ keV $< E_1 + E_2 <$ $(1022 + 2.4)$ keV of each sample is then divided by an area-normalized identical spectrum obtained for a pair of pure (99.999%) Al single crystalline samples prior annealed at 625 °C for 2 h in vacuum (p < 10-5 mbar). Positron annihilation experiments were carried out in Nuclear and Atomic Physics Division, Saha Institute of Nuclear Physics, Kolkata, India.

4.4. Results and Discussion

Several complementary experiments had been performed to characterize the samples and estimate the particle sizes, lattice parameters, optical band gaps, luminosity of the emissions etc. These are summarized below.

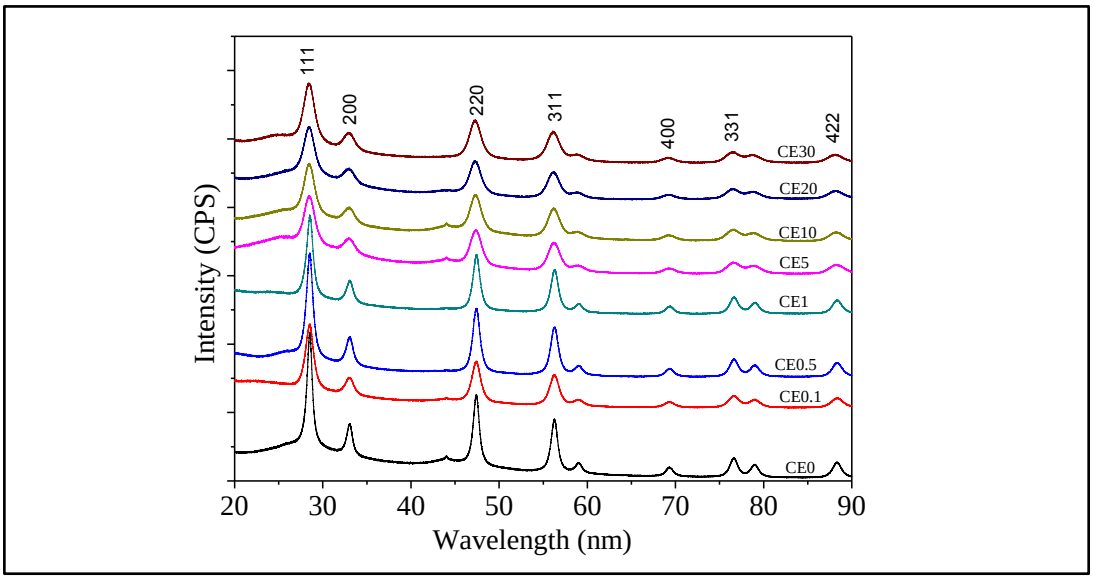

Figure 4.1. Typical x-ray diffraction patterns of the undoped and some of the europium doped cerium oxide nanocrystalline samples.

Some of the illustrative XRD patterns are shown in Figure 4.1. The well-defined peaks corresponding to reflections of the expected fluorite phase are described in the figure. The peak widths indicate that the samples are nanocrystalline in nature. The crystallite sizes (d_c) were estimated using Scherrer formulism.[21] Figure 4.2 shows an expected decrease of crystallite size with increasing concentration of Eu^{3+}, although it increases during the change of concentration from 0.1 to 1%. The decrease in crystallite size suggests that the dopant introduces significant lattice strain (the ionic radius of Eu^{3+} (1.07 Å) is about 10 % larger than that of Ce^{4+} (0.97 Å)) and this reduces ion transport and sintering as noted previously for doped CeO_2.[22] The increase in crystallite size seen between 0.1 and 1% doping concentration may be explained by the creation of charge compensating anion vacancies which will tend to increase oxygen ion mobility favoring sintering.

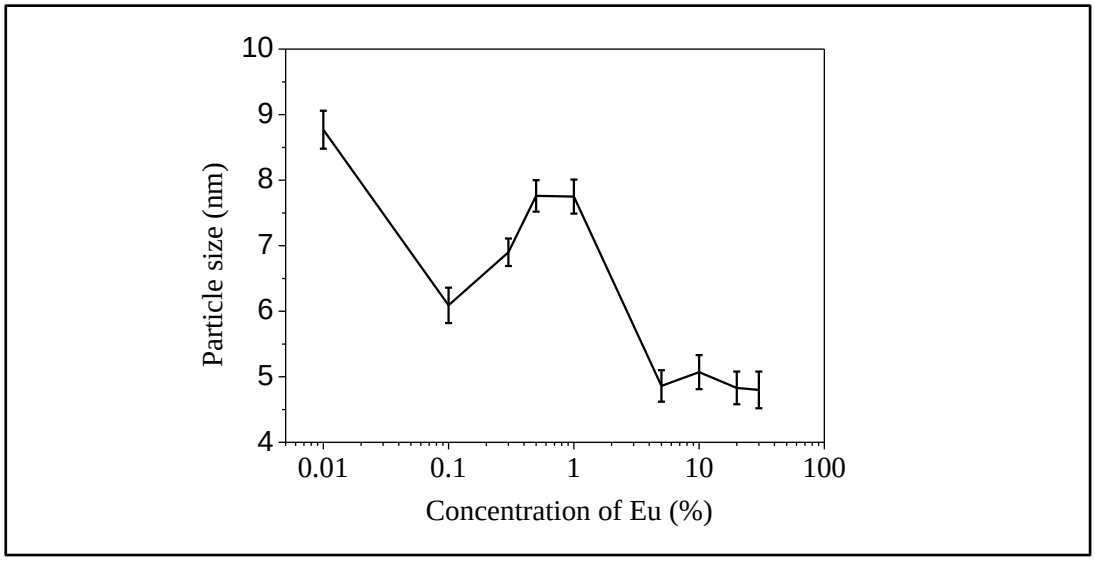

Figure 4.2. The average particle sizes in the undoped (shown against a concentration 0.01) and the europium doped CeO_2 samples.

We have also verified from total reflectance x-ray fluorescence (TXRF) data that the actual concentration of europium in the sample is significantly less than that might be expected from concentrations in the mother liquor. Similar effects have been previously reported by us and can be ascribed due to limited solubility of the trivalent oxides in strongly basic conditions.[23] Figure 4.3 illustrates the actual amount of europium incorporated into the solid against dopant concentration in

solution. As the solution concentration of europium increases, the effectiveness of incorporation decreases. At the highest dopant concentrations, quite large increases in solution concentration have little effect on the solid concentration. As well as complex solution effects, the data might also suggest high surface concentrations since the TXRF technique is not surface sensitive.

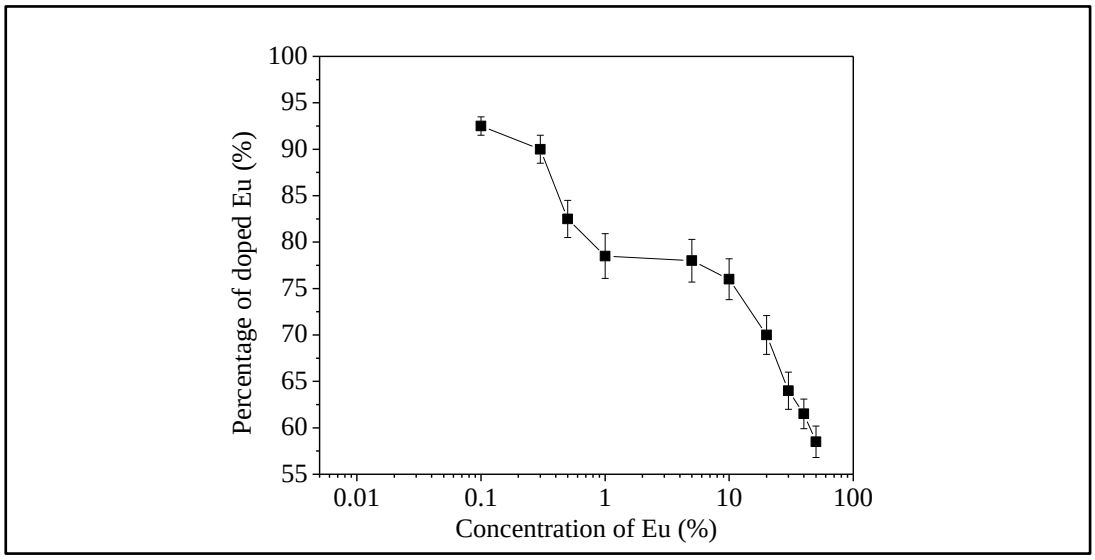

Figure 4.3. The percentage of europium actually incorporated in CeO_2 at different concentrations of europium, as found out from total reflectance x-ray fluorescence studies.

The lattice parameter α of the different samples, undoped and doped, were estimated as

$$\alpha = d\sqrt{h^2 + k^2 + l^2} \qquad \text{Eq. 4.1}$$

where the interplanar separation d is obtained from the Bragg relation $2d \sin \theta = n\lambda$. Figure 4.4 shows unexpected trends of the lattice parameter with the dopant concentration. The lattice parameter of the samples with higher concentrations of doped europium is obviously larger than the ones with lower europium concentration. However, in the region [Eu]= 0.1 to 1% where an increase in particle size had been earlier observed (Figure 4.2), there is a complex dependence of lattice parameter and dimension.

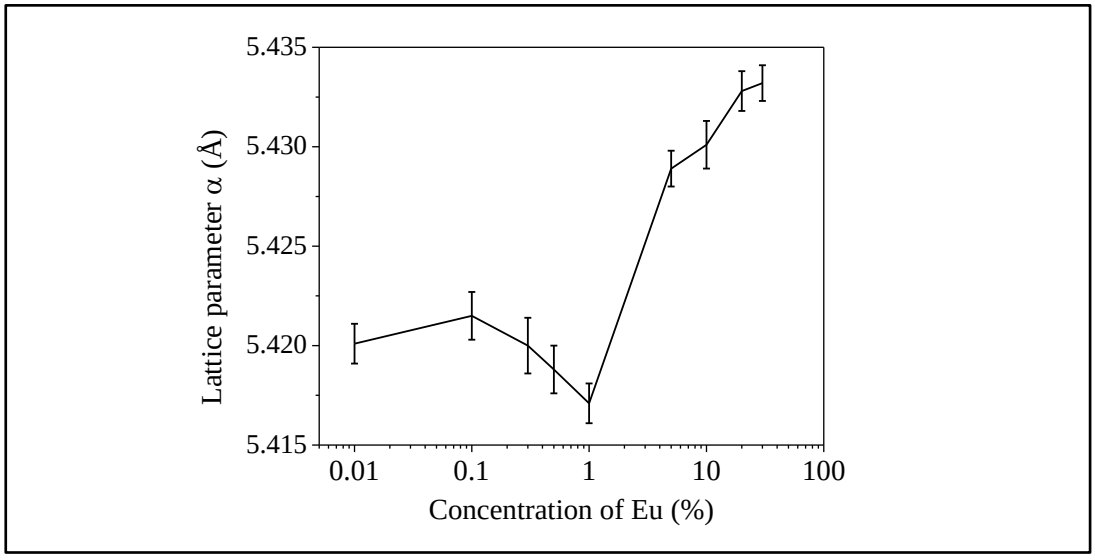

Figure 4.4. The lattice parameter (α) of the undoped (shown against a concentration 0.01) and the europium doped CeO_2 samples.

Figure 4.5 (a) presents a semi-log plot of the two quantities showing that the lattice parameter steadily increases with decrease in nanoparticle sizes. A relationship can be obtained between the change in lattice parameter $\Delta\alpha$ with respect to the lattice parameter of bulk CeO_2 (5.410Å) and the particle size d_c in a log-log plot (Figure 4.5 (b)) as

$$\log\ (\Delta\alpha) = -1.7437 \log(d_c) - 0.4947 \qquad \text{Eq. 4.2a}$$

or

$$\Delta\alpha = 0.32\ d_c^{-1.7437} \qquad \text{Eq. 4.2b}$$

The relation is however markedly different from a similar relation obtained earlier by Deshpande *et al.*[24] The differences could be attributed to the cause of lattice parameter variation, i.e., doping by europium in the present case versus crystallites of different sizes of undoped CeO_2 in the said work.

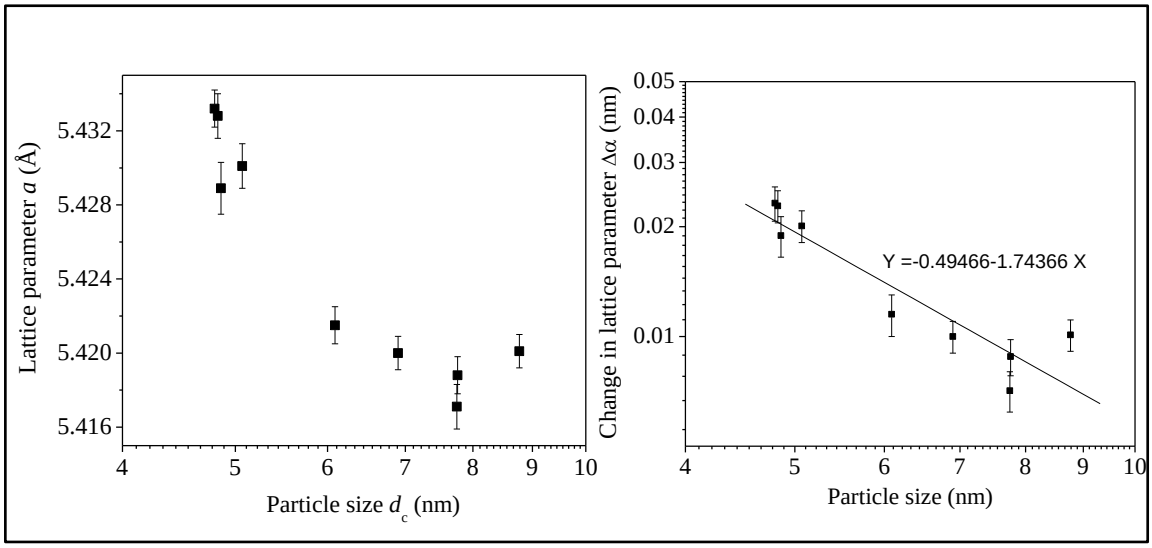

Figure 4.5. (a) A plot of the lattice parameter (α) versus size of the nanoparticles in the undoped and the europium doped CeO_2 samples. (b) The change in lattice parameter ($\Delta\alpha$) versus size of the nanoparticles in the undoped and the europium doped CeO_2 samples.

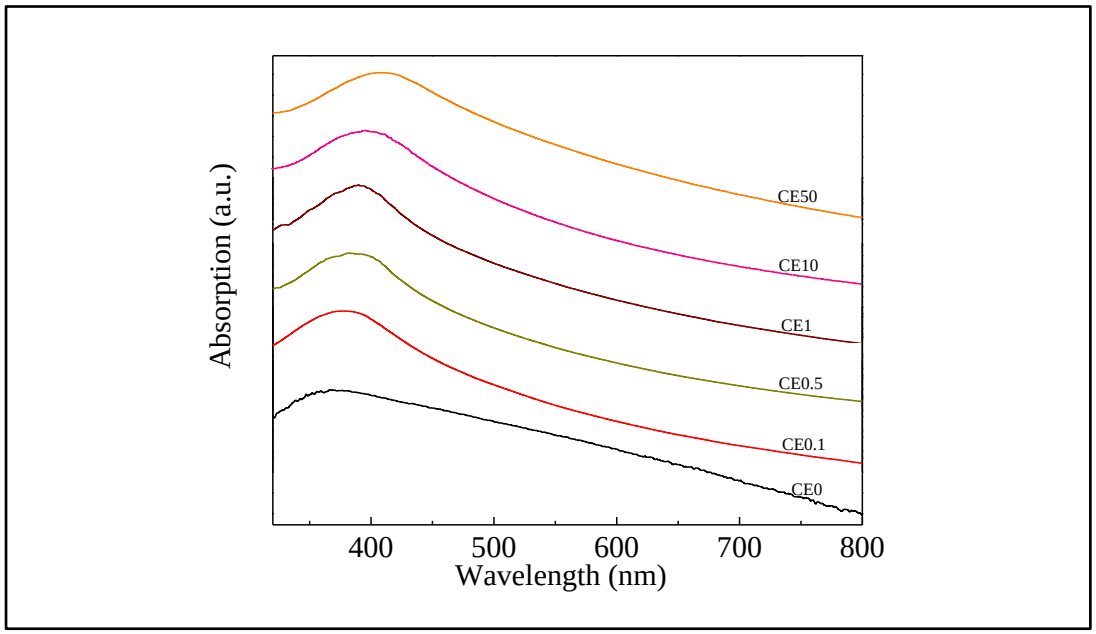

Figure 4.6. Optical absorption spectra of the undoped and a few of the europium doped CeO_2 samples.

The optical properties of CeO_2 also showed an unusual variation in the band gap energy (E_g) with europium doping and, consequently, crystallite size. Typical data are given in Figure 4.6 as optical absorption spectra. E_g can be calculated using:

$$\alpha h\nu = A\left(h\nu - E_g\right)^n \qquad \text{Eq. 4.3}$$

where A is a constant, hν is the photon energy and n depends on the nature of transition (n = 1/2 for direct transition and 2 for indirect transition).[25, 26] CeO_2 is a direct band gap semiconductor and therefore the optical band gap for the samples can be obtained by extrapolating the linear portion of the $(\alpha h\nu)^2$ vs. hν curve to zero. The error in the determination of the band gap energy due to the fitting procedure was estimated ~ 2 meV.

The E_g as a function of europium concentration and crystallite size is shown in Figure 4.7 (a) and (b) respectively and displays a clear maximum around 6-7 nm. It is suggested that this is due to two opposing effects. Firstly, as the europium content increases (and size generally decreases as described above), the apparent value of E_g decreases because of the creation of additional energy levels within the band gap of the undoped sample. However, as the size decreases (i.e. europium content increases) there is a tendency towards higher E_g values because of quantum confinement effects expressed by the relationship[27]

$$E_{g(nano)} - E_{g(bulk)} = \frac{\hbar^2\pi^2}{2er^2}\left(\frac{1}{m_e m_0} + \frac{1}{m_h m_0}\right) - \frac{1.8e}{4\pi\varepsilon\varepsilon_0 r} \qquad \text{Eq. 4.4}$$

Here, r represents the radius, m_0 is the electron mass and m_e and m_h are the relative effective masses of the electron and hole respectively. Li *et al.*[28] reported that the exciton Bohr radius for CeO_2 is 7-8 nm and hence quantum confinement effects including increased band gaps would be seen at and below this value. Interestingly, the increase in E_g seen at low dimension occurs around this size as clearly seen in the Figure 4.7 (b). Similar changes in the band gap E_g have been seen in nanosized CdS particles.[29] The overall decrease of the band gap energy with decreasing particle size is to be understood as due to electron–phonon coupling phenomenon[30] and the effect dominates over quantum confinement when the particle size decreases further below 6.09 nm.

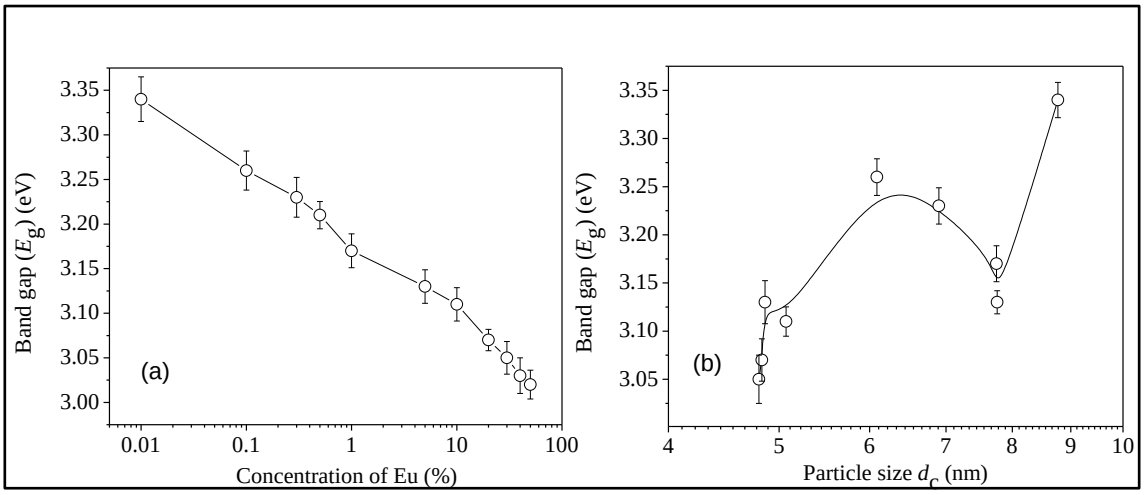

Figure 4.7. (a) The calculated band gap energies of the undoped and europium doped CeO_2 samples (b) The same versus size of the nanoparticles in the undoped and europium doped CeO_2 samples.

The above data clearly detail the response of the host ceria fluorite lattice to europium ion inclusion. However, the defect mechanism associated with this process has not been discussed. It is clear that the number of vacancies will increase with europium doping to charge compensate the 3+ states substituting for 4+ lattice cations. Less clear is an understanding of Ce^{3+}-vacancy combinations that might be formed as a result of lattice and other energy changes resulting from europium inclusion. Positron annihilation studies might prove useful as defect sites can act as positron trapping sites and authors such as Liu *et al.* have demonstrated the usefulness of this spectroscopic method.[31] The results of the present investigation are shown in Figure 4.8 (a) to (e). These results show distinct differences from those of Liu *et al.* on pristine ceria materials. As in earlier work, three different components of positron lifetime were observed in all the samples. The lifetimes are labelled as τ_1, τ_2 and τ_3 in increasing order of their magnitudes and their relative intensities are named as I_1, I_2 and I_3 respectively. As can be seen in the data, the variation of each lifetime component with europium concentration is similar suggesting some interaction between the states.

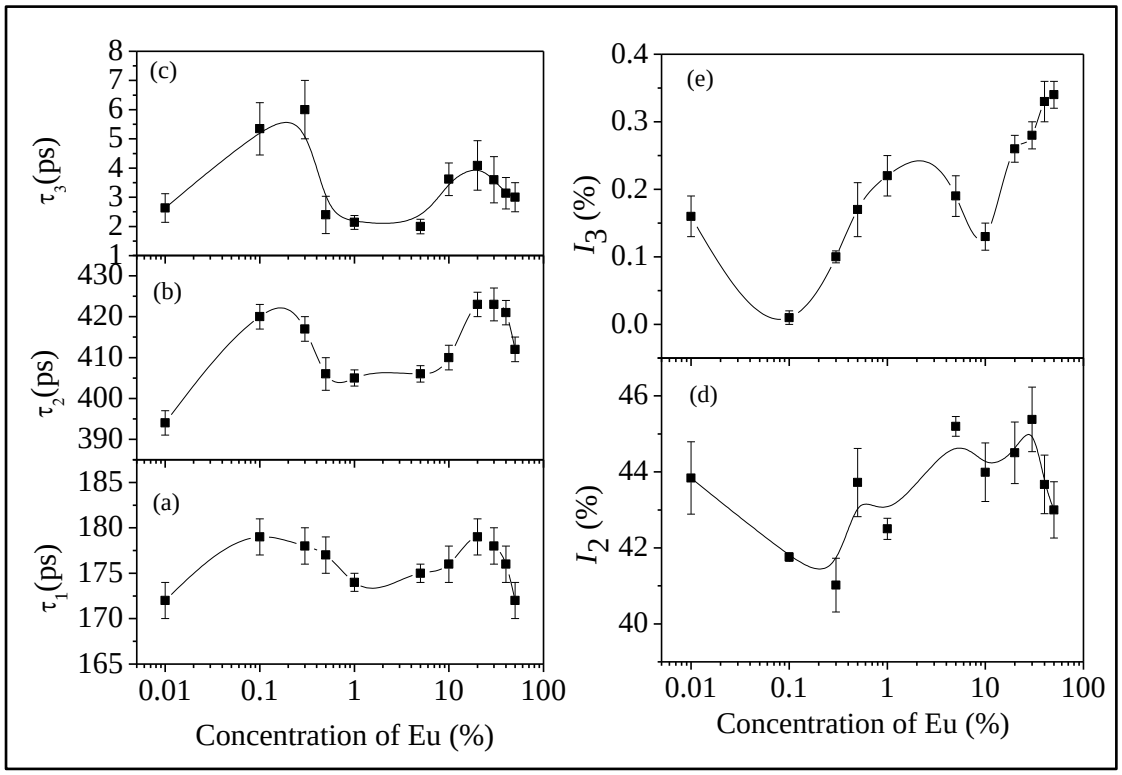

Figure 4.8. The positron lifetimes (a) τ_1, (b) τ_2 and (c) τ_3 and intensities (d) I_2 and (e) I_3 versus the concentrations of europium doping in the CeO_2 nanocrystalline samples. The values shown against 0.01 stand for the undoped sample.

The longest component, τ_3, can be assigned to the formation of orthopositronium atoms in the free volume separating the nanoparticles since positron in such extended defects will have very long lifetimes due to the temporary bound states formed. Although the intensities (I_3) are very small, they were needed to be included in the data analysis to adequately fit the data and since they follow the same pattern of variation as the other positron lifetime parameters, their presence cannot be ignored.

The intermediate positron lifetime τ_2 is not typical of other single lifetime features seen in bulk materials and it is suggested that this lifetime is assignable to Ce^{3+}-vacancy combination sites within the nanocrystallites. The values of τ_2 (> 400 ps) would suggest the presence of large size voids or vacancy clusters, but this is inconsistent with the structure of dense nanocrystallites as described above. Since the size of the nanocrystallites formed here are below the thermal diffusion length of

positrons in typical metallic oxides (~ 50-100 nm), it could be suggested that τ_2 is the lifetime based around contribution from surface positron annihilation and a defect specific lifetime. However, since the variation of τ_2 is quite similar to that of the other parameters, τ_1 and τ_3, changes taking place in the crystal structure may also have important bearing on its values and variation.

Notably, significant difference between the shortest positron lifetime τ_1 and those previously reported can be seen.[31] Liu *et al*. had attributed τ_1 ~ 236-247 ps to neutral Ce^{3+}-oxygen vacancy associates. Here in this work, the magnitudes of τ_1 are smaller (τ_1 ~ 172-179) and their variations are also relatively less. They are also significantly less than those reported in other works that have assigned the same lattice defect where values of τ_1 ~ 262 ps[32] and τ_1 ~ 187.9-211.1 ps[33] have been reported. Although the mean positron lifetime (defined later) may differ by small amounts due to differing sample conditions, the differences between this work and the previous ones would suggest that τ_1 contribution is not due to those types of defects and instead we suggest that the shortest lifetime τ_1 is related to free positrons, i.e., those which do not get trapped by the vacancy defects within the nanoparticles. Note, that these are not typical of bulk lifetimes (τ_b) since the crystallites are so small that free positrons can diffuse to the surface where they are annihilated. Further τ_1 shows a small qualitative variation (Figure 4.8 (a)) similar to that of τ_2 and it is posited that a minor contribution to τ_1 may arise from the Bloch-state residence time of trapped positrons, in accordance with the positron trapping model.

According to the two-state positron trapping model,[34] i.e., a situation where there is only one dominant type of positron trapping sites (i.e. a Ce^{3+}-oxygen vacancy associates), the positron trapping rate κ for the 'bulk-like state' is given by the relationship:

$$\kappa = \frac{1}{\tau_1} - \frac{1}{\tau_b} \qquad \text{Eq. 4.5}$$

where the lifetime τ_b of positrons annihilating in bulk crystals of CeO_2 is taken as 187 ps (Chang *et al.*[32]). But the positron trapping rate when derived from the measured positron lifetimes should also satisfy the relationship:

$$\kappa_{exp} = I_2 \left(\frac{1}{\tau_1} - \frac{1}{\tau_2}\right) \qquad \text{Eq. 4.6}$$

For all concentrations of europium, the data suggest that $\kappa_{exp} > \kappa$. As suggested above, the defect related lifetime τ_2 is larger (394-423 ps) than expected for a cerium-anion vacancy combination (i.e. not all positrons with lifetime τ_2 and intensity I_2 are providing Bloch-state residence time) and it can be suggested that the majority of positrons are being annihilated at the nanoparticle surfaces. Note that κ_{exp} can be reduced to κ either by assuming smaller values of τ_2 or alternatively decreasing I_2 by a factor κ/κ_{exp}. The first option is unlikely since τ_2 is determined by the concentration of positron trapping vacancy clusters and this is unlikely to be significant in these small particles. It is more reasonable to assume that a fraction $(\kappa/\kappa_{exp})I_2$ of positrons get annihilated in vacancy clusters within the nanoparticles and reduce τ_b to τ_1 by admixing the Bloch-state residence time with it.

The experimentally measured τ_2 can be expressed as a linear combination of positron lifetime at the defect vacancy ($\tau_{vacancy}$) and the positron lifetime at surface ($\tau_{surface}$) as:

$$\tau_2 = \frac{\tau_{vacancy}\, I_{vacancy} + \tau_{surface}\, I_{surface}}{I_{vacancy} + I_{surface}} \qquad \text{Eq. 4.7}$$

where $I_{vacancy} = (\kappa / \kappa_{exp})\, I_2$, $I_{surface} = I_2 - I_{vacancy}$ and $\tau_{surface}$ can be estimated as 450 ps, the typical saturation lifetime of positrons at surfaces of metals and metallic oxides.

The results of this analysis are summarized in Figure 4.9 (a) and (b). The magnitudes of the defect related lifetime show two distinct ranges. In the range from [Eu] = 0 to 1%, $\tau_{vacancy}$ is approximately constant within 277-293 ps and its values are typical of the positron lifetime in Ce^{3+}-oxygen vacancy associates and monovacancies as reported by others.[31-33] Beyond this concentration, it increases monotonously to values 325-330 ps. Significantly, these observations are consistent

with the reports available in literature.[31-33] It is also noteworthy to mention that $\tau_{vacancy}$ does not exhibit any explicit dependence on the particle size (Figure 4.9 (b)). For example, the positron lifetime fell considerably from 302 ps to 273 ps when the particle size varied rather little (4.8 to 4.86 nm only) although this change was caused by an increase in the dopant europium concentration from 5 to 30%. On the other hand, during the increase of particle size from 4.86 to 7.75 nm, the positron lifetime changed by about 20 ps only and even the final decrease by about 16 ps took place when the particle size varied only from 7.75 to 8.77 nm. This means that the change in positron lifetimes, which signifies a change in the defect characteristics (i.e., size or environment), is dependent on the dopant concentration and is less sensitive to the sizes of the nanoparticles. This observation is in sharp contrast to the results illustrated in Figure 4.7 (a) and (b) in which the quantum confinement was shown essentially as a finite size effect and less dependent on the dopant concentration.

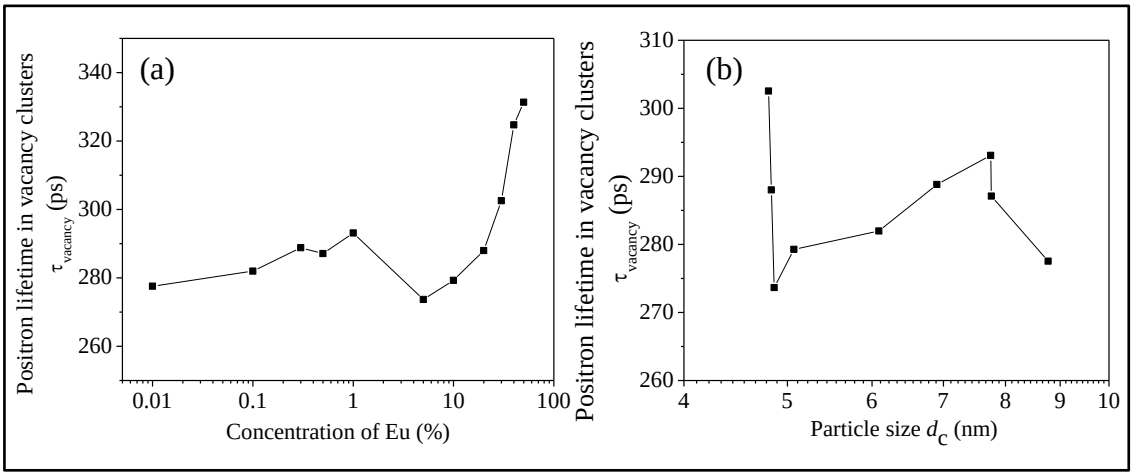

Figure 4.9. (a) The derived positron lifetime in vacancy-type defects $\tau_{vacancy}$ of the undoped (shown against a concentration 0.01) and the europium doped CeO_2 samples. (b) The same versus size of the nanoparticles in the undoped and the europium doped CeO_2 samples.

The variation of the positron lifetimes and their intensities with europium doping and also with the sizes of the nanoparticles can give further information on the evolution of defects and their interaction with the doped ions. The value of $\tau_{vacancy}$ = 277 ps in the undoped sample is larger than the lifetime τ_0 = 187 ps of

positrons annihilating in bulk crystals of CeO_2 by about just 90 ps, which is the typical enhancement in positron lifetime due to trapping in monovacancies. Hence, the positron trapping defects in the undoped sample can be reasonably understood to be of the monovacancy-type within the lattice (i.e., an isolated small polaron state associated with anion vacancy production). The polaron states are generally very strong trapping centre's for positrons and should therefore have short lifetimes. On addition of europium, the additional anion vacancies may allow delocalization of the electrons and hence increase of the positron lifetimes. At high europium concentrations, it seems likely that defect clusters are produced and this results in significant increase in the lifetimes. Although there are no reported values of positron lifetimes in vacancy clusters of CeO_2, similar enhancement in other materials suggests that the values τ_2 = 325-330 ps when compared to τ_2 = 187 ps correspond to vacancy cluster defects consisting of about 4-5 monovacancies. At lower concentrations of doping, since Ce ions were in the 4+ state, the replacement by Eu^{3+} ions creates charge imbalance and formation of an oxygen vacancy which is positively charged. In the region of concentration [Eu] = 0.1 to 1% it would appear that, these anion vacancies are associated with Ce^{4+} ions (effectively reduction to Ce^{3+}) and Ce^{3+}-vacancy clusters or associates are formed. With further increase in the doping concentration, these isolated small associates will agglomerate to form the larger vacancy clusters that results into the very sharp rise of τ_2 to 325-330 ps, as shown here. It might be conjectured that these larger associates are similar in structure to local regions of the M_2O_3 structure consisting of Ce^{3+} and Eu^{3+} metal ions.

As already pointed out, the region of doping [Eu] = 0.1 to 1% is of particular interest since it is associated with an intermittent increase of particle sizes (Figure 4.2) and lattice contraction (Figure 4.4). The calculated vacancy-sensitive lifetime $\tau_{vacancy}$ showed little change in this region (Figure 4.9 (a)) whereas the measured positron lifetimes τ_1, τ_2 and τ_3 fall in this region and the intensities I_2 and I_3 increase. It is, therefore, tempting to assign changes in the measured lifetimes as being due to changing surface effects which appear to cause the apparent high value of τ_2. It is suggested that the first decrease in lifetime seen at low [Eu] = 0.1% concentration is

associated with the lattice contraction mentioned above. There is then an increase in τ_2 which is probably associated with the increased values of $\tau_{vacancy}$. This could be also supported by the nanocrystallite size reduction which allows more rapid movement of positrons to the nanocrystallite surface. The initial decrease of the intensities I_2 and I_3 stems from the lattice expansion effects where the decreasing electron density will reduce the probability of annihilation. Conversely, when the lattice contracts, the intensities would increase. This appears to be true as seen in Figure 4.8 (d) and (e). Further when the crystallite sizes decrease, it would enhance the number of positrons diffusing out to the surfaces and the widening of the intercrystallite region would cause more orthopositronium atoms to form and then undergo pick-off annihilation with the typical lifetimes as shown in Figure 4.8 (c).

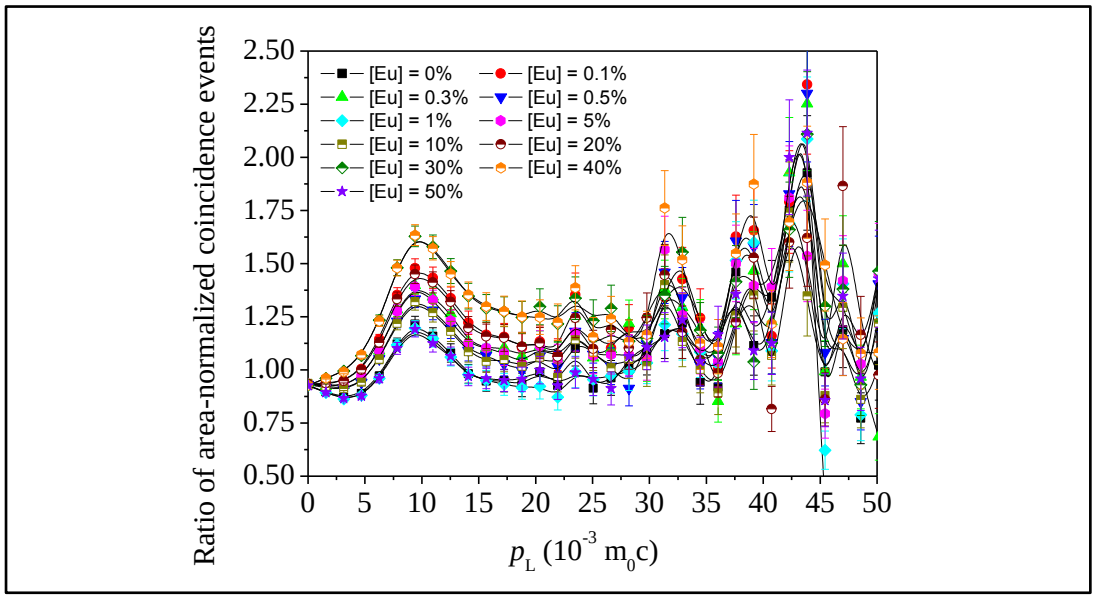

Figure 4.10. The ratio curves or quotient spectra of the different samples with respect to the spectrum of reference Al.

CDBS experiments can provide clarity on changes to the electron momentum distribution in the samples and how positrons develop affinity to these changes. After recording the gamma ray events E_1 and E_2 from the two high sensitive HPGe detectors and noting their time correlations, a two-parameter spectra is generated with $E_1 + E_2$ and $E_1 - E_2$ in the two coplanar axes and counts distributed accordingly.[23,24] The projected one-dimensional spectrum parallel to the energy-difference axis within the energy-sum segment (1022 – 2.4) keV < ($E_1 + E_2$) < (1022

+ 2.4) keV of each sample is then divided by an area-normalized identical spectrum obtained for a pair of pure (99.999%) Al single crystalline samples prior annealed at 625 °C for 2 h in vacuum ($p < 10^{-5}$ mbar). The quotient spectra generated for all the samples are shown in Figure 4.10. The individual features represent positron annihilation events (via interaction with the core electrons of oxygen ions surrounding the cationic vacancies and their clusters) within the samples. The series of the peaks at different momentum appear at p_L ($10^{-3}m_0c$) = 9.4, 23.5, 32.1, 39.2 and 43.1. The features at different positions probably reflect different local structural arrangements of vacancies and the cations ranging from simple, isolated point defects to complex 3D structural arrangements within clusters of defects. Similar features and positions are seen in all samples, but the relative amplitudes of each feature change from sample to sample.

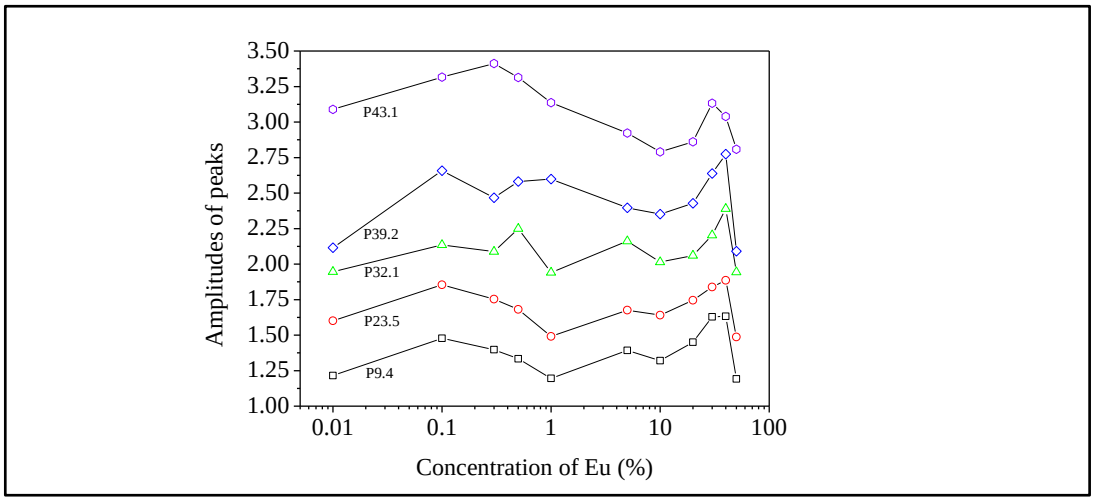

Figure 4.11. The variation of the amplitudes of the different peaks in the CDB spectra of the samples. For the sake of clarity, the amplitudes have been vertically shifted by 0.5 (P23.5), 0.75 (P32.1), 1.0 (P39.2) and 1.25 (P43.1).

The above argument is based on the elemental or ionic sites that are probable in the crystal structure of the europium doped CeO_2 or Ce_2O_3. While the peaks appear at the same values of p_L in all the samples, there are differences in the amplitudes of the peaks for the different samples. The variations in these amplitudes are illustrated in Figure 4.11 and these can be used to further understand the defect mechanism outlined above. In the initial stage of doping, i.e., from the undoped to the 0.1%-doped sample, the amplitudes increase indicating increased annihilation of

positrons. We suggest that this is due to decreasing particle size at this stage which increases positron annihilation at surface states. The succeeding doping interval 0.1 to 1% is the region where the particle size has increased again (Figure 4.2). The opposite effect is, therefore, reflected in the amplitudes. Between 1% and 20% europium loading, there is a general increase in amplitude for the low momentum states indicating increased anion vacancy addition. This increase (to around 10% loading) is seen only at low momentum whereas at high momentum, continued decreases are seen. This may be because these states are more sensitive to clusters of defects which are only present at higher dopant levels and we suggest that high momentum features are due to anion defect clusters and the low momentum states due to isolated defect states.

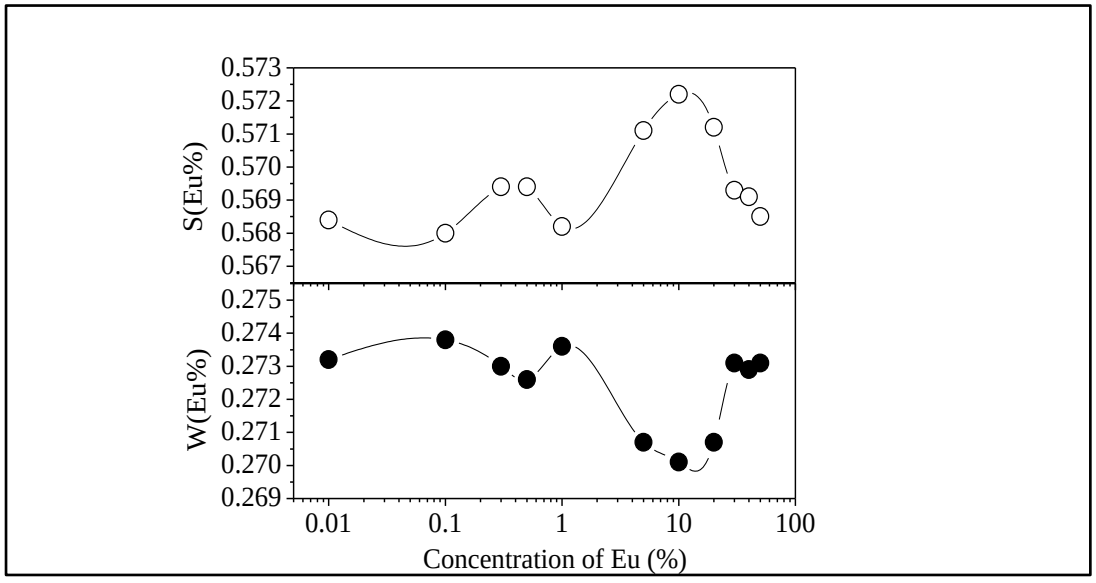

Figure 4.12. The *S* and *W* parameters versus the concentrations of europium doping in the CeO_2 nanocrystalline samples. The values shown against 0.01 stand for the undoped sample. In both the cases, the errors (~ ± 0.0008) are within the sizes of the points.

Between 20% and 40% loading levels, there is a decrease in positron annihilation for all features. It is posited that this decrease is due to the change in stoichiometry of the oxide which is tending towards M_2O_3 rather than MO_{2-x} at these loadings and the structure becomes progressively less defective. However, this region is also characterized by the partial reduction of CeO_2 to Ce_2O_3 by the

formation of oxygen vacancy and hence the decrease is partly arrested in the case of the peaks at high momentum values (i.e., 32.1, 39.2 and 43.1). In the region from 1% to 40% of europium doping, the particle sizes reduce again and the lattice expands due to further reduction of Ce^{4+} to Ce^{3+}. While Ce^{4+} has eight coordinated O^{2-} ions, it decreases to seven when reduced to Ce^{3+} and hence oxygen vacancies further enrich the lattice. Since oxygen vacancies are positively charged, positron trapping is reduced at this stage.

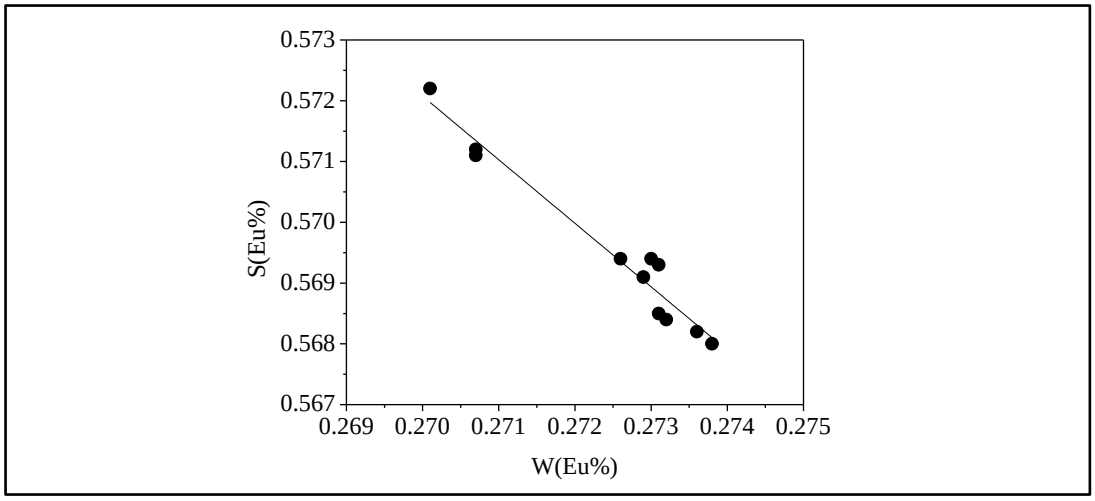

Figure 4.13. The *S* – *W* plot illustrating the linear relationship between the two parameters.

The drastic fall in amplitude of the peak at p_L ($10^{-3}m_0c$) = 43.1 testifies this argument. A rather unusual trend is seen at [Eu] = 50% where all the amplitudes fall down and this may be an indication of segregation of unincorporated Eu^{3+} ions and additional doping may result into the development of new phases, as had been seen in a similar case earlier.[35] Finally, it is worth discussing the results available from a look at the variation of the lineshape parameters *S* and *W* derived from the projected one-dimensional spectra described above, according to the relations

$$S = \frac{\sum_{i=-2}^{2} N_i(\Delta E)}{\sum_{i=-50}^{50} N_i(\Delta E)} \qquad \text{Eq. 4.8a}$$

And $$W = \frac{\sum_{i=-12}^{-4} N_i(\Delta E) + \sum_{i=4}^{12} N_i(\Delta E)}{\sum_{i=-50}^{50} N_i(\Delta E)}$$ Eq. 4.8b

In these equations, $i = 0$ corresponds to $E_1 - E_2 = 2\Delta E = 0$ and each channel was calibrated for 400 eV. The calculated *S* and *W* parameters are plotted against the europium doping concentration and shown in Figure 4.12. Both the parameters vary complementarily as illustrated by plotting one against the other and the straight line that results (Figure 4.13).

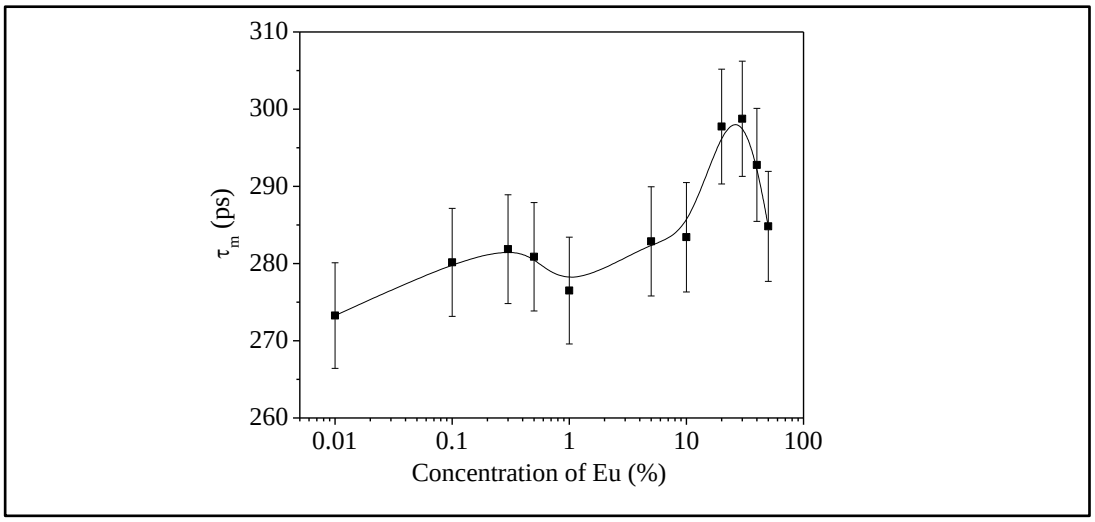

Figure 4.14. The positron mean lifetime τ_m versus the concentrations of europium doping in the CeO_2 nanocrystalline samples. The values shown against 0.01 stand for the undoped sample.

The *S* parameter plot in Figure 4.12 show two distinct peaks at low (around 0.05%) and high (10%) loadings. It is suggested that the lower feature reflects a small increase of anion vacancies being added as the europium is added but this is compensated for by changing crystalline size as described above. The peak at higher europium loadings is due to increased vacancy defect concentration until the formation of an ideal M_2O_3 structure begins to form. These are the regions of increasing particle size accompanied by the generation of additional oxygen vacancies and their complex formation with existing cationic vacancies and quantum confinement effects leading to increase of the band gap energy. These observations further support the findings of the positron lifetime measurements too, as illustrated

by the variation of the positron mean lifetime τ_m in Figure 4.14. τ_m is defined as the weighted average of the positron lifetimes. The similarity of variation of τ_m and *S* derived from two independent experiments cannot be missed in this context.

$$\tau_m = \frac{\sum_{i=1}^{3} \tau_i I_i}{\sum_{i=1}^{3} I_i} \qquad \text{Eq. 4.9}$$

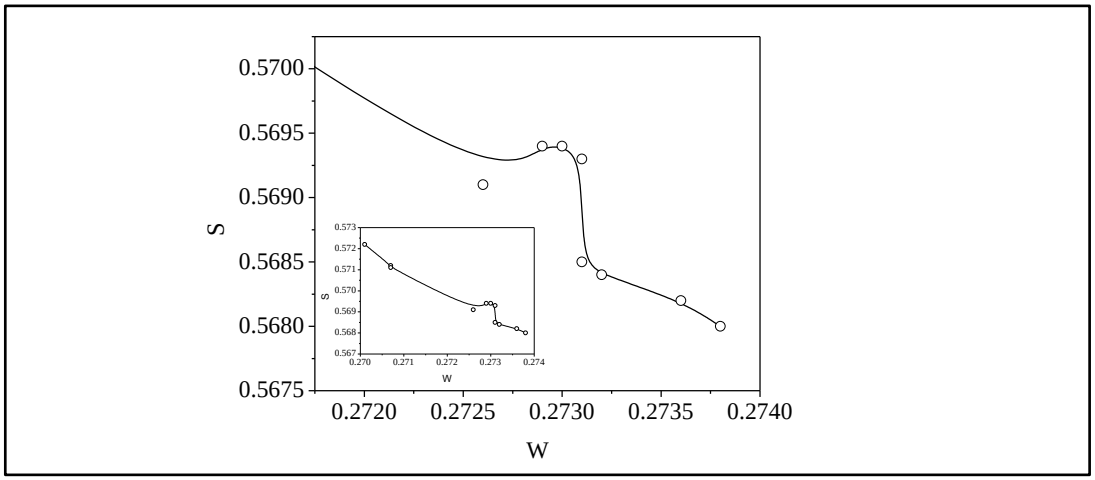

Figure 4.15. The *S* parameter versus *W* in ascending order of magnitude depicting the peak-like variation around the crystallite sizes where quantum confinement effects are prominent. The inset shows the full figure. The region around the peak is expanded in the main figure for clarity.

The *S* parameter values when plotted against the corresponding *W* in ascending order of the latter throws another interesting observation of a distinct kink-like variation in it, as shown in Figure 4.15. Incidentally this happens for the same region of variation of the crystallite size where the indication of quantum confinement effects had been observed from optical absorption measurements (Figure 4.7 (b)). More systematic studies on samples with well-controlled particle sizes are required to comment further on the exact relationship between the fraction of low momentum electrons annihilated by positrons and the changing band gap in the crystallites.

4.4. Conclusions

The results of a detailed investigation carried out using several complementary experimental techniques on CeO_2 nanocrystalline samples doped with varying concentrations of europium are presented in this chapter. A notable observation is the decreasing particle size with increase in the concentration of doping but the trend is interrupted in medium concentrations of doping due to the reduction of Ce^{4+} to Ce^{3+} when an increasing concentration of oxygen vacancies forced an increase in particle size. The change in lattice parameter was just opposite and a linear relation was obtained between the same and the particle size. Optical absorption measurements showed decrease in band gap energy with increasing doping. However, quantum confinement effects being size related manifested in particles of dimensions exactly below the exciton Bohr radius, giving also a characteristic blue shift in the optical absorption spectra. The vacancy type defects were investigated through positron lifetime and CDBS measurements. The intermediate particle size enhancement came as a result of the generation of additional oxygen vacancies in the samples and is indicated by a distinct change in the intensity of positrons trapped in the defects. The positron lifetime within the vacancies was delineated from that due to annihilation at the crystallite surfaces and it was found to enhance due to vacancy agglomeration at higher concentrations of doping. The CDBS measurements demonstrated annihilations taking place with the electrons of ions of different charges and momentum distribution and the variation of the lineshape parameters derived from it further supported the findings from positron lifetime measurements.

4.5. References

1. H. Treichel, R. Frausto, S. Srivatsan, B. Whithers, T. Meyer and R. Morishige, *J. Vac. Sci. Technol., A*, 1999, **17**, 1160-1167.
2. P. Bera, A. Gayen, M. S. Hegde, N. P. Lalla, L. Spadaro, F. Frusteri and F. Arena, *The Journal of Physical Chemistry B*, 2003, **107**, 6122-6130.
3. M. Mogensen, N. M. Sammes and G. A. Tompsett, *Solid State Ionics*, 2000, **129**, 63-94.

4. R. Bene, I. V. Perczel, F. Réti, F. A. Meyer, M. Fleisher and H. Meixner, *Sens. Actuators, B*, 2000, **71**, 36-41.
5. B. Murugan and A. V. Ramaswamy, *J. Am. Chem. Soc.*, 2007, **129**, 3062.
6. P. Dutta, S. Pal, M. S. Seehra, Y. Shi, E. M. Eyring and R. D. Ernst, *Chem. Mater.*, 2006, **18**, 5144-5146.
7. X. Wang, J. C. Hanson, G. Liu, J. A. Rodriguez, A. Iglesias-Juez and M. Fernandez-Garcia, *The Journal of Chemical Physics*, 2004, **121**, 5434-5444.
8. D. A. Andersson, S. I. Simak, N. V. Skorodumova, I. A. Abrikosov and B. Johansson, *Proc. Natl. Acad. Sci. U. S. A.*, 2006, **103**, 3518-3521.
9. H. Borchert, Y. V. Frolova, V. V. Kaichev, I. P. Prosvirin, G. M. Alikina, A. I. Lukashevich, V. I. Zaikovskii, E. M. Moroz, S. N. Trukhan, V. P. Ivanov, E. A. Paukshtis, V. I. Bukhtiyarov and V. A. Sadykov, *J. Phys. Chem. B*, 2005, **109**, 5728-5738.
10. T. H. Etsell and S. N. Flengas, *Chem Rev*, 1970, **70**, 339-376.
11. I. Yeriskin and M. Nolan, *J Phys Condens Matter*, 2010, **22**, 135004.
12. L. Chen, P. Fleming, V. Morris, J. D. Holmes and M. A. Morris, *J. Phys. Chem. C*, 2010, **114**, 12909-12919.
13. S. Tsunekawa, J. T. Wang and Y. Kawazoe, *J. Alloys Compd.*, 2006, **408–412**, 1145-1148.
14. A. Kumar, S. Babu, A. S. Karakoti, A. Schulte and S. Seal, *Langmuir*, 2009, **25**, 10998-11007.
15. P. M. G. Nambissan, *Defect characterization in nanomaterials through positron annihilation spectroscopy*, Studium Press LLC, Houston, USA, 2013.
16. P. M. G. Nambissan, *Journal of Physics: Conference Series*, 2013, **443**, 012040.
17. R. W. Siegel, *Annu Rev Mater Sci*, 1980, **10**, 393-425.
18. J. V. Olsen, P. Kirkegaard, N. J. Pedersen and M. Eldrup, *physica status solidi (c)*, 2007, **4**, 4004-4006.
19. P. AsokaKumar, M. Alatalo, V. J. Ghosh, A. C. Kruseman, B. Nielsen and K. G. Lynn, *Phys. Rev. Lett.*, 1996, **77**, 2097-2100.
20. S. Szpala, P. Asoka-Kumar, B. Nielsen, J. P. Peng, S. Hayakawa, K. G. Lynn and H. J. Gossmann, *Phys Rev B*, 1996, **54**, 4722-4731.
21. A. L. Patterson, *Phys. Rev.*, 1939, **56**, 978-982.

22. K. M. Ryan, J. P. McGrath, R. A. Farrell, W. M. O'Neill, C. J. Barnes and M. A. Morris, *J Phys-Condens Mat*, 2003, **15**, L49-L58.
23. V. Morris, P. Fleming, M. Conroy, J. D. Holmes and M. A. Morris, *Chem. Phys. Lett.*, 2012, **536**, 109-112.
24. S. Deshpande, S. Patil, S. V. N. T. Kuchibhatla and S. Seal, *Appl. Phys. Lett.*, 2005, **87**, 133113.
25. S. Tsunekawa, T. Fukuda and A. Kasuya, *J. Appl. Phys.*, 2000, **87**, 1318-1321.
26. J. Tauc, R. Grigorovici and A. Vancu, *Physica Status Solidi (b)*, 1966, **15**, 627-637.
27. L. E. Brus, *J. Chem. Phys.*, 1983, **79**, 5566-5571.
28. G.-R. Li, D.-L. Qu, L. Arurault and Y.-X. Tong, *J. Phys. Chem. C*, 2009, **113**, 1235-1241.
29. S. Kar, S. Biswas, S. Chaudhuri and P. M. G. Nambissan, *Phys Rev B*, 2005, **72**, 075338.
30. Y. Zhang, T. Cheng, Q. Hu, Z. Fang and K. Han, *J. Mater. Res.*, 2007, **22**, 1472-1478.
31. X. Liu, K. Zhou, L. Wang, B. Wang and Y. Li, *J. Am. Chem. Soc.*, 2009, **131**, 3140-3141.
32. S. Chang, M. Li, Q. Hua, L. Zhang, Y. Ma, B. Ye and W. Huang, *J. Catal.*, 2012, **293**, 195-204.
33. W. Shi, Y. Li, J. Hou, H. Lv, X. Zhao, P. Fang, F. Zheng and S. Wang, *J. Mater. Chem. A*, 2013, **1**, 728-734.
34. P. Hautojärvi and C. Corbel, in *Proceedings of the International School of Physics "Enrico Fermi"*1993, vol. Volume 125: Positron Spectroscopy of Solids, pp. 491 - 532.
35. B. Roy, B. Karmakar, P. M. G. Nambissan and M. Pal, *NANO*, 2011, **06**, 173-183.

Chapter 5

Fabrication of nanopatterned mesoporous silica channels

5.1. Abstract

Mesoporous silica thin films have been studied as potential ultra low dielectric constant materials, where inclusion of ordered pore structure in the silica matrix decreases the dielectric constant. In order to apply this material in various fields, it is important to obtain mesoporous silica films with uniform porosity as well as film thickness. However, a key requirement of these materials is their ability to withstand the various techniques such as reactive ion etching used in processing to generate topographically patterned films. This chapter describes the synthesis of thin films of mesoporous silica with a two-dimensional (2D) hexagonal structure using tetraethyl orthosilicate (TEOS) and triblock copolymers (Pluronics) and fabrication of mesoporous silica topographies with uniform lateral spacing by two different methods. Firstly, by employing lithographic resist followed by etching into the silica and second, *in situ* hard mask block copolymer approach. The crystal structure, morphology, pore arrangement and pore diameters were determined by XRD and SEM. Ellipsometry measurements and cross sectional SEM images were used to determine the thicknesses of mesoporous silica thin films. The ultimate aim was to examine the physical robustness of the films under conventional etch processes used to create porous dielectric films.

5.2. Introduction

Mesoporous silica materials can be synthesized in various forms, such as powders or thin films of thicknesses of about 50 nm to several micrometers. Thin films are interesting object since they can act as coatings on diverse substrates for applications either in catalysis or in drug-delivery. Further, thin films can be prepared with large domains of parallely aligned pores. Large domains with good connectivity are a desired feature for many applications. Mesoporous silica thin films with highly ordered structures are potentially applicable to devices such as optical devices,[1, 2] gas sensors,[3] low dielectric constant films,[4, 5] etc. Specifically, the idea in device applications is to use the mesopores, 4 - 50 nm, to generate ordered arrays of semiconductor nanocrystals, quantum dots within the pore structure.

The most promising hi-tech commercial prospect of mesoporous materials is probably low-dielectric constant (low-*k*) materials in chip fabrication.[6] Traditional chips use condensed silicas as dielectrics with *k* values between 3.9 and 4.2 which cannot meet the demands of nanodevices. Low-*k* materials are, thus, required. A possible solution is of mesoporous silicates showing *k* values lower than 2.2.[7] Zhao *et al*.[8] first reported low-*k* mesoporous silica thin films templated by triblock copolymers with values ranging from 1.45 to 2.1. Larger porosities generally give lower *k* values for the same mesostructure.[9] As-made or long-time resting mesoporous thin films have high *k* values by reason of the polarization of surface silanol groups and the adsorption of water molecules.

Block copolymers have been suggested for many applications based principally on their ability to form regular nanometer-scale patterns. These self-assembled patterns have been considered as nanolithographic masks as well as templates for the further synthesis of inorganic or organic structures. Such applications are made possible by exploiting contrasts in chemical or physical properties that lead to differential etch rates or attractions to new materials. New applications in fuel cells, batteries, and optoelectronic devices rely on the inherent properties of the blocks. All of these uses depend on the extremely regular self-assembly of block copolymers over macroscopic distances.

All porous materials investigated in this work have mesopores and show pore diameters of ~ 6 - 15 nm. The structural framework of the materials consists of silica units and the porosity is created by Evaporation Induced Self-Assembly (EISA) process with the help of a triblock copolymers.

5.3. Experimental

5.3.1. Materials

Tetraethyl orthosilicate (TEOS, ≥99.999%), 0.2 M HCl, anhydrous ethanol (≥99.9%), absolute ethanol, oxalic acid dihydrate ($C_2H_2O_4$•$2H_2O$) and iron(III) nitrate nonahydrate ($Fe(NO_3)_3$•$9H_2O$) were purchased from Sigma-Aldrich and used as received. All Pluronics were purchased from BASF and used as received. A

polystyrene-b-poly(ethylene oxide) (PS-b-PEO) diblock copolymer was purchased from Polymer Source and used without further purification (number-average molecular weight, M_n, PS = 42 kg mol^{-1}, M_n, PEO = 11.5 kg mol^{-1}, M_w/M_n = 1.07, M_w: weight-average molecular weight).

5.3.2. Substrate preparation

Substrate preparation, especially the cleaning of substrates, is critically important in thin film experiments, as any dust or dirt will affect the properties of the final film. Ethanol was used to rinse as-purchased silicon substrates. Silicon substrates were degreased in absolute ethanol by sonication for 30 min, which were then dried under a nitrogen stream.

5.3.3. Synthesis of mesoporous silica thin films

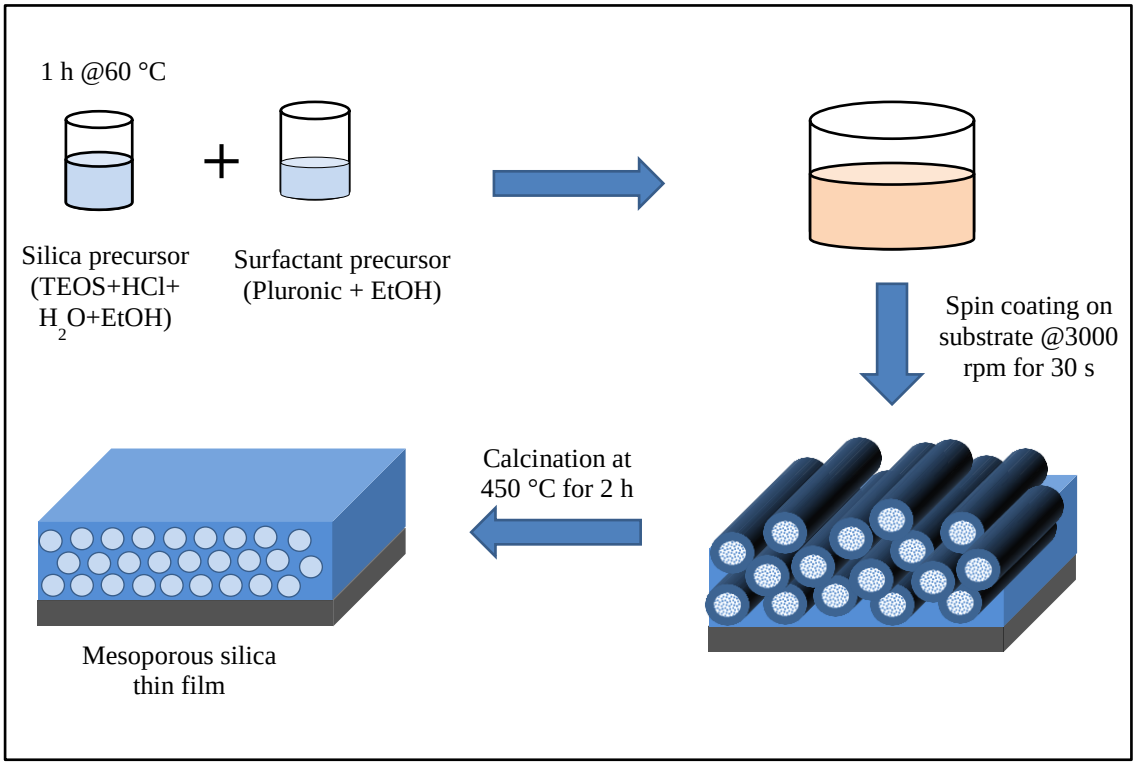

Scheme 5.1. Schematic of the synthesis of mesoporous silica thin films.

We have prepared mesoporous silica thin films using triblock copolymers (Pluronics) on silicon substrates by following a variation in the procedure reported previously.[10] The procedure to synthesis the mesoporous silica thin film is shown in scheme 5.1. The preparation began by mixing 2.08 g of TEOS, 3 g HCl (0.2 M), 1.8 g water and 5 ml anhydrous ethanol in polyethylene bottle. This solution was then heated at 60 °C for 1 h in temperature-controlled preheated electric oven. This solution was allowed to cool down to room temperature. 15 ml of 5 wt% of Pluronic precursor and 10 ml anhydrous ethanol were added with rigorous stirring. Silicon substrates were coated using this solution at 3000 rpm for 30 s. These silicon substrates then calcined at 450 °C for 2 h at ramp rate of 1 °C/min.

5.3.4. Synthesis of mesoporous silica channels using lithographic resist

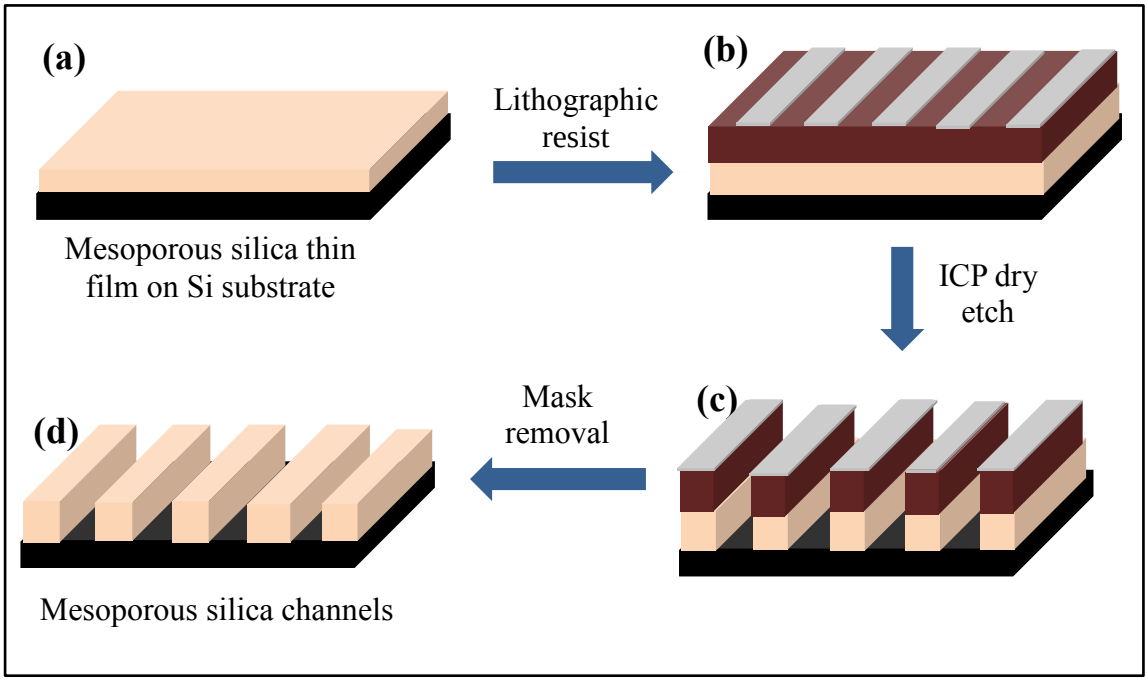

Scheme 5.2. Schematic for the synthesis of mesoporous silica channels using lithographic resist followed by ICP dry etching.

Cheaply available commercial lithographic resist materials such as SU-8 2000 can be used to synthesis the mesoporous silica channels. SU-8 2000 is a commonly used epoxy-based negative photoresist originally developed at IBM.[11] It is a very viscous polymer. Firstly, SU-8 2000 was spin coated over a mesoporous

silica thin film (30 s at 2000 rpm). The thickness of photoresist can range from below 1 micrometer up to above 300 micrometers and still be processed with standard contact lithography. It is used to pattern high aspect ratio (> 20) structures. To obtain vertical sidewalls in the SU-8 2000 resist, a long pass filter was used to eliminate UV radiation below 350 nm. Strong agitation was done while developing thick film structures. Then this photoresist is ICP dry etched for specific time to fabricate the mesoporous silica topographies.

5.3.5. Synthesis of mesoporous silica pillars using *in situ* hard mask block copolymer approach

The PS-b-PEO thin film (molecular weight (in the ratio of PS-PEO) 42 kg mol^{-1}-11.5 kg mol^{-1} (42K-11.5K)) was fabricated by spin coating the polymer solution at 3000 rpm for 30 s on as-synthesized mesoporous silica film. The film was exposed to a toluene–water (50 : 50, v/v) mixed vapour placed at the bottom of a closed vessel kept at 50 °C for 1 h to induce mobility and allow microphase separation to occur. Separate reservoirs were used for each solvent to avoid azeotropic effects. The resultant phase separated film was immersed in ethanol at 40 °C for 15 h. After 15 h film was dried under nitrogen stream. For the fabrication of oxide nanodots, iron(III) nitrate precursor was used. 0.4 wt% of iron(III) nitrate was dissolved in ethanol and spin coated onto the nanoporous film. UV/ozone treatment was used in order to oxidize the precursor as well as to remove polymer residues. These iron oxide nanodot arrays were used as a hard mask for pattern transfer onto the substrate.

5.3.6. Plasma etch pattern transfer

Pattern transfer was accomplished using an STS, Advanced Oxide Etch (AOE) ICP etcher. The system has two different RF generators, one to generate and control the plasma density by direct connection to the antenna coil, while the other one was used to adjust and control the energy of ions by connecting it to the substrate holder. The height of the mesoporous silica features was varied by simply varying the silica etch time. For the removal of iron oxide nanodots, the substrate was immersed into 10 wt% aqueous solution of oxalic acid dihydrate

($C_2H_2O_4$•$2H_2O$) for 2 h at room temperature followed by washing with water and drying of substrates.

5.4. Results and Discussion

5.4.1. Optimization of synthesis conditions for mesopores silica thin films

5.4.1.1. *Concentration of TEOS precursor*

To form uniform mesopores, concentration of silica precursor i.e. TEOS need to be chosen carefully.[12, 13] Figure 5.1.(A), (B) and (C) shows the low angle XRD patterns of mesoporous silica thin films synthesized using 0.01, 0.005 and 0.0033 M concentration of TEOS respectively together with a Pluronic P-123 surfactant. The as-synthesized mesoporous silica thin films using 0.01 M TEOS exhibits the main

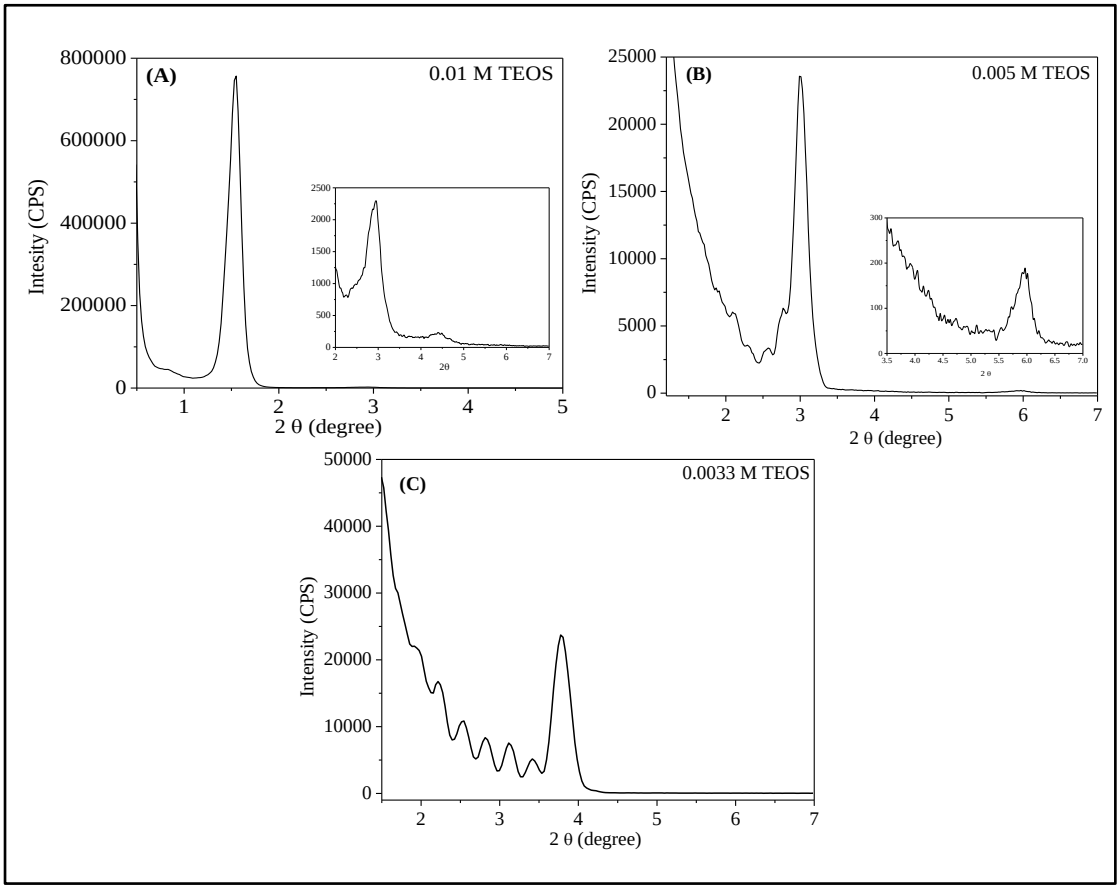

Figure 5.1. XRD graphs of mesoporous silica thin films using (A) 0.01 M (B) 0.005 M and (C) 0.0033 M of TEOS precursor. Inset of figure (A) and (B) shows expanded region around the peak for clarity.

peak, 2nd (200) and 3rd (300) order reflections at 1.54°, 2.95° and 4.42° respectively (Figure 5.1.A), indicating the high degree of long range ordering present in the mesoporous silica thin films. Absence of 3rd (300) order reflections, broadening of the main peaks and presence of additional multiple peaks were seen in mesoporous silica thin films prepared using 0.005 and 0.0033 M TEOS as shown in figure 5.1.(B) and 5.1.(C) respectively, suggesting less structural ordering in the mesoporous silica thin films at the lower TEOS concentrations.[14, 15] The absence of a (110) reflection indicates that the porous arrangements within the films is 2D hexagonal and pores are parallel to the surface plane for 0.01 M TEOS with P-123 system.

5.4.1.2. *Different types of Pluronic*

The pore sizes and pore spacing in mesoporous silica thin films are also dependent on the type of Pluronic used in the synthesis. We have used Pluronic P-123, P-85 and P-65 to form the mesoporous silica thin films. Each Pluronic have different molecular weight that can give different pore sizes due to the specific micellar arrangement in solution.[16, 17] Figure 5.2 shows the XRD patterns of synthesized mesoporous silica thin films using P-123, P-85 and P-65. Mesoporous silica thin films synthesized using Pluronic P-123 and P-85 exhibits the main peak, 2nd (200) and 3rd (300) order reflections at 1.54°, 2.95°, 4.42° and 1.86°, 3.62°, 5.51° respectively, indicating the high degree of long range ordering present in the mesoporous silica thin films. However, the shift in peak positions for mesoporous silica thin films synthesized using P-85 towards the high angle direction confirms the decrease in pore spacing. Whereas, broadening of the main peak and the absence of 2nd and 3rd order reflections indicates less structural ordering in the mesoporous silica thin films synthesized using P-65. The absence of the (110) reflection indicates that the porous arrangements within the films is 2D hexagonal and pores are parallel to the surface plane for P-123 and P-85 with 0.01 M TEOS system.

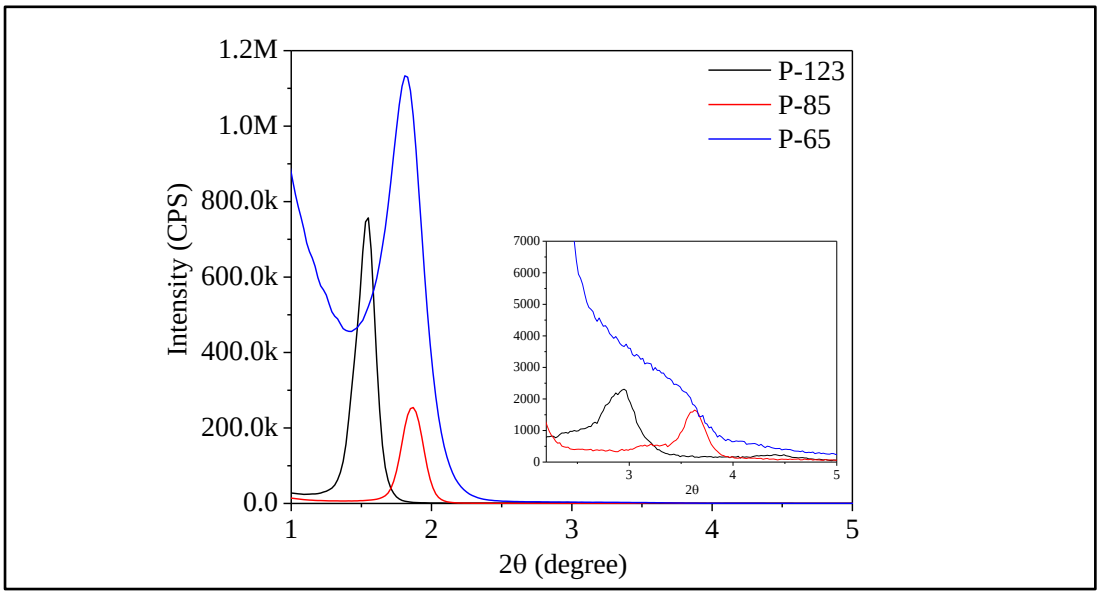

Figure 5.2. XRD graphs of mesoporous silica thin films using different Pluronics (A) Pluronic P-123 (B) Pluronic P-85 and (C) Pluronic P-65

Table 5.1 Film thickness, pore sizes and peak positions of mesoporous silica thin films with various conditions.

Precursor	2θ (°) (main peak)	Film thickness (nm)	Average pore diameter (nm)
0.01 M TEOS + P-123	1.54	100	14
0.005 M TEOS + P-123	2.99	42.2	11
0.0033 M TEOS + P-123	3.78	25.6	10
P-123 + 0.01 M TEOS	1.54	100	14
P-85 + 0.01 M TEOS	1.86	95	7
P-65 + 0.01 M TEOS	1.85	87	Not measurable

5.4.2. Morphological study of mesoporous silica thin films by SEM

The morphology and pore size of mesoporous silica thin films were determined from the SEM studies. Figure 5.3 (a) shows that cross-sectional SEM of mesoporous silica thin film obtained using Pluronic P-123. The SEM images

confirm XRD observations that mesoporous films have a 2D hexagonal structure with the pores lying parallel to the substrate. The mesopores have diameter within the range of 13-15 nm. The thickness of film is found to be 100 nm (measured by ellipsometry). Furthermore, these films showed no evidence of structural deformation either at the film surface or at the film-substrate interface as well as exhibiting good adhesion to the substrate.

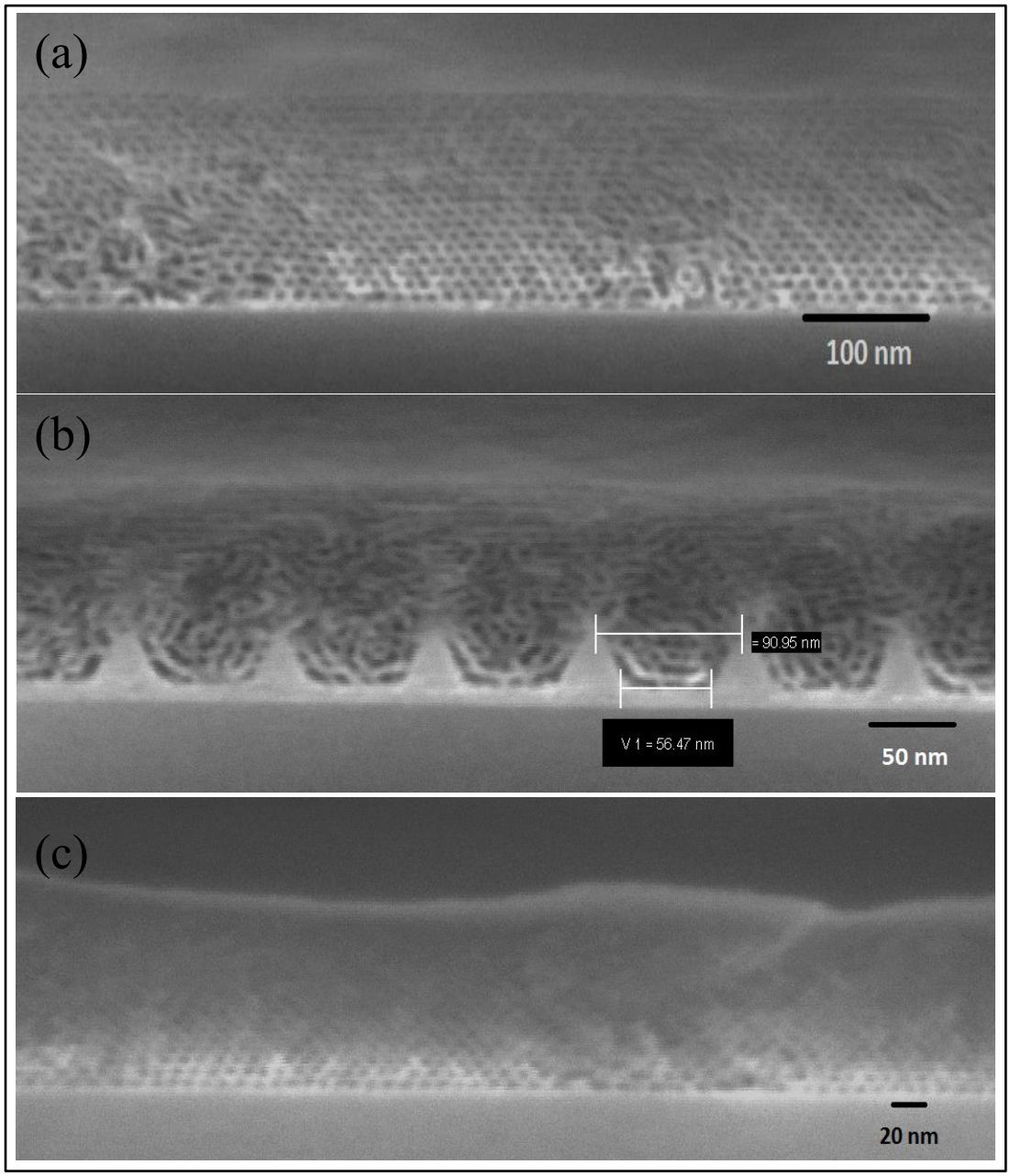

Figure 5.3. Cross-sectional SEM images of mesoporous silica thin films synthesized using (a) Pluronic P-123 (b) Pluronic P-123 on silicon substrate having topographical trenches and (c) Pluronic P-85.

Figure 5.3 (b) shows the cross-sectional SEM images of mesoporous silica thin films spin-coated over silica substrate having topographically patterned trenches. Our group has reported the alignment of nanoporous channels was affected by the use of low aspect ratio (channel width to depth) patterned Si/SiN substrates.[18] Wu et al. have also exploited this technique for aligning mesoporous silica films for use as resist molds.[19] These alignment methods rely on a physically modified substrate to guide the long-range order of the mesoporous silica system. Such an approach has been successfully used to control macroscopic ordering of colloidal spheres and block copolymer films.[20, 21] The mesoporous silica thin films prepared at these substrate showed less well ordered arrangement of the pores than on planar substrates (figure 5.3 (b)). The rather poor order may be due to a number of reasons. These include the trench cross-section, incommensurability of the pore spacing and trench width as well as complex spin-coating film development.

Figure 5.3.c shows the cross-sectional SEM of the mesoporous silica thin films with hexagonally arranged pores synthesized using Pluronic P-85. The average diameter of mesopores was found to be 7 nm. The thickness of film is found to be around 95 nm. These films also showed no evidence of structural deformation either at the film surface or at the film-substrate interface as well as exhibiting good adhesion to the substrate. It is also important to note that in all studies, the upper surface of the film is dense silica and pores are generally not present. This is typical for these films.

5.4.3. Fabrication of mesoporous silica channels using lithographic resist

Figure 5.4 shows the cross-sectional SEM of mesoporous silica channels synthesized using lithographic resist SU-8 2000. SU-8 can be processed with a number of patterning techniques to render high-aspect-ratio and 3D submicron structures. The irradiation source and configuration used for processing determine the maximum lateral resolution, aspect ratio and geometrical complexity of the patterned features.[22] To fabricate mesoporous silica channels, the mesoporous silica thin film surface is partially protected using lithographic resist SU-8 2000 as an etch mask, followed by ICP dry etching. The thickness and width of the mesoporous

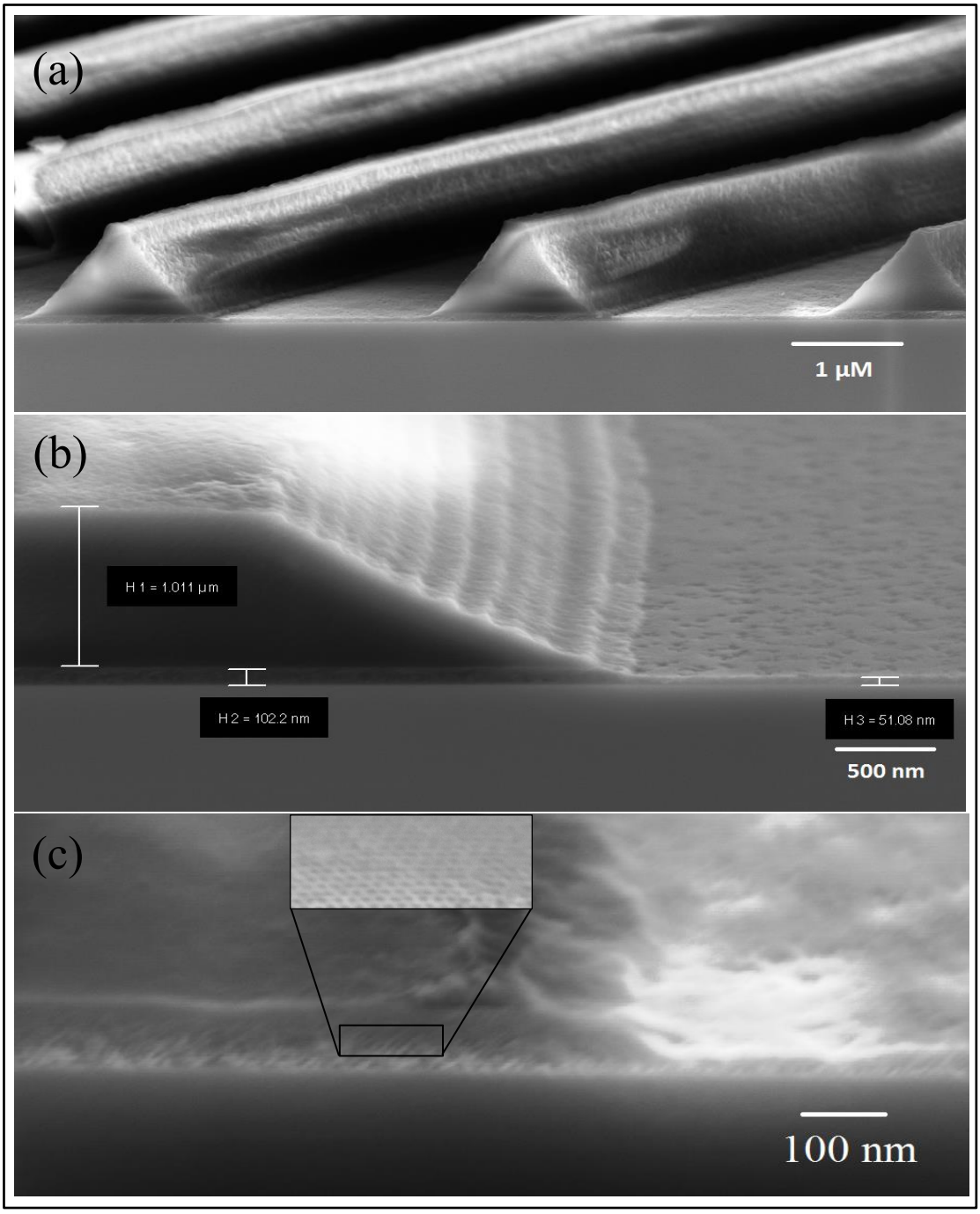

Figure 5.4. Cross-sectional SEM images of mesoporous silica thins films after ICP dry etching (a) etched mesoporous silica thin film with lithographic resist on the top (b) magnifying image of the etched mesoporous silica thin film (c) etched mesoporous silica thin film after removal of lithographic resist (inset shows the magnifying image for clarity).

silica channels can be varied using different lithographic resist as well as by varying the etching time. Figure 5.4 (a) shows ICP dry etched mesoporous silica channels having the lithographic resist on the top. Figure 5.4 (b) shows the magnifying image of etched and unetched (protected below the lithographic resist) mesoporous silica thin film. The thickness of the unetched mesoporous silica thin films was 100 nm. After 10 s ICP dry etching, mesoporous silica film thickness decreased due to etching and found to be approximately 50 nm (as measured by ellipsometry). After etching process, lithographic resist can be easily removed using mild oxalic acid solution. Figure 5.4 (c) shows the 10 s ICP dry etched and unetched mesoporous silica thin film (protected below the lithographic resist) after removing lithographic resist. Magnifying image of ordered mesopores are shown in inset of Figure 5.4 (c). Figure suggests that, after etching treatment pores are quite stable without disturbing the hexagonally arranged pore structure.

5.4.4. Fabrication of mesoporous silica channels using *in situ* hard mask block copolymer approach

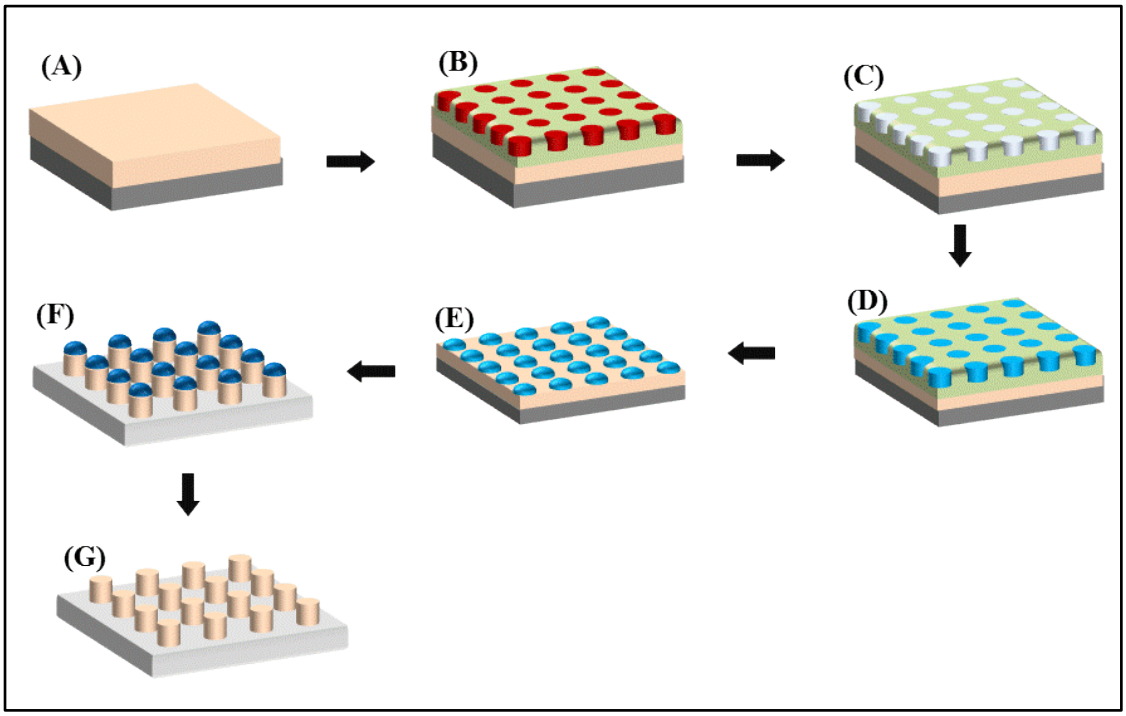

Scheme 5.3. Schematic illustration of the fabrication mesoporous silica channels using *in situ* hard mask BCP approach.

Whilst the standard lithography systems appeared to indicate good resistance of the mesoporous film to pore collapse during etching. These are large features and for proper validation of the film robustness it is necessary to prepare small features. Since these are consistent with modern manufacturing dimensions. It was, thus, though necessary to create small features using block copolymer lithography.

Scheme 5.3. illustrates the process flow diagram of the fabrication of ordered mesoporous silica nanopillars. The as synthesised of mesoporous silica thin film on silicon substrate is shown in Scheme 5.3 A. The as-deposited hexagonally arranged microphase separated BCP film on the mesoporous silica film is illustrated in Scheme 5.3 B. This BCP film was treated with ethanol causing 'activation' of the PEO cylinders (Scheme 5.3 C). Iron nitrate solution was then spin-coated onto the film and diffuses within the PEO structures driven by capillary solution forces (Scheme 5.3 D). UV/ozone treatment was carried out to convert the precursor into iron oxide as well as for complete degradation of the residual polymers (Scheme 5.3 E). Iron oxide nanodots remain on the top of mesoporous silica film. Mesoporous silica pillars having nanodots on the top were formed by ICP dry etching for 20 s (Scheme 5.3 F) using the iron oxide as a hard mask. Iron nanodots were easily removed by using mild oxalic acid solution (Scheme 5.3 G).

Figure 5.5 (a) shows an AFM image of the PS-b-PEO thin film demonstrating the vertically orientated hexagonal arrangement expected. These films were formed by solvent annealing[23, 24] in a mixed toluene–water environment to induce long range-ordering and favour vertical cylinder orientation. The minor component, PEO, forms the cylindrical domains (darker contrast in AFM) and the major component, PS, constitutes the matrix (lighter contrast in AFM). The measured average centre-to-centre cylinder spacing is ≈ 42 nm with a PEO cylinder diameter of ≈ 19 nm. The strong multiple peaks in the Fast Fourier Transform (FFT) pattern shown in the inset of figure 5.5 (a) confirm a microphase separated structure with highly ordered hexagonal arrangement of PEO cylinders. The SEM image in figure 5.5 (b) also represents long range ordering of the PS-b-PEO thin film.

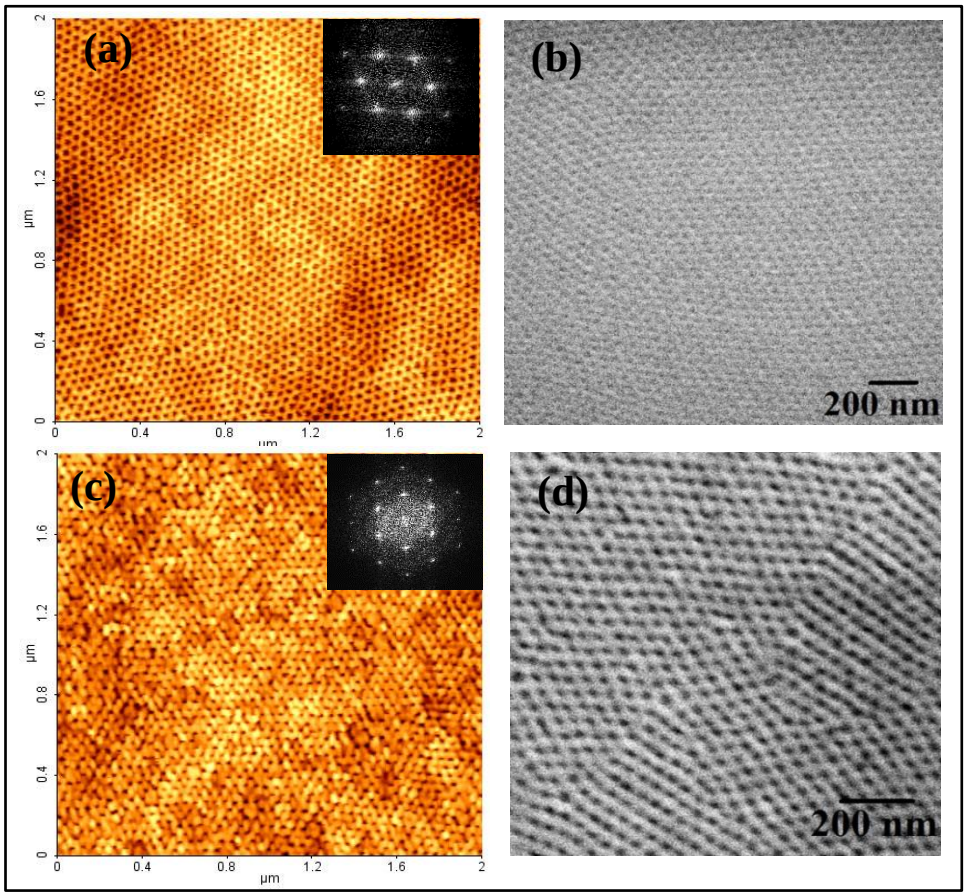

Figure 5.5 AFM (a and c) and SEM (b and d) images of PS-b-PEO thin film and solvent annealed thin film in toluene–water at 50 °C respectively. Insets of (a) and (c) shows the corresponding FFT pattern.

When the solvent annealed films were ethanol treated at 40 °C for 15 h, modification of the film occurred although the structural arrangement and dimensions are unchanged. Longer exposure to ethanol and higher temperatures resulted in structural degradation and 15 h was seen to be an optimum treatment.[25] The AFM image (figure 5.5 (c)) shows some increase in the phase contrast and an increase in the long-range order after this treatment. This is also indicated by the FFT pattern of the AFM image (inset, figure 5.5 (c)) where six-point patterns with multiple higher order reflections are shown, characteristic of exceptional long-range order. Also, the SEM image contrast was enhanced by ethanol exposure as seen in figure 5.5 (d). No thickness loss was observed after the ethanol treatment as measured by optical ellipsometry. The ethanol treatment is a pre-requisite to form

well-defined oxide nanopatterns in later steps and is described as an 'activation step' although it is less clear exactly how much PEO is modified or removed in this process step.

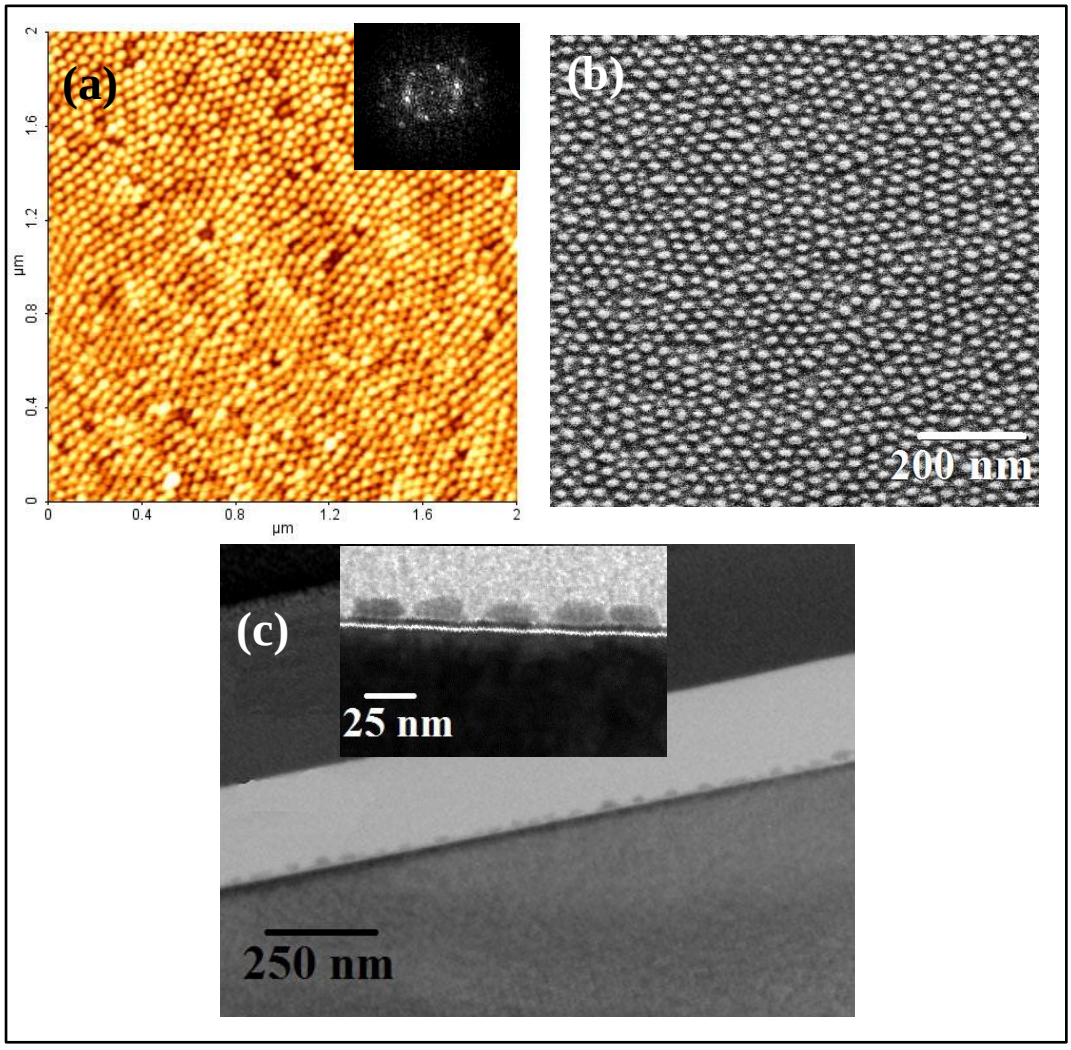

Figure 5.6. (a) AFM (b) SEM and (c) cross-sectional TEM images of hexagonal ordered iron oxide nanodots after UV/ozone treatment. The inset of (a) shows the corresponding FFT pattern and inset of (c) shows the corresponding higher magnification image.

Iron oxide nanodots are formed by simple inclusion of iron ions from a metal nitrate ethanol solution into the PEO component. The hydrophobic nature of PS excludes any probability of the iron inclusion into the PS template, so that the PEO activated sites can be considered as sorbtive cylinders with diameter ≈ 20 nm and depth ≈ 28 nm. PEO is known to have good affinity with cations[26] and it is believed

that swelling of PEO by ethanol allows rapid incorporation of the metal cations or perhaps colloidal entities into these active cylinders. After iron ion inclusion, UV/ozone treatment was carried out immediately so as to remove any solvent, oxidize and cross-link metal ions forming oxides and remove the organic part simultaneously. Alternatively, treatment with UV/ozone to cross-link the metal ions followed by air calcination can also be pursued for oxidation and complete removal of the residual polymer.

Figure 5.6 shows the AFM, SEM and cross-sectional TEM images of well-ordered iron oxide nanodots formed after the UV/ozone treatment. From the AFM and SEM images, the measured average centre-to-centre nanodot distance is ≈ 42 nm and the FFT pattern shown in the inset of figure 5.6 (a) confirms the hexagonal ordering of the iron nanodots. This confirms that these have been produced via direct templating of the PS-*b*-PEO film. Figure 5.6 (a) (AFM) and figure 5.6 (b) (SEM tilt image) show iron oxide nanoparticles of diameter ≈ 21 nm.[27] The structure of these systems is exemplified further by TEM (Figure 5.6 (c)). The cross-sectional TEM image shows well-separated nanodots. The adhesion of the materials is reflected in the integrity of the structures during FIB treatment and the lack of any interfacial cracks etc. at the base of the particles. The same cylindrical-type structure is seen for all imaged nanodots.

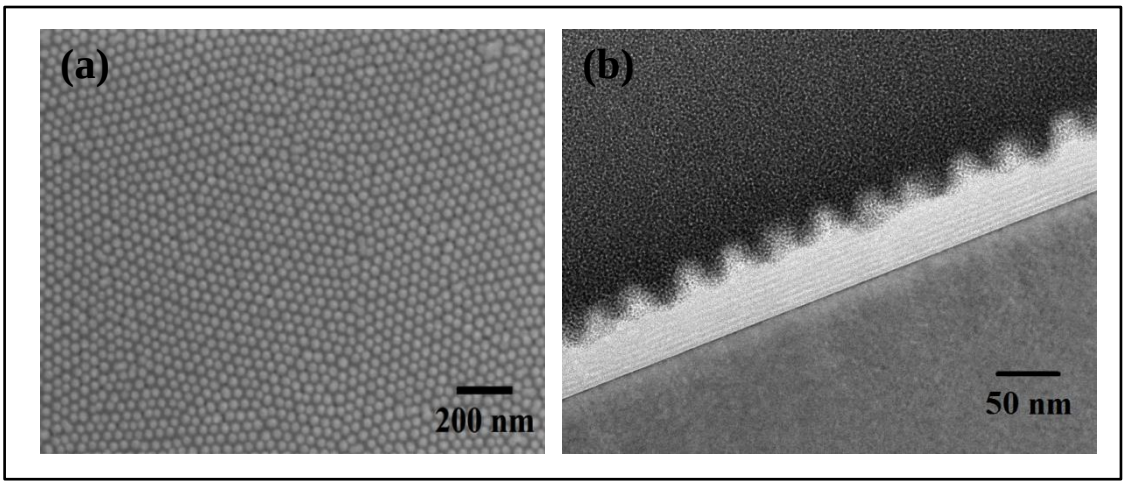

Figure 5.7. (a) Top-down SEM image of nanopillar arrays with iron oxide nanodots at the top formed after pattern transfer onto silica for 10 s (b) cross-sectional TEM image of the mesoporous silica nanopillars.

These iron oxide nanodots were then used as a hard mask for the formation of mesoporous silica nanopillars by pattern transfer into the mesoporous silica film. Briefly, a rapid silica etch process was used to remove the exposed mesoporous silica layer at the substrate surface whilst the layer below the iron oxide nanodots (mask) remained unaffected. The pattern transfer process was performed by the silica etch process described earlier. This process results in the formation of mesoporous silica nanopillars with iron oxide at their uppermost surface. The top–down SEM image (figure 5.7 (a)) demonstrates a densely packed, uniform, ordered arrangement over large areas after the pattern transfer. The high resolution SEM image also reveals that the hexagonally ordered pillars have an average diameter of ≈ 21 nm at a spacing of ≈ 42 nm. This implies that the etching does not damage the original pattern to any extent. The average height of the mesoporous silica nanopillars is found to be around 25 nm and mesoporous silica thin film thickness is found to be approximately 60 nm (measured from the cross-sectional TEM image shown in figure 5.7 (b)) after silica etch for 10 s. These data clearly shows that the mesoporous surface is robust enough to survive etching.

5.5. Conclusion

A simple, generic and cost-effective route was demonstrated to synthesize 2D mesoporous silica thin films over wafer scale dimensions. A morphological study showed that the mesoporous silica thin film has hexagonally arranged pores with uniform pore diameter. Fabrication of mesoporous nanostructures was carried using two different techniques: lithographic resist and *in situ* hard mask block copolymer followed by ICP dry etching. The width of mesoporous silica channels can be varied by using variety of commercially available lithographic resists whereas depth of the mesoporous silica channels varied by varying the etch time. Large area ordered mesoporous silica nanopillar arrays were fabricated with smooth vertical sidewall profiles using an *in situ* hard mask block copolymer approach. The diameter and length of the nanopillars could be precisely varied depending on the diameter of the nanodots and the etching time respectively without altering their shape. The mesoporous silica channels or nanopillars arrays exhibit large surface areas with

direct access to the pore structures. The pore structure survived the etching process and these materials may have importance in a number of applications.

5.6. References:

1. W. C. Molenkamp, M. Watanabe, H. Miyata and S. H. Tolbert, *J. Am. Chem. Soc.*, 2004, **126**, 4476-4477.
2. B. J. Scott, G. Wirnsberger and G. D. Stucky, *Chem. Mater.*, 2001, **13**, 3140-3150.
3. T. Yamada, H. S. Zhou, H. Uchida, M. Tomita, Y. Ueno, T. Ichino, I. Honma, K. Asai and T. Katsube, *Adv Mater*, 2002, **14**, 812-815.
4. C. M. Yang, A. T. Cho, F. M. Pan, T. G. Tsai and K. J. Chao, *Adv Mater*, 2001, **13**, 1099-1102.
5. B. D. Hatton, K. Landskron, W. Whitnall, D. D. Perovic and G. A. Ozin, *Adv. Funct. Mater.*, 2005, **15**, 823-829.
6. M. E. Davis, *Nature*, 2002, **417**, 813-821.
7. S. Baskaran, J. Liu, K. Domansky, N. Kohler, X. H. Li, C. Coyle, G. E. Fryxell, S. Thevuthasan and R. E. Williford, *Adv Mater*, 2000, **12**, 291-294.
8. D. Zhao, P. Yang, N. Melosh, J. Feng, B. F. Chmelka and G. D. Stucky, *Adv Mater*, 1998, **10**, 1380-+.
9. H. Y. Fan, F. Van Swol, Y. F. Lu and C. J. Brinker, *J. Non-Cryst. Solids*, 2001, **285**, 71-78.
10. C. T. Bolger, R. A. Farrell, G. M. Hughes, M. A. Morris, N. Petkov and J. D. Holmes, *ACS Nano*, 2009, **3**, 2311-2319.
11. K. Y. Lee, N. LaBianca, S. A. Rishton, S. Zolgharnain, J. D. Gelorme, J. Shaw and T. H. P. Chang, *J Vac Sci Technol B*, 1995, **13**, 3012-3016.
12. K.-K. Kang and H.-K. Rhee, *Microporous Mesoporous Mater.*, 2005, **84**, 34-40.
13. J. Liu, Q. Yang, X. S. Zhao and L. Zhang, *Microporous Mesoporous Mater.*, 2007, **106**, 62-67.
14. J. Y. Bae, K. T. Ranjit, Z. H. Luan, R. M. Krishna and L. Kevan, *J. Phys. Chem. B*, 2000, **104**, 9661-9669.
15. Z. H. Luan, J. Y. Bae and L. Kevan, *Chem. Mater.*, 2000, **12**, 3202-3207.

16. T. Sakai and P. Alexandridis, *J. Phys. Chem. B*, 2005, **109**, 7766-7777.
17. L. Bronstein, M. Antonietti and P. Valetsky, in *Nanoparticles and Nanostructured Films*, Wiley-VCH Verlag GmbH, 2007, pp. 145-171.
18. R. L. Rice, D. C. Arnold, M. T. Shaw, D. Iacopina, A. J. Quinn, H. Amenitsch, J. D. Holmes and M. A. Morris, *Adv. Funct. Mater.*, 2007, **17**, 133-141.
19. C.-W. Wu, T. Ohsuna, T. Edura and K. Kuroda, *Angew. Chem., Int. Ed.*, 2007, **46**, 5364-5368.
20. R. A. Segalman, H. Yokoyama and E. J. Kramer, *Adv Mater*, 2001, **13**, 1152-1155.
21. I. Bita, J. K. W. Yang, Y. S. Jung, C. A. Ross, E. L. Thomas and K. K. Berggren, *Science*, 2008, **321**, 939-943.
22. A. d. Campo and C. Greiner, *J Micromech Microeng*, 2007, **17**, R81.
23. J. Peng, D. H. Kim, W. Knoll, Y. Xuan, B. Li and Y. Han, *J. Chem. Phys.*, 2006, **125**, 064702.
24. T. Ghoshal, M. T. Shaw, C. T. Bolger, J. D. Holmes and M. A. Morris, *J. Mater. Chem.*, 2012, **22**, 12083-12089.
25. T. Ghoshal, T. Maity, J. F. Godsell, S. Roy and M. A. Morris, *Adv Mater*, 2012, **24**, 2390-2397.
26. C. B. Tsvetanov, R. Stamenova, D. Dotcheva, M. Doytcheva, N. Belcheva and J. Smid, *Macromol. Symp.*, 1998, **128**, 165-182.
27. T. Ghoshal, R. Senthamaraikannan, M. T. Shaw, J. D. Holmes and M. A. Morris, *Nanoscale*, 2012, **4**, 7743-7750.

Chapter 6

Biomineralization at Nanopatterned Surfaces

6.1. Abstract

Staphylococcus aureus and *Pseudomonas aeruginosa* are a ubiquitous environmental bacterium that causes opportunistic human infections. We demonstrate a facile, generic method for the fabrication of ordered silver nanodots on different substrates by using a microphase separated polystyrene-*b*-poly(ethylene oxide) (PS-*b*-PEO) block copolymer (BCP) thin film as a structural template. These silver nanodot arrays are used to examine possible antimicrobial activity over *S. aureus* and *P. aeruginosa* biofilms. A highly ordered PS-*b*-PEO thin film with perpendicularly oriented PEO cylinders was fabricated by solvent annealing over wafer scale dimensions. PEO cylinders were activated by ethanol to create a functional chemical pattern for nanodot development via spin coating and block selective silver ion inclusion. Subsequent UV/ozone treatment forms an ordered arrangement of silver nanodots and removes the polymer components. Silver nanodot arrays have a clear growth-inhibitory effect on *S. aureus* and *P. aeruginosa* biofilms. These silver nanodot arrays shows a potential to be used as a substitute for the resolution of infection complications in many areas.

6.2. Introduction

Biomineralization refers to the processes by which organisms form minerals. The term biomineral refers not only to a mineral produced by organisms, but also to the fact that almost all of these mineralized products are composite materials comprised of both mineral and organic components. Furthermore, having formed under controlled conditions, biomineral phases often have properties such as shape, size, crystallinity, isotopic and trace element compositions quite unlike its inorganically formed counterpart. The term “biomineral” reflects all this complexity.

Nature uses minerals for a wide variety of functions, the most basic of which being skeletal design and mechanical protection. Another fascinating case is the ability of magnetotactic bacteria to synthesize crystalline magnetic nanoparticles for navigation and orientation.[1] Organisms exhibit a level of molecular control over the detailed nano- and microstructure of biomaterials which even the most advanced current materials technologies cannot match. Therefore, understanding the

underlying design principles of biomaterials is the key to developing new approaches to materials fabrication at the nanometer and micrometer scale. Self-assembly is responsible for many fundamental processes in nature, for example, the folding of nucleic acids into their functional forms through specific monomer–monomer interactions.[2] In biomineralization, "matrix" macromolecules can efficiently induce growth of inorganic species at specific locations with controlled orientation. In many cases, these nanomaterials are produced under genetic control, resulting in particular morphologies, sizes and crystallinities of the structures.[3]

Although an extremely interesting and very often useful, phenomenon as described above, biomineralization is not always desirable. The natural accumulation of deposits on surfaces can have issues for materials and health industries. Million cases of nosocomial infections per year are associated with implant devices such as pacemakers, defibrillators, joint orthopaedic replacements and prosthetic cardiac valves.[4] This usually leads to repeated surgical procedures to remove and replace the contaminated material, the consequences of which can be life-threatening for the patient. The nature of increased antibiotic resistance within bacterial biofilms is usually attributed to the shielding of constituent cells within the film, leading to a lack of accessibility. Clearly there is great need to develop new ways of preventing biofilm formation on biological implants. Typical strategies generally rely either on the local application of biocides or on inhibiting bacterial adhesion. In addition, coatings based on antimicrobial peptides (AMPs), enzymes and photoactive materials are thought to have significant microbicidal potential. However, these biomolecules may lose activity upon incorporation into coatings.[5]

Silver coatings have remained a popular area of research for this reason. One common theory is that silver interacts strongly with thiol groups of essential bacterial enzymes, inactivating them.[6] There is also evidence to suggest that the DNA of target bacteria loses its replication ability after exposure to silver.[7] Silver nanoparticles have recently become much more widely used in medical equipment due to notable slow-release antiseptic activities. Yet there remains a lack of information regarding the biological activities of these nanoparticles on human tissue

cells[8] and a number of investigations have reported cytotoxic effects.[9] Furthermore, a uniform dispersion pattern of nanoparticles is extremely difficult to achieve using traditional wet methods of synthesis (generally involving the reduction of a silver salt with a reducing agent in the presence of colloidal stabilizer).[10] Problems in controlling the size and dispersion of particles can lead to agglomeration, which drastically reduces the antimicrobial power of coatings.

An alternative approach is to focus on the fabrication of surfaces which resist bacterial attachment. Research has shown that the adhesion of microbes to surfaces is largely governed by factors such as hydrophobicity, surface roughness, electrostatic interactions and surface compliance.[11] Another method which has been proven to prevent or reduce the adhesion of proteins (and importantly, microorganisms) to materials is to graft PEO chains on the surface. The high mobility of PEO chains and attainment of very large exclusion volumes makes it difficult for incoming particles to approach these surfaces.[12] An investigation by Roosjen *et al*. showed that the application of PEO brushes at surfaces significantly reduced the adhesion of two strains of bacteria under study (S. epidermidis and P. aeruginosa).[13] Although these modified surfaces resist the adsorption of proteins and bacteria, they do not address the issue of deactivating the microbes, which is crucial for preventing microbial contamination.

To date, work carried out by Morris *et al*.[14, 15] in the area of BCP lithography has mainly focussed on applications in electronics and optics. We are now interested in studying the ability of such nanodimensioned templates to resist bacterial adhesion and hence, inhibiting biofilm formation. It is postulated that these nanopatterned surfaces may prevent microbes from adhering due to topographies being far less than typical cell size. As this work is aimed towards the development of new antimicrobial coatings which may have applications in biomedical implant materials, we will investigate the biocidal efficiency of the surfaces on bacterial strains which are most commonly associated with implant infections.

6.3. Experimental

6.3.1. Materials

Silver nitrate ($AgNO_3$, ≥99.0%), toluene (99.9%) and anhydrous ethanol (≥99.9%) were purchased from Sigma-Aldrich and used without further purification. PS-*b*-PEO diblock copolymers of molecular weights 42 kg mol^{-1}-11.5 kg mol^{-1} (42K-11.5K) and 32 kg mol^{-1}-11 kg mol^{-1} (32K-11K) were purchased from Polymer Source and used without further purification.

6.3.2. Substrate preparation

Two different types of substrate were used: glass slides and silicon (100) wafers with a native oxide layer. All glass substrates were cut into 2.5 cm × 2.5 cm squares and silicon wafers into 2 cm × 2 cm squares. Substrates were cleaned by ultrasonication in absolute ethanol for 30 min and dried under a nitrogen stream. Glass substrates were employed for microbiological testing, while both glass and silicon wafers were used for nanoscale imaging purposes.

6.3.3. PS-*b*-PEO thin film fabrication

PS-*b*-PEO diblock copolymers of two different molecular weights were dissolved in toluene to yield a 1 wt. % solution at room temperature. All solutions were aged for 12 h. PS-*b*-PEO thin films were fabricated by spin coating each solution at 3000 rpm for 30 s onto both glass and silicon substrates. The as-cast PS-*b*-PEO (42K-11.5K) thin films were exposed to a 50:50 v/v toluene-water mixed vapour placed at the bottom of a sealed vessel, kept at 50 °C for 1 h in vacuum to induce mobility and allow microphase separation to occur. Separate reservoirs were used for each solvent to avoid azeotropic effects. The as-cast PS-*b*-PEO (32K-11K) thin films were solvent annealed under slightly different conditions. These PS-*b*-PEO (32K-11K) thin films were exposed to 3 ml of toluene alone. The films were kept for 2 h at 50 °C to induce mobility and allow microphase separation to occur.

6.3.4. Activation of PEO cylinders and silver nanodot arrays using nanoporous templates

6.3.4.1. Silver nanodot arrays using PS-b-PEO (42K-11.5K) thin films

The resultant phase separated PS-*b*-PEO (42K-11.5K) thin film was immersed in ethanol at 40 °C for 15 h to activate the PEO cylinders.[14, 16] This nanoporous template was further used for the fabrication of silver nanodot arrays. 0.5 wt% of silver nitrate was dissolved in ethanol and spin coated onto the nanoporous film. The silver precursor solution underwent filtering (to further prevent the risk of particle agglomeration) before spin-coating onto the ethanol-treated polymer thin films. UV/ozone treatment was used in order to convert the precursor in to silver nanodots as well as to remove polymer residues. These silver nanodot arrays were used to examine the potential antimicrobial activity.

6.3.4.2. Silver nanodot arrays using PS-b-PEO (32K-11K) thin films

The resultant phase separated PS-*b*-PEO (42K-11.5K) thin film was immersed in ethanol and ultrasonicated for 15 min to form the nanoporous film by activating PEO cylinders, followed by drying under nitrogen stream. For the fabrication of silver nanodots, 0.5 wt% of silver nitrate was dissolved in ethanol and spin coated onto the nanoporous film. The silver precursor solution underwent filtering (to further prevent the risk of particle agglomeration) before spin-coating onto the ethanol-treated polymer thin films. UV/ozone treatment was used in order to convert the precursor in to silver nanodots as well as to remove polymer residues. These silver nanodot arrays were used to examine the potential antimicrobial activity.

6.3.4.3. Fabrication of high concentration of silver nanodots

To increase the silver concentration on the resulting thin films, we have modified the methods discussed in section 6.3.4.1 and 6.3.4.2. In this modified process, the fabrication of nanodot arrays was carried out as detailed in 6.3.4.1 and 6.3.4.1. In order to increase the amount of silver nanodots, the spin-coating of silver nitrate process and UV/ozone treatment were then repeated four times on the same substrate.

6.3.5. Biofilm Assay (1)

An overnight culture of *S. aureus*[17, 18] was grown in a universal shaking environment at 37 °C overnight.[19] The optical density of the sample was measured at a wavelength of 600 nm (OD_{600}), using a Beckman Coulter DU® 530 life Science UV/Vis Spectrophotometer and diluted to 0.05. The medium used here was luria broth (LB) media of composition tryptone (Merck) 10 g L^{-1}, yeast extract (Becton Dickinson) 5 g L^{-1}, sodium chloride (Sigma) 5 g L^{-1}, agar (Merck) 15 g L^{-1}. Three each of the PS-*b*-PEO, 42K-11.5K and 32K-11K templates, on 2.5 cm × 2.5 cm glass substrates, containing silver nanodot arrays were inoculated. This was achieved by complete submersion in 20 ml of diluted culture in three separate 50 ml conical screw cap tubes. As controls, three plain glass substrates of the same size, which had undergone identical cleaning processes as described above, were inoculated in this way. Also, to investigate the effect of the BCP pattern alone on the occurrence of biofilm formation, three PS-*b*-PEO thin films, 42K-11.5K and 32K-11K each were tested in the same manner. All instruments and mouths of tubes were flamed at regular intervals throughout this procedure to avoid contamination. Sample tubes were incubated at 37 °C for 24 h without shaking. Samples and control slides were washed three times by submersion in 35 ml water and then placed in separate 25 ml solutions of 0.1 % crystal violet stain for 10 min at room temperature. This was followed by three more water washings and drying at room temperature. The entire assay was carried out in three separate replicate experiments in order to verify the authenticity and reproducibility of results.

6.3.6. Biofilm Assay (2)

Overnight cultures of *S. aureus* and *P. aeruginosa*[20, 21] were grown in the same manner[19] as described above and the OD_{600} for both was again diluted to 0.05. Three each of silver nanodot arrays fabricated using PS-*b*-PEO, 42K-11.5K on glass substrates and silicon wafers were inoculated separately for each bacterial culture, and incubated in the same conditions as outlined in Biofilm Assay (1). Washings and crystal violet staining were also carried out in the same way. Again, this assay was conducted in three separate replicate experiments.

6.3.7. A549 Cell Attachment

In order to test the biocompatibility of these materials, the silver nanodot arrays were incubated with A549 human lung epithelial cells at 37 °C in a 5 % carbon dioxide environment. We have chosen A549 human lung epithelial cells because it has been widely used in studying P. aeruginosa.[22, 23] Three silver coated surfaces and three glass substrate controls were inoculated in a six well plate, with 100,000 cells per well. The medium employed was Minimal Eagle's Medium (MEM) from Sigma. This was supplemented with 10 % foetal bovine serum, containing growth factors to aid cell attachment and initiate growth.[24] 2 mmol L-Glutamine (an essential amino acid) and 1 % penicillin-streptomycin (to prevent bacterial contamination of cells) were also contained in the MEM medium.

6.3.8. Biological Imaging

Samples from Biofilm Assay (1) were imaged using a Zeiss AxioCam MRm microscope coupled to AxioVision live software. Samples from Biofilm Assay (2) were imaged in the same way under both Zeiss AxioCam MRm and Leica DM 1000 microscopes. A549 epithelial cell attachment was monitored by visualisation via the Olympus CKX41 microscope in association with Cell^{B} imaging software. Cell attachment was followed over the course of three days, with imaging carried out every 2 h for the first day and three times per day thereafter.

6.4. Results and Discussion

6.4.1. Fabrication of PS-*b*-PEO thin film and activation of PEO cylinders

Figure 6.1a shows an AFM image of the PS-*b*-PEO 42K-11.5K solvent annealed[25, 26] film (40 nm thick as determined by ellipsometry) demonstrating the vertically orientated hexagonal arrangement expected. We suggest that after solvent annealing the surface remains PS rich and a wetting layer exists. The minor component, PEO, forms the cylindrical domains (darker contrast in AFM) and the major component, PS, constitutes the matrix (lighter contrast in AFM). The measured average centre-to-centre cylinder spacing is ≈ 42 nm with a PEO cylinder diameter of ≈ 19 nm. The strong multiple peaks in the FFT pattern shown in the inset of Figure 6.1a confirm a microphase separated structure with highly ordered

hexagonal arrangement of PEO cylinders. The SEM image in Figure 6.1c also depicts long range ordering of the PS-*b*-PEO thin film.

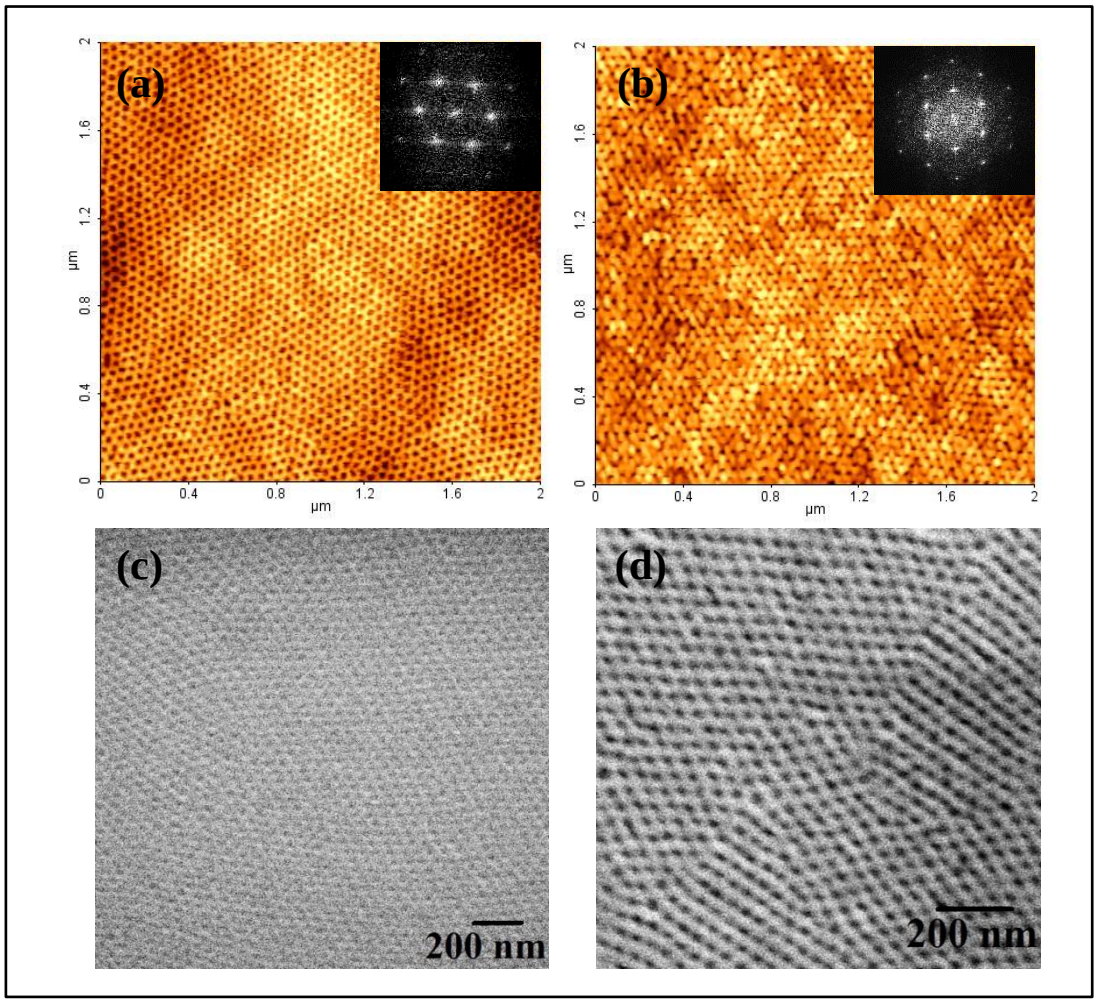

Figure 6.1. (a) and (b) AFM, (c) and (d) SEM images of PS-*b*-PEO 42K-11.5K thin film solvent annealed in toluene-water at 50 °C and nanoporous template after ethanol treatment respectively.

When the solvent annealed films were ethanol treated at 40 °C for 15 h, modification of the film occurred although the structural arrangement and dimensions are unchanged. Longer exposure to ethanol and higher temperatures resulted in structural degradation.[15] The AFM image (Figure 6.1b) shows some increase in the phase contrast and an increase in the long-range order. This is also indicated by the FFT of the AFM image (inset, Figure 6.1b) where six-point patterns

with multiple higher order reflections are shown, characteristic of exceptional long-range order. Also, the SEM image contrast was enhanced by ethanol exposure as seen in Figure 6.1d. No thickness loss was observed after the ethanol treatment as measured by optical ellipsometry. The ethanol treatment is a pre-requisite to form well-defined oxide nanopatterns in later steps and is described as an 'activation step'. On exposure to ethanol, there is a slow change in structure that removes this thin wetting layer through film re-structuring. It is suggested that this ethanol activation process also displaces water (from the solvent annealing process) from the PEO cylinders. Significant amounts of water are expected to be present as PEO is an important hydrogel forming polymer.[16] It is clear that ethanol removal of the water is slow because of the PEO–water affinity.

The films prepared using 32K-11K underwent the same imaging techniques (Figure 6.2) in order to compare the effects of polymer molecular weight on pattern dimensions and structure regularity. The measured average centre-to-centre cylinder spacing is ≈ 32 nm with a PEO cylinder diameter of ≈ 17 nm. It can be seen from the AFM and SEM images that the size of microdomains in the polymer matrix strongly depends on the molecular weight of the starting block copolymers.[27] Those with higher molecular weights give rise to larger features than those with lower molecular weights. Since the higher molecular weights correspond to a greater number of monomer units per polymer chain, a bigger volume is occupied by each microdomain meaning a larger feature size. Thus, the dimensions of surfaces can be readily tuned simply by adjusting polymer molecular weight. The smaller feature size is limited by the degree of segregation, χN, as no phase separation is expected for the lower limit of χN. Here, χ is the magnitude of Flory-Huggins interaction parameter of the polymers and N is the overall degree of polymerization. On the other hand, the larger feature size is limited by the kinetics of ordering, which is significantly slower for BCPs with higher molecular weight.[28]

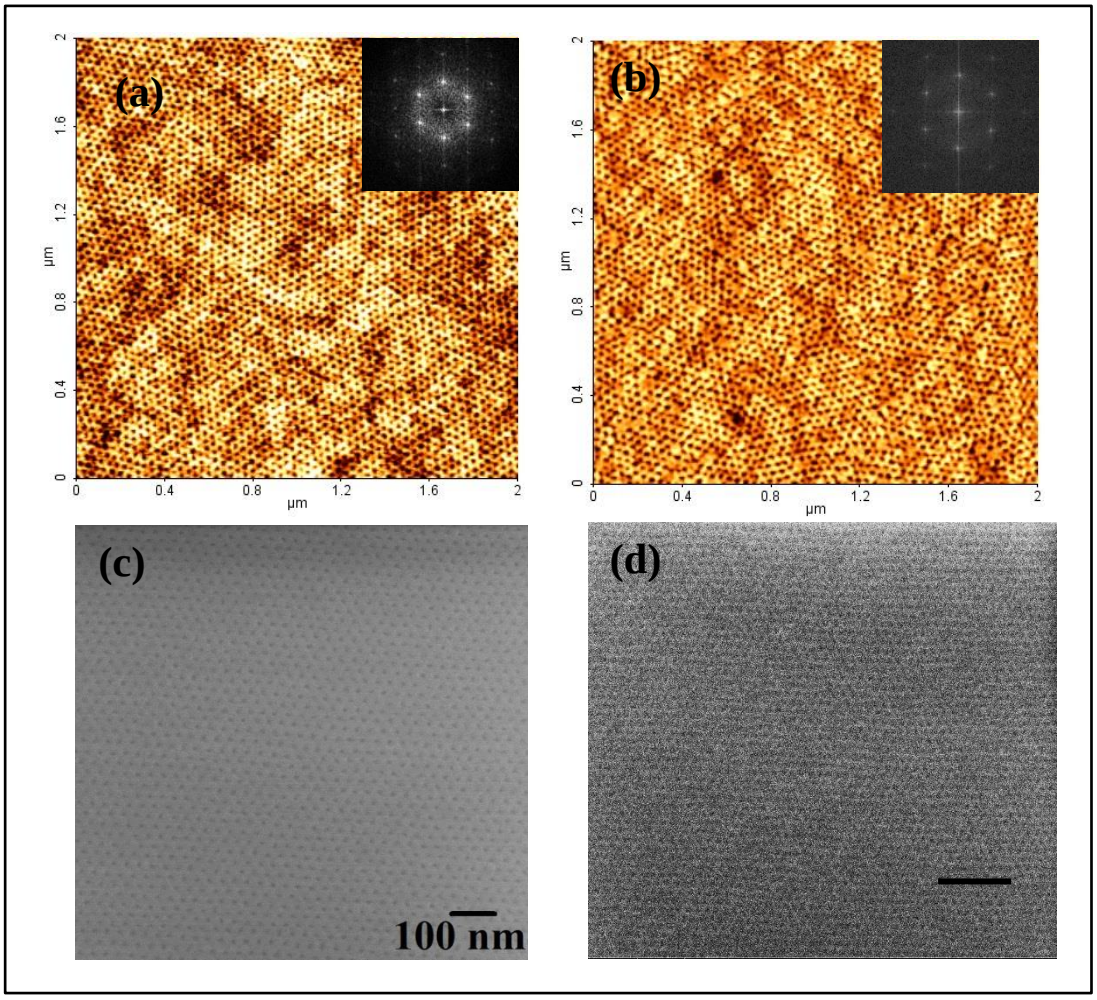

Figure 6.2. (a) and (b) (AFM), (c) and (d) (SEM) images of PS-*b*-PEO 32K-11K thin film solvent annealed in toluene at 50 °C and nanoporous template after ethanol treatment respectively.

6.4.2. Fabrication of silver nanodot arrays

Silver coatings have remained a popular area of antimicrobial research.[6, 7] A diagram of the fabrication process of silver nanodot arrays is shown in Scheme 6.1. The hexagonally arranged microphase separated BCP film (Scheme 6.1A) was treated with ethanol causing 'activation' of the PEO cylinders (Scheme 6.1B) as shown precisely. The metal ion solution was then spin-coated onto the film and diffuses within the PEO structures driven by capillary solution forces (Scheme 6.1C). UV/ozone treatment was carried out to convert the precursor into oxide as well as for complete degradation of the residual polymers (Scheme 6.1D).[26]

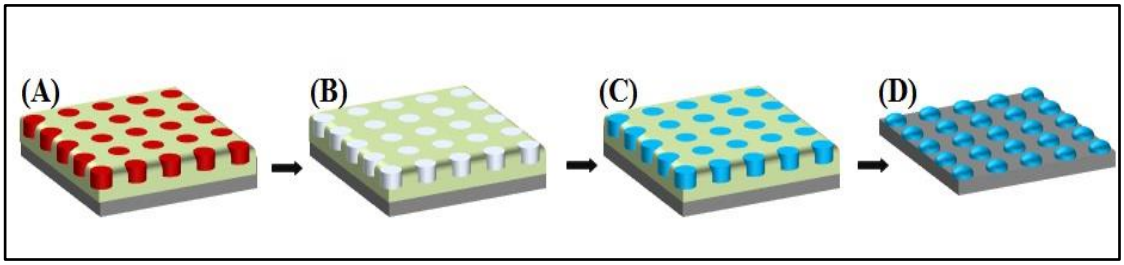

Scheme 6.1. Schematic illustration of the fabrication of silver nanodots. (A) Highly ordered PS-*b*-PEO thin film prepared by a solvent annealed process. (B) A nanoporous template produced by activation of PEO cylinders. (C) Silver oxide precursor moves into the cylinders after spin coating the precursor solution. (D) Silver nanodots remain after UV/ozone treatment.

The silver precursor solution ($AgNO_3$) was subjected to filter (to further prevent the risk of particle agglomeration) before spin-coating onto the ethanol-treated polymer thin films. The hydrophobic nature of PS excludes any probability of ion inclusion into the PS template, so that the PEO activated sites can be considered as sorbtive cylinders. The efficiency of this solution-mediated inclusion indicates that some PEO still remains at this stage of the procedure, as the hydrophobicity of PS means that it is highly unlikely that significant metal uptake would occur if PEO removal had gone to completion. We believe that the mechanism of cation inclusion is probably based on either intra- or intermolecular coordination via electron donation from PEO block oxygen atoms. UV/ozone treatment was carried out immediately after coating, in order to form silver nanodots while simultaneously removing the residual polymer component. In this process, ozone, an active oxidizing agent, is generated *in situ* from atmospheric oxygen by exposure to 185 nm UV light. This subsequently photo-dissociates into molecular oxygen and atomic oxygen upon exposure to 254 nm light. The latter reacts with the polymer to form free radicals and activated species that eventually remove organic portions of the polymer in the form of carbon dioxide, water and a small amount of volatile organic compounds.

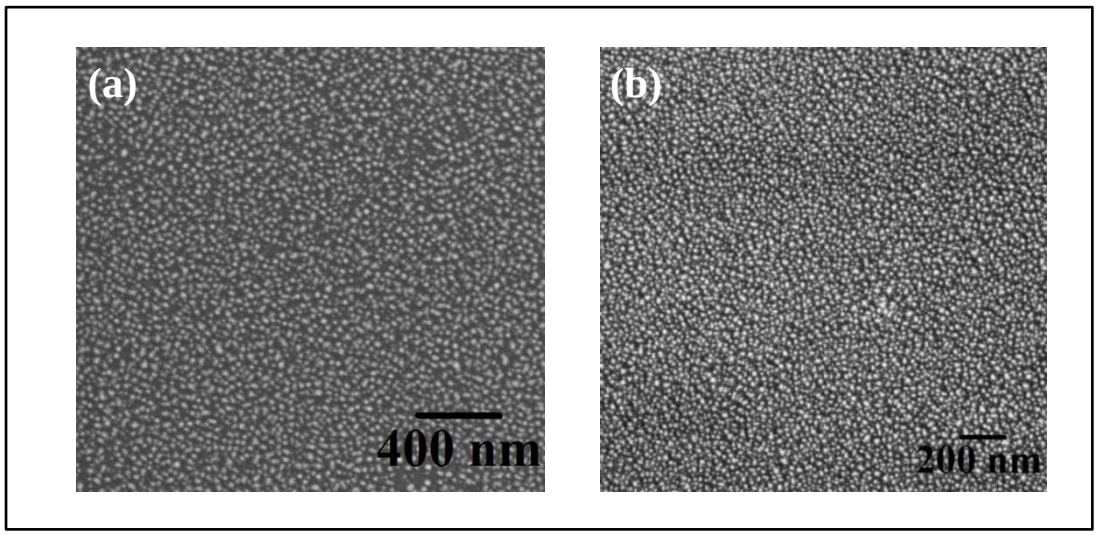

Figure 6.3. SEM images of silver nanodot arrays fabricated using (a) 42K-11.5K PS-*b*-PEO and (b) 32K-11K PS-*b*-PEO.

Figure 6.3 (a) and (b) shows SEM images of the 42K-11.5K PS-*b*-PEO and 32K-11K PS-*b*-PEO templated silver nanodot arrays respectively. A ordered pattern of nanodots were observed for both templates of PS-*b*-PEO. A broader size distribution was revealed for the higher molecular weight (42K-11.5K) polymer templates (Figure 6.3.a). The average centre-to-centre nanodot distance is equivalent to the distance between domain centres in the original microphase-separated PS-*b*-PEO (42 nm for 42K-11.5K and 32 nm for 32K-11K), confirming that these have been produced via direct templating of polymer films. The height of silver nanodots on substrates measured by ellipsometry is 9 nm for 42K-11.5K and 6 nm for 32K-11K.

6.4.3. TEM of the silver nanodots

TEM was used to visualise single as well as clusters of silver nanoparticles. Surfaces of substrates were scratched with a blade and the deposits were dissolved in anhydrous ethanol and introduced into a TEM grid. A TEM image of a group of nanoparticles is shown in Figure 6.4 as well as a single crystalline silver nanoparticle. The nanoparticles were almost circular spherical in shape with a smooth surface morphology. The diameter of the nanoparticles is found to be

approximately 12 nm and 18 nm for 32K-11K and 42K-11.5K templates respectively in agreement with the SEM measurements described earlier.

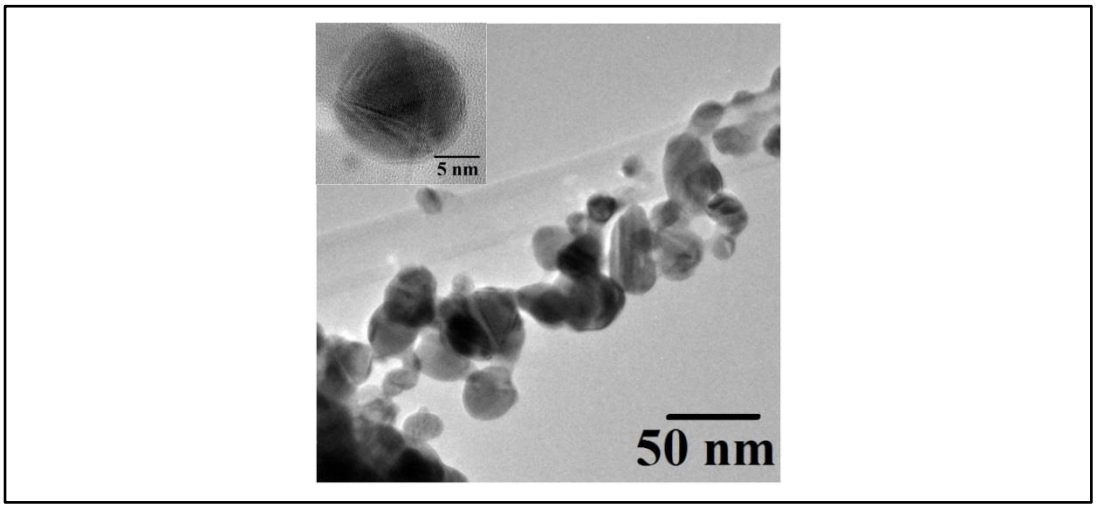

Figure 6.4. TEM image of silver nanoparticles (from 42K-11.5K sample). Inset shows high magnification image of crystalline silver nanoparticle.

6.4.4. EDAX of the silver nanodots

Energy-dispersive X-ray spectroscopy (EDX) coupled to the TEM instrumentation was used to confirm presence of silver nanodots. Figure 6.5 shows that prominent peak of silver is present in EDAX. Silver oxide may also be formed initially under UV-ozone, but this then rapidly decomposes to the metal.

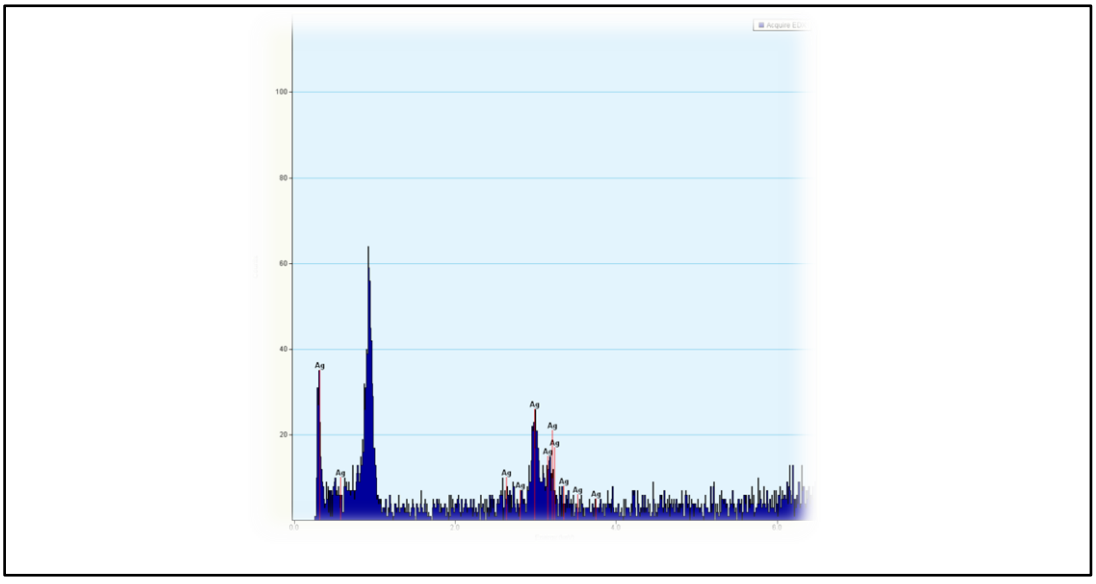

Fig. 6.5. EDX spectrum from TEM. Other peaks shown in the spectrum can be attributed to silicon substrate.

6.4.5. XRD of the silver nanodots

The crystallinities and phase purities of the silver nanoparticles were examined by XRD analysis (Figure 6.6). The diffractograms obtained matched the standard patterns of silver (JCPDS file No. 04-0783). The two diffraction peaks observed can be readily assigned to a face-centered-cubic silver (JCPDS file No. 04-0783) structure and the features at 2θ values of 38.24° and 44.42° can be indexed as (111) and (200) reflection planes respectively. No peaks from other phases were detected, indicating a high degree of phase purity and little indication of a silver oxide component.

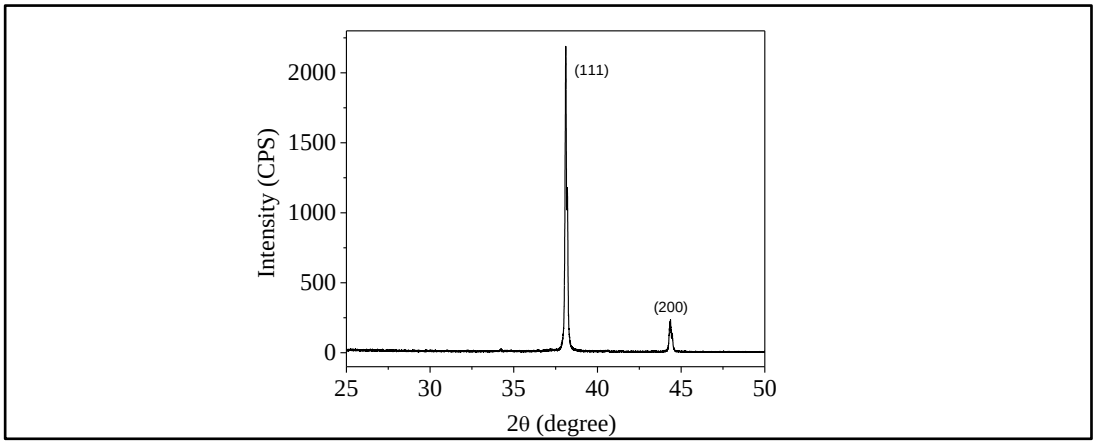

Figure 6.6. XRD spectrum of face-centered-cubic silver nanodots.

6.4.6. Antimicrobial study of silver nanodot arrays using biofilm assay (1) – *S. aureus*

Figure 6.7 shows the images of inoculated samples as viewed using an optical microscope. All films are on glass substrate. The glass control shows large amounts of attachment as expected. However, the lack of bacterial growth on the polymer surfaces alone (without silver nanodots) is surprising. While it may be rationalized that attachment could be inhibited due to topography/variations in surface height or possible hydrophobic effects previously discussed,[29-31] such striking results were not expected for these surfaces alone.

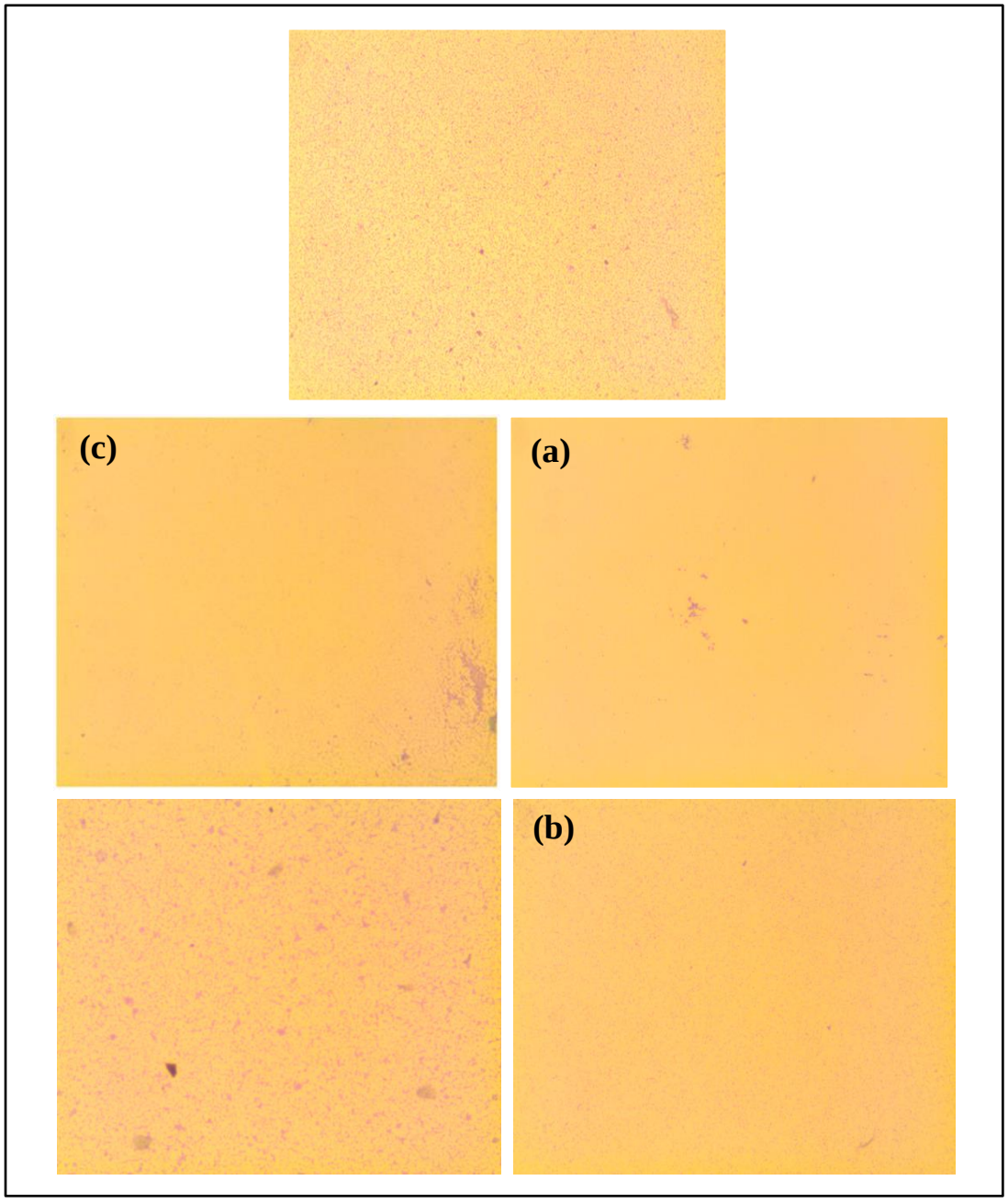

Figure 6.7. Films viewed under optical microscope following overnight incubation with *S. aureus* and staining with 0.1 % crystal violet (a) Plain glass (control) (b) PS-*b*-PEO 32K-11K (c) PS-*b*-PEO 42K-11.5K (d) 32K-11K template containing silver nanodots (e) 42K-11.5K template containing silver nanodots. Pink regions indicate bacterial attachment.

In this study, the polymer surfaces showed superior resistance to attachment compared to the silver nanodot patterns. These findings require further investigation

before definitive conclusions can be drawn. The 32K-11K templated silver nanodot arrays showed little to no resistance. It can be seen, however, that a significant inhibitory effect was produced by the 42K-11.5K templated silver nanodot arrays. For this reason, only the PS-*b*-PEO 42K-11.5K polymer was utilized for further patterning and biological testing. It was concluded that the amount of silver in the coatings needed to be increased in order to achieve the desired effects. The experimental process described above (Section 6.3.4.3) was used to increase the levels of silver present without exceeding the concentration of precursor solution which was earlier established to produce the most ordered nanopatterns. Through this method, we believe that the amount of silver in the coatings accumulates only within the nanodot confinements. Further, silver deposits should bind exclusively to the pre-existing nanodots and not to the plain glass substrate. In this way, structures may grow vertically, but the dispersion pattern is maintained.

6.4.7. Antimicrobial study of silver nanodot arrays using biofilm assay (2) – *S. aureus*

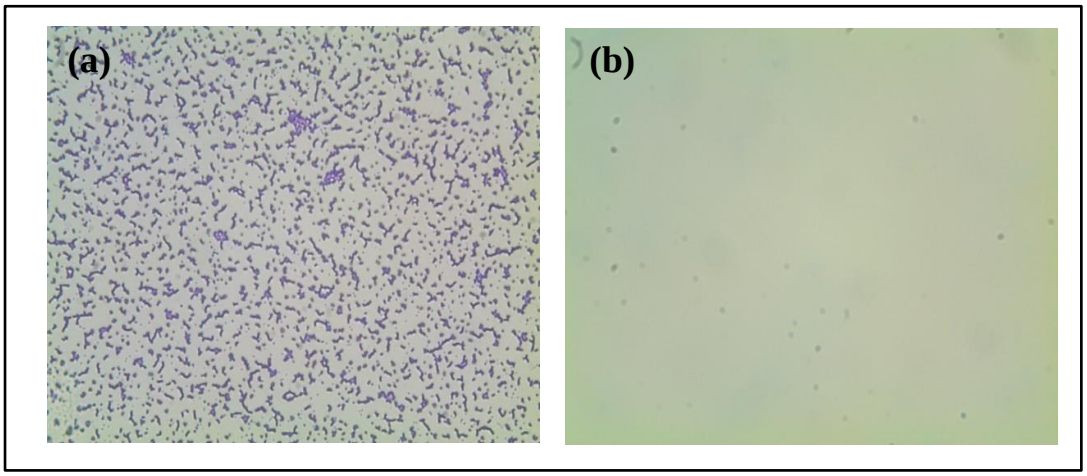

Figure 6.8. Films viewed under optical microscope following overnight incubation with *S. aureus* and staining with 0.1 % crystal violet. (a) Plain glass (controls) (b) PS-*b*-PEO 42K-11.5K template containing silver nanodots (from section 6.3.4.3). Purple regions indicate bacterial attachment.

Figure 6.8 shows the images of overnight inoculated samples with *S. aureus* and staining with 0.1% crystal violet as viewed using optical microscope. Silver

nanodot arrays on 42-11.5K templates are used for this study. Silver nanodot arrays with modified process (section 6.3.4.3) shows exceptional resistance to *S.* aureus attachment. This illustrates that silver nanodots with modified process (from section 6.3.4.3) shows good antimicrobial activity (Figure 6.8b) over the single coting silver nanodots (Figure 6.7e). Thus, antimicrobial activity of silver increased with the higher concentration of silver nanodot arrays. This assay was repeated 3 times in full to check the reproducibility of the results. Identical results were reproduced each time.

6.4.8. Antimicrobial study of silver nanodot arrays using biofilm assay (2) – *P. aeruginosa.*

Figure 6.9 shows the images of overnight inoculated samples with *P. aeruginosa* and staining with 0.1% crystal violet as viewed using optical microscope. Silver nanodot arrays on 42-11.5K templates are used for this study. Figure 6.9 shows that silver nanodot arrays with modified process (from section 6.3.4.3) has exceptional resistance to *P. aeruginosa* attachment.

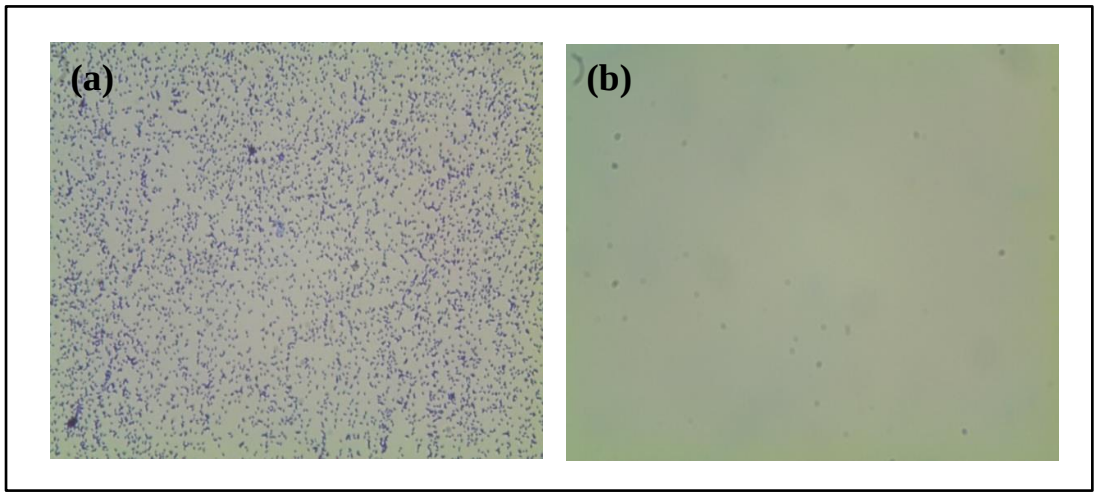

Figure 6.9. Films viewed under optical microscope following overnight incubation with *P. aeruginosa* and staining with 0.1 % crystal violet. (a) Plain glass (controls) (b) PS-*b*-PEO 42K-11.5K template containing silver nanodots (from section 6.3.4.3). Purple regions indicate bacterial attachment.

6.4.9. A549 Cell Attachment

To test the biocompatibility of the modified surfaces, PS-*b*-PEO 42K-11.5K template containing silver nanodots samples were incubated with human lung epithelial A549 cells. These should attach and grow on surfaces which are not cytotoxic. Samples were viewed using an Olympus CKX41 optical microscope. However, due to Cell^{B} imaging software maintenance issues, a complete set of images have not yet been recorded. Figure 6.10.a and 6.10b shows what healthy cells should look like ("teardrop" shape) in this experiment as well as Figure 6.10c and d is an example of cells which have come into contact with a cytotoxic environment.

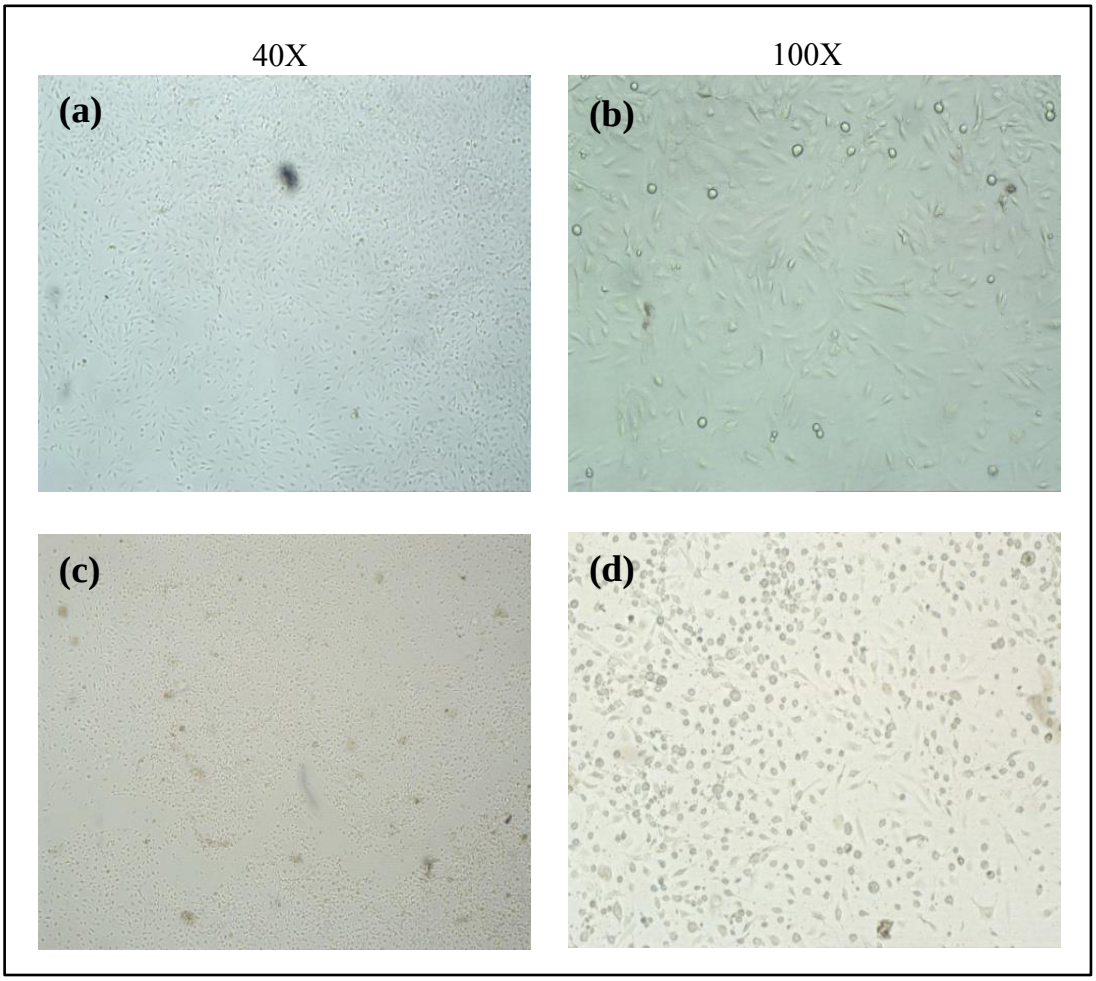

Figure 6.10. (a) and (b) show what healthy epithelial cells should look like upon attachment to plane glass (controls) (c) and (d) PS-*b*-PEO 42K-11.5K template containing silver nanodots samples depict cells which have been damaged due to cytotoxicity (cell "rounding" and bursting).

The silver coatings tested under these conditions showed possible evidence of cytotoxic effects. Cells which were incubated with these samples began to show some of the characteristics pictured in the unhealthy cells above in Figure 6.10c and 6.10d, such as rounding and early signs of leakage. Again, further tests in this area are required before any results can be confirmed. It may be a case that there is now an excessive dosage of silver in the coatings and this could be rectified by further modifying the fabrication procedure.

6.5. Conclusion

A simple, generic and cost-effective route was demonstrated to fabricate well-ordered arrays of silver nanodots over wafer scale. The silver nanodots formed have uniform sizes and shapes and are structurally arranged in a mimic of the original self-assembled BCP pattern. It is suggested that the dots are formed by selective inclusion of a silver ion solution in the hydrophilic PEO cylinders of the microphase separated structure. The nanodots inclusion does not compromise the BCP structure. The size of the silver nanodots can be controlled by variation of the molecular weights of PS-*b*-PEO. AFM and SEM techniques were used to confirm morphology and topography of PS-*b*-PEO films. Several complementary techniques have been used to confirm the size and patterns of silver nanodots. Silver nanodot arrays were successfully tested for antimicrobial activity over *S. aureus* and *P. aeruginosa* biofilms. Result shows that a higher concentration of silver nanodots has good antimicrobial activity for both *S. aureus* and *P. aeruginosa* biofilms. Indication of cytotoxicity was observed for the Ag modified substrates but this may be related to high surface concentrations and some future optimization of Ag content may be required.

6.6. References:

1. A. Komeili, *Annu. Rev. Biochem.*, 2007, **76**, 351-366.
2. S. Neidle, *Oxford Handbook of Nucleic Acid*, Oxford University Press: Oxford, UK, 1999.

3. W. J. Crookes-Goodson, J. M. Slocik and R. R. Naik, *Chem. Soc. Rev.*, 2008, **37**, 2403-2412.
4. R. O. Darouiche, *N. Engl. J. Med.*, 2004, **350**, 1422-1429.
5. I. Banerjee, R. C. Pangule and R. S. Kane, *Adv Mater*, 2011, **23**, 690-718.
6. Y. Matsumura, K. Yoshikata, S. Kunisaki and T. Tsuchido, *Appl. Environ. Microbiol.*, 2003, **69**, 4278-4281.
7. Q. L. Feng, J. Wu, G. Q. Chen, F. Z. Cui, T. N. Kim and J. O. Kim, *J Biomed Mater Res*, 2000, **52**, 662-668.
8. C. Greulich, S. Kittler, M. Epple, G. Muhr and M. Koller, *Langenbeck Arch Surg*, 2009, **394**, 495-502.
9. N. Miura and Y. Shinohara, *Biochem. Biophys. Res. Commun.*, 2009, **390**, 733-737.
10. J. Siegel, O. Kvitek, P. Ulbrich, Z. Kolska, P. Slepicka and V. Svorcik, *Mater. Lett.*, 2012, **89**, 47-50.
11. S. Bratskaya, D. Marinin, F. Simon, A. Synytska, S. Zschoche, H. J. Busscher, D. Jager and H. C. van der Mei, *Biomacromolecules*, 2007, **8**, 2960-2968.
12. P. Pang and P. Englezos, *Colloid Surface A*, 2002, **204**, 23-30.
13. A. Roosjen, H. C. van der Mei, H. J. Busscher and W. Norde, *Langmuir*, 2004, **20**, 10949-10955.
14. T. Ghoshal, R. Senthamaraikannan, M. T. Shaw, J. D. Holmes and M. A. Morris, *Nanoscale*, 2012, **4**, 7743-7750.
15. T. Ghoshal, T. Maity, J. F. Godsell, S. Roy and M. A. Morris, *Adv Mater*, 2012, **24**, 2390-2397.
16. C. B. Tsvetanov, R. Stamenova, D. Dotcheva, M. Doytcheva, N. Belcheva and J. Smid, *Macromol. Symp.*, 1998, **128**, 165-182.
17. R. M. Klevens, M. A. Morrison, J. Nadle, S. Petit, K. Gershman, S. Ray, L. H. Harrison, R. Lynfield, G. Dumyati, J. M. Townes, A. S. Craig, E. R. Zell, G. E. Fosheim, L. K. McDougal, R. B. Carey and S. K. Fridkin, *Jama-J Am Med Assoc*, 2007, **298**, 1763-1771.
18. A. Umeda, Y. Ueki and K. Amako, *J. Bacteriol.*, 1987, **169**, 2482-2487.
19. N. Jiang, N. S. Tan, B. Ho and J. L. Ding, 2007.

20. A. Nikulin, E. Stolboushkina, A. Perederina, I. Vassilieva, U. Blaesi, I. Moll, G. Kachalova, S. Yokoyama, D. Vassylyev, M. Garber and S. Nikonov, *Acta Crystallogr D*, 2005, **61**, 141-146.
21. D. S. Kim, J. Marsillach, C. E. Furlong and G. P. Jarvik, *Pharmacogenomics*, 2013, **14**, 1495-1515.
22. E. Chi, T. Mehl, D. Nunn and S. Lory, *Infect. Immun.*, 1991, **59**, 822-828.
23. Y. X. Q. O'Malley, K. J. Reszka, G. T. Rasmussen, M. Y. Abdalla, G. M. Denning and B. E. Britigan, *Am J Physiol-Lung C*, 2003, **285**, L1077-L1086.
24. M. Kalbacova, A. Broz and M. Kalbac, *J Biomed Mater Res A*, 2012, **100A**, 3001-3007.
25. J. Peng, D. H. Kim, W. Knoll, Y. Xuan, B. Li and Y. Han, *J. Chem. Phys.*, 2006, **125**, 064702.
26. T. Ghoshal, M. T. Shaw, C. T. Bolger, J. D. Holmes and M. A. Morris, *J. Mater. Chem.*, 2012, **22**, 12083-12089.
27. T. Ghoshal, T. Maity, R. Senthamaraikannan, M. T. Shaw, P. Carolan, J. D. Holmes, S. Roy and M. A. Morris, *Sci Rep-Uk*, 2013, **3**, 2772.
28. J. Bang, U. Jeong, D. Y. Ryu, T. P. Russell and C. J. Hawker, *Adv Mater*, 2009, **21**, 4769-4792.
29. K. Kuroda, G. A. Caputo and W. F. DeGrado, *Chem-Eur J*, 2009, **15**, 1123-1133.
30. V. Sedlarik, *Antimicrobial Modifications of Polymers* 2013.
31. F. P. Edmund, V. Satyavani and K. Kenichi, in *Tailored Polymer Architectures for Pharmaceutical and Biomedical Applications*, American Chemical Society 2013, vol. 1135, ch. 19, pp. 319-330.

Chapter 7

Summary and Conclusions

This Ph.D. thesis consists of two distinct parts. In the first part, synthesis and characterization of crystalline metal oxide nanoparticles such as cerium oxide (CeO_2) and silicon dioxide (SiO_2) were described. During the course of these studies, the properties of nanometer-scale oxide nanoparticles have been probed. The initial focus of this work was centered on the properties of doped metal oxide nanoparticles. The second part of the thesis focuses on the formation of mesoporous thin films and nanopatterned features by BCP approach. These would appear to be a marked difference in these approaches. The reason for these two different approaches was largely the result of trying to use chemically synthesized particles in processes such as thin film generation. Although, we used quite complex and exacting methods, it was not possible to use particles in film processing because they simply lacked the requisite size and shape monodispersity required. All chemical based methods will give a statistical distribution of size/shape and it was not possible to obtain the properties needed for our work. Thus, we developed a second approach, based on film processing. These methods give more refined film structures. In actual application, both approaches are needed. Where large quantities of materials are needed of low cost, wet synthesis methods such as co-precipitation are favoured. For making low volume, high quality samples, thin films have advantage.

Chapter 1 of this thesis provided a literature overview of various synthesis methods used to synthesize metal oxide nanoparticles. Different characterization techniques and applications of metal oxide nanoparticles were summarised. Synthesis and applications of mesoporous silica thin films and use of BCPs for nanopattering were also briefly introduced. It can be seen that a dizzying array of preparations are possible and careful choice of methodology is needed.

A stable method to synthesize various sized and functionalized silica nanoparticles was described in chapter 2. IR-820 and FITC dyes were successfully incorporated into silica matrix by simple impregnation method. The stability of dye-doped silica nanoparticles were tested with the UV-Vis spectroscopy. A clear zero-sum increase-decrease relation of the absorbance intensity at 366 and 750 nm for IR-820 dye has been observed, where the decrease at 750 nm indicates the degradation

of the IR-820 dye molecules in aqueous solution while the increase at 366 nm implies the formation of some new substances. However, the feature absorbance peak of FITC at 490 nm is constant for all FITC dye-doped silica nanoparticles indicating the FITC molecules are more stable than the IR-820 dye-doped silica nanoparticles under the same conditions. Also, a new type of dual dye-doped hybrid silica nanoparticles has been developed. The combination use of TEM, SEM, UV-Vis and confocal microscope shows the synthesis parameters have significant effects on the particle shape and size and the size is tuneable from a few nanometers to a few hundred nanometers. The ability to create size controlled nanoparticles with associated (optical) functionality may have significant importance in bio-medical imaging.

Chapter 3 described the Eu doping of CeO_2 nanoparticles which were synthesized by a simple solvothermal process. These materials were chosen because of their luminescent properties which could allow synthesis of particles where dyes could be avoided. The size of the CeO_2 was varied in the range of 3-9 nm and was dependent on the Eu concentration. The concentrations and distributions of the dopants within the nanoparticles were investigated by different microscopic and spectroscopic techniques. This showed that even with careful experimental conditions, great care is necessary to control the composition and distribution of atoms in there binary metal-oxide systems. An increase in the measured lattice parameter was observed due to inclusion of the larger Eu cations but at very small doping concentrations, lattice contraction was observed due to surface tension-type effects. It was definitively shown that the insertion of the rare earth cations in the CeO_2 structure provokes an increase in the oxygen vacancies concentration through the promotion of the non-stoichiometric condition of the cerium oxide, by the reduction of Ce^{4+} to Ce^{3+}. The crystal structure and spectroscopic analysis reveals almost similar concentrations for Ce^{3+} and Eu^{3+} and suggest the Eu species are mainly located in the lattice sites. The incorporation and homogeneous distribution of Eu ions in the ceria nanoparticle is also confirmed. The band gap of the doped CeO_2 nanocrystals were found to decrease with the doping due to the formation of localized states within the band gap owing to the increase in oxygen vacancies and

Ce^{3+} concentrations. The luminescent property enhancement with doping and the detailed explanations for this were reported. Additionally, the morphological and structural evolution and optical properties were correlated as a function of concentrations of Eu doping as well as with further annealing. High temperature calcinations reduce the defect density, increasing the crystallite size thereby increasing the degree of crystallization. The ability to tailor the ionization state of cerium and the oxygen vacancy concentration in CeO_2 has applications in a broad range of fields, which include catalysis, biomedicine, electronics and environmental sensing.

Chapter 4 focused on a positron annihilation spectroscopic study of vacancy type defects formed due to Eu doping in ceria crystallites supported by UV-Vis spectra and XRD. This provided much more detail than the more established techniques used in chapter 3. A notable observation is the decreasing particle size with increase in the concentration of doping but the trend is interrupted in medium concentrations of doping due to the reduction of Ce^{4+} to Ce^{3+} when an increasing concentration of oxygen vacancies resulted an increase in particle size through ion diffusion process. Optical absorption measurements showed a distinct decrease in band gap energy with increasing doping. However, size defined quantum confinement effects for particles of dimensions below the exciton Bohr radius, were apparent in a characteristic blue shift of the optical absorption spectra. The vacancy type defects were investigated through positron lifetime and CDBS measurements. The intermediate particle size enhancement came as a result of the generation of additional oxygen vacancies in the samples and is indicated by a distinct change in the intensity of positrons trapped in the defects. The positron lifetime within the vacancies was delineated from that due to annihilation at the crystallite surfaces and it was found to enhance due to vacancy agglomeration at higher concentrations of doping. The CDBS measurements demonstrated annihilations taking place with the electrons of ions of different charges and momentum distribution and the variation of the lineshape parameters derived from it further supported the findings from positron lifetime measurements.

It can be readily seen that absolutely precisely defined nanostructures could not be produced from these particulate methods and instead precision was examined using thin film techniques. A simple, generic and cost-effective route was used to demonstrate the synthesis of 2D mesoporous silica thin films over wafer scale dimensions in chapter 5. Morphological studies show that the mesoporous silica thin film has hexagonally arranged pores with highly uniform pore diameter. In order to access the pores, we attempted to topographically pattern these films. Lithographic resist and *in situ* hard mask block copolymer followed by ICP dry etching were used to fabricate mesoporous silica nanostructures. The width of mesoporous silica channels can be varied by using a variety of commercially available lithographic resists whereas depth of the mesoporous silica channels can be varied by altering the etch time. Large area ordered mesoporous silica nanopillar arrays were fabricated by an *in situ* hard mask BCP with smooth vertical sidewall profiles. In the *in situ* hard mask BCP approach, the diameter and length of the nanopillars is precisely defined depending on the diameter of the nanodots and the etching time respectively without altering their shape. The mesoporous silica channels or nanopillars arrays exhibit large surface areas and may allow direct access to the pore structures for many applications in the manufacturing of future nanoscale devices.

A novel, simple and *in situ* hard mask technology was used to demonstrate that well-ordered arrays of silver nanodots over wafer scale could be fabricated in chapter 6. The particle size and shape of these could be much more precisely controlled then any wet techniques. The silver nanodots that were formed had highly uniform sizes and shapes and are structurally arranged in a mimic of the original 2D hexagonal self-assembled BCP pattern. It is suggested that the dots are formed by selective inclusion of a silver ion solution in the hydrophilic PEO cylinders of the microphase separated structure. The nanodots inclusion does not compromise the BCP structure. The size of the silver nanodots can be controlled by variation of the molecular weights of PS-*b*-PEO. AFM and SEM techniques were used to confirm morphology and topography of PS-*b*-PEO films. Several complementary techniques have been used to confirm the size and patterns of silver nanodots. Silver nanodot arrays were successfully tested for antimicrobial activity over *S. aureus* and *P.*

aeruginosa biofilms. Result shows higher concentration of silver nanodots has good antimicrobial activity for both *S. aureus* and *P. aeruginosa* biofilms.

There is no doubt from this work that methods such as block copolymer self-assembly can provide a route to nanodot or nanoparticle arrays where the individually defined particles have a highly regular size. The method takes advantage of the precision of block copolymer patterns which provide surface arrangements of lithographic quality. As such, techniques such as colloidal growth, precipitation, sol-gel etc. cannot reproduce this precision because of the statistical value of the growth mechanism. However, the BCP method is related only to films. To use the method to create free nanoparticles, they could have to be released from the surface. This in itself might be a limitation, because after release the particles may form aggregates and this would provide a greater particle size and a more conventional distribution of sizes.

Whilst of might be easy to think of detachment methods (e.g. dissolution of a support film), an estimate of how many particles can be produced is important. If we assume a substrate of 1 m^2, particles of around 1000 nm^3 and a coverage of particles on the surface of 50 %. The approximate weight of particles is 10^{-20} g and there would be around 10^{16} particles across the substrate. That is one could liberate around 10^{-4} g of material. This implies major developments in processing and equipment if manufacture of large quantities was possible. Thus, as a means of mass production it is not yet viable. For this to be the case, several challenges would be needed:-

a) Very large area substrates such as roll-to-roll
b) A reusable BCP template
c) A non-damaging particle removal process

Whilst all of these are possible, their integration seems remote and traditional material synthesis will remain as a viable method despite the relatively poor particles formed. BCP particulate methods are thus likely to remain as specialist techniques of substrates or for possible very small volume, high cost niche markets. That said, this area of science/technology is developing rapidly. Although at the moment many of

the techniques may be related to e.g. semiconductor manufacture, improvements in understanding, processing methods and material availability may see these methods and achieve large volume production/use in areas such as catalysis.